



This is to certify that the

dissertation entitled

A SINGLE AND DOUBLE MAGNETIC RESONANCE SPECTROSCOPIC CHARACTERIZATION OF MEMBRANE PROTEINS

presented by

Matthew Paul Espe

has been accepted towards fulfillment of the requirements for

Ph D degree in Chemistry

Major professor

Date $\frac{4/23/94}{}$

MSU is an Affirmative Action/Equal Opportunity Institution

0-12771

LIBRARY Michigan State University

PLACE IN RETURN BOX to remove this checkout from your record. TO AVOID FINES return on or before date due.

DATE DUE	DATE DUE	DATE DUE

MSU is An Affirmative Action/Equal Opportunity Institution choircidatedus.pm3-p.1

A SINGLE AND DOUBLE MAGNETIC RESONANCE SPECTROSCOPIC CHARACTERIZATION OF MEMBRANE PROTEINS

By

Matthew Paul Espe

A DISSERTATION

Submitted to
Michigan State University
in partial fulfillment of the requirements
for the degree of

DOCTOR OF PHILOSOPHY

Department of Chemistry

ABSTRACT

A SINGLE AND DOUBLE MAGNETIC RESONANCE SPECTROSCOPIC CHARACTERIZATION OF MEMBRANE PROTEINS

By

Matthew Paul Espe

The membranous enzymes Photosystem II (PSII) and cytochrome c oxidase were studied by EPR, ENDOR, and ESEEM to characterize the geometric and electronic structure of several of their paramagnetic sites. These include the stable tyrosine radical, Y_D^+ , and the manganese cluster of PSII, and the bound manganese of cyotochrome oxidase.

By using ENDOR, and selective deuterium substitution, the two largest components of the 2,6 protons and the smallest component of the 3,5 protons hyperfine coupling tensor were measured for Y_D^+ . From these results, and ^{17}O hyperfine coupling values, the unpaired spin density in the phenol group is estimated to be: $C_3 = C_5 \cong 0.25$, $C_1 \cong 0.3$, and $O \cong 0.3$. The ENDOR spectra of PSII's isolated from *Synechocystis* contain a set of peaks with A=3.0 MHz that are D_2O exchangeable. These peaks are assigned to the A_\perp component of the hyperfine coupling tensor for a proton hydrogen bonded to the tyrosine radical.

The multiline EPR signal from the manganese cluster in PSII is unaffected by removal of the 17 and 23 kDa polypeptides and the light-harvesting complex proteins. EPR studies show that Sr²⁺ can be substituted for Ca²⁺ without use of chelators, by incubating PSII particles in a buffer containing 20 mM Sr²⁺. Three-pulse ESEEM studies of the multiline signal in samples containing Ca or Sr are the same. The ESEEM spectrum arises from the hyperfine interaction between the manganese cluster and a histidine ligand. The substitution of Sr for Ca does not effect the structure of the portion of the manganese cluster containing the histidine ligand.

Cytochrome c oxidase from *Rh. Sphaeroides* contains nonstochiometric quantities of tightly bound manganese. The quantity of bound manganese is controlled by the manganese concentration in the growth medium of the cells. Mutagenesis of residue histidine-411 or aspartate-412, in subunit 1, results in an enzyme devoid of manganese. These two residues form a portion of the manganese binding site. The EPR spectra of the bound manganese, from the fully reduced and the fully oxidized enzyme, are different. X-and Q-band EPR studies indicate small changes in manganese-ligand(s) bond length or bond angle of < 0.1 Å or 10°, respectively.

ACKNOWLEDGMENTS

During the course of graduate school there were many people who contributed to the completion of this work and I would like to thank them. First, to Chris Bender who put up with my many questions while teaching me the basics of EPR and ENDOR. I am also indebted to Curt Hoganson for his very helpful discussions on the ENDOR studies of Y_D^+ .

The ESEEM work was made possible by the collaboration with Professor John McCracken and his pack of "ESEEMers": Kurt, Michelle and Hong-In. My understanding of ESEEM would not have been possible without the many lengthy conversations I had with John.

I also had the privilege of collaborating with Neil Bowlby and Professor C.F.

Yocum on photosystem II and John Hosler and Professor Sheleigh Ferguson-Miller on cytochrome oxidase. I thank them for the great deal of biochemistry that they taught me. While my interactions with Neil and John proved fruitful scientifically, working with them was also a lot of fun. I also must thank Professor Yocum for his many "brilliant intellectual insights" that were bestowed upon us during group meetings.

The many fellow graduate students and post-docs in the lab made the time I did at MSU very enjoyable. Michelle, Craig, Einhard, Nikos, Hong, Matt, Curt, Kurt, Kerry, Doug and Michelle, thank you for keeping science fun. Also, a thanks to Kerry for keeping the job of taking care of the EPR such an adventure. I also must extend a special thanks to Michelle Mac for all her work on the PSII project and for keeping the countless

hours of PSII preps entertaining. Michelle also allowed me to use her ESEEM data on the multiline, in this thesis, for which I am indebted.

Most importantly, I thank G.T. Babcock for all that he did for me while working in his lab. I do not think I could have asked for a better situation in which to do my graduate work. In addition to the chemistry that you taught me, I also learned patience, perseverance, integrity, confidence, and the importance of controls while working for you. (The passion I already had). For all of this Jerry, I wish to thank you.

Lastly, but most importantly, I thank my family, Patty and Marisa, for persevering through this lengthy event and supporting me to the end.

TABLE OF CONTENTS

List of Tables		
List of Figures	viii	
Chapter1: Introduction to Photosystem II	1	
References	15	
Chapter 2: Magnetic Resonance	19	
References		
Chapter 3: ENDOR and ESEEM studies of YD+		
Introduction	41	
Materials and Methods		
Results and Discussion	49	
References	81	
Chapter 4: EPR and ESEEM studies of the multiline	signal of Photosystem II	
Introduction	•	
Materials and Methods		
Results and Discussion		
References	116	
Chapter 5: EPR and ESEEM characterization of Cyt	tochrome c Oxidase from	
Rh. Sphaeroides		
Introduction	120	
Materials and Methods	128	
Results and Discussion	131	
References	177	

LIST OF TABLES

Table 3.1: Hyperfine coupling constants for matrix protons	51
Table 3.2: Hyperfine coupling values for ring protons	62
Table 3.3: Hyperfine coupling values for tyrosine radicals	65
Table 3.4: Unpaired spin density distribution in tyrosine radicals	65
Table 5.1: Stochiometry of bound Mn in Rh. Sphaeroides oxidase	142
Table 5.2:Mn binding stochiometry and enzyme activity of subunit 1 mutan	t s 149
Table 5.3: EPR parameters determined from the Q-band EPR data	155

LIST OF FIGURES

Figure 1.1.	Model for the structure of the photosystem II/oxygen-evolving complex. Masses in kilodaltons are indicated for each polypeptide except for D1 and D2, which have masses of 34 and 32 kDa respectively. The b-559 heterodimer consists of polypeptides with masses of 4 and 9 kDa 2
Figure 1.2.	Model for the interaction of the D1 and D2 proteins based on the structure of the L and M subunits of the bacterial reaction center. The D_2E_2 helical core contains the chromophores involved in the primary charge separation events. The pseudo- C_2 symmetry axis is along the $P_{680} \rightarrow Fe^{2+}$ direction.
Figure 2.1.	Energy level diagram for a $S = 1/2$, $I = 1/2$ system in a constant magnetic field. The allowed EPR transitions are displayed
Figure 2.2.	Energy level diagram for a $S = 1/2$, $I = 1/2$ system in a constant magnetic field. The allowed EPR and ENDOR transitions are displayed 29
Figure 2.3.	A) experimentally observed lineshape for an axial hyperfine tensor, B) lineshape observed for a rhombic hyperfine coupling tensor
Figure 2.4	Magnetization of spin packets 1 and 2 during a 2-pulse experiment. a) in static field; b) after $\pi/2$ pulse; c) dephasing after time τ ; d) after π pulse and e) refocusing of spin packets after time τ to yield echo
Figure 2.5.	Energy level diagram for a $S = 1/2$, $I = 1/2$ system in a constant magnetic field. The allowed and semi-forbidden EPR transitions are displayed.36
Figure 2.6	Magnetization of spin packets 1 and 2, including the effect of semi-forbidden transitions, during a two-pulse experiment. A) a) after a $\pi/2$ pulse; b) dephasing of spin packets during time τ ; c) after π pulse showing the effect of branching and d) refocusing of spin packets 1 and 2 precessing at frequencies ω_1 and ω_2 . B) Echo amplitude versus the magnitude of τ giving rise to the echo-decay envelope
Figure 3.1	Free tyrosine showing the numbering system used in the text 42

Figure 3.2	EPR spectrum of Y _D ⁺ in PSII particles from Synechocystis 6803. Conditions: μwave power, 2mW; modulation, 4 Gpp; T, -155°C 44
Figure 3.3	ENDOR spectrum of (A) Y_D^+ in PSII particles from spinach and (B) benzoquinone anion radical. Conditions: (A) μ wave power; 3.5 mW, RF power; 120 W, RF modulation depth; 10 kHz, temperature; 120 K; (B) μ wave power; 2 mW, RF power; 85 W, RF modulation depth; 10 kHz, temperature; 110 K
Figure 3.4	ENDOR spectrum of Y _D ⁺ in PSII particles from spinach (A) untreated PSII particles, (B) reaction center complexes, and (C) tris washed reaction center complexes. Conditions: µwave power; 3.5 mW, RF power; 120 W, RF modulation depth; 10 kHz, temperature; 120 K
Figure 3.5	ENDOR spectrum of Y _D ⁺ in PSII particles from spinach (top) and Synechocystis (bottom). Conditions: same as in Figure 3.4
Figure 3.6	ENDOR spectrum of Y_D^+ in PSII particles from <i>Synechocystis</i> in (A) H_2O and (B) D_2O , with $pH = pD = 7.0$. Spectrum C is the difference of spectra A and B. Conditions: same as Figure 3.4 except RF modulation depth is 50 kHz.
Figure 3.7	ENDOR spectrum of Y _D ⁺ in PSII particles from (top) wild type and (bottom) W167A mutant <i>Synechocystis</i> . Conditions: same as Figure 3.4 except RF modulation depth is 30 kHz
Figure 3.8	ENDOR spectra of Y _D ⁺ in PSII particles from <i>Synechocystis</i> A) labeled with ring-d ₄ tyrosine, B) ring-d ₄ tyrosine sample in D ₂ O and C) wild type PSII particles in H ₂ O. Conditions: same as Figure 3.6
Figure 3.9	ENDOR spectra of Y _D ⁺ from Synechocystis A) wild type (H ₂ O), B) ring- d ₄ tyrosine incorporated (D ₂ O). Conditions: same as Figure 3.6 except the RF modulation depth is 100 kHz
Figure 3.10	A) 3-pulse ESEEM echo decay from Y _D ⁺ in PSII particles from Synechocystis. B) Fouier transform of data in (A). Conditions: μwave frequency; 8.865 GHz, tau = 150 nsec, magnetic field = 3160 G 69
Figure 3.11	3-pulse ESEEM spectra of Y_D^+ in PSII particles from <i>Synechocystis</i> . Spectra were recorded at magnetic field values: a) 0, B) -10, C) +10, D) -20, E) +20 G relative to $g = 2.0046$. Conditions: same as Figure 3.10.70
Figure 3.12	3-pulse ESEEM spectra of reaction center complexes collected at $g=2.0046$ before (A) and after (B) 15 minutes of illumination at 77K. Conditions: μ wave frequency, 8.850 GHz; $\tau=150$ nsec; magnetic field, 3153 G
Figure 3.13	3-pulse ESEEM spectra of Y _D ⁺ in PSII particles from <i>Synechocystis</i> supplemented with (A) ¹⁵ NO ₃ ⁻ and (B) ¹⁴ NO ₃ ⁻ in the growth medium.

Figure 3.14	3-pulse ESEEM spectrum of Y_D^+ in PSII particles from Synechocystis, containing the D2 protein mutation, histidine-190 to glutamine. Conditions: μ wave frequency, 8.925 GHz; $\tau = 150$ nsec; magnetic field, 3185 G
Figure 3.15	EPR spectrum of glycylalanyltyrosine radical in 3M Mg(ClO ₄) glass. Conditions: μwave power, 2 mW; modulation, 4 Gpp; μwave frequency, 9.5464 GHz; temperature, -160°C
Figure 3.16	3-pulse ESEEM spectra of glycylalanyltyrosine radical collected at g=2.0061. Conditions: μ wave frequency, 8.790; τ = 150 nsec (A) and 225 nsec (B); magnetic field, 3142 G
Figure 4.1	Multiline EPR spectra from reaction center complexes generated by 8 minutes of illumination at 210 K. The spectra are the light-dark difference. A) RCC's prepared using dialysis and B) RCC's prepared using PEG. Conditions: µwave power, 8 mW; µwave frequency, 9.4710 GHz; modulation, 20 Gpp; temperature, 10 K
Figure 4.2	Multiline EPR spectra from reaction center complexes generated by 8 minutes of illumination at 210 K. The spectra are the light-dark difference. A) RCC's treated with 20 mM Sr ²⁺ and B) RCC's treated with 20 mM Ca ²⁺ . Conditions: μ wave power, 8 mW; μ wave frequency, 9.4710 GHz; modulation, 20 Gpp; temperature, 10 K
Figure 4.3	Multiline EPR spectra from reaction center complexes generated by 8 minutes of illumination at 210 K. The spectra are the light-dark difference. Spectra A and C are from RCC's that have bound Ca^{2+} and spectra B and D are from RCC's that have bound Sr^{2+} . Conditions: μ wave power, 8 mW; μ wave frequency,9.4710 GHz; modulation, 20 Gpp; temperature, 10 K
Figure 4.4	2-pulse ESEEM difference spectrum of the multiline signal from RCC's. Conditions: μ wave frequency, 8.840; magnetic field, 3250 G; τ = 200 nsec; pulse repetition rate, 90 Hz; temperature, 1.8 K
Figure 4.5	3-pulse envelope-echo decay traces for RCC's containing Ca^{2+} (A) after illumination, (B) before illumination and (C) the difference of traces A and B. Conditions: μ wave frequency, 8.955 GHz, magnetic field, 3290 G, $\tau = 213$ nsec; pulse repetition rate, 90 Hz; temperature, 1.8 K 106
Figure 4.6	The light, dark and difference 3-pulse ESEEM spectra after Fourier transformation of the data of Figure 4.5
Figure 4.7	3-pulse envelope-echo decay traces for RCC's containing Sr ²⁺ (A) after illumination, (B) before illumination and (C) the difference of traces A and B. Conditions: same as in Figure 4.5
Figure 4.8	The light, dark and difference 3-pulse ESEEM spectra after Fourier transformation of the data of Figure 4.7

Figure 5.1	Energy level diagram for the t_{2g} d orbitals in a site with rhombic distortions and in the presence of an applied magnetic field
Figure 5.2	EPR spectrum of <i>Rb. sphaeroides</i> oxidase at (A) 10 K and (B) 110 K. Figure C is the EPR spectrum from beef heart oxidase at 110 K. Conditions: (A) μwave power; 2 mW, modulation; 12.5 Gpp, (B and C) μwave power; 20 mW.
Figure 5.3	The g=2.0 region of the EPR spectrum from <i>Rb. sphaeroides</i> grown in the presence of different [Mn]: A) 0, B) 9μM, C) 27 μM, D) 1mM. E) beef heart oxidase. Conditions: μwave power; 20 mW, modulation; 12.5 Gpp, Temperature; 110 K.
Figure 5.4	A) EPR spectrum <i>Rb. sphaeroides</i> oxidase grown in the presence of [Mn]=0.5μM, B) after incubation with 1mM [Mn], and C) after washing the sample with 50 mM EDTA. Conditions: μwave power; 2 mW, modulation; 12.5 Gpp, temperature; 10 K
Figure 5.5	EPR spectrum of <i>Rb. sphaeroides</i> oxidase grown in the presence of [Mn]=9µM with [Mg] equal to A) 1.2 mM and B) 10 mM. Conditions: same as Figure 5.4
Figure 5.6	Plot of the % Mn binding to <i>Rb. sphaeroides</i> oxidase versus the [Mn]/[Mg] ratio in growth medium. Insert: expansion of first four points.
Figure 5.7	EPR spectra of subunit 1 mutants: A) H411A, B) D412N, C) H411A, D) D412N, E) H411N, F) T413N, G) Y414F. Samples were grown in the presence of [Mn] = 9 μ M except spectra C and D where [Mn] = 27 μ M Conditions: same as Figure 5.3
Figure 5.8	Model of the metal binding sites in subunit 1 of <i>Rb. sphaeroides</i> oxidase. The view is along the axis of the transmembrane helices
Figure 5.9	EPR spectra of A) oxidized and B) reduced oxidase recorded at 110 K. EPR spectra of the oxidized (c) and reduced (D) enzyme recorded at 10 K Conditions: (A, B) same as Figure 5.3; (C, D) same as Figure 5.4 156
Figure 5.10	Q-band EPR spectra of the oxidized (A) and reduced (B) Rb. sphaeroides oxidase. Conditions: µwave power; 1 mW, modulation; 5 Gpp, temperature; 150 K
Figure 5.11	3-pulse ESEEM spectra of <i>Rb. sphaeroides</i> oxidase grown in the presence of [Mn] = 1 mM, in the (A) oxidized and (B) reduced forms. Spectrum C is from oxidase with no bound Mn and spectrum D is from beef heart oxidase. Conditions: tau; 225 nsec, g=2.01

Figure 5.12	of [Mn] = 1 mM, in the (A) oxidized and (B) reduced forms collected at g=1.90. Conditions: same as Figure 5.11
Figure 5.13	3-pulse ESEEM spectra of <i>Rb. sphaeroides</i> oxidase grown in the presence of [Mn] = 1 mM, in the reduced form, collected at g=1.90. Microwave frequencies are 8.9 GHz (A) and 11.2 GHz (B). Conditions: same as Figure 5.11 except (A) tau = 300 nsec and (B) tau = 252 nsec 165

CHAPTER1 INTRODUCTION TO PHOTOSYSTEM II

The photosynthetic apparatus of plants and cyanobacteria uses the energy from light to convert CO₂ into sucrose and starch for plant growth and maintenance. The light absorbing enzymes of photosynthesis are located in the thylakoid membranes of chloroplasts, in plant cells, or in the plasma membrane of cyanobacteria. The two photosystems, Photosystem I (PSI) and Photosystem II (PSII), absorb the energy from light and use this energy to transfer electrons from a stable substrate, water, to nicotinamide adenine dinucleotide phosphate (NADP+) yielding O₂ and the highly reducing species NADPH (E_{m,7}=-320 mV). In addition, the two photosystems also generate a proton gradient across the membrane, which is used in the synthesis of adenosine triphosphate (ATP) by the membrane-bound ATPase. The ATP and NADPH are used in the synthesis of six-carbon sugars from CO₂ in the Calvin cycle.

The photosystem II/oxygen-evolving complex (PSII/OEC) is a membrane-bound, multisubunit enzyme that is involved in light absorption, charge separation, charge storage, and water oxidation. A schematic representation of the PSII/OEC enzyme is illustrated in Figure 1.1. Photosystem II (PSII) is the photochemical portion of the enzyme, involved in light absorption and promoting and stabilizing charge separation. The oxygen-evolving complex (OEC) contains the machinery for the oxidation of water. The enzyme catalyzes the light driven oxidation of water to oxygen, reaction 1.

$$2H_2O--->O_2+4H^++4e-$$
 (1)

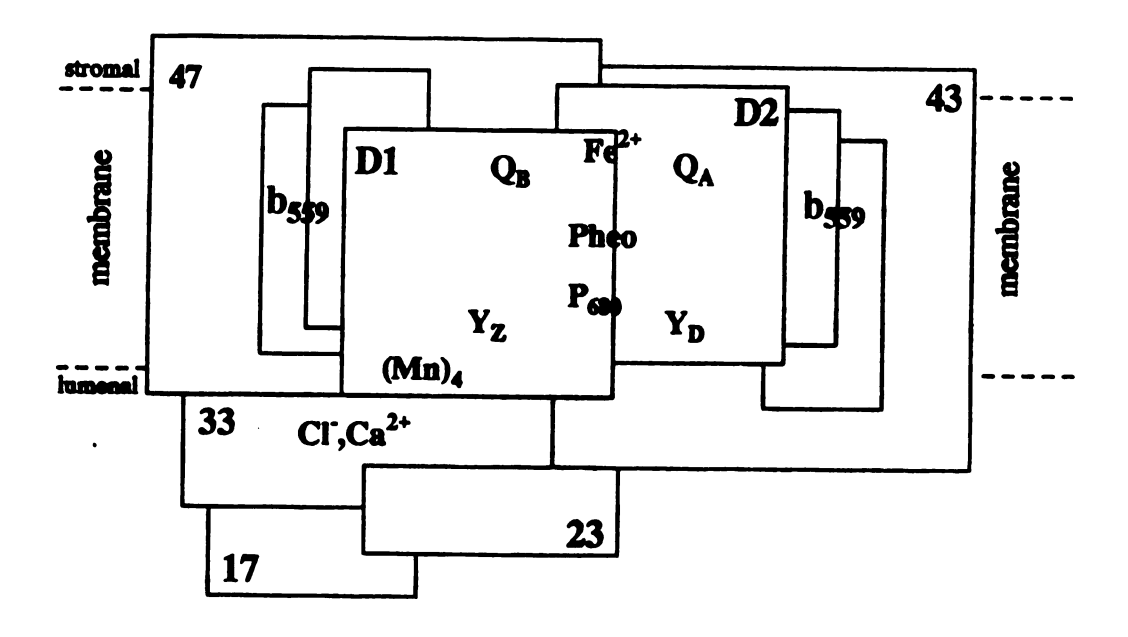


Figure 1.1. Model for the structure of the photosystem II/oxygen-evolving complex.

Masses in kilodaltons are indicated for each polypeptide except for D1 and D2, which have masses of 34 and 32 kDa respectively. The b-559 heterodimer consists of polypeptides with masses of 4 and 9 kDa.

When thylakoid membranes are given short flashes of light, O₂ is given off after every fourth flash.² The PSII/OEC enzyme accumulates the oxidizing equivalent produced by each flash in the OEC and after four oxidizing equivalents have been acquired, the OEC oxidizes water to oxygen. The OEC can exist in five redox states depending on the number of oxidizing equivalents stored, as shown in reaction 2.³ These redox states are designated S₀-S₄, where

the subscripts designate the number of stored oxidizing equivalents, with S₄ being the most oxidizing and capable of oxidizing water.

Photons are absorbed by the light harvesting complex (LHC) proteins, located in the thylakoid membrane, and the energy is transferred to PSII.⁴ Within PSII, the energy is absorbed by a specialized monomer or dimer of chlorophyll a, denoted P_{680} . The excited state singlet of P_{680} reduces a nearby pheophytin (pheo), the free base form of the macrocycle, within approximately 3 ps, forming P_{680} + pheo^{-.5} The pheo⁻ is rapidly oxidized by a plastoquinone, Q_A , in 250-550 ps,⁶ which in turn is oxidized by a second plastoquinone, Q_B , in 200-400 μ s.⁷ These rapid electron transfer steps separate the electron and the hole effectively and retard charge recombination events. Recombination of the separated charges results in the waste of the photon energy and a decline in the efficiency of the enzyme. Overall, PSII uses the light energy to promote an electron from P_{680} , with a redox potential of $\approx 1.1-1.2$ V,⁸ to Q_B , with a redox potential near 0 volts.⁷

The P_{680}^+ Q_A^- recombination time is approximately the same as the time for Q_A $\rightarrow Q_B$ electron transfer. The charge recombination is prevented by the rapid reduction of P_{680}^+ by the redox active tyrosine Y_Z . Y_Z reduces P_{680}^+ in 20-280 ns 10 in a reaction whose rate is S state dependent. The $Y_Z^+Q_A^-$ state is stable for 20 ms and $Y_Z^+Q_B^-$ persists for 400 ms. 11 The tyrosine is, in turn, rereduced by the OEC, oxidizing

the OEC from S_n to S_{n+1} , in times that are S state dependent as follows, 30 μ s for S_0 , 100 μ s for S_1 , 300 μ s for S_2 , and 1.0-1.2 ms for S_3 , 12 thus, the role of Y_Z is to rapidly reduce P_{680}^+ , which lengthens the charge recombination time so that the slower electron transfer from the OEC to Y_Z^+ can occur before deleterious charge recombination takes place.

Following the initial absorption and the sequence of charge transfer reactions descibed above, PSII is reset to absorb a second photon, which produces charge separation along the same electron transfer path and transfers a second electron to QB forming QB². The quinone is then protonated, giving QBH₂, and dissociates from its binding site. Subsequently, a new oxidized quinone is bound. The protons involved in transforming the quinone, QB, to a quinol, QBH₂, originate from the stromal side of the membrane. The protons released in the oxidation of water are released on the lumenal side of the membrane. These two sets of protonation events, in conjunction with Photosystem I, generate a proton gradient of approximately ΔpH=3 across the membrane, which is used in the synthesis of ATP by the ATPase. ¹³ The quinol, QBH₂, is a cofactor of the cytochrome b₆f complex and provides reducing equivalents to this protein.

The PSII/OEC complex, *in vivo*, contains at least 20 polypeptides, however, the minimal oxygen evolving complex contains eight intrinsic, membrane spanning, polypeptides. ¹⁴ A heterodimer of the polypeptides D1 and D2 forms the photochemical reaction center of PSII by binding the specialized chlorophyll P₆₈₀, the pheophytins, and the quinones. ¹⁵ There are also two antennachlorophyll binding proteins, CP47 and CP43, which bind 10-26 and 10-12 chlorophylls, respectively. ¹⁶ The function of the CP43 and CP47 proteins is to transfer the excitation energy from the LHC to the reaction center. ¹⁷ Also present are two small polypeptides, each providing a histidine ligand to the heme of cytochrome b-559. ¹⁸ Whether there are one or two cytochrome b-559 present per PSII is still unclear. ¹⁹ Cytochrome b-559 is not involved in the electron

tranfer events leading to oxygen evolution and its role in the PSII/OEC is not well understood.²⁰

In addition to the intrinsic polypeptides there are also three extrinsic polypeptides with molecular weights of 17,23, and 33 kDa. The three polypeptides can be removed from the PSII/OEC complex by treatment with high salt concentrations (1-2 M NaCl) or with tris (tris[hydroxymethyl]aminomethane).²¹ The 17 and 23 kDa extrinsic polypeptides can also be rebound to the PSII/OEC.²² Under certain conditions oxygen evolution can still occur when all three extrinsic polypeptides have been removed, but at severely reduced rates.²³ These polypeptides are not essential for oxygen evolution, but their presence is critical for optimal enzyme activity.

The PSII/OEC complex can be purified from plants and cyanobacteria, with spinach as the most common source. Purified PSII/OEC particles are commonly obtained by the procedure of Berthold et al and are referred to as BBY particles.²⁴ In BBY particles, the PSII/OEC is still located in the thylakoid membrane and contains all three extrinsic polypeptides. In addition, the light harvesting complex proteins are also present in the membrane. More refined preparations have been developed that remove the membrane and the LHC, however, the 17 and 23 kDa polypeptides are removed as well.²⁵ Highly refined PSII particles, containing only D1, D2, and cytochrome b-559, have also been purified but these particles do not evolve oxygen.¹⁵

The purple non-sulfur bacteria, like plants and cyanobacteria, also contain a photosynthetic reaction center. The reaction centers from plants and bacteria have many similarities and have often been compared. This comparison is highly fruitful for the study of PSII, as the crystal structures of the bacterial reaction center from *Rb. viridis* and *Rb. sphaeroides* have been determined to a resolution of 2.3 Å²⁷ and 2.8 Å,²⁸ respectively. The electron transfer components and sequence are similar in the bacterial and plant reaction centers, with the photochemical core of the bacterial reaction center consisting of a heterodimer of the L and M proteins. The bacterial reaction center, a

bacteriochlorophyll dimer is the specialized chlorophyll which absorbs the light energy.²⁷ The bacteriochlorophyll dimer transfers an electron to a pheophytin, which, in turn, transfers an electron to a quinone, Q_A and then to a second quinone, Q_B.²⁶ There is also a strong protein sequence homology between the L and M subunits and the D1 and D2 subunits.²⁶ The similarity of the bacterial reaction center with the reducing side of PSII, both in the components involved in electron transfer from P₆₈₀ to Q_B, and the protein sequence homologies, suggest that the bacterial reaction center provides a good model for PSII.²⁶

There are, however, also significant differences between the two reaction centers.

The bacterial reaction center does not oxidize water and thus does not contain the OEC.²⁶ The bacterial system also does not contain a redox active tyrosine to reduce the specialized chlorophyll dimer as does PSII, but instead the specialized bacteriochlorophyll dimer is rereduced by a cytochrome, which is contained in a separate subunit.²⁷ The bacterial reaction center thus provides little insight into the structure and mechanism of the OEC.

While it had been known for some time that manganese was neccessary for maximum quantum efficiency and high rates of oxygen evolution, its exact role within the OEC had not been well characterized. Early studies of the Mn stochiometry determined that there were 5-8 Mn/PSII.² Accurate measurments of the Mn stochiometry in isolated thylakoid membranes showed that there are four Mn/ PSII.³⁰ This stochiometry is unchanged for BBY particles, as well as for more refined oxygen evolving preparations.^{23,25} In an EPR study of thylakoid membranes containing the PSII/OEC, Siderer and Dismukes observed that there is at least one multinuclear Mn complex that is oxidized upon illumination of the sample.³¹

Dark-adapted PSII samples are primarily in the S_1 state.³ Application of a short light pulse turns over the OEC to the S_2 state and rapid freezing can be used to trap this state. The EPR spectrum of the S_2 state, collected at 10 K, shows a "multiline" signal

with 18-20 peaks and centered at g=2.0.31 The hyperfine splitting between the lines is approximately 80 G, on average. When a PSII sample is given a series of flashes, the multiline signal has maximum amplitude after the first and fifth flashes.³¹ Since each flash causes a single S state transition, the multiline signal arises from the S_2 state (see reaction 2). The multiline signal can also be generated by continues illumination at 160-200K.³² At this temperature the OEC will only undergo the S_1 to S_2 transition.

After removal of the Mn from PSII by treatment with tris, no multiline signal can be generated.³¹ The transfer from the S₁ to the S₂ state of the OEC is proposed to involve an oxidation of a Mn, which converts the Mn complex of the OEC in S₁ from an EPR silent form to an EPR detectable form in S₂.³¹ The multiline signal also shows a strong similarity to a mixed valence (III,IV) Mn dimer.³³ The EPR spectrum of the dimer has 16 lines that arise from hyperfine coupling to the two ⁵⁵Mn nuclei, which have nuclear spin I=5/2. The splitting between the peaks is similar to that observed for the multiline signal. The multiline signal has been assigned as arising from a multinuclear Mn complex consisting of 2-4 Mn.³¹ Additional EPR studies have determined that the Mn cluster of the OEC is most likely a tetranuclear complex (discussed in Chapter 4).

While the EPR data show that there is an oxidation of Mn in the S_1 to S_2 transition, the oxidation states of the individual Mn ions in the cluster in the S_1 and S_2 states could not be determined. This type of information can be obtained from X-ray absorption near edge structure spectroscopy (XANES). Studies of isolated PSII particles and Mn model complexes by several groups indicate that the oxidation state of the four Mn are (III,III,IV,IV), in the S_1 state.³⁴ The difference between the XANES data from the S_1 and S_2 states is indicative of a Mn(III) to Mn(IV) oxidation.³⁴ Similar results were also obtained from absorbance difference spectroscopy³⁵ and NMR³⁶ and EPR³⁷ relaxation measurements, all of which are suggetive of a Mn(III) to Mn(IV) oxidation in the S_1 to S_2 transition. The S_2 state, then, has the ensemble oxidation state of (III,IV,IV,IV).

While there is a growing consensus within the PSII arena of the oxidation states of the S₁ and S₂ states, there is significant disagreement concerning the oxidation states of the Mn in the other S states. EPR, absorbance difference spectroscopy, and XANES studies have all suggested that one or more of the S state transitions do not involve Mn oxidation.^{38,39} There is, however, little consistency between the techniques as to which S state transitions do, and which do not, involve Mn oxidation. The oxidation states of the Mn in the OEC are currently under extensive investigation.

In addition to Mn, Ca is also required for oxygen evolution by the PSII/OEC, 40 with a stochiometry of two Ca per center. 40 The binding affinities of the two Ca binding sites are different, with the tighter binding site having a K_m value of 1-4 μM , while the weaker shows two K_m values, $\approx \! 100 \, \mu M$ and $> \! 1 m M.^{41}$ The two different K_m values of the second site may arise from a dependence of the binding affinity on S state. 42

Removal of the 17 and 23 kDa extrinsic polypeptides by washing PSII particles with 1-2 M NaCl, results in a 60-70% loss of oxygen activity, which is not restored with rebinding of the polypeptides. ⁴⁰ However, after removal of the extrinsic polypeptides, addition of 15 mM Ca²⁺ restored oxygen activity to 80% of the value observed for samples retaining the 17 and 23 kDa polypeptides. ⁴³ After rebinding the 17 and 23 kDa polypeptides, if the PSII samples are subsequently incubated for one hour or more in the presence of 0.5mM Ca²⁺, oxygen evolution is restored. ⁴⁴ This result was interpreted as evidence that the Ca activation observed was physiologically significant and that the 17 and 23 kDa polypeptides constitute part of a apparatus that is responsible for concentrating and retaining Ca at its site of action in PSII/OEC. Later studies established the 23 kDa polypeptide as the species that, when extracted from PSII, causes the release of Ca. ⁴⁵ High-salt concentration washes of PSII, with or without chelators, are believed to remove only the more loosely bound Ca. ¹⁴

While Ca is neccessary for oxygen evolution, the mechanism of its action in PSII has not been determined. Circumstantial evidence locates at least one of the Ca nearby,

and interacting with the Mn structure of the OEC. Removal of Ca stops S state advancement; however, the exact S state at which the OEC becomes locked is currently a major point of controversy. In fact, all four of the S state transitions have been implicated as the transition that is blocked by removal of the Ca. 14 The binding of Ca is also S state dependent, with the K_m values increasing in the order S₃>S₀=S₂>S₁.42 The process of photoactivation, whereby the Mn complex is constructed from aqueous Mn²⁺, does not require Ca. In order to restore oxygen evolution, however, Ca must be added to the system. 46 Neither of the two Ca appears to be an integral part of the Mn complex since it can assemble in the absence of Ca. The evidence that more directly links Ca within the vicinity of the Mn comes from studies in which Sr is substituted for Ca. After removal of Ca, Sr can be substituted, with 40% restoration in oxygen evolution rate. 43 The mutiline signal generated with Sr present, is modified compared to the untreated samples, suggesting a change in the structure, or ligand environment of the Mn complex. 47 These data imply that at least one of the two Ca bound by PSII interacts with the Mn complex.

The third extrinsic polypeptide, the 33 kDa protein, is involved in optimizing the catalytic efficiency of the Mn complex. In samples in which the 33 kDa protein has been removed, oxygen evolution rates are only 24% of the untreated samples.²³ In addition, absence of the 33 kDa protein causes the extent of stable charge separation, rates of oxygen evolution and rates of electron transfer to be diminished.¹⁴ The structure of the Mn complex is perturbed only slightly in PSII particles devoid of the 33 kDa protein, as the multiline signal from the S₂ state is nearly the same as in samples containing all the extrinsic polypeptides.⁴⁸ The role of the 33kDa protein appears to be to cover, protect, and influence the Mn complex without directly providing it with ligands.¹⁴

Tyrosines

The PSII/OEC contains two redox active tyrosines, Y_Z and Y_D . Whereas the oxidized form of Y_Z , Y_Z^+ , is rapidly reduced by the OEC, in 0.03 to 1.2 ms (see above), Y_D^+ is stable for hours at ambient temperature. The EPR spectra of Y_D^+ and Y_Z^+ have been recorded and are very similar, which leads to the conclusion that Y_D and Y_Z are from species with the same chemical structure. Through the use of selective isotopic labeling and site-directed mutagenesis, Y_Z has been shown to be tyrosine-161 on the D1 protein and Y_D is tyrosine-160 on the D2 protein. $S_{0,51,52}$

The D1 and D2 proteins are predicted to contain five membrane spanning helices, ⁵⁵ which has been verified by immunological studies. ⁵⁶ This folding pattern is analogous to that of the L and M subunits of the bacterial reaction center. ²⁶ The fourth and fifth helices of L and M are intertwined and form the binding site for the specialized chlorophyll dimer, the pheophytins and the quinones, Figure 1.2. ²⁶ This structure is proposed to model the reaction center of PSI, Figure 1.2. Y_Z and Y_D are then located at the end of helix three, near the lumenal side, in the proposed protein folding model of Trebst, ⁵⁵ for D1 and D2. This model places Y_Z and Y_D on opposite sides of the reaction center and symmetrically displaced about the C₂ axis, that is oriented along the vector connecting P₆₈₀ and the non-heme iron, Figure 1.1.

The role of Y_Z is understood, as it mediates electron transfer between the OEC and P_{680}^+ . The principal role of Y_D , if any, is, however, not well understood. Studies of non-oxygen evolving PSII particles have shown that Y_D can transfer electrons to P_{680}^+ but, at a rate that is three orders of magnitude slower than Y_Z . There is no evidence that Y_D^+ can oxidize the OEC through all the S states, suggesting that the reduction of P_{680}^+ by Y_D has little physiological importance. In cyanobacteria mutants in which Y_D (tyrosine-160 on the D2 protein) has been changed to a phenylalanine by

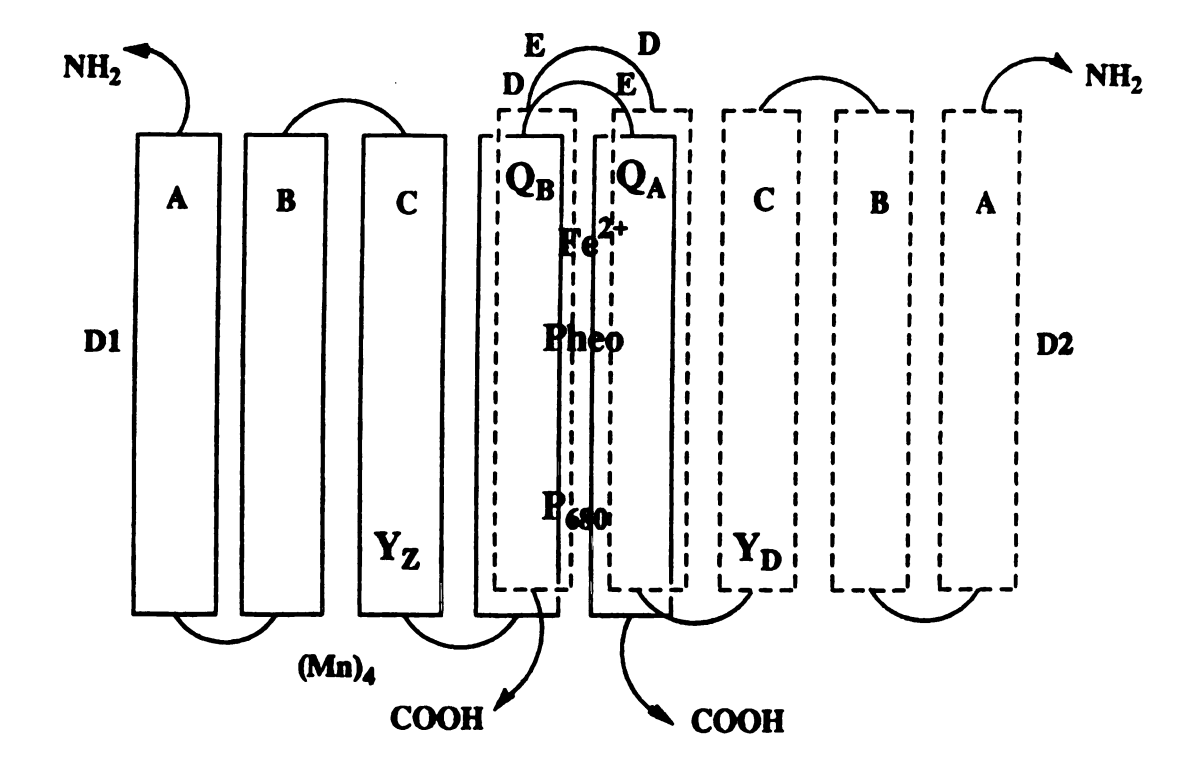


Figure 1.2. Model for the interaction of the D1 and D2 proteins based on the structure of the L and M subunits of the bacterial reaction center. The D_2E_2 helical core contains the chromophores involved in the primary charge separation events. The pseudo- C_2 symmetry axis is along the $P_{680} \rightarrow Fe^{2+}$ direction.

directed mutagenesis, oxygen evolution rates of the mutant are the same as wild type cells.51

The unneccessary redundancy of an electron transfer component is also observed in the bacterial reaction center. ²⁶ In the bacterial reaction center, from the specialized chlorophyll dimer to the quinones, there are two identical electron transfer pathways. Both have an accessory chlorophyll, a pheophytin and a quinone, Q_A or Q_B; the two pathways are related by C₂ symmetry. In the bacterial reaction center only one of the two pathways is used and the purpose of the second pathway is not understood. ²⁶ The strong similarity of the EPR spectra of Y_D and Y_Z is consistent with the tyrosine side chains being oriented similarly in the enzyme, and being located in similar protein environments. ⁴⁹ As for the bacterial reaction center, which shows a structural similarity in the two electron transfer branches, the electronic and geometric structure of Y_Z and Y_D are also expected to be similar.

 Y_D is not part of the main electron transfer pathway involved in charge separation and water oxidation, but it is involved in several dark electron transfer reactions. The reduced, diamagnetic, form of Y_D is oxidized by the OEC, reducing the S_3 and S_2 states to the S_2 and S_1 states.⁵⁴ Y_D^+ can also be reduced by the OEC: in the dark the S_0 state is oxidized by Y_D^+ , yielding S_1Y_D .⁵⁴ The electron transfer reactions involving Y_D are slow, with $t_{1/2}$ values ranging from seconds to minutes.⁵⁴ The oxidation of the OEC by Y_D^+ is proposed to occur to keep the Mn of the OEC in higher oxidation states so that Mn is more strongly coordinated. This reduces the possibility of release of Mn from the OEC and inactivation of oxygen production.⁵⁴

The rapid electron transfer between Y_Z and the Mn complex of the OEC suggests that these two species are near each other; the electron transfer between Y_D and the Mn complex suggests that this tyrosine is also in the Mn complexes vicinity. Several methods have been used to study the geometric relationship between the Mn complex and Y_Z and Y_D . The Y_Z^+ EPR spectrum was observed to be the same whether the Mn

complex was present in PSII particles or absent. From these results a distance of >10 $\mathring{\text{A}}$ between Y_Z and the Mn complex was estimated.⁴⁹ Measurements of the temperature dependence of the relaxation properties of Y_D lead to the estimate of 30-40 $\mathring{\text{A}}$ between Y_D and the Mn complex.³⁷ While the exact distance between the tyrosines and the Mn complex is not known, Warden et al., showed that the magnetic interaction between the Mn complex and Y_D and Y_Z was stronger for Y_Z , suggesting that Y_Z is closer to the Mn complex than Y_D .⁵⁷ The shorter distance between the Mn complex and Y_Z is consistent with the fast electron transfer between Y_Z and the Mn complex.

Besides the different distances to the Mn complex, there are several another differences between Y_Z and Y_D , which may explain why Y_Z is the primary acceptor in electron transfer from the Mn complex. The redox potential of YD has been estimated to be 720-780 mV, 54,58 whereas the redox potential is estimated to be ≈ 1.1 V for Y_Z . 59The redox potential for the S states are <700 mV for S_1/S_0 and $\approx900\text{mV}$ for S_2/S_1 and $S_3/S_2.54,59$ On the basis of these potentials, one can conclude that Y_D , which can and does oxidize So to S1, cannot oxidize the OEC to higher S states. The accessibility of the two tyrosines to reductants is also very different. Upon the removal of the extrinsic polypeptides and the Mn complex Yz+ can be reduced by carbonyl cyanide m-chlorophenylhydrazone (CCCP) with a second order rate constant of 2.0x10⁶ M⁻¹ s⁻¹.60 The reduction of Y_D⁺ by CCCP has a rate constant that is significantly lower, 6.5x10² M⁻¹s⁻¹, suggesting that Y_D is buried more deeply in the protein and considerably less accessible to exogenous reductants. The inaccessibility explains the stability of the oxidized form of YD, despite its high redox potential. EPR studies of the relaxation properties of YD⁺ in PSII's in the presence of Dy³⁺ are consistent with this interpretation.61 From these EPR results, the distance from YD+ to the stromal side of the enzyme is estimated to be 26 Å, whereas the distance to the lumenal side is 41 Å. Removal of the extrinsic polypeptides and the Mn complex reduces the distance to the lumenal side to 27 Å. Even after the removal of the extrinsic polypeptides, YD is still

buried deep within the protein. While models predict that Y_D and Y_Z are located near the end of a transmembrane helix and near the surface of the membrane, the models do not predict the distance from Y_D to the outer edge of the enzyme. The interhelical loops of D1 and D2, which extend outside the membrane, in addition to portions of the other polypeptides of the PSII/OEC, may cover the region of the protein that contains Y_D and shield it from the aqueous phase and exogenous reductants.

From this discussion of the PSII/OEC, it is clear that, while much is known about the structure and function of this enzyme, there are also many areas of uncertainty. In particular, the oxygen-evolving complex and the the redox active tyrosines, Y_Z and Y_D , are, in general, less well understood, since they do not have analogies in the bacterial reaction center. In the work presented here magnetic resonance techniques have been used to obtain structural and electronic information about the Mn complex of the OEC and YD. EPR and electron spin echo envelope modulation (ESEEM) have been used to study the extent of structural perturbation that occurs at the Mn complex when Sr is substituted for Ca. These results have given some insight into the interaction between the Ca and the Mn complex. Electron nuclear double resonance (ENDOR) is used to study the radical YD⁺ to understand better both its geometric and electronic structure. The ENDOR results have allowed the determination of the distribution of the unpaired spin density within the phenol side chain of the tyrosine and the orientation of the side chain relative to the protein backbone. YD+ was also used as a probe to gain information on its protein environment, which may give insight into its lowered redox potential as compared to YZ. In addition, the monomer Mn binding site in the enzyme cytochrome c oxidase, an enzyme that reduces O2 to water, was studied by EPR and ESEEM. The geometry and ligand environment of the Mn was determined, and the effect on the Mn binding site from protein structure perturbations was studied. These latter results were useful in interpreting the studies of the Mn complex of the OEC.

LIST OF REFERENCES

- 1) Babcock, G.T., Barry, B.A., Debus, R.J., Hoganson, C.W., Atamian, M., McIntosh, L., Sithole, I. and Yocum, C.T. Biochemistry, 1989, 28, 9557
- 2) Joliot, P., Barbieri, G. and Chabaud, R. Photochem. Photobiol., 1969, 10, 309.
- 3) Kok, B., Forbush, B. and McGloin, M.P. Photochem Photobiol., 1970, 11, 457.
- 4) Renger, G. in The Photosystems: Structure, Function and Molecular Biology (Barber, J., ed.) Elsevier, Amsterdam, 1992, 45.
- 5) Wasielewski, M.R., Johnson, D.G., Seibert, M. Govindjee Proc. Natl. Acad. Sci. USA, 1989, 86, 524.
- a) Nuijs, A.M., Van Gorkam, H.J., Plijter, J.J. and Duysens, L.N.M. Biochim. Biophys. Acta, 1986, 848, 167 b) Eckert, H.J. and Renger, G. FEBS Lett., 1988, 236, 425.
- 7) Crofts, A.R. and Wraight, C.A. Biochim. Biophys. Acta, 1983, 726, 149
- 8) Klimov, V.V., Allakhverdiev, S.I., Demeter, S. and Kransnovskii, A.A. Dokl. Akad. Nauk. USSR, 1979, 249, 227 b) Van Gorkom, H.J. Photosyn Res., 1985, 6,97
- 9) Mathis, P. and Rutherford, A.W. Photosyn.: New Compr. Biochem., 1987, 15, 63 b) Hoganson, C.W. and Babcock, G.T. Biochemistry, 1989, 28, 1448.
- 10) Meyer, B., Scholdder, E., Dekker, J.P. and Witt, H.T. Biochem. Biophys. Acta, 1989, 974, 36.
- 11) Rutherford, A.W. Trends Biol. Sci., 1989, 14, 227.
- 12) Babcock, G.T., Blankenship, R.E. and Sauer, K. FEBS Lett., 1976, 61, 286.
- Nicholls, D.G. and Ferguson, S.J. Bioenergetics 2, Academic Press, London, 1992, p65.
- 14) Debus, R.J. Biochim. Biophys Acta, 1992, 1102, 269.
- 15) Nanba, O. and Satoh, K. Proc. Natl. Acad. Sci. USA, 1987, 84, 109.
- 16) a)Dekker J.P., Bowlby, N.R. and Yocum, C.F. FEBS Lett., 1989, 254,150 b) Barbato, R., Race, H.L., Friso, G. and Barber, J. FEBS Lett., 1991, 286, 86

- 17) Bricker, T.M. Photosyn. Res., 1990, 24, 1
- Babcock, G.T., Widger, W.R., Cramer, W.A., Oertling, W.A. and Metz, J.G. Biochemistry, 24, 3638.
- 19) Buser, C.A., Diner, B.A. and Brudvig, G.W. Biochemistry
- 20) Thompson, L.K. and Brudvig, G.W. Biochemistry, 1988, 27, 6653.
- a) Kuwabara, T. and Murata, N. Plant Cell Physiol., 1982, 24, 741 b) Akerlund, H.E. and Jansson, C. FEBS Lett., 1981, 124, 229.
- 22) Andersson, B. and Akerlund, H.H. Biochim. Biophys. Acta, 1978, 503,462.
- 23) Bricker, T.M. Biochemistry, 1992, 31, 4623.
- 24) Berthold, D.A., Babcock, G.T. and Yocum, C.F. FEBS Lett., 1981, 134, 231.
- 25) Ghanotakis, D.F., Demetriou, D.M. and Yocum, C.F. Biochim. Biophys. Acta, 1987, 891, 15
- 26) Michel, H. and Deisenhofer, J. Biochemistry, 1988, 27, 1
- 27) Deisenhofer, J., Epp, O., Miki, K., Huber, R. and Michel, H. Nature, 1985, 318, 618.
- 28) Allen, J.P., Feher, G., Yeates, T.O., Komiya, H. and Rees, D.C. Proc. Natl. Acad. Sci. USA, 1988, 85, 8487.
- 29) Cheniae, G.M. Methods Enzymol., 1980, 69, 349
- Yocum, C.F., Yerkes, C.T., Blankemship, R.E., Sharp, R.R. and Babcock, G.T. Proc. Natl. Acad. Sci. USA, 1981, 78, 7507.
- 31) Dimukes, G.C. and Siderer, Y. Proc. Natl. Acad. Sci USA, 1981, 78, 274.
- 32) Brudvig, G.W., Casey, J.L. and Sauer, K. Biochim. Biophys. Acta, 1983, 723, 366.
- 33) Cooper, S.R., Dismukes, G.C., Klein, M.P. and Calvin, M. J. Amer. Chem. Soc., 1978, 100, 7248.
- a) Sauer, K., Yachandra, V.K., Britt, R.D. and Klein, M.P. in Manganese Redox Enzymes (Pecoraro, V.L., ed) VCH, New York, 1992, pp141 b) Riggs, P.J., Mei, R. Yocum, C.F. and Penner-Hahn, J.E. J. Amer. Chem. Soc., 1992, 114, 10650.
- Dekker, J.P. in Manganese Redox Enzymes (Pecoraro, V.L., ed) VCH, New York, 1992, pp85.
- 36) Srinivasan, A.N. and Sharp, R.R. Biochim, Biophys. Acta, 1986, 851, 369.
- Evelo, R.G., Styring, S., Rutherford, A.W. and Hoff, A.J. Biochim. Biophys. Acta, 1989, 973, 428.

- 38) Manganese Redox Enzymes (Pecoraro, V.L., ed) VCH, New York, 1992.
- Rutherford, A.W., Zimmerman, J.L. and Boussac, A. in The Photosystems: Structure Function and Molecular Biology (Barber, J., ed) Elsevier, Amsterdam, 1992, pp179.
- 40) Yocum, C.F. Biochim. Biophys. Acta, 1991, 1059,1.
- Kolosaka, K., Beck, W.R., Brudvig, G., Cheniae, G.M. in Current Research in Photosynthesis (Baltscheffsky, M., ed) Kluwer Academic Publishers, Dordrecht, 1990, pp721.
- 42) Boussac, A. and Rutherford, A.W. Biochemistry, 1988, 27, 3476.
- 43) Ghanotakis, D.F., Babcock, G.T. and Yocum, C.F. FEBS Lett., 1984, 167, 127
- Ghanotakis, D.F., Topper, J.N., Babcock, G.T. and Yocum, C.F. FEBS Lett., 1984, 170, 169.
- 45) Miyao, M. Murata, N. Photosyn. Res., 1986, 10, 489.
- Tamura, N., Inoue, Y. and Cheniae, G.M. Biochim Biophys Acta, 1989, 976, 173.
- 47) Boussac, A. and Rutherford, A.W. Biochemistry, 1988, 27, 3476.
- 48) Miller, A.F., de Paula, J.C. and Brubvig, G.W. Photosyn, Res., 1987, 12, 205.
- 49) Hoganson, C.W. and Babcock, G.T. Biochemistry, 1988, 27, 5848.
- 50) Barry, B.A. and Babcock, G.T. Proc. Natl. Acad. Sci. USA, 1987, 84, 7099.
- 51) Debus, R.J., Barry, B.A., Babcock, G.T. and McIntosh, L. Proc. Natl. Acad. Sci. USA, 1988, 85, 427.
- 52) Debus, R.J., Barry, B.A., Sithole, I., Babcock, G.T. and McIntosh, L. Biochemistry, 1988, 27, 9071.
- Buser, C.A., Thompson, L.K., Diner, B.A. and Brudvig, G.W. Biochemistry, 1990, 29, 8977.
- 54) a) String, S. and Rutherford, A.W. Biochemistry, 1987, 26, 2401 b) Vass, I. and Styring, S. Biochemistry, 1991, 30, 830.
- 55) Trebst, A. Z. Naturforsch., 1986, 41C, 240.
- 56) Sayre R.T., Anderson, B. and Bogorad, L. Cell, 1986, 47, 601.
- Warden, J.T., Blankenship, R.E. and Sauer, K. Biochim, Biophys. Acta, 1976, 423, 462.
- 58) Boussac, A. and Etienne, A.L. Biochim. Biophys. Acta, 1984, 766, 576.

- 59) Bouges-Bocquet, B. Biochim. Biophys. Acta, 1980, 594, 85.
- Ghanotakis, D.F., Yerkes, C.T. and Babcock, G.T. Biochim. Biophys. Acta, 1982, 682, 21.
- 61) Innes, J.B. and Brudvig, G.W. Biochemistry, 1989, 28, 1116

CHAPTER 2 MAGNETIC RESONANCE

Electron paramagnetic resonance is a technique for studying paramagnetic species, or systems with S>0, and provides many insights into the electronic and geometric structure of a molecule. For transition metals, EPR can provide information about the ligand geometry, the number and type of ligands, and the extent of covalency of the metal ligand bonds. In the study of organic radicals, EPR allows insight into the shape, or probability density, of the molecular orbital containing the unpaired electron and the solvation environment of the radical. EPR spectra are interpreted with the use of a spin Hamiltonian. This Hamiltonian acts upon spin-only wave functions and predicts their energies for the particular system under study.

Electron paramagnetic resonance (EPR)

In a system with an unpaired electron, S=1/2, the electronic spin can have one of two values, $\pm 1/2$. In the absence of an externally applied magnetic field the two spin wavefunctions are degenerate. In the presence of a strong magnetic field applied along the Z direction the two wavefunctions are split in energy and the Z component of the electron spin is $m_S=+1/2$ for the upper energy state and $m_S=-1/2$ for the lower energy state. The lower energy state has the electronic spin antiparallel to the magnetic field whereas the upper energy state has the spin parallel to the magnetic field. Applying a photon source to the sample, with the energy of the photons equal to the energy difference

between the $m_S=\pm 1/2$ states, promotes an electron from the lower $m_S=-1/2$ to the upper $m_S=+1/2$ state. This absorption of a photon by the sample is measured and gives the resultant EPR spectrum. For an externally applied field of approximately 3000 G, photons in the microwave frequency region are absorbed. In the following description of EPR, it is assumed that the magnetic field is kept constant and the microwave frequency is swept, although, experimentally the opposite is true. The Hamiltonian that is applicable to the EPR experiment is equation 1.1

$$\mathbf{H} = \mathbf{\beta_e} \, \mathbf{Hz} \, \mathbf{g}^{\mathrm{T}} \cdot \, \mathbf{S} - \mathbf{g_N} \, \mathbf{\beta_N} \, \mathbf{Hz} \cdot \mathbf{I} + \mathbf{S} \cdot \, \mathbf{A}^{\mathrm{T}} \cdot \, \mathbf{I}$$
 (1)

H = Hamiltonian operator

 g^{T} = electron g-tensor

 β_e = electron Bohr magneton

 g_N = nuclear g value

 β_N = nuclear Bohr magneton

Hz = Zeeman field (externally applied magnetic field)

A^T= hyperfine coupling tensor

S = electron spin angular momentum operator; I= nuclear spin angular momentum operator

In this discussion of EPR, it is assumed that the high field approximation applies. In this case, the labotatory magnetic field is strong enough, relative to internal fields, that the electron and nuclear spins are quantized along the applied magnetic. Application of the spin operators, S and I, to the spin wavefunctions for a system with S=1/2 and I=1/2, yields the scalar values $m_S=\pm 1/2$ and $m_I=\pm 1/2$.

The first term of equation 1, the electron-Zeeman term, describes the interaction between the unpaired electron and the externally applied magnetic field (Zeeman field).

The effect of this interaction is to split the degeneracy of the two spin-only wavefunctions

for the unpaired electron, Figure 2.1. The electron-Zeeman term is the dominant term in the Hamiltonian. Since the electron-Zeeman term is a function of the g-tensor, its magnitude will be orientationally dependent, anisotropic. That is, the magnitude of this interaction will depend on the direction of the Zeeman field relative to the g-tensor. The g-tensor is diagonal in at least one coordinate system and this coordinate system is usually related to the symmetry axis of the molecule.

The second term in equation 1 is the nuclear-Zeeman term, which represents the interaction between the nuclear spin and the Zeeman field. This term is non-zero only for those nuclei that have non-zero nuclear spin. Unlike the situation for the electron-Zeeman term, the nuclear g value is taken as isotropic. The nuclear-Zeeman interaction is directly analogous to the electron-Zeeman interaction, except that in this case, the degeneracy of the nuclear spin wavefunction is split. The splitting of the two wavefunctions is the nuclear-Zeeman splitting and is shown in Figure 2.1.

The third term is the electron-nuclear hyperfine coupling. A nucleus with non-zero nuclear spin generates a magnetic field at the unpaired electron. The net magnetic field at the electron is a vector sum of the external field and the hyperfine field. In the case of a proton, with nuclear spin I=1/2 and $m_I=\pm 1/2$, the hyperfine field can either add to or subtract from the external field. The hyperfine interaction causes a shift in the energy levels of the spin system, Figure 2.1.

While the electrons are aligned along the magnetic field, they precess around the field direction. The precessional frequency of the electrons is dependent on the strength of the magnetic field. In the EPR experiment, the selection rules are $\Delta m_S=+1$ and $\Delta m_I=0$. The absorption of a photon, which carries one quantum of angular momentum, causes a change in the spin angular momentum of the electron with no change in the nuclear spin. This absorption of a photon occurs when the precessional frequency of the electrons is equal to the microwave frequency. The two allowed transitions for the simple S=1/2 and I=1/2 system are shown in Figure 2.1 and occur at frequencies,

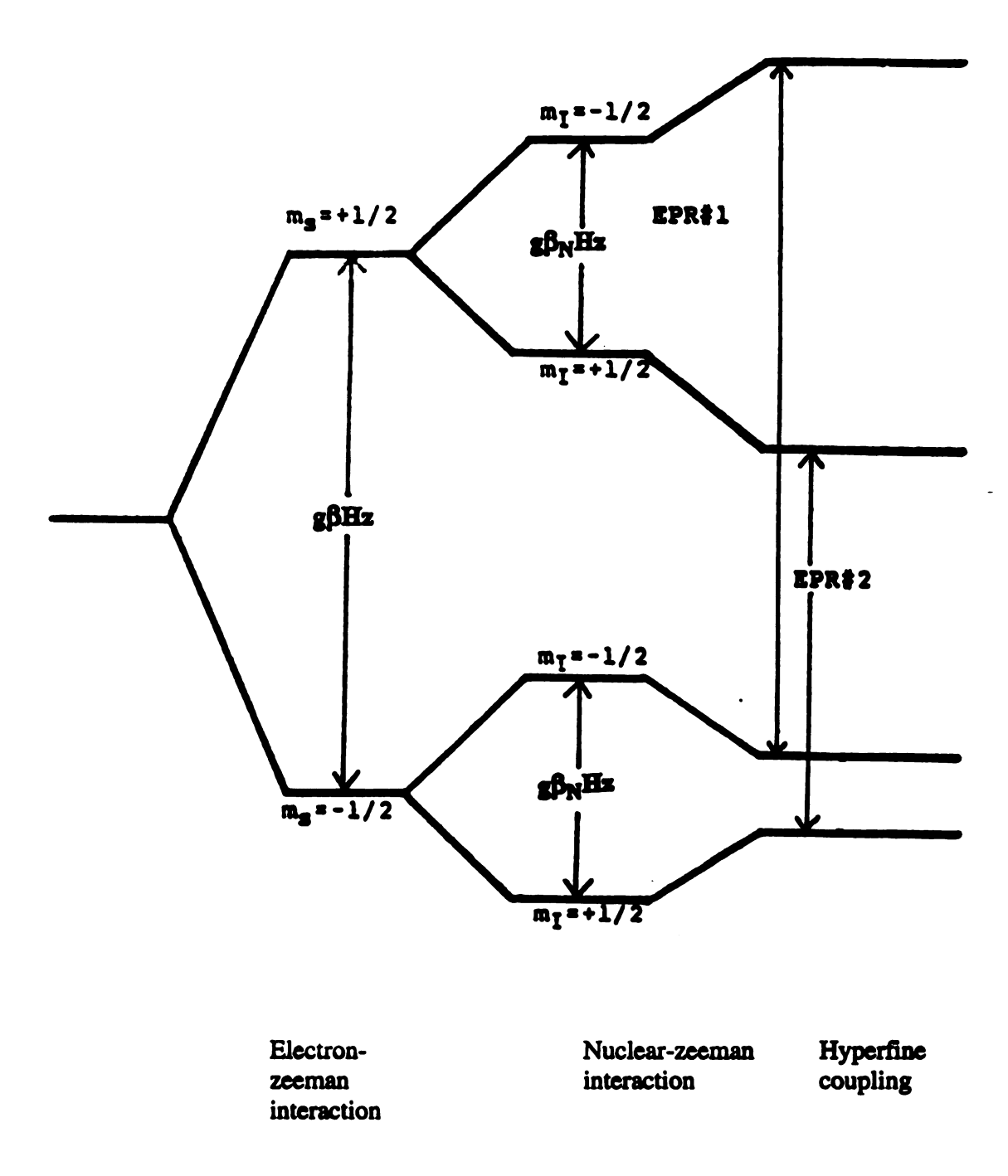


Figure 2.1. Energy level diagram for a S = 1/2, I = 1/2 system in a constant magnetic field. The allowed EPR transitions are displayed.

$$\Delta E_1 = hv_1 = g\beta H_z + A/2$$

$$\Delta E_2 = hv_2 = g\beta H_z - A/2$$
(2)

The EPR spectrum for this simple system consists of two peaks, centered at the value of g βH_Z and separated from the center by A/2. The two peaks are then separated by A. Depending on the spin state of the electron it can have the precessional frequencies hv_1 or hv_2 . The number of peaks in an EPR spectrum, for a system with one set of equivalent nuclei, is (2nI+1), where n is the number of magnetically equivalent nuclei. Each set of equivalent nuclei will have a (2nI+1) term and the total number of peaks in the EPR spectrum is Π (2nI+1).

The hyperfine coupling constant, A, is composed of isotropic (A_{iso}) and dipolar (A_{Dip}) components, as shown in equation 3.

$$A=a(S\cdot I) + S\cdot A^{T}\cdot I$$

$$A=A_{iso} + A_{Dip}$$
(3)

The isotropic coupling results from a non-zero probability of the unpaired spin density being located at the nucleus of the coupled atom and can be calculated by equation 4.

Aiso =
$$3\pi g_e \beta_e g_N \beta_N \psi | (0) |^2 S \cdot I$$
 (4)

 $\psi(0)$ = wavefunction evaluated at the nucleus

In order for the unpaired spin to be at the nucleus of an atom, it must be located in an s orbital. For the simplest system, a C_{α} -H fragment from an aromatic system, such as the benzene anion radical, isotropic hyperfine coupling is the result of spin polarization.²

Hund's rule predicts that the highest multiplicity state will be the ground state for an atom. This is due, in part, to the favorable exchange interaction that occurs between unpaired electrons in different orbitals with parallel spins. A similar exchange interaction between the unpaired electron on C_{α} , and the electrons in the σ bond to the proton occurs. If the unpaired electron, located in the p_z orbital, is aligned spin up (-1/2), then the electron at the C_{α} end of the σ bond has a greater probability of having the spin-up alignment. This causes the electron on the H end of the σ bond (in the H 1s orbital) to have a greater probability of being aligned spin down. The net effect is unpaired spin density at the hydrogen nucleus with the spin down configuration. The coupling between the hydrogen nucleus and the unpaired spin at the nucleus gives rise to the isotropic hyperfine coupling. The unpaired spin density in the p_z orbital, with spin up alignment, is designated as positive. Since the electronic spin at the proton has a net spin down orientation,

the hydrogen 1s orbital contains negative spin density. The negative spin density yields a negative isotropic hyperfine coupling.²

When looking at the whole molecule, rather than a C_{α} -H fragment, the unpaired spin is located in a π molecular orbital.. For benzene, the electron is distributed over the whole molecule so each carbon contains 1/6 of an unpaired electron. All the protons then have the same isotropic coupling. In systems with lower symmetry, the unpaired electron may not be distributed equally at all sites. The unpaired spin density at a carbon can be determined from the magnitude of the isotropic coupling to the proton bound to the carbon, by the McConnell relationship, equation 5.

$$A_{iso} = \rho^{\pi}Q \tag{5}$$

Where ρ^{π} is the unpaired spin density in the p_z orbital of C_{α} and Q is a proportionality constant. Q has been determined for many π radicals and is usually in the range 23-26 G, although substantially greater variation in the magnitude of this "constant" can occur. 1

The isotropic coupling to β -protons, that is, protons on a carbon that is one bond removed from the site of unpaired spin density, is of the same order as isotropic coupling to α -protons. An example of β -protons is the methyl group of toluene. The mechanism of isotropic coupling to β -protons is different than for α -protons. For β -protons the unpaired spin density on the protons is accomplished by hyperconjugation. Each of the sp³ hybridized orbitals from C_{β} (the carbon of the methyl group) contain some fraction of the C_{β} pz orbital. The overlap of the C_{α} pz orbital and the C_{β} pz orbital allows spin density to transfer to the C_{β} pz orbital. Since each of the orbitals bonding to the methyl protons contain some fraction of C_{β} pz, there is unpaired spin density on each β -proton. The fraction of C_{β} pz orbital in each of the hybridized orbitals will depend on the orientation of the proton relative to the direction of the pz orbital. The less C_{β} pz orbital involved in the C_{β} -H bond, the less overlap with C_{α} pz, and the less unpaired spin density at the proton. This in turn means a smaller isotropic hyperfine coupling. The orientation effect on the magnitude of the hyperfine coupling is described by equation 6.

$$A_{iso} = B_2 \rho \cos^2 \theta \tag{6}$$

The angle θ is the dihedral angle between the direction of the of the p_Z orbital and the plane containing C_{α} , C_{β} , and H_{β} . The β -proton has a maximum isotropic hyperfine coupling when θ =0° and a minimum when θ =90°. Since there is direct transfer of unpaired spin density from C_{α} to H_{β} , there is positive spin density on H_{β} and the isotropic hyperfine coupling is positive.⁴

The EPR spectra of transition metals, that have $I\neq 0$, also show isotropic coupling to the nucleus of the metal. The unpaired electrons in the d orbitals, through the process

of spin polarization, cause there to be unpaired spin density in the ns orbitals.⁵ The unpaired electrons in the d orbitals also polarize the electrons in the metal ligand bonds, resulting in observable isotropic hyperfine coupling to ligand nuclei.⁶

The second component of the hyperfine coupling tensor (equation 3) is the dipolar coupling. The dipolar coupling arises from the through space interaction of two dipoles, in this case two magnetic dipoles. The strength of the dipole coupling can be calculated by using equation 7. The dipole hyperfine coupling tensor is traceless. 1

$$A_{Dip} = g_e \beta_e g_N \beta_N (3\cos^2 \theta - 1)/r^3$$
 (7)

 $g_N = nuclear g-value$

 β_N = nuclear Bohr magneton

r = magnitude of vector r between the electron spin and nuclear spin

 θ = angle between **r** and the Zeeman field

For an α -proton in a radical such as \cdot CH(COOH)₂, the principal values of the dipolar coupling tensor are $(0.5A_{iso}, -0.5 A_{iso}, 0)$ for A_X , A_Y , and A_Z , respectively. A_Y is oriented along the C-H bond, A_Z along the C_{α} p_Z orbital and A_X is orthogonal to the other two tensor components. The A_Z component is near zero, since the unpaired electron in the p_Z orbital will, on average, be located at a position where the term $(3\cos^2\theta - 1)$ is near zero. Summing the dipolar and isotropic hyperfine coupling constants for an α -proton yields a hyperfine coupling tensor that is approximately $(1.5A_{iso}, 0.5A_{iso}, A_{iso})$. The dipolar portion of the hyperfine coupling for α -protons is generally 50% the isotropic coupling.

For β -protons the dipolar coupling is generally much smaller than that observed for α -protons since the protons are further removed from the unpaired spin density on C_{α}

. The dipolar coupling is commonly only 10% the isotropic coupling and the dipolar coupling tensor is nearly axial with $A_X \cong A_Z$.

When paramagnetic species are in solution and tumbling rapidly, the g and A tensors are averaged. The observed g value is then $(g_X+g_Y+g_Z)/3$. The dipolar hyperfine tensor is traceless so $(A_X+A_Y+A_7)/3=0$ and only A_{is0} is observed. In the data presented in this text, all the spectra were recorded with frozen solution samples. In these samples all possible molecular orientations are present and each oriention will have g and A values that are dependent on the orientation of the molecule relative to the applied magnetic field. The experimentally observed powder pattern EPR spectrum is the composite of the EPR spectrum observed for each orientation. The EPR spectrum is recorded as the first derivative and peaks are observed at the corresponding positions for the principal values of the g and hyperfine coupling tensors. The peaks in the EPR spectra of frozen solutions are generally broad, especially for transition metals, and in some cases, some components of the A tensor are obscured by spectral congestion. The broad linewidths of transition metals commonly obscure the hyperfine coupling to ligands. In order to resolve the hyperfine coupling component, the techniques of ENDOR and ESEEM have been applied. These techniques have the advantage of reducing the number of peaks in the spectrum and narrowering their linewidths, both of which aid in observing the hyperfine coupling to weakly coupled nuclei, without sacrificing the information content in the spectrum.

Electron nuclear double resonance (ENDOR)

The Hamiltonian that describes the ENDOR experiment is exactly the same as the one used for EPR (equation 1).⁸ Since the Hamiltonian is the same in both experiments, the energy levels are also the same for the system under study. The difference in the two

experiments is that the ENDOR experiment promotes and detects transitions between nuclear spin states, rather than between electronic spin states, as in EPR.

In discussing the ENDOR experiment we shall consider the case of an unpaired electron interacting with a single proton. The hyperfine coupling to the proton is described in equations 4 and 7. The energy level for this system is shown in Figure 2.2. Transitions between energy levels 1 and 3 and energy levels 2 and 4 are the EPR transitions. In the ENDOR experiment, the selection rules are Δm_I=1, Δm_S=0 and the system undergoes a nuclear spin flip. The ENDOR transitions then are between energy levels 1 and 2 and between energy levels 3 and 4; the energy differences between these levels falls in the radiofrequency (RF) range. In ENDOR, unlike EPR, the effect of the RF radiation on the EPR resonances are detected, rather than direct detection of the absorption of RF power, at frequencies corresponding to ENDOR#1 and ENDOR#2.

The Zeeman field strength is adjusted so that one of the EPR transitions, EPR#1, is in resonance. The microwave power is then increased to saturate this EPR transition partially, and this has the effect of equalizing the populations of energy levels 2 and 4. The system is next irradiated with a swept RF field. When the frequency of the RF fulfills the resonance condition of ENDOR#1, the transition will be saturated and the population of energy levels 3 and 4 will be equalized. This results in a lowering of the population of level 4 and a desaturation of the EPR#1 transition. The EPR transition will then increase in intensity and this change in intensity is detected as a peak in the ENDOR spectrum. A second ENDOR peak is detected when the RF fulfills the resonance condition for the ENDOR#2 transition. The ENDOR spectrum is, thus, simply the change in EPR intensity plotted as a function of RF frequency.

The ENDOR spectrum, considering only isotropic hyperfine coupling, consists of two peaks centered at v_N , the free proton resonance. v_N is equal to the nuclear-Zeeman splitting, Figure 2.2, and the splitting between the ENDOR resonances is A_{iso} . The

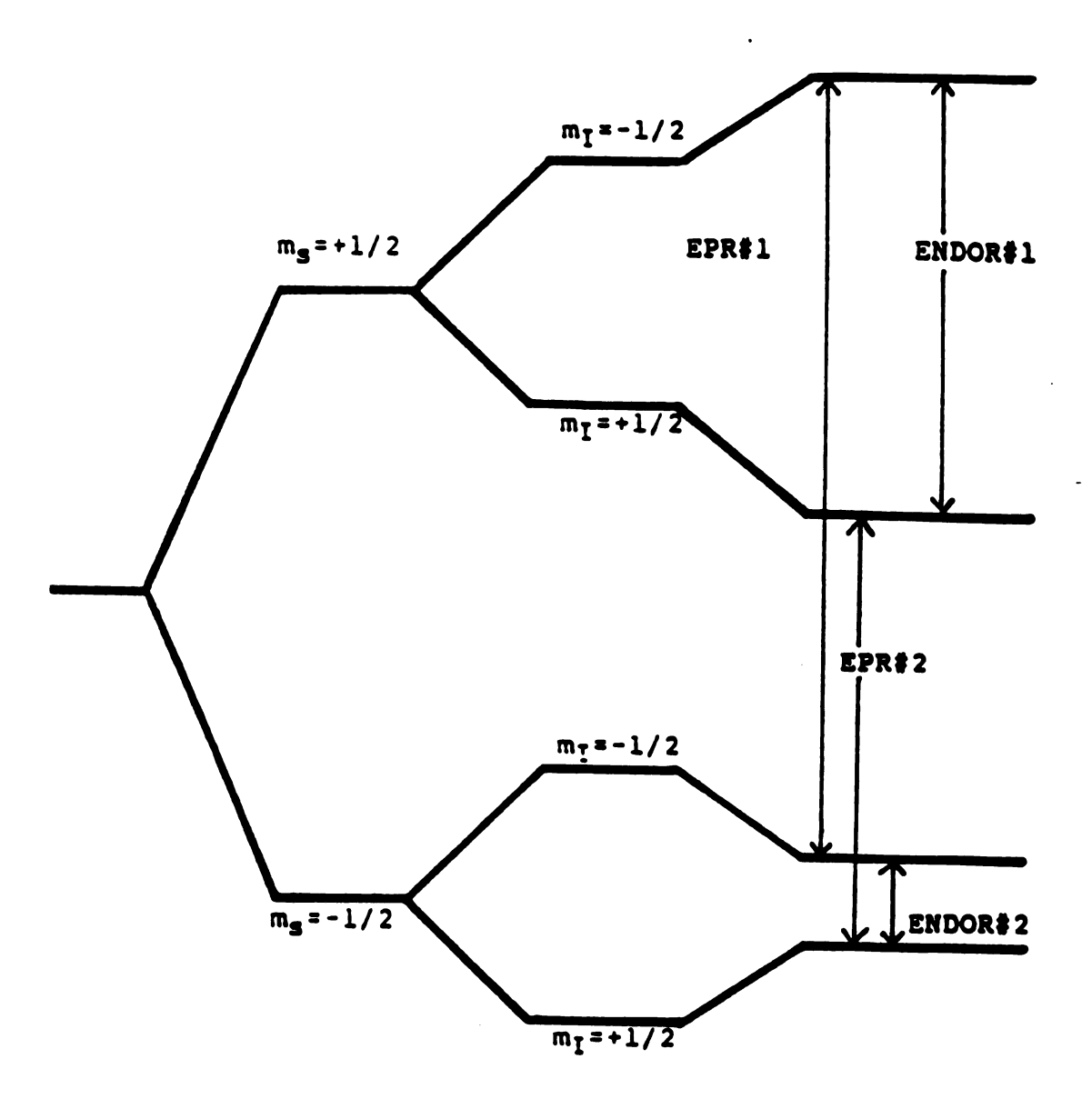


Figure 2.2. Energy level diagram for a S = 1/2, I = 1/2 system in a constant magnetic field. The allowed EPR and ENDOR transitions are displayed.

energy at which the two ENDOR peaks will occur is predicted by equation 8, where v_N is ≈ 14.5 MHz for a proton in a magnetic field near 3500 G.

$$hv = v_N \pm |A/2| \tag{8}$$

The ENDOR spectrum is simplified compared to the EPR spectrum due to the fewer number of peaks. Each set of equivalent peaks gives rise to a single pair of peaks in the ENDOR spectrum. Two sets of two magnetically equivalent protons, with I=1/2, gives rise to four peaks in the ENDOR spectrum but nine peaks in the EPR spectrum. Hence, reduction in spectral density, without a reduction in spectral information, occurs in ENDOR relative to EPR.

The ENDOR spectrum of a spin system in a frozen solution will have distinct features depending on whether the hyperfine coupling tensor is axial $(A_x=A_z\neq A_y)$ or rhombic $(A_x\neq A_y\neq A_z)$. The lineshape that appears for an axial hyperfine coupling tensor, shown in Figure 2.3, is comprised of a pair of absorptive shaped peaks and a pair of derivative shaped peaks.⁹ For a hyperfine coupling tensor that is purely dipolar, equation 7 predicts that A_{\parallel} , with $\theta=0^{\circ}$, is twice as large as A_{\perp} , with $\theta=90^{\circ}$. The absorptive shaped peaks are then split by an amount equal to A_{\parallel} and the derivative shaped peaks by A_{\perp} . The lineshape for a rhombic hyperfine coupling tensor is shown in Figure 2.3. The absorptive shaped peaks are split by A_z , the derivative peaks by A_y , and the rhombic shaped peak by A_x , where $A_z > A_y > A_x$.⁹

The dipolar hyperfine coupling discussed in the EPR section is for aliphatic systems in which all, or nearly all of the unpaired spin density is located in a single p_Z orbital. For π radicals in conjugated systems, the unpaired electron is located in a molecular orbital that is distributed over the entire π system. An α -proton is dipolar coupled to the unpaired electron on C_{α} and to the other sites in the molecule that contain unpaired spin density. The total dipolar coupling is a summation of the dipolar couplings

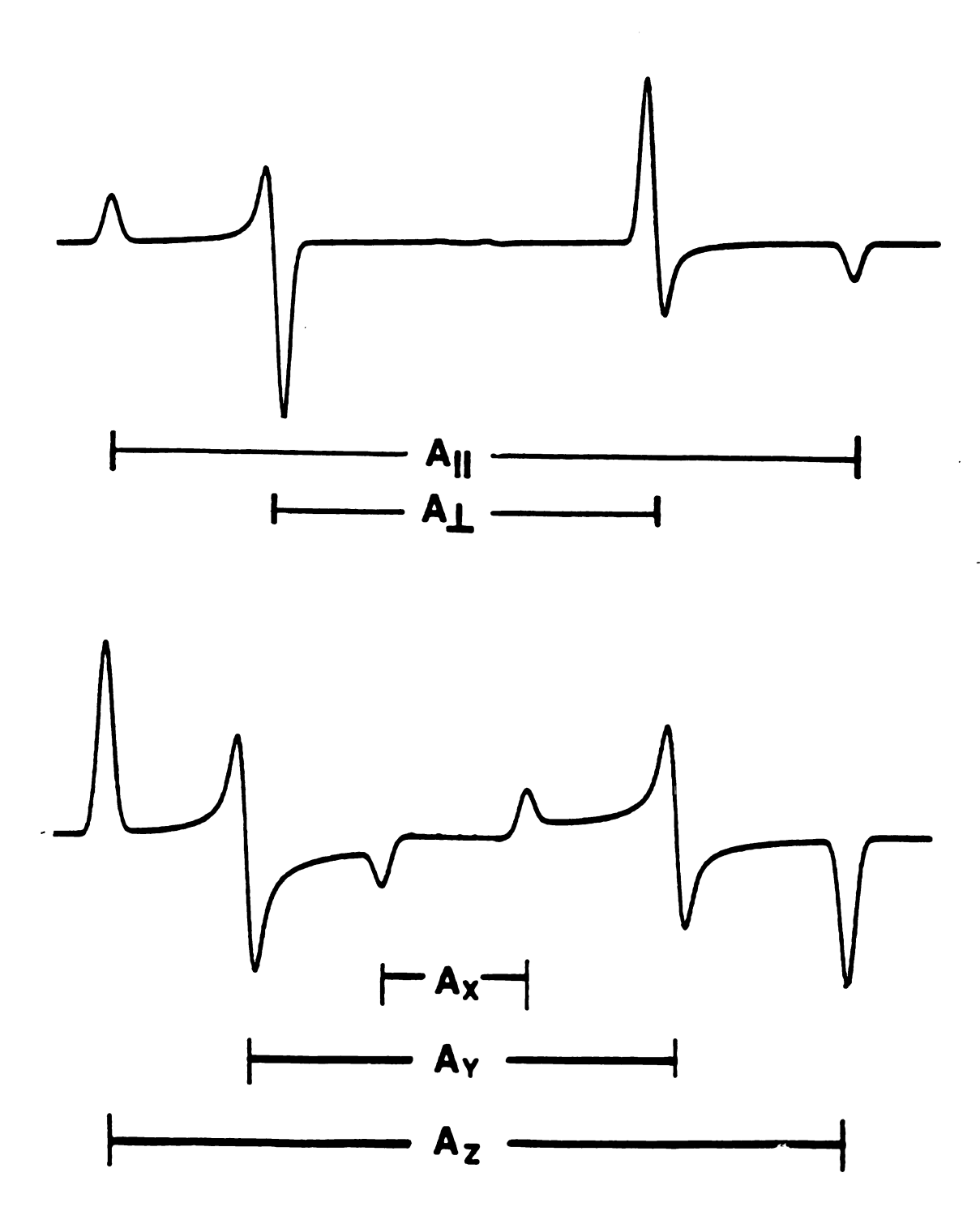


Figure 2.3. A) experimentally observed lineshape for an axial hyperfine coupling tensor, B) lineshape observed for a rhombic hyperfine coupling tensor.

to each site in the molecule that contains unpaired spin density. By using equation 7, each of the dipolar hyperfine coupling tensors can be calculated, if the unpaired spin density at each site is known, and the total dipoler hyperfine coupling determined. O'Malley and Babcock have used this approach in the study of benzoquinone radicals. ¹⁰ They observed that the ring protons (α -protons) did not have a hyperfine tensor of (1.5Aiso, Aiso, 0.5Aiso), but rather (-10.2, -3.9, -9.0 MHz) for A_X , A_Y , and A_Z , with Aiso =-7.7 MHz. It was determined that the deviation away from the values seen for aliphatic radicals was the result of sizeable dipolar couplings to the unpaired spin density at the carbon and oxygen of the carbonyl moiety. The reverse approach can also be applied. If the hyperfine tensor for each of the protons is known, the unpaired spin density at each site can be determined.

The situation is different for protons that are not covalently bonded to the paramagnet. The protons from the first several solvation spheres are observed as an intense, and in many cases, nearly featureless peak, with an overall width of approximately 2 MHz. This intense "matrix" peak, arising from the solvent protons, is centered at v_N .⁸ Protons that are in the near vicinity of the radical can also have sizeable hyperfine couplings (0-7 MHz) that are purely, or nearly purely, dipolar. By using equation 7, and the hyperfine coupling constants determined from ENDOR, the distance from the unpaired electron to nearby protons can be calculated.

Assignments of ENDOR peaks to particular protons can be accomplished by deuterium substitution. The value of g_N for deuterium is $\approx 1/6$ that for protons. In Figure 1.1, the nuclear zeeman splitting is reduced by $\approx 1/6$ for deuteriums due to the lower value of g_N . The peaks in the ENDOR spectrum that arise from deuterium are centered at 2.2 MHz rather than 14.5 MHz for protons. Selective deuterium substitution causes the disappearence of the corresponding proton peaks in the ENDOR spectrum, which allows assignments of ENDOR peaks to the different protons in a paramagnetic system.

Electron spin echo envelope modulation

Electron spin echo envelope modulation (ESEEM) is a pulsed-EPR technique. While the phenomenological description of the ESEEM technique is completely different from ENDOR, the data that is recorded from both experiments are identical and the same Hamiltonian is applicable. The ESEEM and ENDOR techniques are complementary, ENDOR is superior in studying the hyperfine coupling to protons and ESEEM is better at observing hyperfine couplings to deuterium and weakly coupled nitrogen nuclei.

In the description of the 2-pulse ESEEM experiment, the simple S=1/2, I=1/2 system of Figure 1.1 will be used. In an applied magnetic field, there will be more spins aligned antiparallel to the applied magnetic field than parallel, as a result of the boltzman distribution of the $m_S=\pm 1/2$ states. If the magnetic field is assumed to be directed along the -Z direction there are more spins aligned along Z and there is a net macroscopic magnetization along the z direction. This is shown in Figure 2.4A as a vector along Z. The vector along Z is, then, the summation of all the paramagnetic species in the sample. For the simple system described here, there are two sets of spins, with precessional frequencies hv_1 (ω_1) and hv_2 (ω_2). Each set of spins, with a specific precessional frequency, comprises a spin packet.

Application of a second magnetic field along the X direction produces a torque on the magnetization vector along the Y direction, Figure 2.4B. The length of time that the second magnetic field is present determines the angle that the magnetization vector makes with the Z axis. The second magnetic field is applied by using a short pulse of microwaves. If the pulse length is of a duration sufficient to cause a 90° rotation of the magnetization vector, the pulse is referred to as a a $\pi/2$ pulse. The spin packets still precess about the Z axis but now in the XY plane. In Figure 2.4, a rotating axis system is used, in which the axis system is rotating at a frequency ω_0 (=g β Hz), which is the precessional frequency at the center of the EPR spectrum. Since the two spin packets

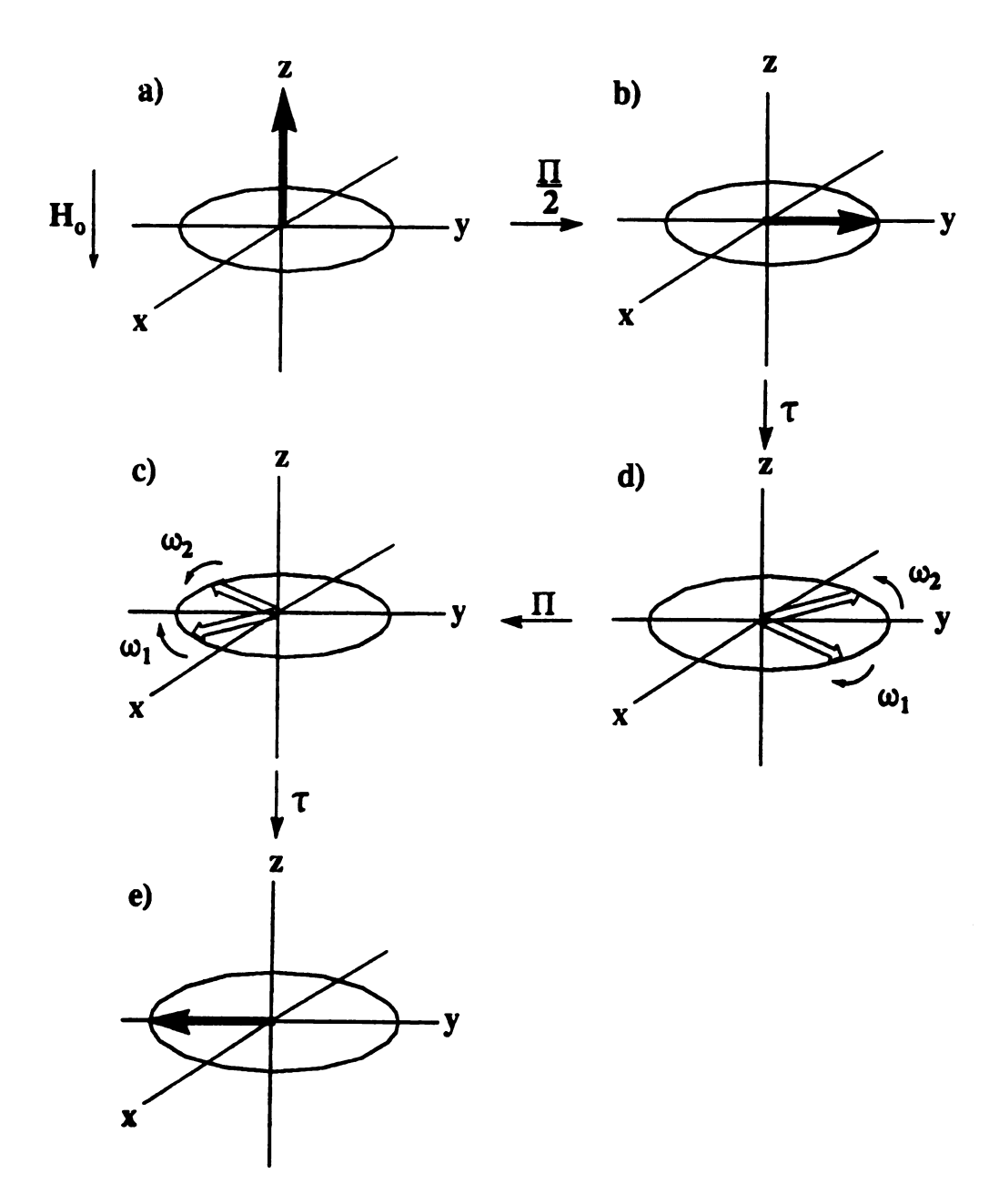


Figure 2.4 Magnetization of spin packets 1 and 2 during a 2-pulse experiment. a) in static field; b) after $\pi/2$ pulse; c) dephasing after time τ ; d) after π pulse and e) refocusing of spin packets after time τ to yield echo.

precess at different frequencies, ω_1 and ω_2 , the two magnetization vectors dephase, Figure 2.4C. After a time τ , a π pulse is applied, which rotates the spin packets 180° around the X axis, Figure 2.4D. The original precessional frequencies, however, remain unaltered. Since the precessional direction does not change either, the result is that the spin packets refocus after the same time τ into a macroscopic magnetization, which produces a two pulse echo, Figure 2.4E.

As the value of τ is increased, the magnitude of the echo recorded a time τ after the second pulse decreases. The amplitude of the echo versus τ is the echo envelope. Effects on the spin packets by magnetic fields in the molecules causes the spin packets to change their precessional frequencies. After the second pulse the magnitization vectors do not refocus properly and the macroscopic magnetization is decreased. The time for the echo amplitude to decrease is the phase memory time T_M . The value of T_M is generally about 2 µsec for aqueous or proteinaceous samples. Spin diffusion from the flipping of the nuclear spin of protons principally determines the magnitude of T_M . It is expected that the echo amplitude should decrease monotonically, but under many conditions it is observed to contain modulations. These modulations arise from hyperfine coupling to magnetic nuclei. 11

In the energy level diagram for the S=1/2 I=1/2 system, there are four levels and two allowed transitions, labeled A and B. There are, in adition, two semi-forbidden transitions, C and D, the semi-forbidden transitions represent a simultaneous electron and nuclear spin flip, Figure 2.5. The transitions C and D are partially allowed when the hyperfine coupling is anisotropic because the anisotropy mixes the spin states and non-zero transition probabilities for the C and D transitions occur. The application of a $\pi/2$ pulse to a S=1/2 and I=1/2 system is shown in Figure 6A. In this example, the axis system rotates with frequency ω_2 , so spin packet 2 is fixed along the Y direction. After a time τ , spin packet 1 has dephased, Figure 6B. After the second π pulse, spin packet 2 is rotated to be along -Y. In addition, a portion of spin packet 2 undergoes transition C, in

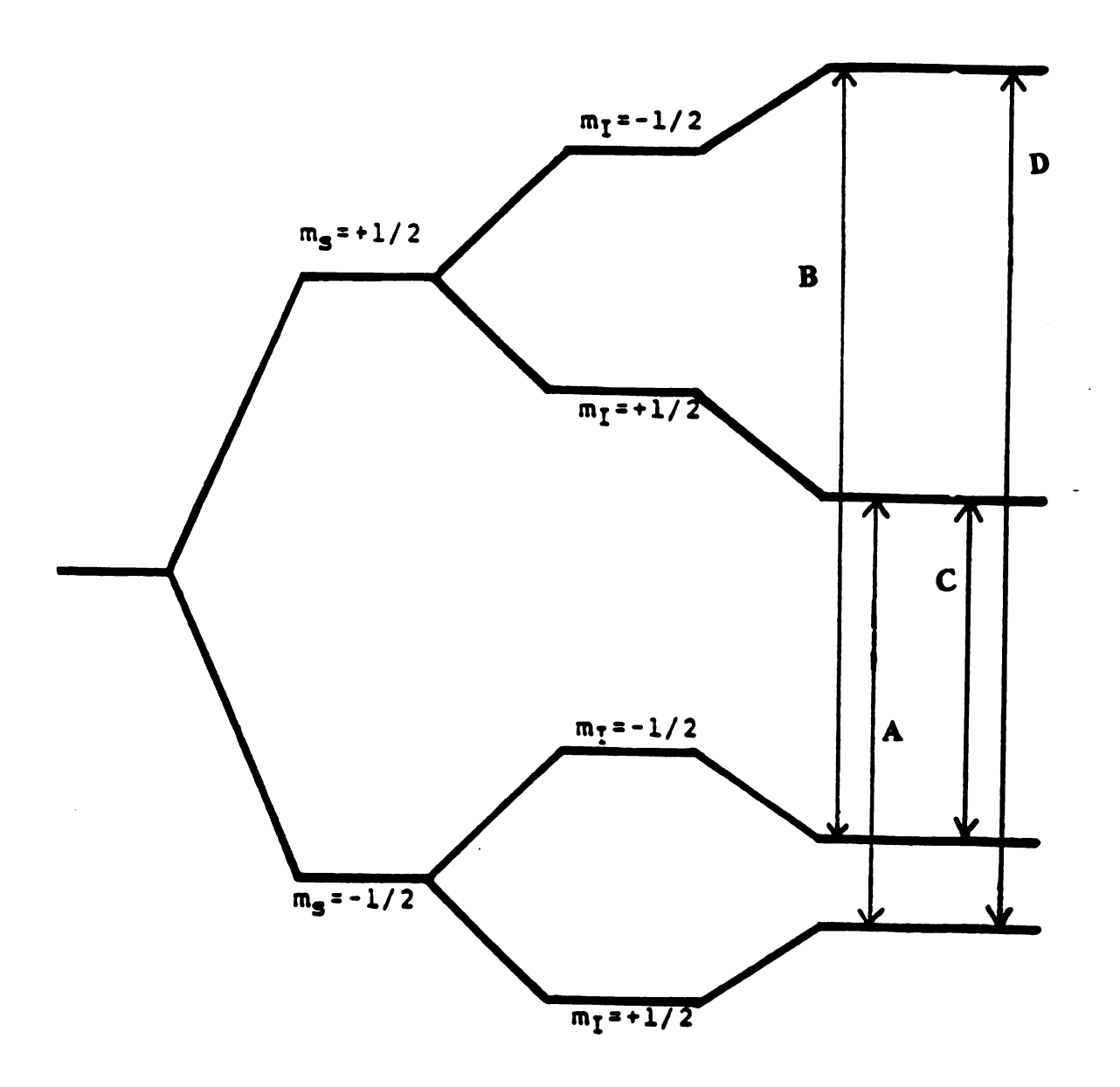


Figure 2.5. Energy level diagram for a S = 1/2, I = 1/2 system in a constant magnetic field. The allowed and semi-forbidden EPR transitions are displayed.

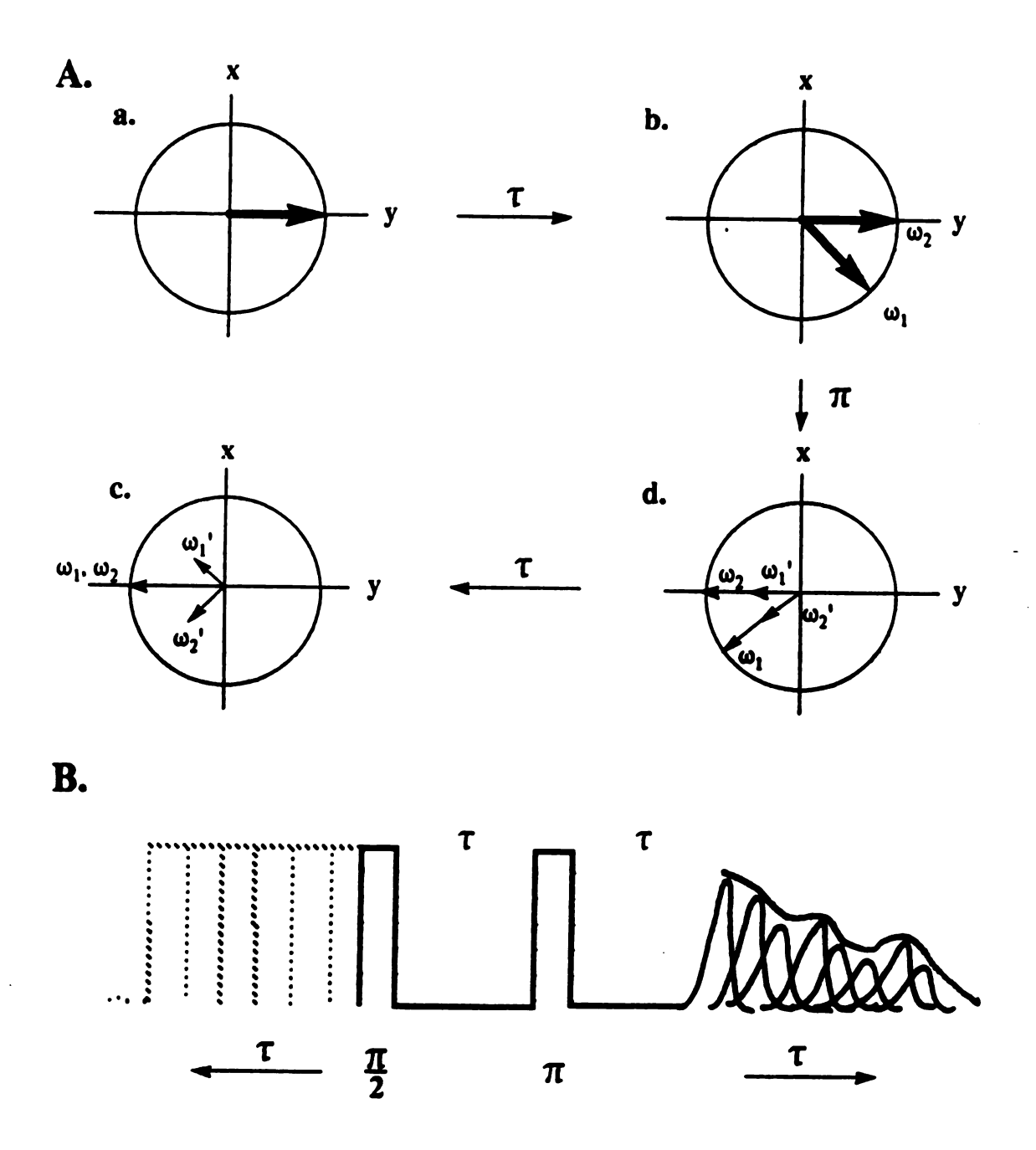


Figure 2.6 Magnetization of spin packets 1 and 2, including the effect of semi-forbidden transitions, during a two-pulse experiment. A) a) after a $\pi/2$ pulse; b) dephasing of spin packets during time τ ; c) after π pulse showing the effect of branching and d) refocusing of spin packets 1 and 2 precessing at frequencies ω_1 and ω_2 . B) Echo amplitude versus the magnitude of τ giving rise to the echo-decay envelope.

Figure 2.5, and is aligned along -Y but with precessional frequency ω_1 (ω_1), Figure 2.6C. A similar branching is observed for spin packet 1, with a portion of the spin packet now precessing at ω_2 (ω_2). The spin packets precessing at ω_1 and ω_2 will refocus after the time τ and give rise to the two pulse echo. The spin packets precessing at ω_1 and ω_2 are not aligned along -Y but are added vectorally to the macroscopic magnetization. Depending on the length of τ , the spin packets ω_1 and ω_2 will add different amounts to the amplitude of the echo. The two pulse echo is recorded for a series of τ values and the echo envelope, with the modulation from hyperfine coupling to a proton, is shown in Figure 2.6E. Fourier transform of the echo-decay envelope yields the ESEEM spectrum. This spectrum is the same as that recorded by ENDOR, except that it is not acquired in the first derivative mode.

The phase memory time for the two pulse echo is short, which results in broad lines in the ESEEM spectrum. 11 In order to increase the phase memory time a threepulse, or stimulated echo, pulse sequence is used. The pulse sequence is $(\pi/2-\tau-\pi/2-T-\pi)$ /2) and at a time τ after the third pulse the echo is recorded. The value of T is incremented and the echo is recorded for each value of T. This experiment is analogous to the two pulse experiment except that the π pulse in the two pulse experiment is divided into two $\pi/2$ pulses. In the three pulse experiment the first pulse rotates the magnetization into the XY plane. After a time τ the second pulse rotates the magnetization into the -Z direction. With the spin packets aligned along -Z they are affected to a lesser extent by the processes that cause the decrease in the two-pulse echo. With the spins aligned along -Z the magnetization is most affected by spin lattice relaxation, the process that returns the system to its equilibrium condition. Spin lattice relaxation is slower than T_M and, thus, the echo amplitude decays more slowly. After a time T, the third pulse rotates the spin packets back into the XY plane and the spin packets refocus along the -Y direction. There is a modulated echo envelope exactly as in the two-pulse experiment. The slower decay of the echo amplitude in the three-pulse experiment, allows the echo-decay

envelope modulations to be recorded for a longer time than in the two pulse experiment.

This results in narrower lines in the ESEEM spectrum and better resolution.

LIST OF REFERENCES

- 1) Wertz, J.E. and Bolton, J.R. Electron Spin Resonance: Elementary Theory and Practical Applications, McGraw-Hill, New York, 1973.
- 2) McConnell, H.M., Heller, C., Cole, T. and Fessenden, R.W. J. Chem. Phys., 1959, 82, 766.
- 3) Hutchinson, C.A. and Mangum, B.W. J. Chem. Phys., 1961, 34, 908.
- 4) a) Anderson, R.J.M., and Kohler, B.E. J. Chem. Phys., 1976, 65, 2451. b) Vincent, J.S. J. Chem. Phys., 1971, 54, 2237.
- 5) Abragam, A. and Bleaney, B. Electron Paramagnetic Resonance of Transition Ions Dover Publications, New York, 1970, p. 411.
- 6) Abragam, A. and Bleaney, B. Electron Paramagnetic Resonance of Transition Ions Dover Publications, New York, 1970, p. 192.
- 7) Kwiram, A.L. J. Chem. Phys., 1968, 49, 2860.
- 8) Kevan, L. and Kispert, L.D. Electron Spin Double Resonance Spectroscopy, John Wiley & Sons, New York, 1976.
- 9) Atkins, P.W. and Symons, M.C.R. The Structure of Inorganic Radicals, Elsevier, Amsterdam, 1967, p.268.
- 10) O'Malley, P.J. and Babcock, G.T. J. Am. Chem. Soc., 1986, 108, 3995.
- a) Mims, W.B. and Peisach, J. Electron Spin Echo Spectroscopy and the Study of Metalloproteins, in Biological Magnetic Resonance (Berliner, L.J. and Reuben, J.,eds.) Plenum Press, New York, 1981, pp 213-263. b) Mims, W.B. Phys. Rev., 1972b, B5, 2409.

CHAPTER 3 ENDOR AND ESEEM STUDIES OF YD+

Introduction

Recently, it has been recognized that amino acids are important redox co-factors in a number of enzymes. Stable enzymatic intermediates containing oxidized tyrosine radicals have been observed in Photosystem II (PSII), ribonucleotide diphosphate reductase (RDPR), prostaglandin synthase (PGHS), and galactose oxidase. The oxidation of tyrosine, observed in the enzymes listed above, is essential for enzymatic activity. In galactose oxidase the redox active tyrosine is chemically modified; the carbon *ortho* to the oxygen is covalently bonded to the sulfur from a cysteine side-chain. The tyrosine radicals observed in this class of enzymes show variability in their lifetimes, redox potential and EPR spectra. In photosystem II the oxidized tyrosine Yz+, is reduced in milliseconds even in the absence of the oxygen evolving complex (OEC), whereas the tyrosine radical of RDPR is stable for a week at 4°C.8

The tyrosine EPR spectra from RDPR and PGHS are similar, showing a broad doublet with a peak to peak splitting of 20 G and a peak to trough splitting of 35 G. 3,4 . The radical from galactose oxidase has an overall linewidth of 33 G, however, the spectrum has three peaks with approximately the same amplitudes. The stable radical from PSII, $^{+}$, yields an EPR spectrum that is significantly different from the others. The EPR spectrum from $^{+}$ is a singlet with five partially resolved peaks and a peak to trough linewidth of 20 G, Figure 3.2.9 The isotropic component of the g-tensors for the

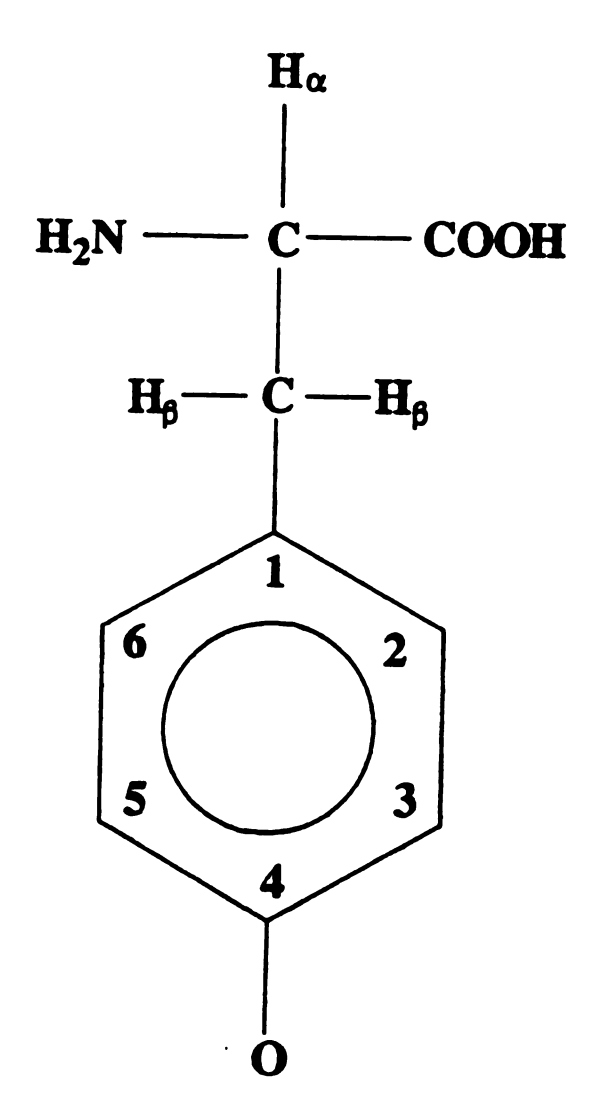


Figure 3.1 Free tyrosine showing the numbering system used in the text.

unmodified tyrosines are in the range 2.0047-2.0049. These values are closer to the values reported for neutral radicals, in which the phenol group is deprotonated upon oxidation, of 2.0045 than to the cation radical, 2.0033.9 Raman¹⁰ and ENDOR¹⁵ studies of RDPR have shown that the redox active tyrosine is deprotonated in its oxidized form.¹⁰ By using electron nuclear double resonance (ENDOR) it has been established that YD⁺, in PSII membranes isolated from spinach, is deprotonated but hydrogen bonded.¹¹ The deprotonation of tyrosine upon oxidation is expected from the change in pKa. The pKa of tyrosine at pH=7.0 is 10 whereas the pKa of the cation radical is -2, far lower than any of the amino acids.¹²

The shape of the EPR spectrum from a tyrosine radical is dictated by the hyperfine coupling between the unpaired spin and the ring and methylene protons. The magnitude of the hyperfine coupling of each proton is dependent on the amount of unpaired spin density at the carbon to which the proton is bound. Insight into the unpaired spin density distribution in tyrosine can be obtained from studies of phenol and phenoxy radicals.

Phenol is a odd-alternate conjugated system and odd-alternate systems have a nonbonding π molecular orbital for the highest occupied molecular orbital. The oxidation of phenol (or tyrosine) leaves the unpaired electron in this π non-bonding orbital. Theoretical approaches have determined that in the π non-bonding orbital containing the unpaired electron, the unpaired spin density is located primarily on carbons C_1 , C_3 , C_5 , and the oxygen (see Figure 3.1 for numbering system). These results were confirmed by EPR studies of phenoxy radicals, which show that the largest hyperfine couplings are to the protons at the C_3 and C_5 positions, [3,5] protons, (6-7 G) and at the C_1 position (10 G). The hyperfine coupling to the protons of a methyl group substituent at C_1 is 12 G, the large hyperfine coupling resulting from hyperconjugation. The EPR spectra of phenoxy radicals, as well as tyrosine radicals, are thus largely determined by the hyperfine coupling to the [3,5] and methylene protons.

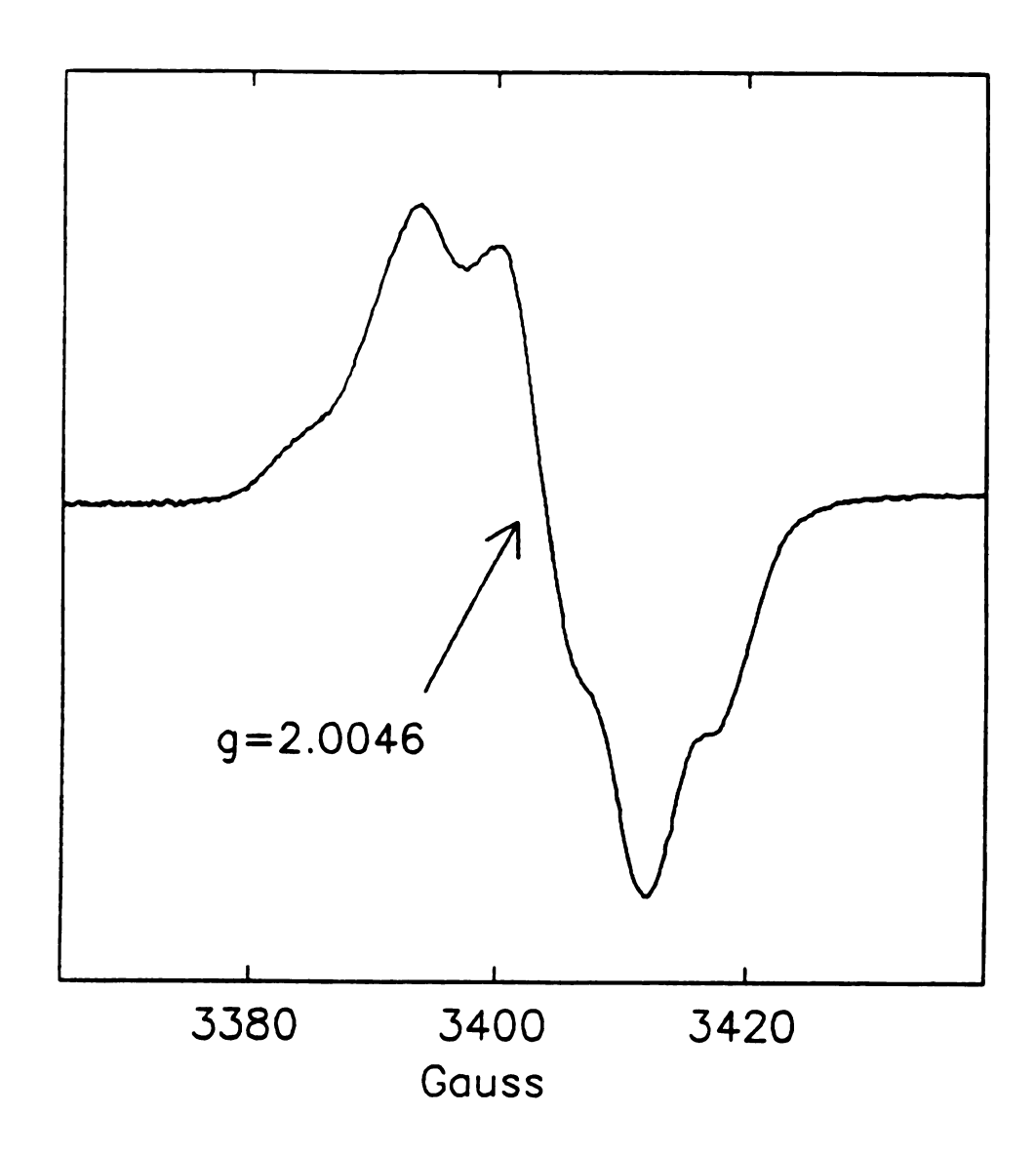


Figure 3.2 EPR spectrum of Y_D⁺ in PSII particles from Synechocystis 6803. Conditions: µwave power, 2mW; modulation, 4 Gpp; temperature, -155°C

As discussed in Chapter 2, the hyperfine coupling to a β -proton (the methylene protons in tyrosine) is dependent both on the unpaired spin density at C_1 and the dihedral angle between the p_Z orbital of C_1 and the plane containing C_1 , C_{β} , and H_{β} . EPR and ENDOR studies of the tyrosine radical in RDPR, Y_D^+ , and a tyrosine single crystal have determined that the methylene group is oriented such that one methyl proton has a large hyperfine coupling (8-20 G) and the second has a small hyperfine coupling (<2 G). If the unpaired spin density is constant in the enzymes containing a stable tyrosine radical, then the changes in the EPR spectra are a result of different orientations of the methylene group relative to the ring. Since the EPR spectra are recorded in frozen solutions, the tyrosine is locked into a single conformation.

In order to understand fully the shape of the EPR spectra from the different tyrosine radicals, the hyperfine coupling tensors from the ring and methylene protons must be known. This information can be obtained with ENDOR where the higher resolution allows, in many cases, all three components of the hyperfine tensor to be measured. By using ENDOR and selective deuterium labeling, the hyperfine tensors from the [3,5] and methylene protons were determined for RDPR. 15 From the ENDOR results the unpaired spin density distribution in the phenol head group of the tyrosine radical in RDPR was calculated. In these calculations the dipolar coupling between protons and all sites of unpaired spin density in the molecule was considered. In this way, a self-consistent determination of the spin distribution was possible. From the spin density at C_1 the dihedral angle of the methylene proton was calculated to be $\theta=33^{\circ}.15^{\circ}$

This chapter discusses a similar ENDOR investigation of the tyrosine Y_D^+ , of Photosystem II. This work was undertaken for several reasons. Knowledge of the unpaired spin distribution in Y_D allows a comparison with the results from other tyrosine radicals, both *in vivo* and *in vitro*, to determine if the distributions are similar. Currently, the estimates of the spin density on C_1 range from 0.49 for RDPR¹⁵ to possibly as low as 0.15 for Y_D^{+} . For Y_D^+ there is a range of spin densities that is applicable to the EPR

data. ¹⁶ The questions to be addressed, then, are whether there is such a large variation in the spin density distribution in tyrosine radicals and whether this distribution affects such attributes of the redox active tyrosines as redox potential. In PSII, YD⁺ has a redox potential of +760 mV, ²¹ while free tyrosine in solution has a redox potential of +930 mV. ¹² Since the crystal structure of RDPR has been solved and there are proposed models for the structure of PSII, knowledge of unpaired spin densities may allow insight into the effect that the protein environment has on the electronic structure of the radicals. Determination of the spin density on C₁ also allows the dihedral angle to be calculated. Since the crystal structure of PSII is not known, models based on the bacterial reaction center have been developed. ¹⁷ Knowledge of the dihedral angle puts constraints on the orientation of the tyrosine side-chain in these models.

Hyperfine coupling between the unpaired electron on Y_D^+ and protons in the protein, in the vicinity of the radical, can be detected by ENDOR. In addition to the ENDOR study of Y_D^+ itself, Y_D^+ has also been used as a probe to monitor localized protein structural variations that occur upon biochemical and genetic manipulations of the protein.

Materials and Methods

BBY PSII particles were isolated from spinach by the method of Bethold et al.³⁸ For ENDOR experiments, a sample with [Chl]=6 mg/ml was loaded into an EPR tube, illuminated for 45 seconds, at 0°C, with a 750 W projector, dark adapted for 10 minutes at 0°C, and frozen and stored at 77 K. BBY's were further purified by the method of Ghanotakis et al. to make reaction center complexes (RCC).³⁹ RCC's were resuspended in buffer A, which contains 0.4 M sucrose, 50 mM 2-(N-morpholino)ethanesulfonic acid (MES), 10 mM NaCl, and 10 mM CaCl₂ at pH=6.0. The sample was centrifuged into a quartz EPR tube, illuminated for 45 seconds, at 0°C, with a 750 W projector, dark-

adapted 10 minutes and frozen and stored at 77 K. Removal of the extrinsic polypeptides and the Mn complex was accomplished by adding four parts of tris buffer to one part RCC's at [Chl]=0.5 mg/ml. The tris buffer contains 1 M tris[hydroxymethyl]aminomethane (tris), 1.25 mM ethylenediaminetetraacetic acid (EDTA), and 0.4 M sucrose at pH=8.0. The sample was incubated for 30 minutes on ice in room light, centrifuged for 30 minutes at 40,000xg, washed with buffer A, centrifuged for 30 minutes at 40,000xg, and resuspended with buffer A. The sample was loaded into an EPR tube, illuminated for 45 seconds at 0°C, dark adapted for 10 minutes at 0°C and frozen and stored at 77 K.

PSII particles were isolated from the cyanobacteria *Synechocystis* 6803 by using the method of Noren et al.⁴⁰ The PSII particles were redissolved in buffer B containing 25% (v/v) glycerol, 0.05% (w/v) lauryl maltoside, 50 mM MES, 20 mM CaCl₂, and 15 mM NaCl at pH=6.0. To this sample was added an equal volume of 50% (w/v) polyethylene glycol (PEG) and the sample was centrifuged into an EPR tube. In order to reduce any P₇₀₀+, present from PSI contamination, the PSII pellet was washed with an equal volume of buffer C, which contained equal volumes of buffer B and 50% PEG and 500 μM K₄Fe(CN)₆. The pellet was mixed thoroughly with buffer C, then centrifuged, and the supernatent removed. The sample was illuminated at 0°C for 45 seconds with a 250 W projector, dark-adapted for 10 minutes at 0°C and frozen and stored at 77 K.

Tyrosine incorporation into *Synechocystis* 6803 was accomplished by using the previously published procedure of Barry and Babcock. The PSII purification procedure for these samples is the same as desribed above. For the ring-d₄ labeled tyrosine PSII sample, the small volume of material precluded the use of a centrifuged sample for ENDOR studies. After centrifuging the PSII sample into the EPR tube, the sample was redissolved with an equal volume of buffer B containing 200 µM K₄Fe(CN)₆. The sample was illuminated for 30 seconds with a 250 W projector at 0°C, dark-adapted for 10 minutes on ice and frozen and stored at 77 K. ENDOR spectra were acquired from a

PSII sample, that did not contain deuterium labeled tyrosine, both as a centrifuged pellet and redissolved in buffer B containing 200 μ M K₄Fe(CN)₆ and the spectra were the same (data not shown).

H/D exchange was accomplished by redissolving the PSII particles from Synechocystis 6803 with buffer B, made in D₂O (pD=7.0; pD=pH+0.4), to a final chlorophyll concentration of 0.5 mg/ml. The sample was incubated on ice in the dark for 6-7 hours. The sample was illuminated for 1-2 minutes every 2 hours. The sample was precipitated with 50% PEG/50% D₂O. This procedure was repeated again except that the PSII particles were precipitated into an EPR tube. The sample was washed with buffer C (D₂O), centrifuged and the supernatent removed. The sample was illuminated and dark adapted as described above.

Glycylalanyltyrosine was dissolved in 1M NaOH to a final concentration of 10 mM. For the EPR sample the tripeptide was diluted to 500µM in 3M Mg(ClO4)₂. The sample was frozen slowly in liquid nitrogen to form a glass. The sample was illuminated with the full spectrum of a UV lamp for 15 seconds at 77 K.

The ENDOR spectra were acquired with a Bruker ER200 EPR spectrometer equipped with a Bruker ENDOR accessory. The ENDOR coils used were home built and contained 18 or 24 turns. The baseline in the 10-20 MHz region showed no distortions so baseline subtractions were not performed. The ENDOR spectra were recorded in the temperature range -157--161°C by using a N₂ gas flow system cooled with LN₂. The samples were kept dark during storage and were loaded into the ENDOR cavity in the dark.

The electron spin echo envelope modulation (ESEEM) data were recorded with a home built pulsed-EPR spectrometer constructed in the laboratory of Professor J.

McCracken and is described in detail elsewhere.⁴¹ The samples used for ENDOR measurements were also used for ESEEM. The ESEEM spectra were collected by using a stimulated echo (90°-τ-90°-T-90°) pulse sequence. For all spectra the experimental

conditions were: T (the time between the second and third pulse)=40 nsec, 5 nsec steps between data points, 15 nsec pulse widths, repetition rate = 80 Hz, and 30 events/data point were collected. The data were collected at 4.2 K by using a helium immersion dewar. Experimental conditions that were variable are listed in the figure captions. ESEEM spectra were obtained from the time domain data by using a modified version of the dead time recontruction protocol described by Mims.⁴⁴

Results and Discussion

The high resolution matrix region ENDOR spectrum of YD+ is shown in Figure 3.3A. For comparison, the ENDOR spectrum of the one-electron-oxidized benzoquinone in isopropanol is shown in Figure 3.3B, both spectra were collected at 160°C. The free proton resonance for these two spectra is 14.7 MHz. In the region 14-15.5 the spectrum is dominated by peaks from protons in the first several solvation spheres of the radical. The hyperfine coupling to solvent protons is purely, or almost purely, dipolar. In the semiquinone sample there are many different solvation arrangements near the radical, which leads to a continuum of unpaired electron-proton distances. This, in turn, leads to many ENDOR peaks that are closely spaced, which is observed as a broad structureless peak near the free proton resonance, Figure 3.3B. In contrast, the spectrum from YD⁺ shows many well resolved peaks, with peak splittings as small as 0.3 MHz detectable, Table 1. The protein environment, or solvation sphere, around Y_D^+ is well ordered and homogeneous throughout the protein sample. A well ordered protein environment is not surprising since high resolution(<2 Å resolution) crystal structures have been obtained for many proteins. If peaks a,a', with a splitting of 0.3 MHz, are from a purely dipolar coupled proton, which is generally the case for weakly coupled solvent or "matrix" protons, then by using the equation for dipolar coupling (equation 7, Chapter 2) the proton is calculated to be located approximately 6 Å from YD+. In this calculation, it is

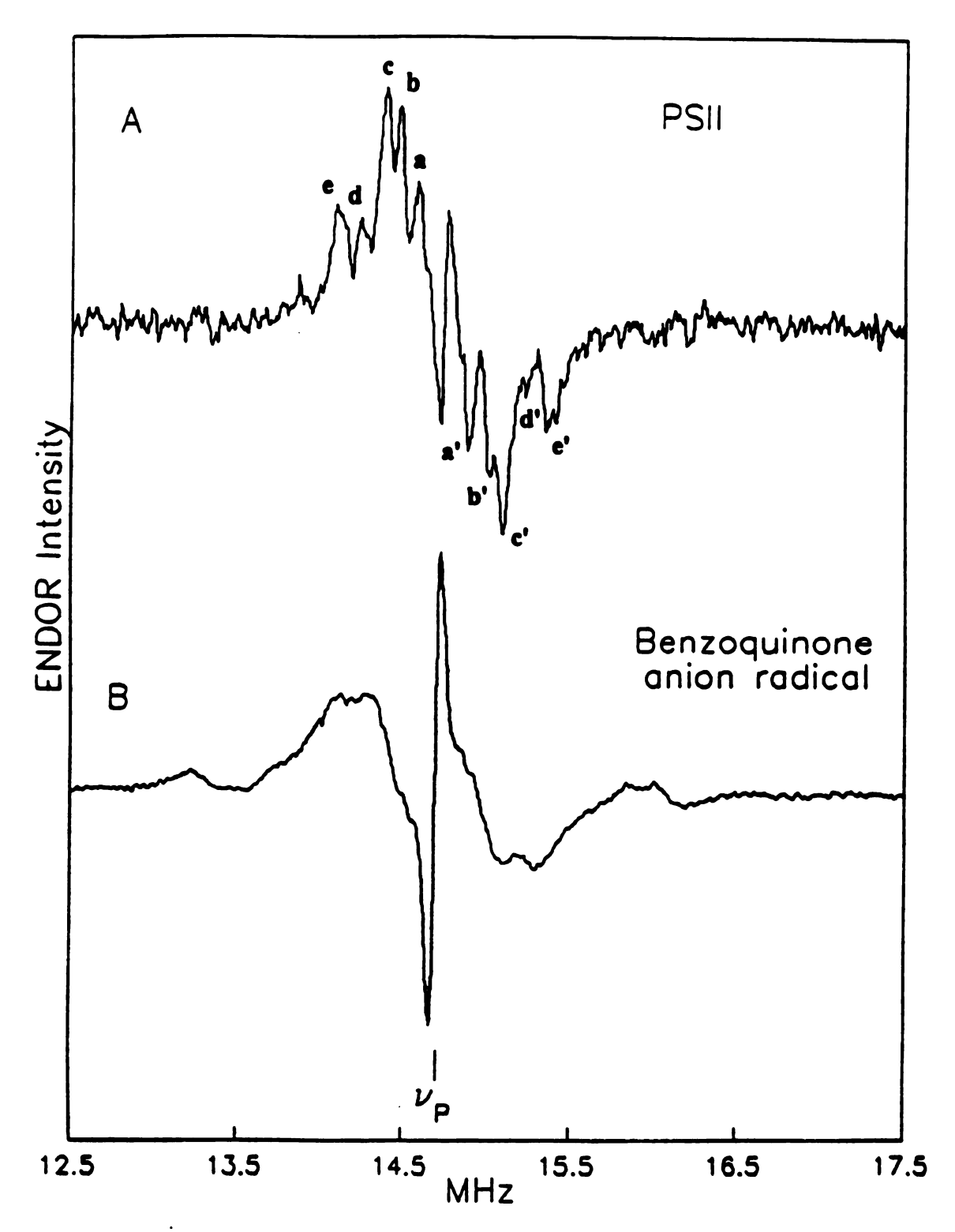


Figure 3.3 ENDOR spectrum of (A) Y_D⁺ in PSII particles from spinach and (B) benzoquinone anion radical. Conditions: (A) μwave power; 3.5 mW, RF power; 120 W, RF modulation depth; 10 kHz, temperature; 120 K; (B) μ wave power; 2 mW, RF power; 85 W, RF modulation depth; 10 kHz, temperature; 110 K.

assumed that peaks a,a' are from the A_{\perp} component of the hyperfine tensor for this matrix proton. By using Y_D^+ as a paramagnetic probe, magnetic nuclei within ≈ 6 Å of the radical can be monitored by ENDOR.

The environment surrounding Y_D^+ was monitored for protein structural changes as the extrinsic polypeptides and the Mn complex were removed. Figure 3.4A is the matrix ENDOR spectrum of Y_D^+ from BBY particles. The ENDOR spectrum from reaction center complexes (RCC), PSII particles lacking the 17 and 23 kDa extrinsic polypeptides, is shown in Figure 3.4B, and Figure 3.4C is from tris washed RCC's, where all three extrinsic polypeptides and the Mn complex have been removed. The spectra are the same, showing that the protein environment near Y_D^+ is unaffected by removal of the extrinsic polypeptides and Mn complex. These results suggest that Y_D^+ is well removed from that portion of the protein that interacts with the extrinsic polypeptides. These results are consistent with the studies of Innes et al., where the distance from Y_D to the surface of the protein was found to be 41 Å, with the extrinsic polypeptides present, and 27 Å after their removal. 18

Table 1. Hyperfine coupling constants for matrix protons.^a

spinach			Synechocystis			
Peaks	ν_	ν ₊	Δν	ν.	ν ₊	Δν
a,a'	14.60	14.90	0.30	14.54	14.90	0.36
b,b'	14.48	15.00	0.52	14.45	14.95	0.5
c,c'	14.40	15.10	0.70	14.33	15.05	0.72
d,d'	14.25	15.25	1.0	14.22	15.20	0.98
e,e'	14.11	15.40	1.29	14.00	15.41	1.41

a all values are in MHz

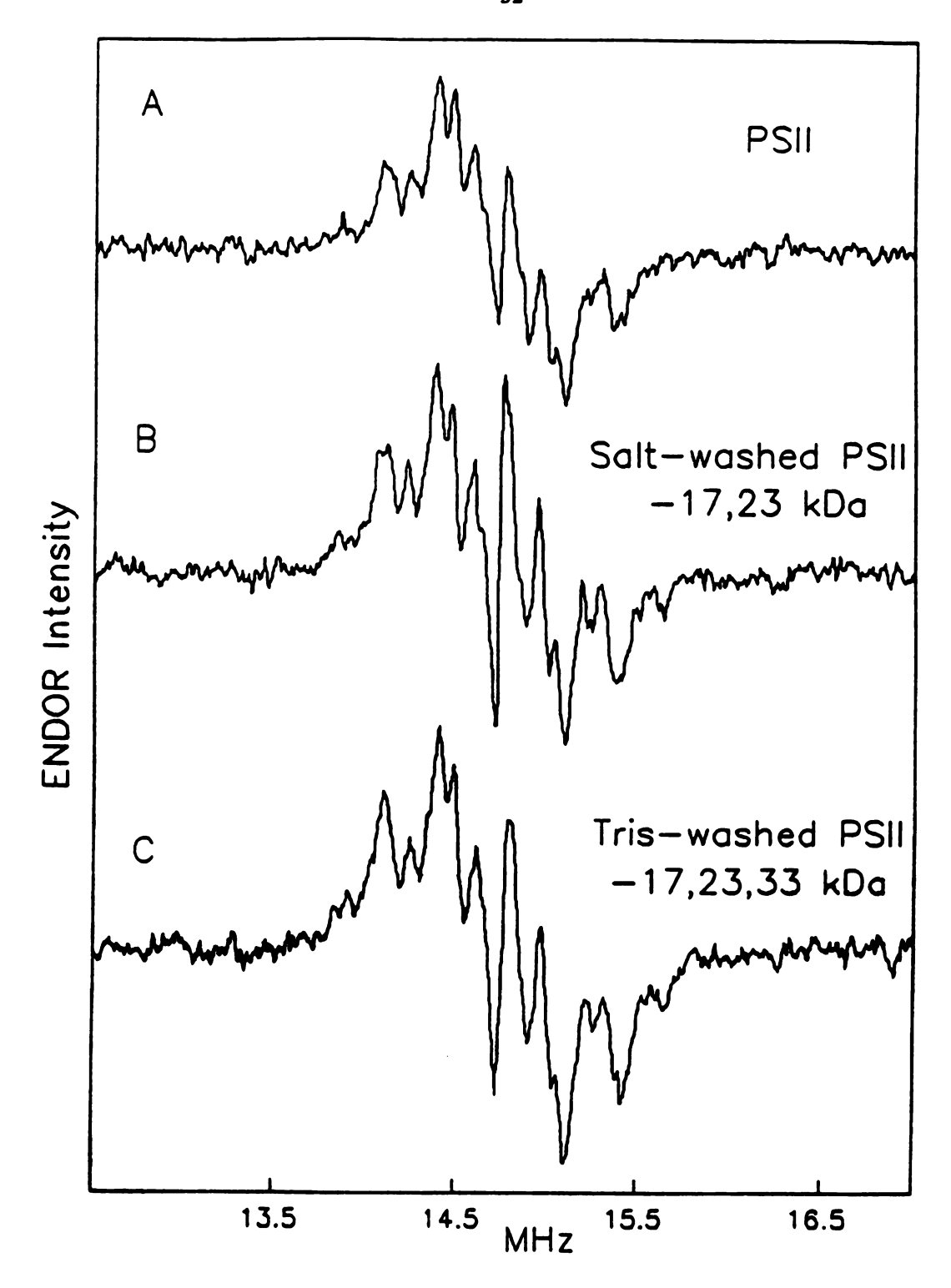


Figure 3.4 ENDOR spectrum of Y_D⁺ in PSII particles from spinach (A) untreated PSII particles, (B) reaction center complexes, and (C) tris washed reaction center complexes. Conditions: μwave power; 3.5 mW, RF power; 120 W, RF modulation depth; 10 kHz, temperature; 120 K.

Incorporation of specifically deuterated tyrosines and directed mutagenesis are not posssible with higher plants; however, these techniques can be performed with cyanobacteria. The photosystem II enzyme in cyanobacteria is nearly identical to that present in higher plants. In the succeeding sections all ENDOR studies were done with PSII's isolated from the cyanobacteria *Synechocystis* 6803. Figure 3.5 shows the ENDOR spectra of Y_D^+ in PSII's isolated from spinach (top) and *Synechocystis* (bottom). While there are some differences in peak intensities, the peak splittings are nearly the same for both spectra, Table 1. The protein environment near Y_D^+ is thus very similar in both systems. This would be expected in light of the strong sequence homology between the D1 and D2 proteins from higher plants and cyanobacteria. 17b

Hydrogen bonding

In a previous ENDOR study of Y_D^+ , in PSII's isolated from spinach, an H_2O/D_2O exchangeable proton was observed with hyperfine couplings of 3.5(A_\perp) and 7.0 (A_{\parallel}) MHz.¹¹ The ENDOR spectrum from this proton gave an axial lineshape with purely dipolar coupling (A_{\parallel} =2 A_\perp). The proton was assigned to a hydrogen bond to the phenol oxygen of Y_D^+ . ENDOR spectra of PSII particles from *Synechocystis*, incubated in either buffer B (H_2O), or buffer B (D_2O) are shown in Figure 3.6A and 3.6B, respectively. These data were collected with a larger RF modulation depth than Figures 3.3-5, 50 kHz versus 10 kHz, which lowers the spectral resolution. The H/D exchangeable peaks g,g' at 13.2 MHz and 16.2 MHz, with A=3.0 MHz, are absent in the D_2O treated sample. This is more clearly seen in Figure 3.6C, which is the difference spectrum of Figures 3.6A and 3.6B. The peaks g,g' are assigned to the A_\perp component of a hydrogen bond, however, the A_{\parallel} component was not detected, Figure 3.6C. Similar results were seen by Tang et al. in an ENDOR study of Y_D^+ in PSII particles from *Synechocystis*.³⁷ If the hyperfine coupling to the hydrogen bond in cyanobacteria is

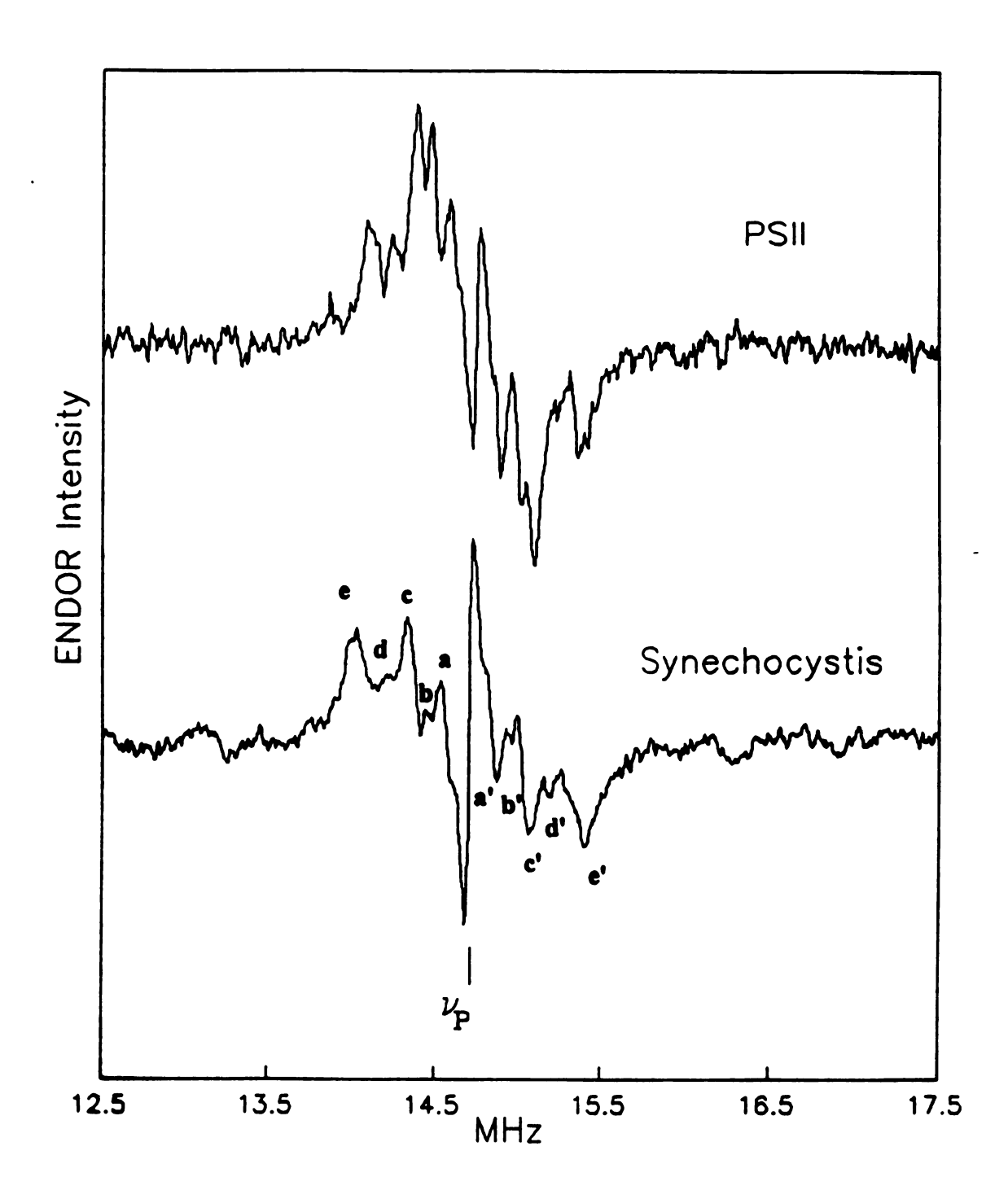


Figure 3.5 ENDOR spectrum of Y_D⁺ in PSII particles from spinach (top) and Synechocystis (bottom). Conditions: same as in Figure 3.4.

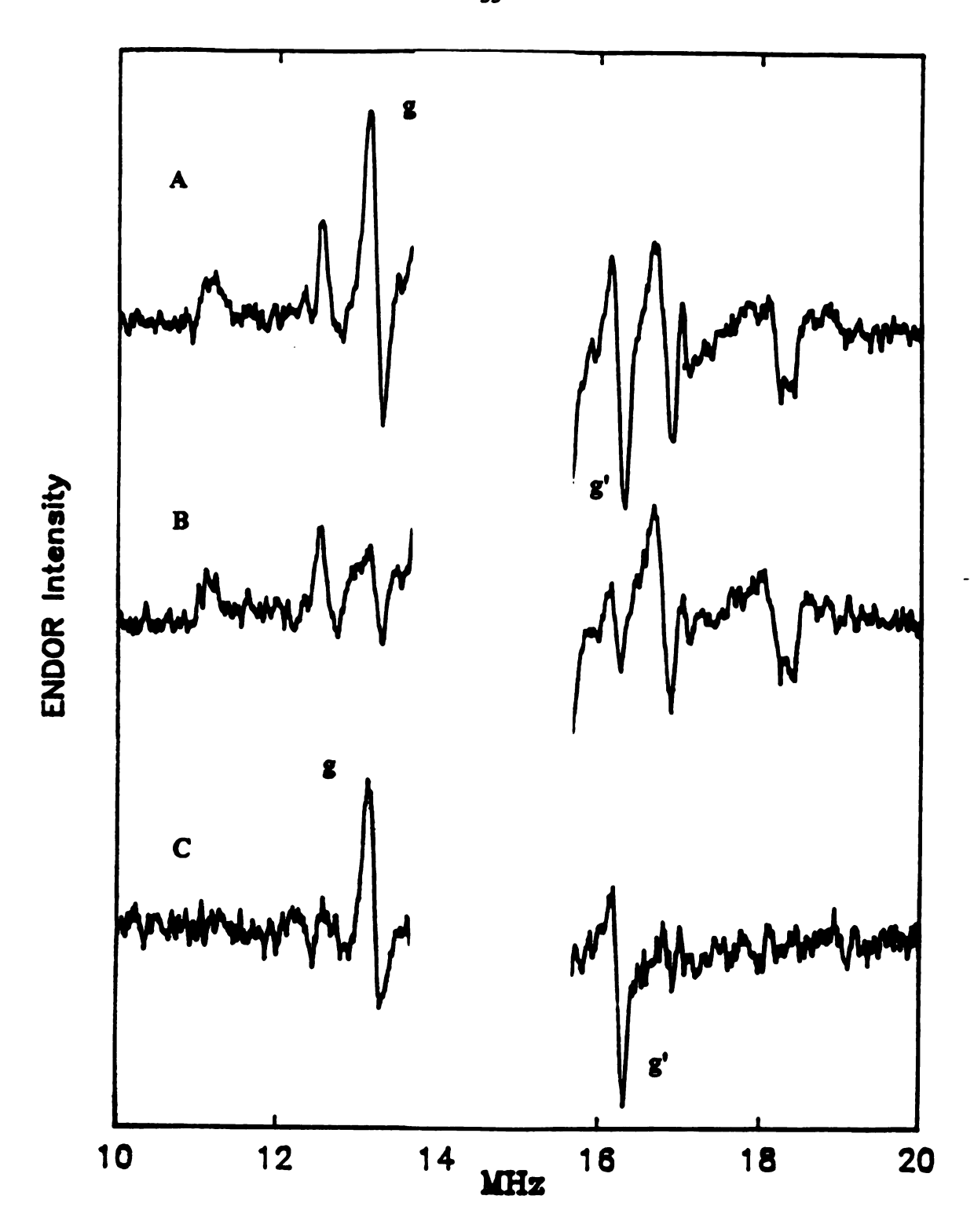


Figure 3.6 ENDOR spectrum of Y_D⁺ in PSII particles from *Synechocystis* in (A) H₂O and (B) D₂O, with pH = pD = 7.0. Spectrum C is the difference of spectra A and B. Conditions: same as Figure 3.4 except RF modulation depth is 50 kHz.

purely dipolar, as is the case for spinach, then A_{\parallel} is 6.0 MHz. The inability to detect the A_{\parallel} component of a hydrogen bond by ENDOR has been observed for other protein-bound free radicals.

The ENDOR spectra of the semiquinone form of Q_A and Q_B , in the bacterial reaction center, show several H/D exchangeable protons that are assigned to hydrogen bonds to the quinone oxygens. ¹⁹ There are two hydrogen bonds to each quinone detected but only in one case, that of one of the hydrogen bonds for Q_A , was the A_{\parallel} component observed. An ENDOR characterization of the bound ubiquinone of cytochrome c reductase also detected a hydrogen bond. In this case, as for the bacterial reaction center quinone Q_A , the A_{\parallel} component was detected but it is much weaker than the A_{\perp} component. ²⁰

From the hyperfine coupling values and knowledge of the unpaired spin density, the oxygen-proton distance of the hydrogen bond can be calculated (equation 7, Chapter 2). An ENDOR study of RDPR has determined that the unpaired spin density at the tyrosine phenol oxygen is 0.16.15 The oxygen-proton distance for YD+ is 1.61 Å for cyanobacteria and 1.53 Å for spinach, assuming that the spin density on the oxygen of YD⁺ is also 0.16. More recent EPR studies of ¹⁷O-labeled tyrosine have estimated the spin density at the oxygen of the tyrosine radical of RDPR to be 0.30 (Curt Hoganson, unpublished results). With this spin density, the proton distance is 2.00 Å in cyanobacteria and 1.90 Å in spinach. The hydrogen bond distances calculated for YD+ are similar to those seen for quinones. The unpaired spin density on each of the oxygens of QA and QB was measured to be 0.3. From this spin density and by using the point dipole approximation, the oxygen-hydrogen distance of the hydrogen bond for QA and QB are in the range 1.55-1.97 \mathring{A} . A similar distance was observed for the quinone of cytochrome c reductase.²⁰ The difference in the hyperfine coupling of the hydrogenbonded proton in spinach and cyanobacteria may be either from different oxygen-proton distances, or a different spin density on the oxygen. An ENDOR study of YD+, in PSII

particles isolated from spinach and cyanobacteria, has suggested that there is some small differences in the distribution of the unpaired spin in these two systems, however, the spin density on the oxygen of YD⁺, has not been determined accurately. Whether the differences in hyperfine coupling to the hydrogen-bonded proton is from different unpaired spin density on the oxygens or different hydrogen bond lengths is not yet known.

Debus et al. predicted that the base that forms the hydrogen bond with Y_D^+ is histidine 190 of the D2 protein (his190).²² A model of the PSII reaction center, based on the bacterial reaction center crystal structure, predicts his190 to be within 3-4 Å of Y_D^+ and oriented properly to form the hydrogen bond. ^{17b} Strong evidence for his190 forming the hydrogen bond has come from mutagenesis experiments. When leucine or tyrosine are substituted for his190, the EPR spectrum of Y_D^+ changes from having a linewidth of 20 G and partially resolved hyperfine structure to a 10 G wide signal with no resolved hyperfine structure.⁴² This change in the EPR spectrum is attributed to a modification of the protein environment surrounding Y_D^+ and, possibly, a shift in the spin density distribution. The substitution of glutamine for his190 perturbs the EPR and ENDOR spectra only slightly, but the peaks in the ENDOR spectra assigned to the hydrogen bond are no longer present.³⁷ His190 is most likely the donor for the hydrogen bond to Y_D^+ .

Tryptophan-167 of the D2 protein, which is seven residues down from Y_D⁺ and expected to be in the extramembrane loop portion of the protein, between helices C and D,²³ has been mutated to an alanine (the mutant was obtained from the laboratory of Dr. L. McIntosh). The EPR spectrum for the mutant is the same as the wild type sample (data not shown). ENDOR spectra from wild type PSII's and the tryptophan-167 to alanine mutant (W167A) are shown in Figure 3.7. There are several differences in these two spectra. First, there is a set of derivative shaped peaks, f,f', with A=2.5 MHz, that are absent in the mutant. These peaks are not from a proton on the tyrosine radical itself (see

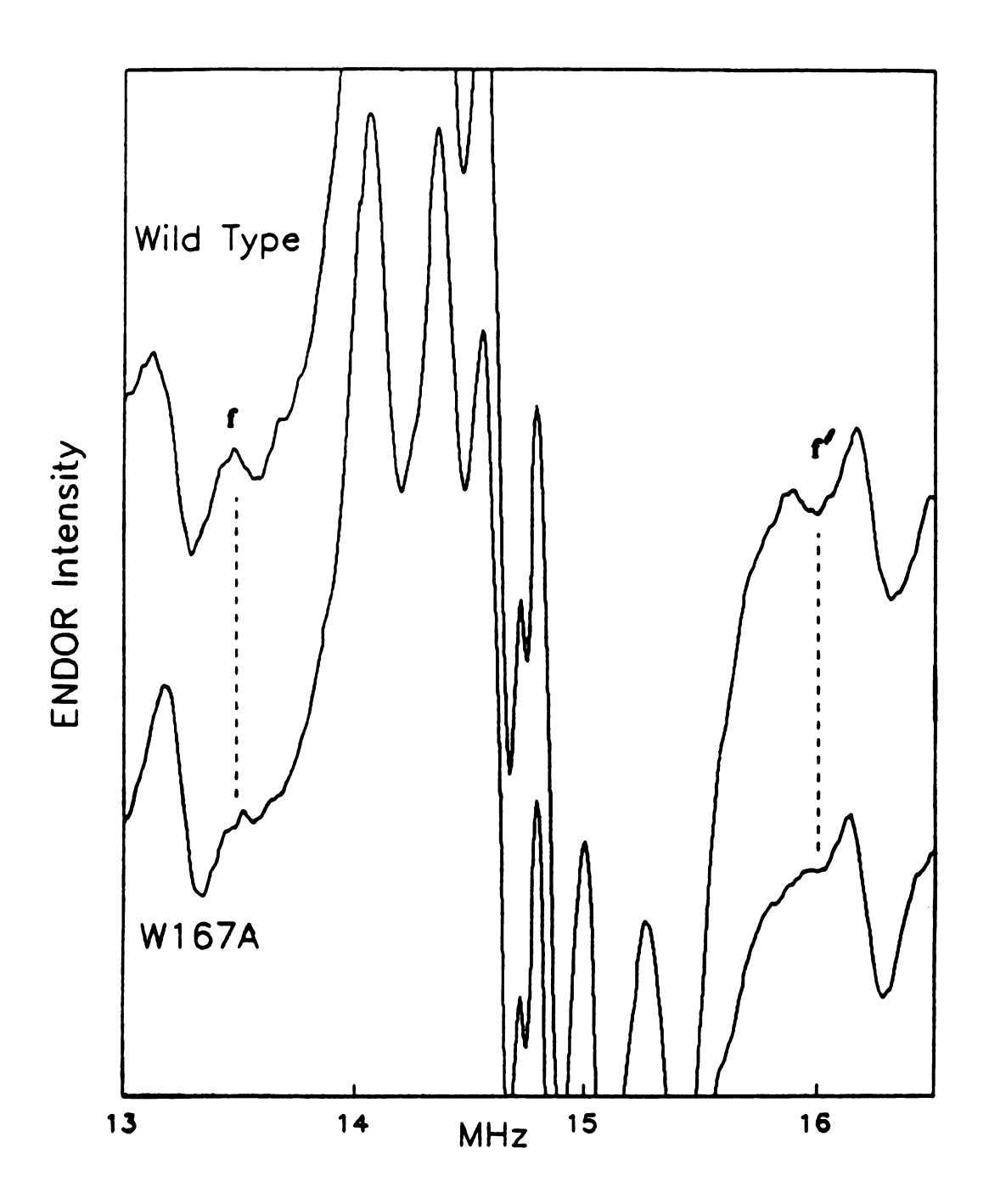


Figure 3.7 ENDOR spectrum of YD⁺ in PSII particles from (top) wild type and (bottom) W167A mutant *Synechocystis*. Conditions: same as Figure 3.4 except RF modulation depth is 30 kHz.

below), so they must arise from the protein. Protein protons are expected to show purely dipolar hyperfine coupling. By using the point dipole approximation, this proton is estimated to be 2-4 $\rm \mathring{A}$ away from $\rm Y_D^+$. The absence of the peaks at 13.7 and 16.0 MHz in the mutant may occur for two reasons. First, the peaks may arise from a proton on tryptophan-167 itself and in the substitution of alanine for tryptophan the proton is removed. Second, the substitution of the methyl group on alanine for the bulky side chain of tryptophan may cause a minor rearrangement of the protein structure near $\rm Y_D^+$. The hyperfine coupling to the proton giving rise to the peaks f,f is reduced and the peaks arising from this proton are now obscured by the intense matrix peak. The second effect on the ENDOR spectra from this mutation is a slight decrease in the $\rm A_\perp$ component of the hydrogen bonded proton, from 3.0 MHz to 2.9 MHz.

A model of the reaction center of PSII predicts that the proton on trp167 that is nearest YD+ is still 8 Å away. 17a The model also predicts that the environment around YD⁺ is hydrophobic with several phenylalanines and tryptophan-192 side chains in close proximity. 17 The model though may be incorrect and trp167 is near enough to YD+ to be detected by ENDOR, the hydrophobicity of trp167 being consistent with the predicted protein environment of YD⁺. Trp167, however, is most likely in the second solvation sphere of YD⁺ and its substitution by alanine perturbs the local environment near YD⁺, including the proton with a hyperfine coupling of 2.5 MHz. As discussed above, mutations of residues directly interacting with YD+, such as his 190, cause significant changes in its EPR spectrum. Even the mutation of glutamine-164, which is three residues away from YD+, to leucine, modifies the EPR spectrum. The perturbation of the protein environment by the mutant W167A mutant affects the putative hydrogen bond donor, his 190, as well, as the hyperfine coupling to the hydrogen bonded proton is shifted. The ENDOR results suggest that trp167 is near YD⁺ and its side-chain is probably oriented towards YD+ rather than away. The model of the PSII reaction center is consistent with this interpretation of these results. 17a

Ring protons

By using the method of Barry and Babcock, ²⁴ specifically deuterated tyrosines were incorporated into *Synechocystis*. The ENDOR spectra of Y_D+, with and without ring-d₄ labeled tyrosine incorporated, are shown in Figures 3.8A and 3.8C, respectively. The set of peaks at 12.6 and 16.8 MHz (h,h') and the peaks at 11.2 and 18.3 MHz (j,j') are absent in the the sample with the deuterium labeled tyrosine. These two sets of peaks have hyperfine couplings of +7.2 and +4.2 MHz and are assigned to the two largest components of the [2,6] protons based on their lineshapes, Table 2. The ENDOR spectrum of Y_D+, with tyrosine deuterated only at the [3,5] position, did not show any change in these peaks when compared to the unlabeled tyrosine sample (data not shown). The hyperfine tensor for the [2,6] protons should be rhombic, however, the third component is obscured by the much larger matrix peak. These hyperfine coupling values are similar to those reported for the tyrosine radical in RDPR, which are +7.6 and +4.8 MHz.¹⁵ The assignments in RDPR were based on the similarity to model compounds, but were not confirmed by deuterium substitution. The data presented here represents the first *in vivo* unequivocal assignment of the ENDOR peaks from the [2,6] protons.

When the ENDOR spectra for the unlabeled PSII particles are recorded at a lower RF modulation depth, 30 kHz, the peaks j,j' are clearly resolved into two peaks (data not shown). Solution EPR studies of alkylphenol cation radicals have observed nonequivalent isotropic hyperfine couplings for the protons on C₂ and C₆ of the phenol ring.⁴³ In the cation radical, the phenol oxygen is still protonated and the phenol hydrogen is proposed to remain in the plane of the ring, in a trigonal planar orientation, at low temperatures. Since the hydroxylic proton will be oriented towards one side of the ring the symmetry of the radical is reduced. The protons at C₂ and C₆ are then not magnetically equivalent and different isotropic couplings are observed. In solution EPR

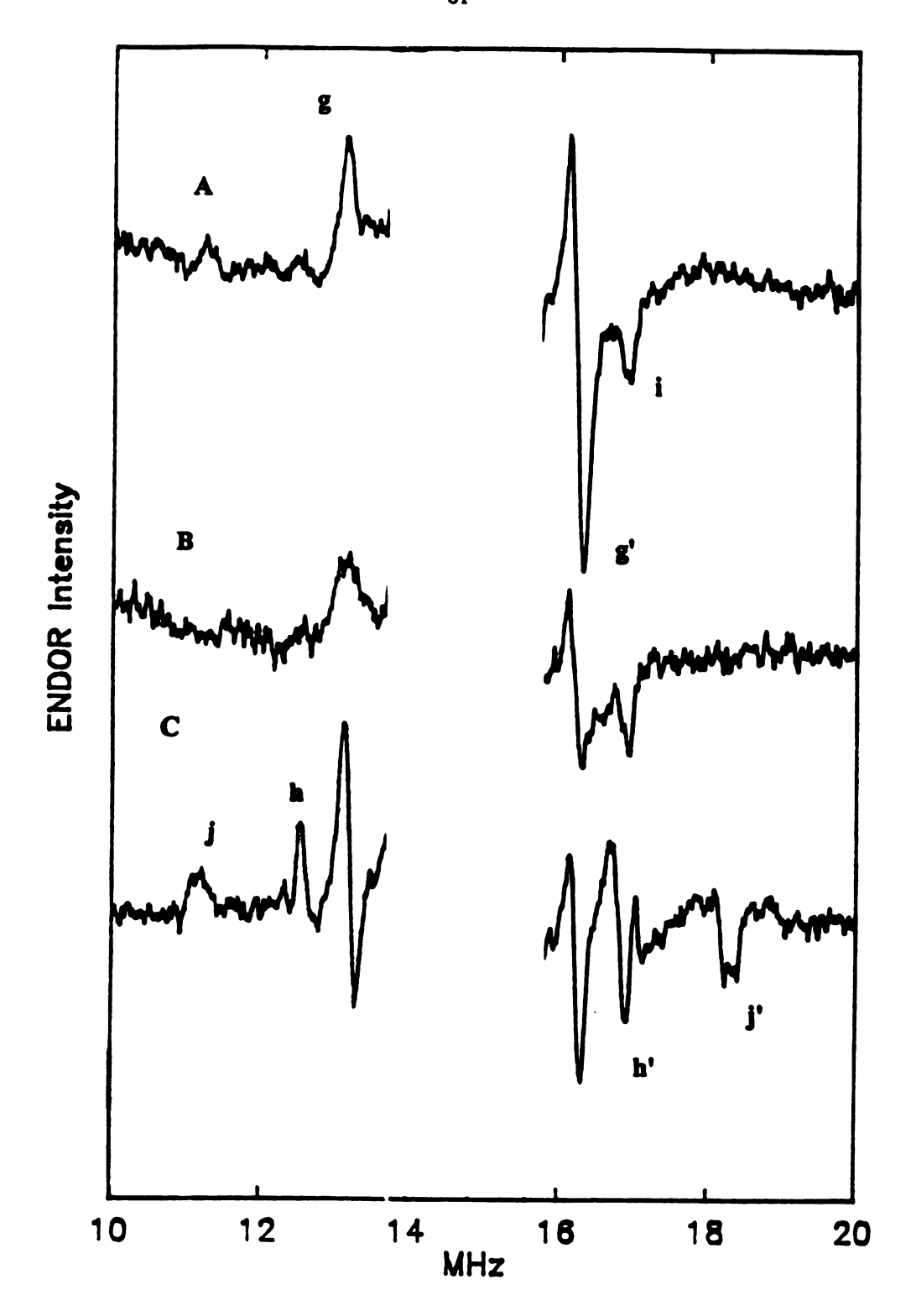


Figure 3.8 ENDOR spectra of YD⁺ in PSII particles from Synechocystis A) incorporated with ring-d₄ tyrosine, B) ring-d₄ tyrosine sample in D₂O and C) wild type PSII particles in H₂O. Conditions: same as Figure 3.6.

studies, both possible proton orientations are observed simultaneously. The splitting of peaks j,j' suggests that the hydrogen-bonded proton of YD⁺ is not located along the C₄-O axis but is oriented toward one side of the tyrosine ring. Both sets of peaks that are observed for peaks j,j' are absent in the ring-d₄ labeled tyrosine samples.

The [3,5] protons, with their large isotropic hyperfine coupling, have a broad linewidth and a weaker ENDOR intensity. Recording the spectra at a larger RF modulation depth will increase the signal to noise, making the peaks from the [3,5] protons more easily detected. The ring-d₄ and unlabeled tyrosine incorporated PSII samples were exchanged with D₂O, to eliminate the possibility of masking the ENDOR peaks from the [3,5] protons with peaks from the hydrogen bonded proton. The ENDOR spectra of the ring-d₄ labeled tyrosine sample and the unlabeled tyrosine sample, recorded at 100 kHz RF modulation, are shown in Figure 3.9. The two peaks with absorptive lineshapes occuring at 10.7 and 18.6 MHz (k,k') are absent in the deuterium labeled sample. This set of peaks, with a hyperfine coupling of +8.0 MHz, are assigned to the [3,5] protons. Again, the hyperfine coupling is similar to that observed for RDPR where the corresponding component for the [3,5] proton is +7.8 MHz. The similarity in the hyperfine couplings of the [2,6] and [3,5] ring protons in YD+ and RDPR leads to the conclusion that the unpaired spin density, at these four positions of the ring, is nearly the same in the two radicals.

Table 2: Hyperfine coupling values for ring protons^a

ENDOR Peaks	ν+	ν_	Δν	assignment
h,h'	16.8	12.6	+4.8	[2,6]
j,j'	18.3	11.2	+7.6	[2,6]
k,k'	18.6	10.7	+8.0	[3,5]

a all values are reported in MHz

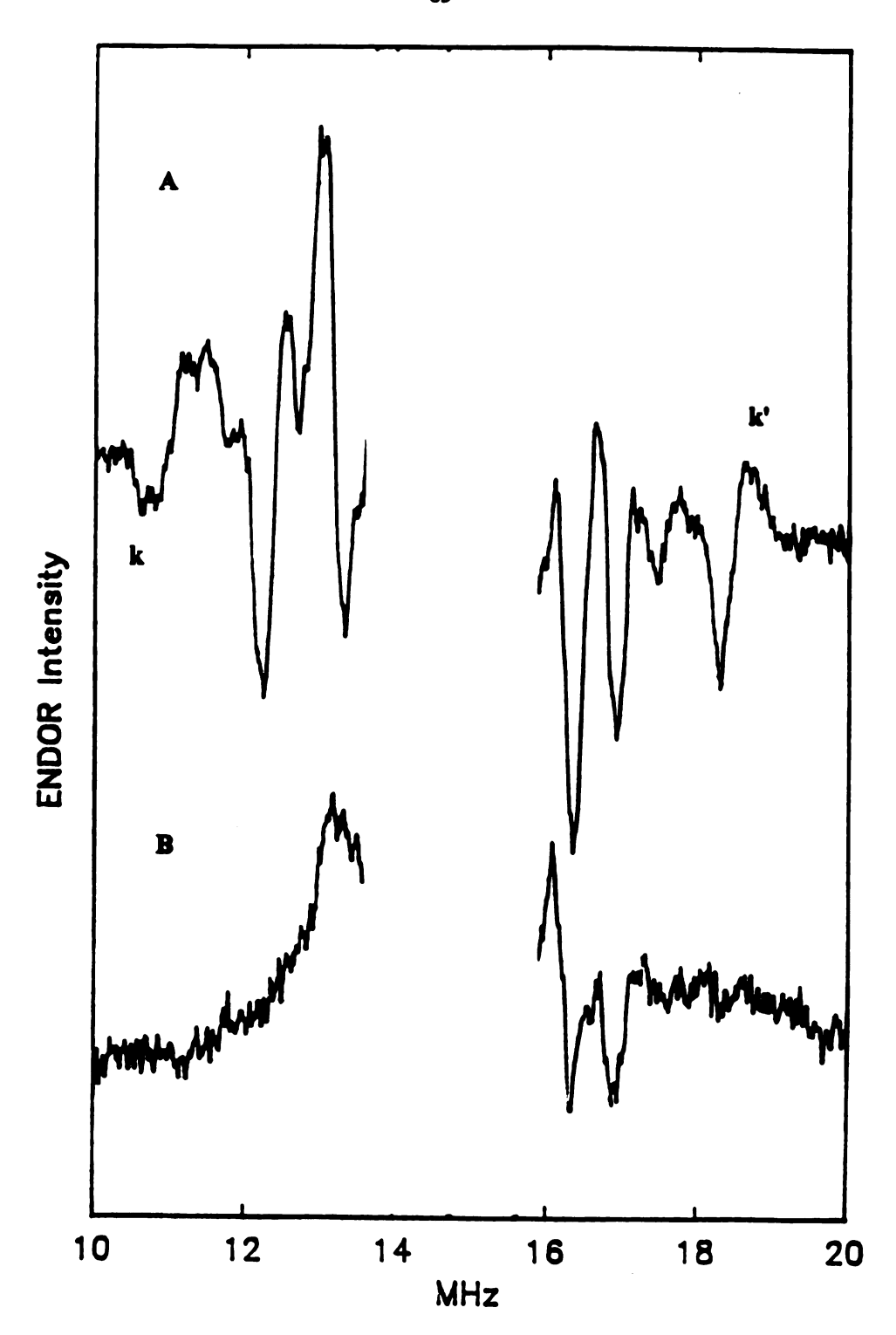


Figure 3.9 ENDOR spectra of Y_D⁺ from Synechocystis A) wild type (H₂O), B) ringd₄ tyrosine incorporated (D₂O). Conditions: same as Figure 3.6 except the RF modulation depth is 100 kHz.

There is an additional peak in the ENDOR spectrum at 16.9 MHz (i) that is unaffected by deuterium labeling and H_2O/D_2O exchange, Figure 3.8B. The partner of this peak, due to its weak intensity, is unobservable above the noise. There are several possibilities for the origin of this peak. The peak may arise from the proton on C_{α} of the protein backbone, H_{α} . In the *p*-isopropylphenol radical, A_{iso} of the methyl group protons is 1.1 MHz, ¹⁴ and the isotropic coupling to H_{α} of tyrosine, determined by solution EPR measurements, is 1.1 MHz.²⁵ The ENDOR peak may also arise from a protein proton that is near enough to the tyrosine ring to have a dipolar hyperfine coupling component of 4.4 MHz.

One additional possibility is a second hydrogen bond. It is commonly observed that tyrosine oxygens have bifurcated hydrogen bonds. Since the peak is unaffected by 12 hours of incubation in a D_2O buffer at pH=7.0, the pKa for the hydrogen donor must be > 7. This would include the following side chains arginine, cysteine, lysine, and tyrosine. There currently is no evidence to favor any one of these possible origins for the peak at 16.9 MHz in Figure 3.6.

While the hyperfine coupling tensors are beginning to be resolved, estimation of their values have been determined from simulations of the EPR spectra. A series of EPR spectra of YD⁺, with selectively deuterated tyrosines incorporated, have been recorded.²⁸ By using the hyperfine couplings of RDPR as initial values the EPR spectra were simulated and the hyperfine coupling tensors for the ring and [3,5] protons were determined.¹⁶ Similar labeling experiments were done with *in vitro* tyrosine²⁸ and the simulation parameters for both systems are shown in Table 3. The simulations could not determine the hyperfine couplings for the [2,6] protons since the couplings to these protons have only a negligible effect on the EPR spectrum.¹⁶ The ENDOR data presented above shows that the hyperfine coupling tensor components for the [2,6] and

[3,5] protons, determined by simulations, are close to the actual values, however, they are slightly too large.

Table 3: Hyperfine coupling values for tyrosine radicals^a

Radical	A _{3,5} X	A _{3,5} Y	A3,5Z	Aβ1	Aβ1⊥	A _{β2}	A _{β2⊥}
PSII YD+	-29.4	-9.0	-19.6	23.2	21.6	<7.0	<7.0
invitro tyrosine	-27.3	-7.8	-19.0	36.4	31.6	<6.2	<6.2

a all values are in MHz

From the simulations of Y_D^+ and *in vitro* tyrosine complete descriptions of the unpaired spin density distribution were calculated and these are listed in Table 4, along with the spin densities calculated for RDPR. 15,16 In light of the current ENDOR results the spin density at the [3,5] positions may need to be reduced slightly. There is a range of spin densities listed for C_1 , since the hyperfine coupling to the methylene proton is dependent on both the spin density present at C_1 and the dihedral angle of the methylene

Table 4: Unpaired spin density distribution in tyrosine radicals.

	E.coli RDPR	PSII Y _D +	in vitro tyrosine
C ₁	0.49	0.14-0.34	0.20-0.44
C ₃ , C ₅	0.26	0.29	0.26
О	0.16	0.45-0.25	0.45-0.21

proton.¹⁶ It is clear from Table 4 that the spin density at the C₃ and C₅ positions are nearly all the same, but there are differences in the spin densities at C₁ and oxygen.

From these data it appears that differences in the spin density distribution occurs only at

the C₁ and oxygen. Recent data from our lab has refined the magnitude of the spin density at the oxygen in RDPR. EPR spectra of the tyrosine radical of RDPR and *in vitro* tyrosine labeled with ¹⁷O show very similar ¹⁷O hyperfine couplings of 40 and 43 G, respectively. By using these couplings the spin density on the oxygen was calculated to be 0.3 for RDPR and 0.28 for in vitro tyrosine (Curt Hoganson, unpublished results).

Even though all hyperfine coupling tensor components have not been measured for all tyrosine radicals, enough information has been obtained that some trends can be recognized. Since the spin density at the oxygen is near 0.3 for RDPR and *in vitro* tyrosine, this suggests that a similar value is expected for Y_D^+ . Simulations of the EPR spectra for RDPR, isolated from a different source (mouse), are also best fit with an oxygen spin density of $0.3.^{16}$ From the EPR and ENDOR data a comprehensive spin density distribution relevent for all tyrosine radicals studied to date can be proposed. While there is some small spread in the values, the general spin denisty distribution is: $C_3 = C_5 \cong 0.25$, $C_1 \cong 0.30$, and $O \cong 0.30$. The spin densities at the C_4 , C_2 , and C_6 positions have only been determined for RDPR and are estimated to be negative and < |0.07|. These values are very similar to the original values proposed by Fassanella and Gordy in their study of a tyrosine single crystal. Their estimates of the spin densities are $C_3 = C_5 \cong 0.24$ and $C_1 \cong 0.32^{29}$

With the knowledge of the unpaired spin density at C_1 the dihedral angle of the methylene protons can be determined by using equation 1.

$$A_{iso} = B_2 \rho \cos^2 \theta \tag{1}$$

 B_2 has previously been determined to be 162 MHz. From the EPR simulations of Y_D^+ and *in vitro* tyrosine, A_{iso} for the larger methylene proton couplings have been calculated to be 22.1 and 33 MHz, respectively. Substituting these values into equation 1 and using ρ =0.3, the dihedral angles(θ) is 48° for Y_D^+ and 35° for *in vitro* tyrosine.

The spin density distribution in the tyrosine radicals are affected only slightly, if at all, by their solvation environment, since the radicals are present in significantly different solvents. The *in vitro* tyrosine radicals are generated in an aqueous solution with salt concentrations varying from 12mM to 5M without any change in the EPR signal (data not shown). In contrast Y_D^+ is located in the organic environment of a protein and is proposed to be located in a hydrophobic region of the protein. ¹⁷ The spin density is also not affected substantially by a hydrogen bond, as Y_D^+ is hydrogen bonded and RDPR is not. ^{10,11} Electrostatic effects from transition metals in high oxidation states also has little effect on the distribution of the spin density, as the tyrosine in RDPR is 5 Å away from a Fe (III,III) dimer⁸ and the nearest metal to Y_D^+ is > 30 Å. ¹⁷

These conclusions regarding the effects on the spin density distributions are based on the assumption that the unknown hyperfine coupling constants are not going to be significantly different than those already observed. If they are different, there may be significant perturbations to the spin density distributions, and this may account for the the differences in the stability and redox potentials of the different tyrosine radicals. If the spin densities are the same, however, then the protein must be controlling the reactivity of the redox active tyrosines. We conclude that protein effects such as hydrogen bonding, π - π interactions, and nearby charged amino acid side chains affect the redox behavior of the tyrosines.

Electron spin echo envelope modulation of YD+

If the hyperfine coupling to the hydrogen bonded proton has significant isotropic character this may result in a substantial hyperfine coupling to the nitrogen acting as the hydrogen bond donor. The strength of the ESEEM technique is its ability to detect weakly coupled nuclei with nuclear spin >1. ESEEM was used to study Y_D^+ to detect the nitrogen of his 190 that is proposed to form the hydrogen bond. Previous ESEEM

studies of protein bound iron-sulfur complexes have detected hyperfine coupling to a peptide nitrogen forming a hydrogen bound to the iron-sulfur complex.³⁰

The 3-pulse echo-decay envelope and fourier transform ESEEM spectrum collected at the zero field crossing of YD⁺ (g=2.0046), are shown in Figure 3.10. The 3pulse ESEEM spectrum for PSII's from spinach (data not shown) is very similar to the spectrum of PSII's from Synechocystis, Figure 3.10. In the low frequency portion of the ESEEM spectrum, 0-8 MHz, there are several peaks. The peak near 13.5 MHz is from weakly coupled protons and is equivalent to the matrix peak seen in the ENDOR spectra of YD+. A difficulty in studying PSII's by ESEEM is that there are several paramagnets that have intensity in the EPR spectra of PSII's, in the g=2 region. The peaks in the ESEEM spectrum that arise from YD+ must be seperated from those originating from the other paramagnets. ESEEM spectra were aquired at a series of field values, from 20 gauss lower than the zero field crossing of YD+ to 20 G above, Figure 3.11. The amplitude of the peaks at 2.1, 2.5, 2.9, 3.5, and 4.0 follow the amplitude of the EPR signal from YD+ and are assigned to YD+. The peaks in the ESEEM spectra at field values of ±20 G from the zero field crossing are assigned to adventitiously bound copper, based on the similarity to nitrogen ligated copper complexes.³¹ There are, under certain conditions, other organic radicals in the PSII samples that have EPR signals with similar linewidths to YD+. These include chlorophyll cation radicals and the P700+ signal of Photosystem I (PSI).³² In the PSII samples from cyanobacteria there is some PSI contamination. The ESEEM spectrum of a PSII sample, isolated from Synechocystis where PSI had been eliminated by mutagenesis, is the same as the wild type sample, eliminating P700⁺ as the source of the low frequency peaks (data not shown). Chlorophyll cation radicals can be generated by strong illumination of PSII's at 77K.32 A PSII sample from spinach, before and after 15 minutes of illumination at 77K, is shown in Figure 3.12. If the low frequency peaks were from a chlorophyll cation radical, then, there should be an increase in the intensity of all the peaks, corresponding to the increase

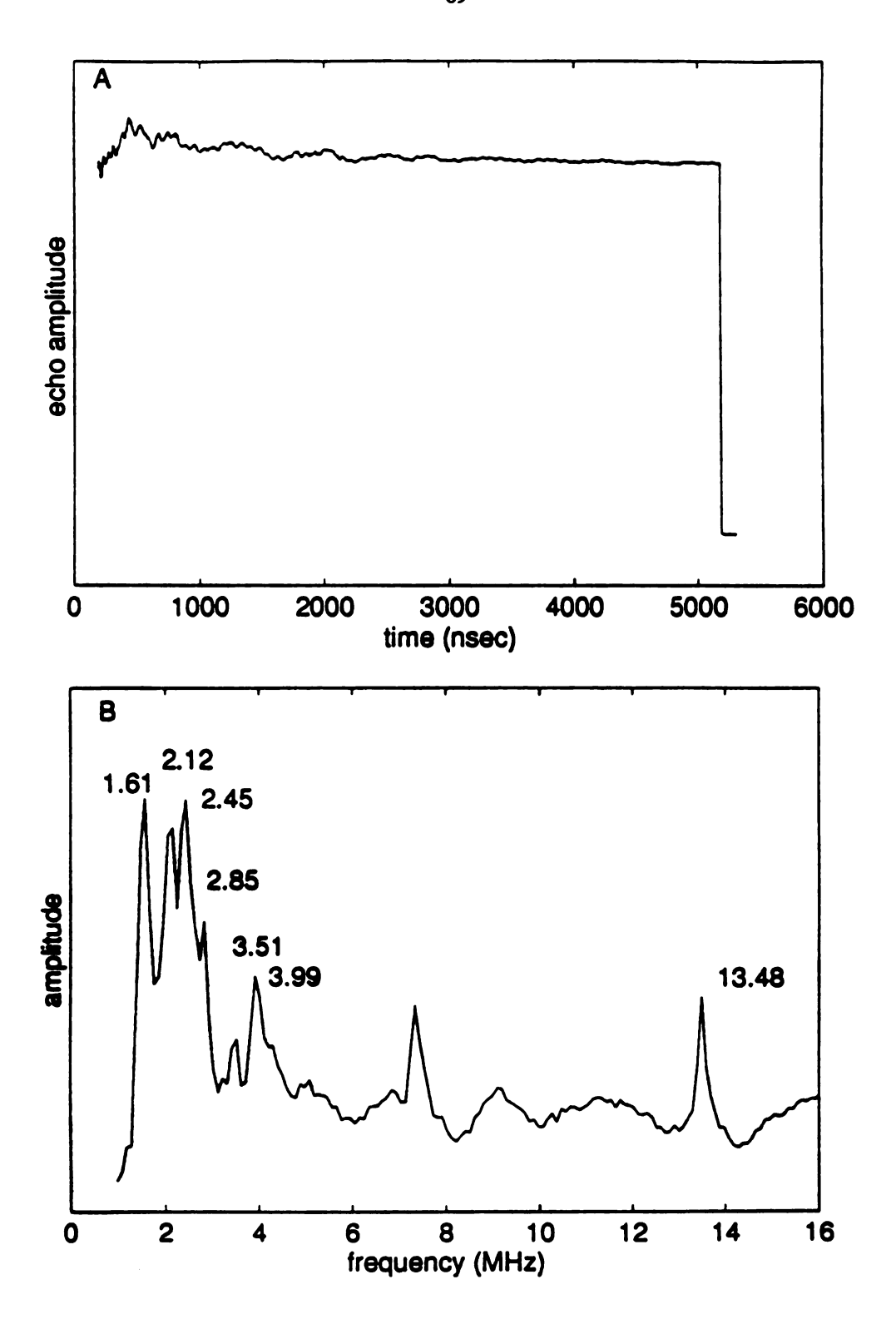


Figure 3.10 A) 3-pulse ESEEM echo decay from Y_D⁺ in PSII particles from Synechocystis. B) Fouier transform of data in (A). Conditions: μwave frequency; 8.865 GHz, tau = 150 nsec, magnetic field = 3160 G.

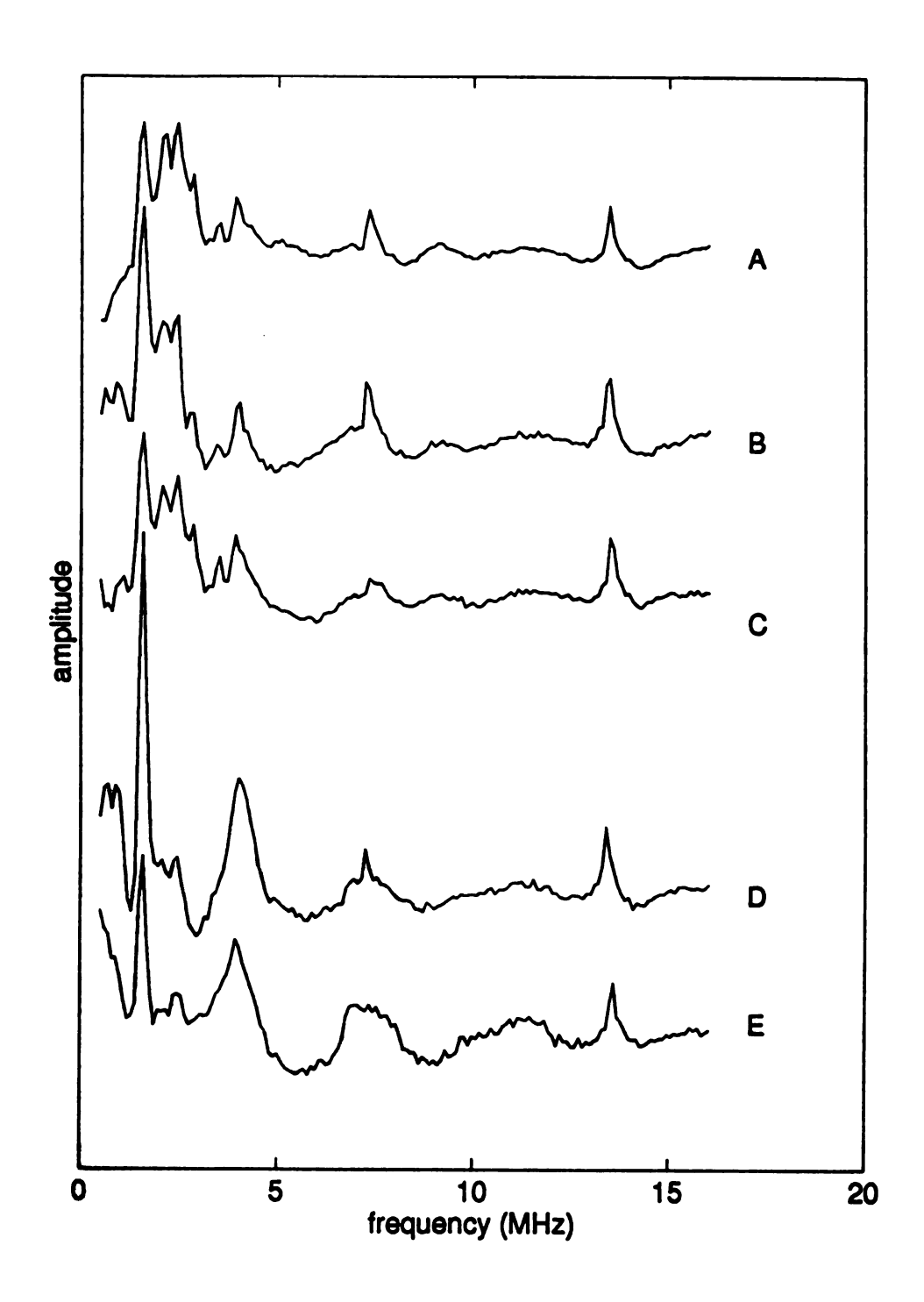


Figure 3.11 3-pulse ESEEM spectra of Y_D^+ in PSII particles from *Synechocystis*. Spectra were recorded at the magnetic field values: a) 0, B) -10, C) +10, D) -20, E) +20 G relative to g = 2.0046. Conditions: same as Figure 3.10.

in the chlorophyll radical generated by low temperature illumination. The ESEEM spectrum after illumination shows the same peak intensities as seen before illumination and, in addition, a large peak at 2.6 MHz is observed, thus, the low frequency peaks do not arise from a chlorophyll radical and are assigned to YD⁺.

The source of the nuclei giving rise to the low frequency peaks was determined by isotopic substitution. Synechocystis were grown on ¹⁵NO₃⁻, their sole source of nitrogen. Substitution of ¹⁵N for ¹⁴N causes significant changes in the ESEEM spectrum. The changes are the result of the differences in the nuclear spin of the two isotopes, ¹⁴N has a nuclear spin I=1, whereas ¹⁵N has I=1/2. Considering only isotropic coupling, ¹⁴N can give rise to as many as six peaks in the ESEEM spectrum where ¹⁵N gives rise to only two. Substitution of ¹⁵N for ¹⁴N reduces the complexity of the spectrum by reducing the number of peaks. The spectrum for the ¹⁴N and ¹⁵N labeled PSII samples are shown in Figure 3.13. The peaks at low frequency in the ¹⁴N sample are absent in the ¹⁵N sample and are replaced by a new feature between 1 and 3 MHz. It was not possible to determine the origin of the peaks in the ¹⁵N spectrum as the Cu²⁺ and heme of cyt-b₅₅₉ both showed peaks in this region. From the data of Figure 3.13 the peaks at 2.1, 2.5, 2.9, 3.5, and 4.0 are assigned to a nitrogen weakly coupled to the unpaired spin of Y_D+.

Directed mutagenesis of his 190 to glutamine removes the hydrogen bond to Y_D^+ , as determined by ENDOR.²² If the nitrogen coupling to Y_D^+ , observed by ESEEM, arises from this nitrogen, then the ESEEM spectrum of the mutant should not contain the low frequency peaks. The Y_D^+ ESEEM spectrum of the mutant his 190glu is shown in Figure 3.14. The weakly coupled nitrogen is unaffected by the mutation, and, thus, the low frequency peaks in the spectrum are not from his 190. The ESEEM spectrum of PSII's from cyanbacteria where ¹⁵N labeled histidine has been incorporated also showed no difference from the wild type samples, eliminating any histidine as the source of the nitrogen observed by ESEEM (data not shown).

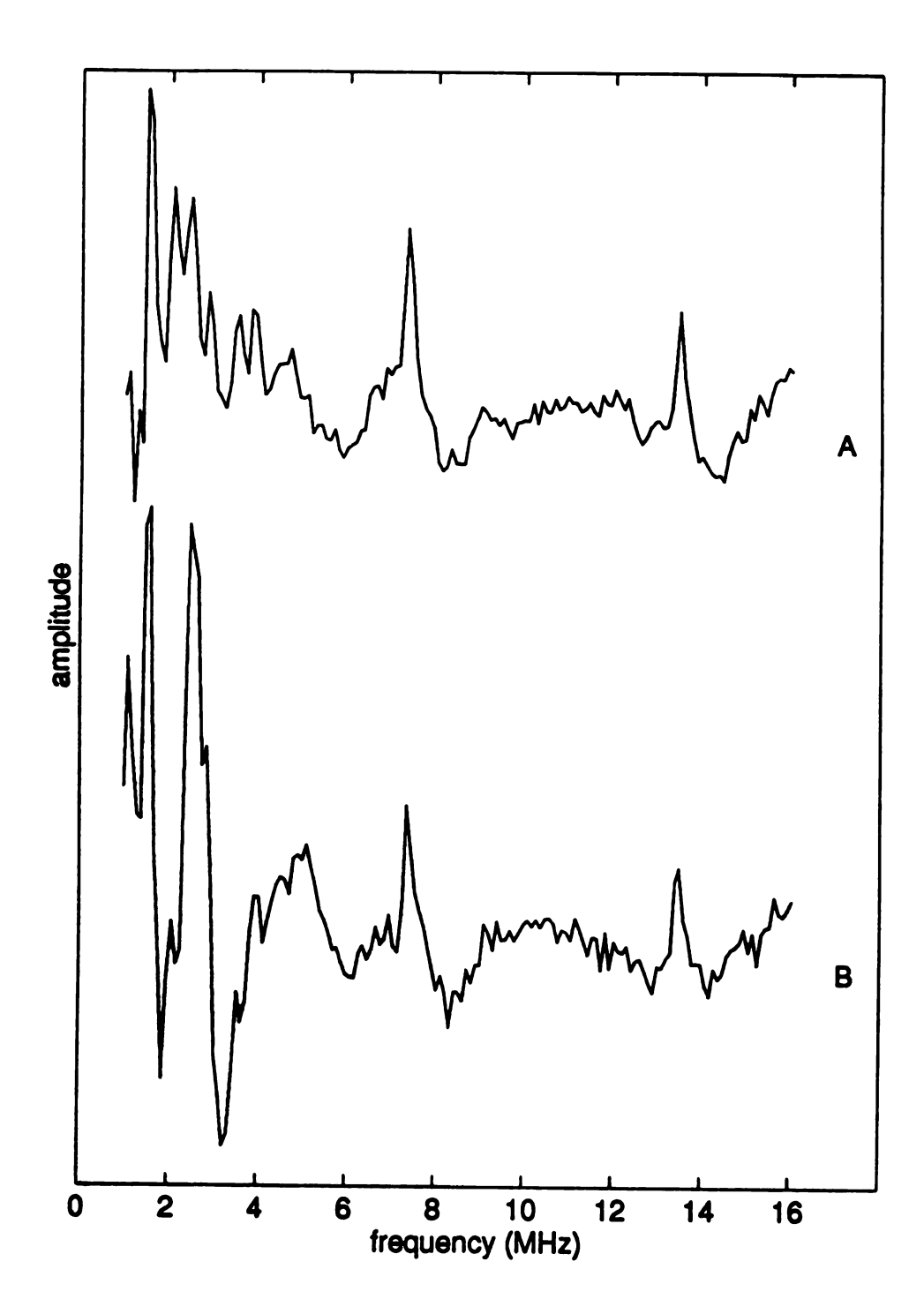


Figure 3.12 3-pulse ESEEM spectra of reaction center complexes collected at g=2.0046 before (A) and after (B) 15 minutes of illumination at 77K. Conditions: μ wave frequency, 8.850 GHz; τ = 150 nsec; magnetic field, 3153 G.

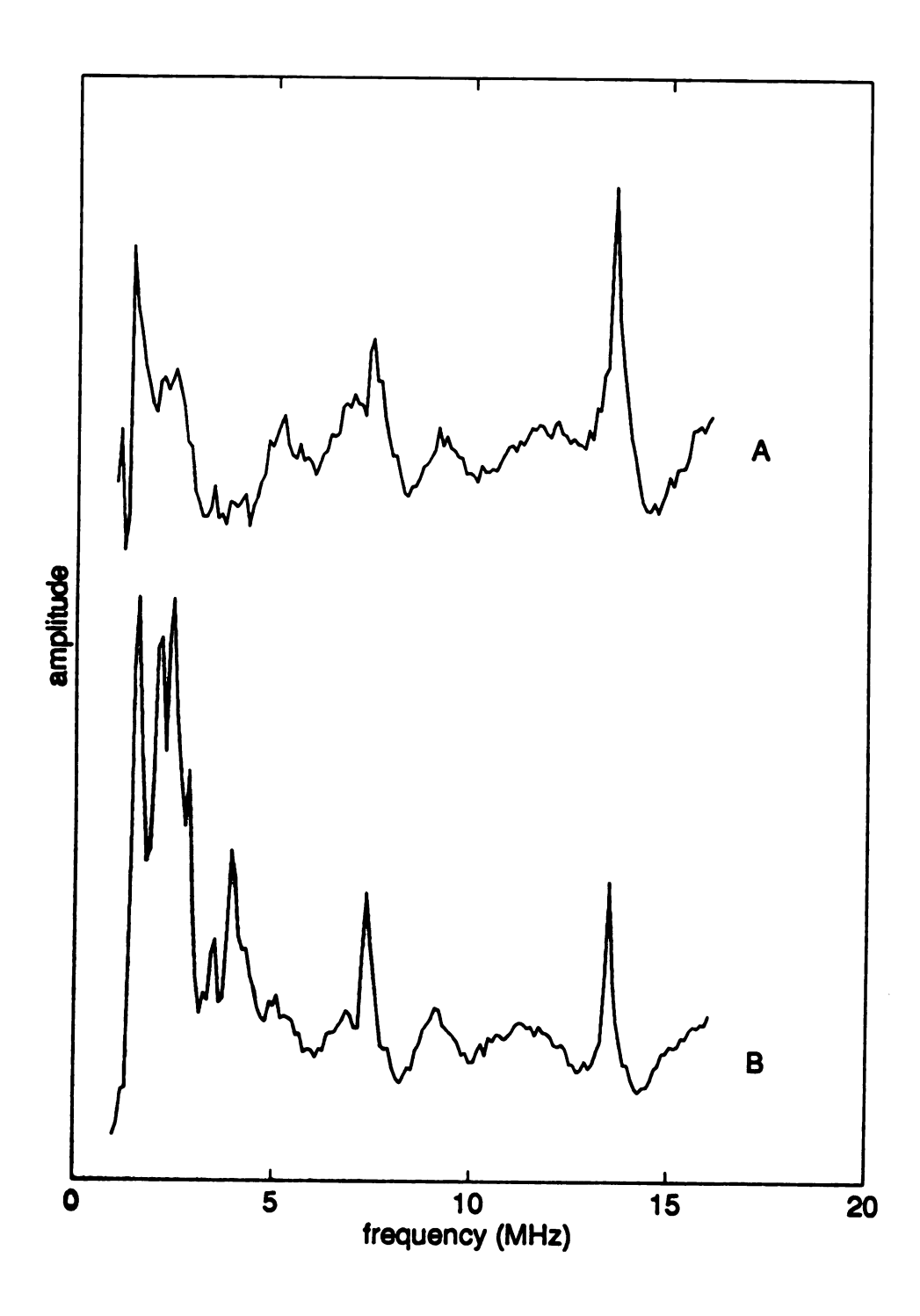


Figure 3.13

3-pulse ESEEM spectra of YD⁺ in PSII particles from Synechocystis supplemented with (A) ¹⁵NO₃⁻ and (B) ¹⁴NO₃⁻ in the growth medium. Conditions: same as Figure 3.10.

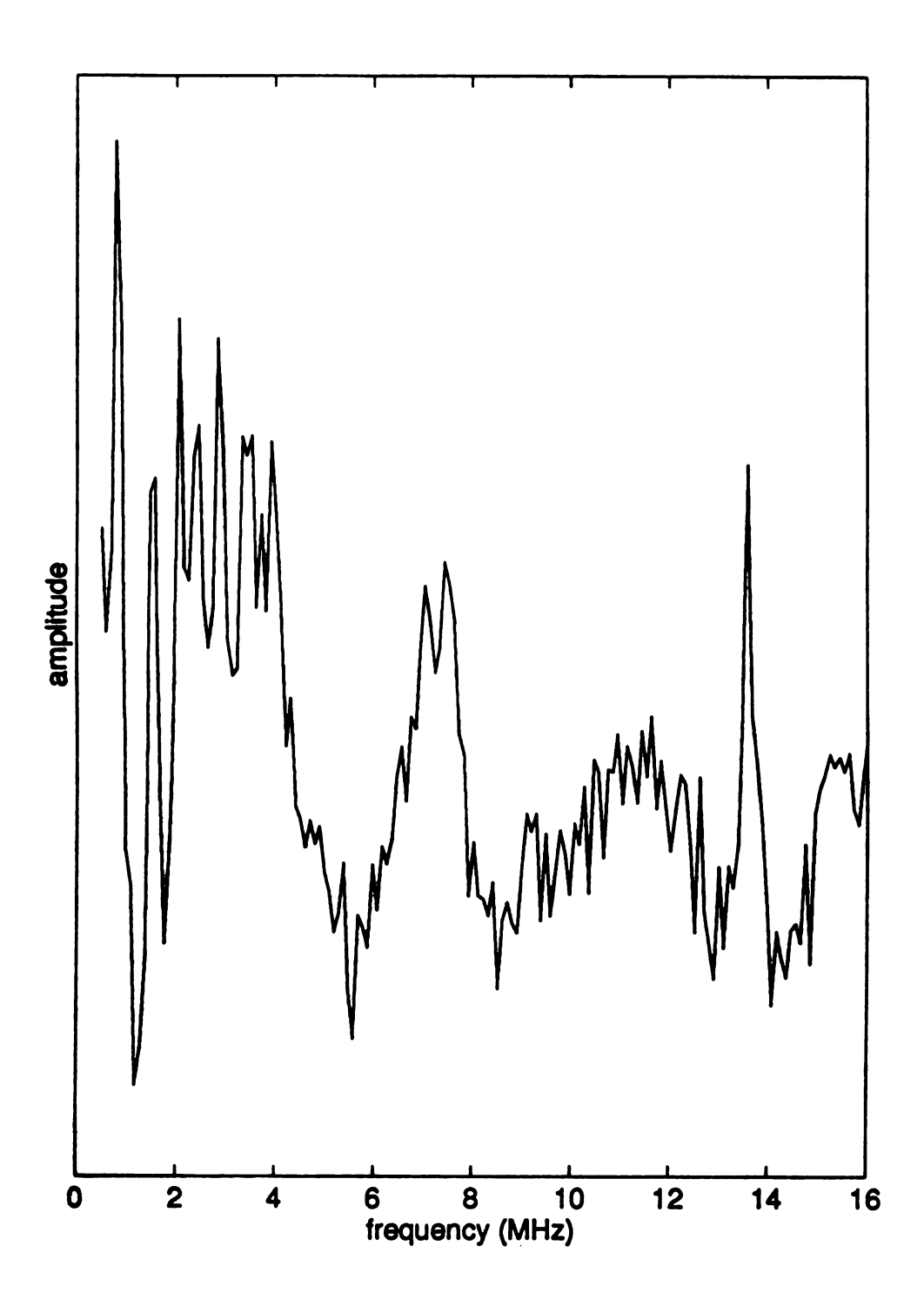


Figure 3.14 3-pulse ESEEM spectrum of Y_D^+ in PSII particles from Synechocystis, containing the D2 protein mutation, histidine-190 to glutamine. Conditions: μ wave frequency, 8.925 GHz; τ = 150 nsec; magnetic field, 3185 G.

A more refined labeling process was used to determine the source of the nitrogen observed by ESEEM. Synechocystis were grown in the presence of \$15\text{NO}_3\$- and tyrosine, phenyalanine, and tryptophan, which causes the incorporation of tyrosine from the growth medium. With this procedure, all nitrogens in the proteins are labeled with \$15\text{N}\$, except the backbone amide nitrogen of tyrosine. The spectrum from this "reversed" labeled sample is again the same as the wild type sample (data not shown). This implicates the backbone amide nitrogen of \$Y_D\$+ itself as the source of the nitrogen detected by ESEEM.

Even though the amide nitrogen is removed from the phenol group containing the unpaired spin density by three bonds, there is precedence for significant isotropic coupling to nitrogen and protons that are two and three bonds removed from the site of unpaired spin density. In solution studies of tyrosine radicals, the isotropic coupling to H_{α} is 1.1 MHz.²⁵ The isotropic coupling for a nitrogen is even larger, 5.3 MHz for the phenoxy radical with the para substituent -CH₂N(CH₃)₂.³³ Solution EPR studies of the primary radical CH₂=CHCH₂CH₂· showed that the isotropic hyperfine coupling to the protons furthest removed from the unpaired electron is still ≈ 1 MHz.³⁴

The spin densities discussed in the previous section concerned the unpaired spin in a π molecular orbital. As the nitrogen in tyrosine is not part of the conjugated system, there will be no π spin density on the nitrogen. The spin density on the nitrogen, evidenced by a non-zero isotropic hyperfine coupling, must then be the result of spin polarization through the σ bonds. This would also be true for the observed isotropic hyperfine coupling to the H_{α} proton of tyrosine. The polarization mechanism would be analogous to the description of hyperfine coupling to an α -proton of an aromatic system, however, it would be propogated through several bonds rather than only one. The hyperfine coupling to the nitrogen of tyrosine is the most distant site from the phenol ring observed to contain unpaired spin density. These results show that the effect of spin polarization can be effective at least through three bonds from the π -system.

The tripeptide glycylalanyltyrosine was also studied by ESEEM to investigate further the hyperfine coupling to amide nitrogens in proteins. A peptide, rather than free tyrosine, was used in this this study since in the peptide the nitrogen is in a peptide bond. Previous EPR studies of the dipeptide glycyltyrosine has shown that, upon UV illumination, a ring-based tyrosine radical is formed.³⁵ The EPR spectrum of glycylalanyltyrosine, after UV illumination, Figure 3.15, is similar to the EPR spectrum observed for the *in vitro* tyrosine radical²⁸ confirming that a tyrosine ring based radical is formed. The magnesium perchlorate present in these samples serves both as a glassing agent and as electron scavenger.³⁶ The peak at g=2.2 in the EPR spectrum is from the oxygen radical that is formed by reaction 1.³⁶

$$ClO_4 + e^- \longrightarrow ClO_3^- + O^-$$
 (1)

The ESEEM spectra of glycylalanyltyrosine at tau values of 150 and 225 nsec are shown in Figure 3.16. The intense peak at 1.3 MHz is the matrix peak for Cl, and arises from dipolar coupling between the Cl in solution and the oxygen radical. Both spectra show one or two peaks between 2.0 and 2.5 MHz. Whether these peaks arise from hyperfine coupling between the tyrosine radical and protons or nitrogens has not been determined. The ESEEM spectra do not show any peaks in the region of 2.5-4.0 MHz, where for Y_D^+ , there are three peaks arising from the amide nitrogen. If the peaks near 2.0 MHz in the glycylalanyltyrosine sample are from the amide nitrogen, then the magnitude of the hyperfine coupling is different from that observed for Y_D^+ . The peaks near 2.0 MHz may also be from a proton and this would suggest that the hyperfine coupling to the amide proton is significantly lower than that observed for Y_D^+ .

The hyperfine coupling to the amide nitrogen may be a function of the geometry of the tyrosine. Since the EPR spectrum for glycylalanyltyrosine and *in vitro* tyrosine are similar, this implies that the dihedral angle of the methylene protons is nearly the same in

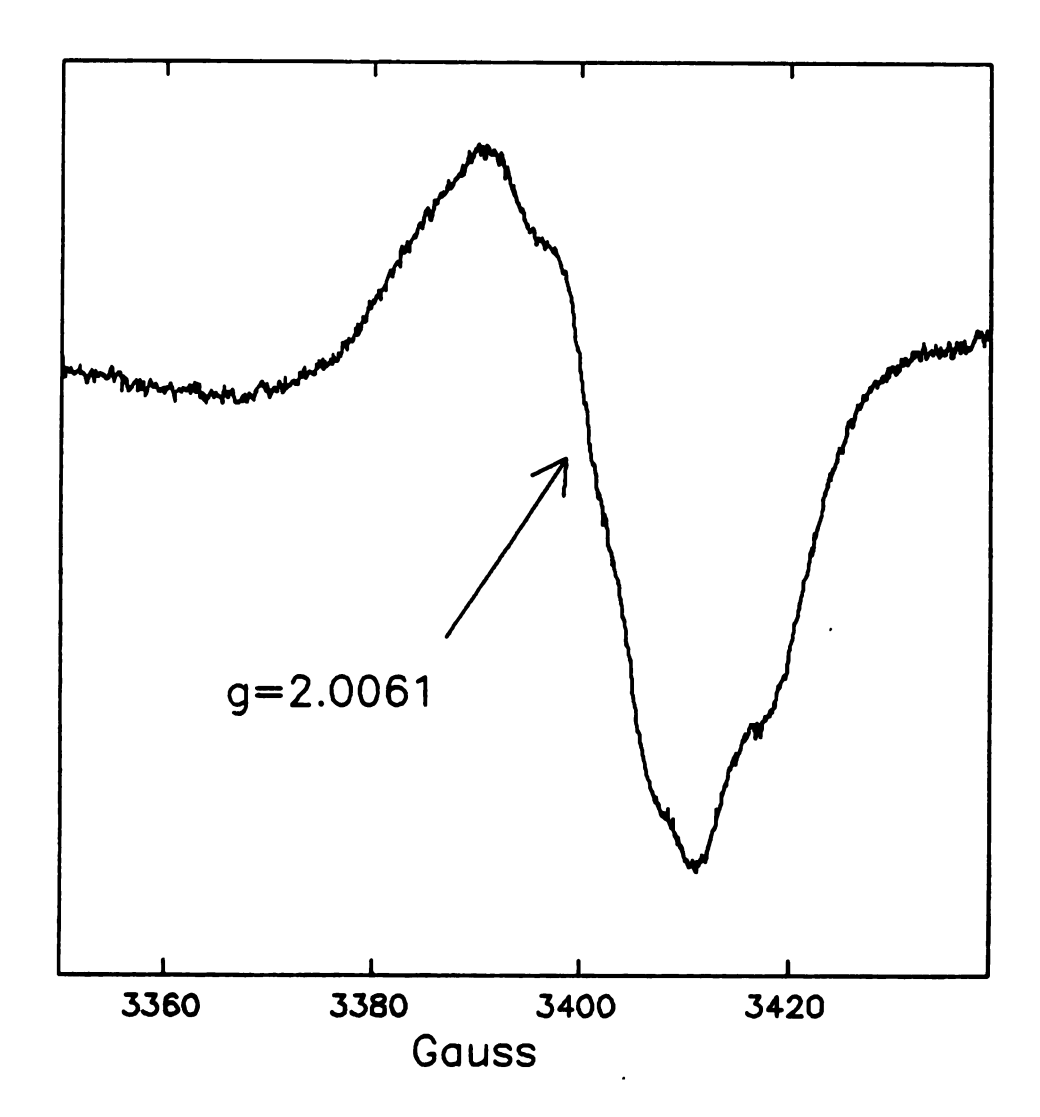


Figure 3.15 EPR spectrum of glycylalanyltyrosine radical in 3M Mg(ClO₄) glass. Conditions: μwave power, 2 mW; modulation, 4 Gpp; μwave frequency, 9.5464 GHz; temperature, -160°C.

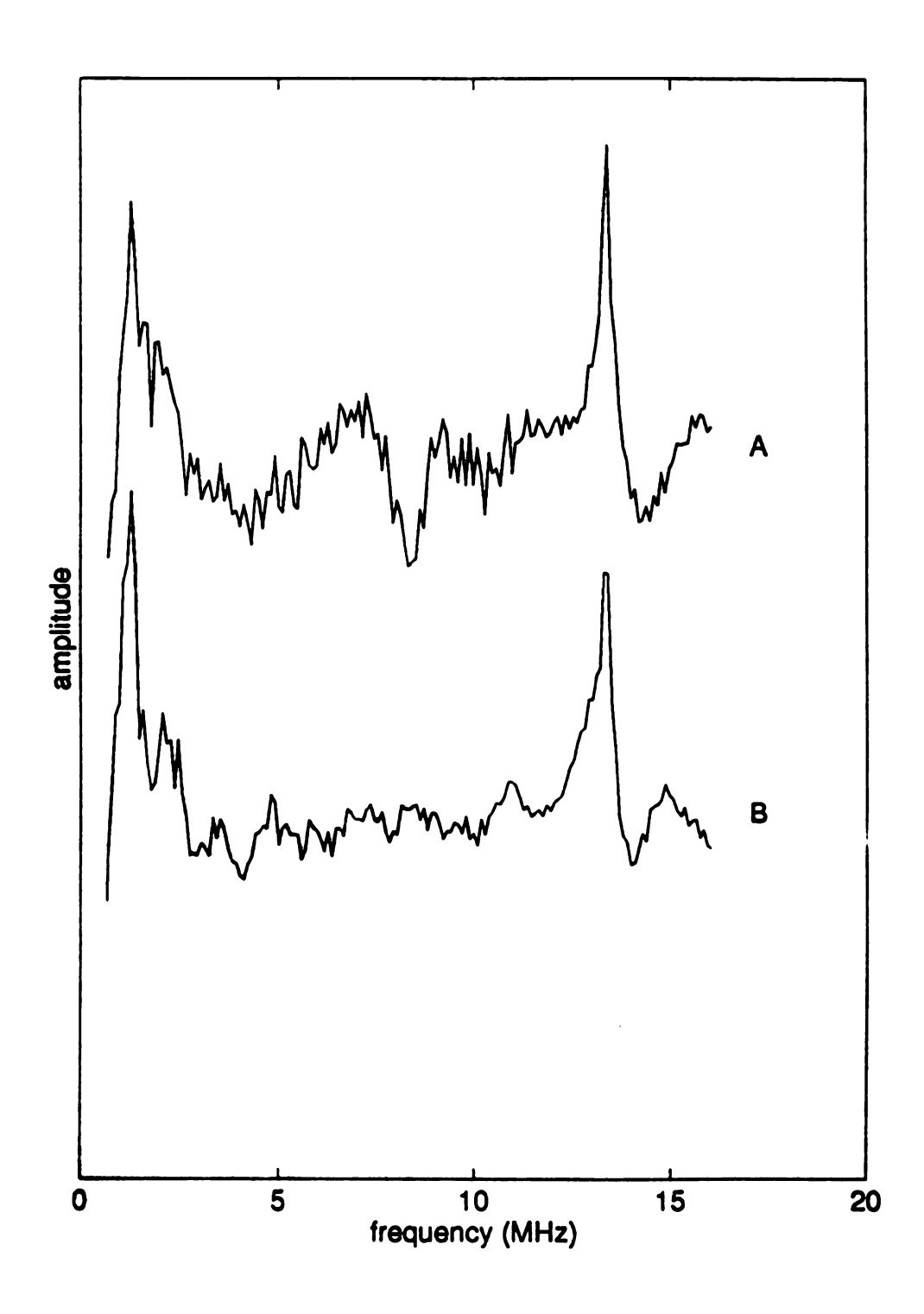


Figure 3.16 3-pulse ESEEM spectra of glycylalanyltyrosine radical collected at g=2.0061. Conditions: μ wave frequency, 8.790; τ = 150 nsec (A) and = 225 nsec (B); magnetic field, 3142 G.

both radicals. 28 However, there are two other degrees of rotational freedom between the phenol group and the amide nitrogen in tyrosine. The side chain can be rotated about the C_{α} - C_{β} bond and the backbone can be rotated about the C_{α} -N bond. Rotation about one or both of these bonds may inhibit the spin polarization through the σ -bond network, and reduce the isotropic coupling to the amide nitrogen. It has been observed that the coupling to the methyl protons of the propyl primary radical, $CH_3CH_2CH_2$, is orientation-dependent. 34 Changes in the position of the ring relative to the amide nitrogen will also affect the magnitude of the dipolar coupling to the nitrogen. If the tyrosine ring is farther away from the nitrogen in the glycylalanyltyrosine compared to Y_D , the dipolar coupling is reduced. A shift in distance of 0.5 \mathring{A} reduces the dipolar coupling by one-half. The parameters that control the magnitude of the hyperfine coupling to the amide nitrogen are not well understood and further studies are needed.

Conclusion

ENDOR studies of PSII particles from cyanobacteria show that, similar to PSII's from spinach, there is a hydrogen bond to Y_D^+ . The A_\perp component of the hyperfine tensor, the only component observed, is slightly smaller that that observed for spinach. The ENDOR study of the mutant W167A shows that this mutation perturbs the protein environment surrounding Y_D^+ . The perturbation is small, however, as the EPR spectrum is unchanged from wild type samples. If the mutation causes the ring to rotate relative to the methylene protons then the EPR spectrum would be changed. Models of the PSII reaction center locate trp167 near Y_D^+ , suggesting that the bacterial reaction center crystal structure may be a suitable model for this region of the PSII reaction center.

The hyperfine couplings to the [2,6] and [3,5] protons in Y_D^+ have been assigned on the basis of deuterium substitution. The hyperfine couplings are similar to those measured for RDPR and the unpaired spin density at the *ortho* and *meta* positions of the

tyrosine rings is similar in these two proteins. From the different tyrosine radicals studied, both *in vivo* and *in vitro*, the unpaired spin density distributions appear to be nearly the same for all systems. The distribution is approximately: $C_3 = C_5 \cong 0.25$, $C_1 \cong 0.3$, and $O \cong 0.3$.

ESEEM characterization of YD⁺ has revealed a nitrogen weakly coupled to the unpaired spin. By using isotopic labeling techniques this nitrogen has been identified as the amide nitrogen of tyrosine. A similar coupling to the amide nitrogen was not detected in a tripeptide with tyrosine at the carboxy terminus. Structural variations within the tyrosine may account for the changes in the magnitude of the hyperfine coupling. While the parameters that control the coupling to the amide nitrogen are not well understood the magnitude of the hyperfine coupling may provide insight into structural contraints of the orientation of the tyrosine ring relative to the protein backbone.

LIST OF REFERENCES

- 1) Stubbe, J. Annu. Rev. Biochem., 1989, 58, 257.
- 2) Babcock, G.T., Barry, B.A., Debus, R.A., Hoganson, C.W., Atamian, M., McIntosh, L., Sithole, I. and Yocum, C.F. Biochemistry, 1989, 28, 9557.
- 3) Sjoberg, B.-M., Reichard, P., Graslund, A. and Ehrenberg, A. J. Biol. Chem., 1978, 253, 6863.
- 4) DeGray, J.A., Lassmann, G., Curtis, J.F., Kennedy, T.A., Marnett, L.J., Eling, T.E. and Mason, R.P. J. Biol. Chem., 1992, 267, 23583.
- 5) Whittaker, M. M. and Whittaker, J. W. J. Biol. Chem., 1990, 265, 9610.
- 6) Ito, N., Phillips, S.E.V., Stevens, C., Ogel, Z.B., McPherson, M.J., Keen, J.N., Yadav, K.D.S., and Knowles, A.P.F. Nature, 1991, 350, 87.
- 7) Hoganson, C.W., Ghanotakis, D.F., Babcock, G.T. and Yocum, C.F. Photosynthesis Research, 1989, 22, 285.
- 8) Nordlund, P., Sjoberg, B.-M. and Eklund, H. Nature, 1990, 345, 593.
- 9) Barry, B.A. and Babcock, G.T. Chemica Scripta, 1988, 28A, 117.
- Backes, G., Sahlin, M. Sjoberg. B.-M., Loeher, T.M. and Sanders-Loehr, J. Biochemistry, 1989, 28, 1923.
- 11) Rodriguez, I.D., Chandrashekar, T.K. and Babcock, G.T. in Progress in Photosynthesis Research (Biggins, J., ed) Vol I, Martinus Nijhoff Publishers, Hague, The Netherlands, 1987, p 471.
- a) Harriman, A. J. Phys. Chem., 1987, 91, 6102. b) Dixon, W.T. and Murphy,D. J.C.S. Faraday II, 1976, 72, 1221.
- 13) Carrington, A. and Smith, I.C.P. Mol. Phys., 1965, 9, 137.

- a) Dixon, W.T. and Norman, R.O.C. J. Chem. Soc., 1964, 4857.
 b) Atherton, N.M., Blackhurst, A.J. and Cook, I.P. Trans. Faraday Soc., 1971, 67, 2510.
 c) Dixon, W.T., Moghimi, M. and Murphy, D. J.C.S. Faraday II, 1974, 70, 1713.
- 15) Bender, C.J., Sahlin, M., Babcock, G.T., Barry, B.A., Chandrashekar, T.K., Salowe, S.P., Stubbe, J., Lindstrom, B., Petersson, L., Ehrenberg, A. and Sjoberg, B.-M. J. Am. Chem. Soc., 1989, 111, 8076.
- Hoganson, C.W. and Babcock, G.T. Biochemistry, 1992, 31, 11874.
- a) Ruffle, S.V., Donnelly, D., Blundell, T.L. and Nugent, J.H.A. Photosynthesis Research, 1992, 34, 287.b) Svensson, B., Vass, I., Cedergren, E. and Styring, S. EMBO J., 1990, 9, 2051.
- 18) Innes, J. B. and Brudvig, G.W. Biochemistry, 1989, 28, 1116.
- 19) Feher, G., Isaacson, R.A., Okamura, M.Y. and Lubitz, W. in Antenna and Reaction Centers of Photosynthetic Bacteria (M.E. Michel-Beyerle, ed.), Springer-Verlag, Berlin Heidelberg, 1985, pp 174.
- Salerno, J.C., Osgood, M., Liu, Y., Taylor, H. and Scholes, C.P. Biochemistry, 1990, 29, 6987.
- 21) Boussac, A. and Etienne, A.L. Biochim. Biophys. Acta, 1984, 766, 576.
- Debus, R.J., Barry, B.A., Babcock, G.T. and McIntosh, L. Proc. Natl. Acad. Sci., USA, 1988, 85, 427.
- 23) Trebst, A. Z. Naturforsch 1986, 41C, 240.
- 24) Barry, B.A. and Babcock, G.T. Proc. Natl. Acad. Sci., USA, 1987, 84, 7099.
- 25) Sealy, R.C., Harman, L., West. P.R. and Mason, R.P. J. Am. Chem. Soc., 1985, 107, 3401.
- Jeffrey, G.A. and Saenger, W. in Hydrogen Bonding in Biological Structures, Springer-Verlag, Berlin Heidelberg, 1991, p 253.
- White, A., Handler, P. and Smith, E.L. in Principles of Biochemistry, 5th ed., McGraw-Hill, New York, 1973, p 104.
- 28) Barry, B.A., El-Deeb, M.K., Sandusky, P.O. and Babcock, G.T. J. Biol. Chem, 1990, 265, 20139.

- 29) Fasanella, E.L. and Gordy, W. Proc. Natl. Acad. Sci., USA, 1969, 62, 299.
- 30) Cammack, R., Chapman, A., McCracken, J., Cornelius, J., Peisach, J. and Weiner, J.H. Biochim. Biophys. Acta, 1988, 956, 307.
- 31) Mims, W.B. and Peisach, J. J. Chem. Phys., 1978, 69, 4921.
- 32) Miller, A.F. and Brudvig, G.W. Biochim. Biophys. Acta, 1991, 1056, 1.
- 33) Becconsall, J.K., Clough, S. and Scott, G. Trans. Faraday Soc., 1960, 56, 459.
- 34) Fessenden, R.W. and Schuler, R.H. J. Chem. Phys., 1963, 39, 2147.
- 35) Meybeck, A. and Windle, J.J. Photochemistry and Photobiology, 1969, 10, 1.
- 36) Sevilla, M.D. and D'Arcy, J.B. J. Phys. Chem., 1978, 82, 338.
- Tang, X.-S., Chisholm, D.A., Dismukes, G.C., Brudvig, G.W. and Diner, B.A. Biochemistry, 1993, in press.
- 38) Berthold, D.A., Babcock, G.T. and Yocum, C.F. Biochim. Biophys. Acta, 1978, 503, 462.
- 39) Ghanotakis, D.F., Demetriou, D.M. and Yocum, C.F. Biochim Biophys. Acta, 1987, 891, 15.
- 40) Noren, G. H., Boerner, R.J. and Barry, B.A. Biochemistry, 1991, 30, 3943.
- 41) McCracken, J., Shin, D.H. and Dye, J.L. Appl. Magn. Reson., 1992, 3, 305.
- Tommos, C., Davidsson, L., Svensson, B., Madsen, C., Vermaas, W. and Styring, S. Biochemistry, 1993, 32, 5436.
- 43) Nemoto, F., Tsuzuki, N., Mukai, K. and Ishizu, K. J. Phys. Chem., 1981, 85, 2450.

CHAPTER 4 EPR AND ESEEM OF THE MULTILINE SIGNAL IN PHOTOSYSTEM II

Introduction

The oxygen evolving complex (OEC) is the site of water oxidation in photosystem II (PSII). The OEC cycles through the five S-states, S₀-S₄, described by Kok. Each increase in S state correlates to a single oxidation of the OEC. As discussed in Chapter 1, in at least one of the S state transitions, the oxidizing equivalent is stored on manganese. While it is known that there are four manganese per PSII, the structure of the Mn complex or complexes that are oxidized in the S state transitions is just beginning to be understood. Little is also known about the protein environment near the Mn complex. It is expected that the protein will provide many of the ligands to the Mn. Since a Mn complex is the site of water oxidation in PSII, knowledge of its structure is important in understanding the mechanism of oxidation of water to oxygen. Two spectroscopic techniques have proved very useful in determining structural and electronic parameters about the the Mn complex(es) of the OEC, EPR and extended X-ray absorption fine structure (EXAFS).

EPR

Multiline signal

In the S_2 state, a Mn complex in the OEC gives rise to a multiline EPR signal. This signal has 18-20 peaks with an average hyperfine splitting of ≈ 80 G.⁴ The multiline signal is generated by illuminating PSII samples at 160-200K. Multifrequency X and Q-band EPR studies have determined that g=1.982 for the multiline signal and that there is little anisotropy in the g-tensor.⁶ The multiline signal is proposed to arise from a multinuclear Mn complex based on the similarity to the EPR spectrum from a mixed valence Mn(III,IV) dimer.⁷ The EPR spectrum of the dimer has 16 lines that arise from hyperfine coupling to the two ⁵⁵Mn nuclei, which have nuclear spin I=5/2. In the spin hamiltonian for Mn dimers, there is an additional term to account for exchange interactions. This term is necessary to explain to shape of the EPR spectrum for mixed valence Mn dimers.

Mn exchange coupling

The exchange interaction between two atoms, both of which have a non-zero electronic spin, contains both an isotropic and dipolar component. This discussion will be restricted to the isotropic exchange coupling, as this term is much more important than the dipolar component for Mn dimers, which is the system of interest. As a model system a valence trapped (III,IV) dimer will be used.

Isotropic, or Heisenberg exchange coupling arises from direct, or ligand promoted overlap of the electron wavefunctions on the two ions and couples their spins. The hamiltonian for isotropic exchange coupling is given by equation 1,

$$H=2JS_{\mathbf{A}}\cdot S_{\mathbf{B}} \tag{1}$$

where S_A and S_B are the electronic spins on ions A and B and J is the exchange coupling constant. For antiferromagnetic coupling, J is negative, and for ferromagnetic coupling J is positive. The term $2S_A \cdot S_B$ can be expanded, equation 2,

$$2S_{A} \cdot S_{B} = S(S+1) - S_{A}(S_{A}+1) - S_{B}(S_{B}-1)$$
 (2)

$$S=S_A+S_B$$

By using the vector coupling model of Kambe⁸, the total spin of the system can be determined for systems up to tetranuclear complexes. For a dimer, the total spin can take the following values,

$$S=S_A+S_B, S_A+S_B-1,..., |S_A-S_B|$$
 (3)

Application of the exchange Hamiltonian, equation 1, to a dimer, yields equation 4 for the energy of the different spin states.⁹

$$E=-J[S(S+1)-S_A(S_A+1)-S_B(S_B+1)]$$
 (4)

For the case of a Mn dimer with Mn(III), S_A=2, and Mn(IV), S_B=3/2, the total spin, S, may take the values 7/2, 5/2, 3/2, 1/2. With antiferromagnetic coupling, which is the predominant coupling seen for mixed valence dimers, the S=1/2 state is the lowest in energy. ¹⁰ The vector coupling approach allows the spin of the ground state to be determined. In addition, the energy of the excited spin states, relative to the ground state

can also be determined. The S=3/2,5/2 and 7/2 spin states are 3J, 5J and 7J in energy above the ground state.

EPR spectra for the S=1/2 spin state have g values near 2 and have isotropic or nearly isotropic g tensors. ¹¹ Since the S=1/2 state is the ground state, then, as the sample temperature is lowered, depopulation of the excited states occurs, and the amplitude of the EPR signal increases. The system then follows Curie law behavior. ¹²

The hyperfine coupling to the Mn nuclei is different in the dimers as compared to that observed for ion monomers. The magnitude of the hfc will be proportional to the projection of the electronic spin of the ion, S_A or S_B , onto the electronic spin of the dimer, S_A . This projection of S_A or S_B onto S_B

$$A_{AD} = \begin{bmatrix} S_A \cdot S \\ S^2 \end{bmatrix} \times A_A = \begin{bmatrix} S^2 + S_A^2 - S_B^2 \\ S^2 \end{bmatrix} \times A_A$$
 (5)

 A_{AD} is the hfc coupling for ion A in the dimer and A_{A} is the coupling for the ion as a monomer. For Mn(III) the dimer hfc will be twice the monomer hfc, whereas for Mn(IV) the dimer and monomer couplings will be the same. These calculation do not determine the actual value of the hfc as there is a spread of observed hfc values, dependent both on oxidation state of the Mn and the ligand environment. In the case for which $A_{A} = A_{B}$, then $A_{AD} = 2A_{BD}$. The EPR spectrum for this system will contain sixteen equally spaced peaks if the g and A tensors are isotropic. If the two monomer couplings are inequivalent the spectrum may contain as many as 36 peaks.

The vector coupling approach can also be applied to Mn trimers and tetramers to understand their magnetic properties.⁹ In the case of a tetramer there are six exchange couplings within the cluster. The vector coupling model cannot be solved for a tetramer of arbitrary symmetry, but can be solved for systems where three or more of the J values are equal.⁹

The spin states and energies can be determined for a Mn tetramer with C_{2V} symmetry and this has been done for a tetramer with oxidation states (III,III,III,IV). ⁴ The structure consists of two dimers; the first a (III,III) dimer from ions A and C and the second a (III,IV) dimer from ions B and D. For this system $J_{AB} = J_{BC} = J_{CD} = J_{DA} = J$ $\neq J_{AC} \neq J_{BD}$. Vector coupling gives,

$$S_{AC}=S_A+S_C, S_A+S_{C-1},..., |S_A-S_C|$$

 $S_{BD}=S_B+S_D, S_B+S_{D-1},..., |S_B-S_D|$ (6)
 $S=S_{AC}+S_{BD}, S_{AC}+S_{BD}-1,..., |S_{AC}-S_{BD}|$

As in the case of the dimer, the value of the Mn hfc for each ion is a function of the projection of the spin of the ion onto the total spin of the system. For ion A of the Mn tetramer, the projection of the ion spin S_A onto S is determined from the projection of S_A onto the quantized resultant S_{AC} and in turn by the projection of S_{AC} onto S, equation 7.

$$A_{AT} = \begin{bmatrix} S_A \cdot S_{AC} \\ \hline S_{AC}^2 \end{bmatrix} \begin{bmatrix} S_{AC} \cdot S \\ \hline S^2 \end{bmatrix} \times A_A$$
 (7)

where A_{AT} is the hfc of ion A in the tetramer.¹³ The eight different S=1/2 spin states have different values for S_{AC} and S_{BD} and thus different hfc values for the ions. In one S=1/2 spin state, the (III,III) dimer has S=0 and will have hfc values of zero for ions A

and C. The other two Mn ions, forming the (III,IV) dimer, will have the same hfc as an isolated (III,IV) dimer. In the extremes, then, the EPR spectrum for a (III,III,III,IV) Mn tetramer with C_{2V} symmetry will be the same as a (III,IV) dimer or may have hfc values equal to or larger than the monomeric values for all four Mn and a spectral width almost twice as large as a (III,IV) dimer.

The temperature dependence of the multiline signal has been studied by both cw and pulsed EPR techniques and the signal follows Curie-law behavior. ¹⁴ The multiline signal thus originates from a ground spin state. Since the multiline signal is at g=1.982 with a nearly isotropic g -tensor, which are characteristics of a S=1/2 spin state, this EPR signal has been proposed to arise from a S=1/2 ground state. ¹⁴ The signal must then arise from a Mn complex containing 2-4 Mn.

g=4.1 signal

When PSII samples are illuminated at 200 K in the presence of sucrose, which serves as a cryoprotectant for the enzyme, an additional EPR signal, besides the multiline, is observed. This signal occurs at g=4.1 and has a linewidth of 320-360 G with no resolved hyperfine structure. The amplitude of the g=4.1 signal oscillates with the number of light flashes given to the sample, exactly as had been seen for the multiline signal. The g=4.1 signal can also be produced by illumination at 140 K and after warming the sample, this EPR signal disappears with the concommitant appearance of the multiline signal. From these results the g=4.1 signal has been assigned to an alternative form of the S₂ state. The Temperature studies of the g=4.1 signal show that the signal follows Curie-law behavior and is assigned to a ground spin state.

Oriented PSII samples that had been treated with NH₃ show both the g=4.1 and multiline EPR signals. ¹⁸ The g=4.1 signal, however, shows at least 16 Mn hyperfine coupling lines with a regular spacing of 36 G. ¹⁹ With 36 lines in the spectrum the g=4.1

signal must come from a Mn complex consisting of at least a dimer. An EPR signal arising from Mn and occuring at g=4 is consistent with a spin state higher than S=1/2.²⁰ Simulations of the g=4.1 multiline signal were consistent with an S=3/2 or S=5/2 spin state of a Mn tetramer.¹⁸ Multifrequency (4-15 GHz) EPR experiments were also performed on the g=4.1 signal.²¹ Simulations of this data were best fit with a Mn tetramer in a S=5/2 spin state.²¹ For a Mn tetramer with C_{2V} symmetry, the Mn hfc are 2/3, -1/3, 1/3 and 1/2 the monomer values for the S=3/2 stateand if the spin state is S=5/2 the hfc are even smaller.¹³ These smaller hfc account for the narrow spectral width of the g=4.1 signal and the small 36 G splitting seen in the NH₃ treated sample.¹⁹

The EPR data from the multiline and g=4.1 signals of the S₂ state suggest a tetranuclear form of the Mn complex in the OEC of PSII. The conversion between the two EPR signals is most likely the result of a structural perturbation in the Mn complex. ¹⁷ This structural change causes a change in the magnitude of the exchange coupling parameters that changes the multiplicity of the ground state.

Recent saturation-recovery experiments are also consistent with a nuclearity of four for the Mn complex. The spin-lattice relaxation rate of Y_D was measured as a function of the S state of the OEC. The relaxation rate of Y_D is expected to be affected if there is a paramagnetic species in the vicinity. There was no difference in the spin-lattice relaxation rate of Y_D between the dark-adapted S_1 state and when the Mn was removed from the enzyme. These results show that the S_1 state must be diamagnetic, such that it has no effect on the relaxation rate of Y_D . The only configurations of four Mn, that are mixed valence and form a diamagnetic complex, are a dimer of dimers or a tetranuclear complex. The saturation-recovery results, in conjunction with the EPR results, strongly suggest that the Mn complex of the OEC is a tetramer.

EXAFS

Extended X-ray fine structure spectroscopy furnishes information about the number, type and distance to ligands and to neighboring atoms of metals. The technique is element specific and is thus a good technique to study the Mn in the OEC. EXAFS cannot look at each Mn atom individually but provides a composite measure of the coordination of all the Mn atoms. The most well studied S states of the OEC are S₁ and S₂ and these results will be discussed.²³

Each Mn atom of the OEC has 1-1.5 Mn atoms at a distance of 2.7 Å. 23 This distance is common for Mn complexes that contain two μ_2 - or two μ_3 -oxo bridges. 24 The EXAFS results also show that there are 2 nitrogen or oxygen per Mn at a distance of 1.8 Å. 23 Bridging Mn-O distances are typically about 1.8 Å in multinuclear μ_2 - or μ_3 -oxo bridged Mn complexes. 25 Since each Mn has one Mn neighbor at 2.7 Å, the data support the model of two di- μ -oxo bridged dimers in the OEC. 26 A Mn-Mn distance of 3.3 Å, with a stochiometry of 0.5-1.0 Mn neighbor per Mn, has also been observed by EXAFS. 23

From these results a model has been constructed for the Mn complex of the OEC. In this model there are two di- μ -oxo bridged dimers with a Mn-Mn distance of 2.7 Å. The two dimers are connected on one end by one μ_2 -oxo bridge and two μ_2 -acetate bridge giving a Mn-Mn distance of 3.3 Å. The two terminal Mn point away from each other and are separated by a distance greater than can be detected by EXAFS.²⁶

The culmination of the EPR, EXAFS and saturation experiments strongly support a tetramer Mn complex for the OEC. The EPR results have also shown that there are several different conformations of the tetramer which give rise to different ground spin states. While substantial insight into the structure of the Mn complex has been obtained,

little is known about the protein environment that surrounds the Mn complex and provides the terminal ligands.

Pulsed EPR

EPR spectra of the multiline signal collected at higher resolution has shown that there are shoulders on some of the 18-20 major peaks and that some of the peaks are split. There are also additional peaks with smaller intensity. By using a series of biochemical techniques it has been shown that none of the peaks in the multiline spectra arises from hfc to hydrogens, nitrogens or chloride, all of which have a non-zero nuclear spin and are present in PSII.^{27,28} The reason that hyperfine couplings to these elements are not detected is that their hyperfine coupling may be small relative to the broad linewidths of the multiline signal and they are not resolved. In order to observe small hyperfine couplings to the Mn compex of the OEC, pulsed EPR techniques have been applied.

Two-pulse ESEEM of PSII's, isolated from the cyanobacteria Synechococcus sp., in the S₂ state has a peak at 4.5 MHz.²⁸ When the cyanobacteria are grown in the presence of ¹⁵NO₃⁻, the cells sole nitrogen source, the peak at 4.5 MHz in the 2-pulse ESEEM data disappears thus, the 4.5 MHz peak arises from a nitrogen ligand to Mn.²⁸ The isotopic labeling technique is comprehensive and does not allow the identity of the nitrogen to be determined. Recently, a histidine tolerant mutant of the cyanobacteria Synechocystis 6803 was developed that will take histidine from the growth medium, rather than synthesize it internally. The ESEEM data from PSII's isolated from cells grown in the presence of ¹⁵N-histidine did not contain the 4.5 MHz peak. This experiment leads to the conclusion that the nitrogen coupling to the Mn complex detected by ESEEM arises from a histidine ligand to the Mn.²⁹ To date, this is the only definitive information available regarding the ligands to the Mn ensemble supplied by the protein.

As discussed in Chapter 1, there are two bound Ca²⁺ per PSII.³⁰ If the more loosely bound Ca²⁺ is removed, which can be done by several techniques, oxygen evolution is severely impaired.³⁰ It has been shown, however, that a series of metals can bind in the vacant Ca binding site, including Na, K, Cs, Mg, Sr, Mn and La.³⁰ Of these, only Sr²⁺ was able to activate oxygen evolution, however, at reduced rates, with oxygen evolution rates that are 42% of that observed for samples in which the Ca was not removed.³¹ In the Sr substituted PSII's, the multiline signal can be generated by continuous illumination at 200K.³² The multiline signal for the Sr substituted samples is modified, compared to the native enzyme, with peak splittings, shifts and intensity redistributions. The changes are small, however, as many of the peaks in the multiline spectra from the Ca and Sr samples are still aligned.³²

The cause of the differences observed in the multiline signal, from the Sr substituted sample, are not understood but are assigned to perturbations in the exchange couplings between the Mn of the OEC. 26,47 If the Mn tetramer of the OEC has more than one S=1/2 spin state, as in the case of C_{2V} symmetry, then changes in the exchange couplings may result in a different S=1/2 spin state being the ground state. This will result in different Mn hyperfine couplings. Changes in the Mn exchange coupling can be accomplished by a change in ligands to a Mn or by changes in the structure of the Mn tetramer of the OEC. 25,48

The nitrogen coupling observed in the ESEEM studies of the OEC discussed above²⁸, can be used as a probe of structural changes that occur in the Mn tetramer. Changes in the ligand geometry, surrounding the Mn with the nitrogen ligand detected by ESEEM, may cause a change in the mutiline ESEEM spectrum. In this chapter the results from two and three-pulse experiments on native and Sr substituted PSII's will be discussed.

Reaction center complexes

Due to the extensive width of the multiline signal, approximately 2000G, the pulsed EPR experiments only probe a small percentage of the spin systems. In addition, the sample volume for these experiments is small, 50 mL. It is important, then, to use the most concentrated samples possible. Previous cw and pulsed EPR experiments have been performed with BBY-type PSII's. In these samples, the PSII's are still in the thylakoid membranes and the light harvesting complex (LHC) is still present. A more refined preparation procedure has been developed that removes the membrane and the LHC and retains high oxygen activity. With these new particles, reaction center complexes (RCC), a more concentrated sample can be obtained due to the smaller volume per PSII.

The spectroscopic characterization of RCC's, to date, has not been extensive.³³ An EPR characterization of RCC's has shown that the multiline signal is the same as that observed for the more commonly used BBY's.³³ Before using RCC's for the ESEEM experiments, these PSII particles were characterized by EPR to confirm that the OEC was not modified by the additional purification steps. Both the native and Sr substituted RCC's were studied by EPR and compared to the EPR spectra seen for BBY samples.

Materials and Methods

BBY PSII particles were prepared from market spinach according to the procedure of Berthold et al.⁴⁹ and used immediately to prepare reaction center complexes (RCC). The RCC's were prepared as in Ghanotakis et al.³³ with minor modifications including those of Bowlby.⁵⁰ BBY's were diluted to 2.5 mg Chl/ml with buffer A (0.4 M sucrose, 50 mM MES, 10 mM NaCl, pH = 6.0) and then diluted with an equal volume of

Buffer B (1.0 M sucrose, 50 mM MES, 0.8 M NaCl, 10 mM CaCl₂, 70 mM octylglucaside, pH = 6.0). The sample was incubated for 10 minutes at 4°C in the dark. The sample was gently stirred by hand every 2 minutes. Two times the present volume of buffer C (1.0 M sucrose, 50 mM MES, 0.4 M NaCl, 5 mM CaCl₂, pH = 6.0) was added and the sample was centrifuged for 90 minutes at 40,000xg. The supernatent was placed in a cold beaker and an equal volume of 30%(w/v) polyethylene glycol (PEG) was added while gently stirring. The sample was centrifuged for 30 minutes at 40,000xg, the pellet was resuspended in buffer E (0.4 M sucrose, 50 mM MES, 10 mM NaCl, 5 mM CaCl₂, pH = 6.0), centrifuged for 15 minutes at 40,000xg and resuspended a final time in buffer E.

In order to eliminate the use of PEG, after the 90 minute centrifugation step, the supernatent was placed in 12-14kDa molecular weight cutoff dialysis tubing and dialysed in buffer D (50 mM MES, 10 mM NaCl, 5 mM CaCl₂, pH = 6.0) for 90 minutes. Before use, the dialysis tubing was boiled for 30 minutes in distilled water containing 5mM EDTA and rinsed thoroughly. After dialysis, the sample was collected and to every 3 parts sample one part high salt buffer (1.6 M sucrose, 50 mM Mes and 4 M NaCl, pH=6.0) was added, and the sample was incubated in the dark on ice for 10 minutes. The sample was centrifuged for 30 minutes at 40,000xg, the pellet was resuspended in buffer E, centrifuged for 20 minutes at 40,000xg and resuspended a final time in buffer E.

Sr substitution

For RCC samples, after treatment with PEG and centrifugation, the pellet was resuspended with buffer A, centrifuged for 15 minutes at 40,000xg and resuspended in buffer A containing 20 mM Ca²⁺ or 20 mM Sr²⁺. The samples were incubated for 15 minutes before loading into an EPR tube. For RCC samples that were dialysed, rather than treated with PEG, the dialysis medium was buffer D without the Ca²⁺. After

incubation in the high salt buffer, the sample was washed with buffer A. In the final resuspension the pellet was resuspended in buffer A containing 20 mM Ca²⁺ or 20 mM Sr²⁺.

Ca removal with EGTA

The removal of Ca was accomplished using the procedure previously described for BBY's with several minor modifications. 32 RCC's were prepared as above by using the PEG containing procedure, with buffer A used in the final two washing steps. RCC's were diluted to 0.3 mg Chl/ml with buffer A and incubated on ice under illumination for 20 minutes. EGTA was added to a final concentration of 50 μ M and the sample was incubated for three more minutes. The sample was centrifuged for 30 minutes at 40,000xg, resuspended in buffer F (50 mM MES, 10 mM NaCl, 50 μ M EGTA), centrifuged for 20 minutes at 40,000xg and resuspended in buffer F containing 20 mM Ca²⁺ or 20 mM Sr²⁺.

Samples were centrifuged into quartz EPR tubes, approximately 9 cm in length, using a table top centrifuge. The final [Chl] is 6-7 mg Chl/ml. The samples were dark adapted 30-60 minutes and frozen and stored at 77K.

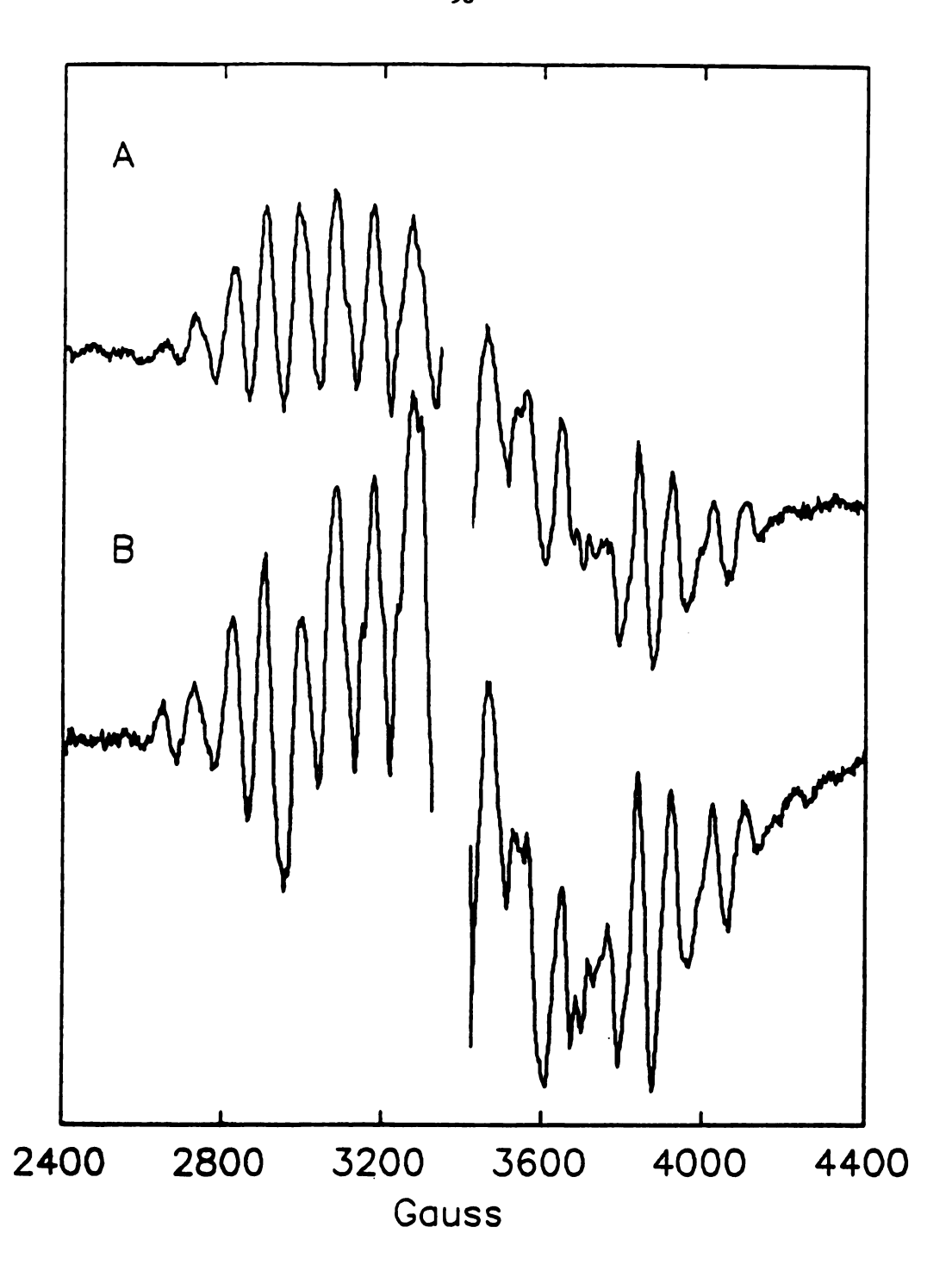
The multiline signal was generated by 8 minutes of illumination at 205-210 K, in a non-silvered dewar, with a 750W projector. The sample was kept cold by placing it in a N₂ gas stream cooled with a dry ice/ethanol bath. Before illumination the sample was allowed to equilibrate for 5 minutes in the N₂ gas stream. The EPR spectra were recorded on a Bruker ER200 X-band EPR spectrometer equipped with an Oxford ESR-9 liquid helium flow cryostat. The pulsed EPR data were collected on a home built pulsed EPR spectrometer described in chapter 3. The spectrometer settings are described in the figure captions.

Results and Discussion

The multiline signal from RCC's, generated by continuous illumination at 210 K for six minutes, is shown in Figure 4.1. All the multiline spectra presented here are the difference between the the sample before and after illumination at 210 K. Calculating the difference spectrum removes the EPR signals from paramagnets present in the dark adapted samples, leaving only the multiline signal originating from the Mn complex. The spectrum has 18 peaks with an average hyperfine peak spacing of 89 G. In comparing Figure 4.1A with NaCl washed BBY's (SW-BBY), for which the 17 and 23 kDa extrinsic polypeptides have been removed, the spectra are nearly indentical.³² (RCC's also lack the 17 and 23 kDa polypeptides).³³ The number of peaks, the spacing between peaks, and the peak intensities are the same between RCC's and SW-BBY's.

The RCC purification process was accomplished by two slightly different protocols (see materials and methods). When polyethylene glycol (PEG) was used to disrupt solvation and allow the RCC's to be collected by centrifugation, the multiline signal that results from 210 K illumination has the form shown in Figure 4.1B. However, when dialysis is used to remove the detergent, so that the protein could be recovered by centrifugation, the multiline spectrum of Figure 4.1A is observed. While the two spectra of Figure 4.1 have the same number of peaks and the peaks are located in the same position within the spectrum, there are some slight differences in lineshapes and peak intensities.

Similar effects on the multiline signal have been observed for BBY samples treated with buffers containing 4% ethanol. After treatment with ethanol, the mutiline signal from BBY's show additional fine structure on several of the low field peaks. 15 These splittings, which appear as shoulders on several of the major peaks on the low field side of the spectrum, are also present in RCC samples treated with PEG. Changes in the multiline signal are also observed in BBY samples resuspended in buffers containing



Multiline EPR spectra from reaction center complexes generated by 8 minutes of illumination at 210 K. The spectra are the light-dark difference. A) RCC's prepared using dialysis and B) RCC's prepared using PEG. Conditions: μwave power, 8 mW; μwave frequency, 9.4710 GHz; modulation, 20 Gpp; temperature, 10 K.

glycerol or ethylene glycol, which are used as cryoprotectants. ¹⁵ The PEG used in the RCC preparation, with an average weight of 10,000, has some monomer present that can interect with the RCC's, which may account for the differences of the EPR spectra of Figure 4.1. While the presence of alcohols in PSII sample buffers causes a change in the mutiline spectrum, the reason for the change is not understood. It has been suggested that the small changes observed in the multiline signal arise from perturbations of the exchange couplings, as a result of a slight modification of the structure of the Mn complex of the OEC. ^{1,26}

Substitution of Sr²⁺ for Ca²⁺ in BBY's causes a modification of the multiline signal, generated by 200 K illumination³²; this modification is also seen in RCC's, Figure 4.2A. For comparison to the untreated sample, Figure 4.1A is repeated as Figure 4.2B. The multiline signal from the Sr-substituted RCC sample contains 18 lines with an average spacing between lines of 80 G. The Sr-modified multiline signal shown here is very similar to the spectrum observed for SW-BBY's with Sr substituted for Ca. For the SW-BBY sample, however, the average spacing between peaks is reported to be 71.0 G.32 The discrepency between RCC's and SW-BBY's in average spacings is a result of an additional spitting in one of the peaks in the spectrum from SW-BBY's that is not seen in RCC's. The Sr-substituted sample shows shifts in peak positions and intensity and lineshape changes. With the smaller average splittings in the Sr sample, the peaks in the wings of the spectrum do not occur at the same position as the Ca sample. While there are differences between the two spectra, many of the peaks in the two spectra do occur at the same position, indicative of only small changes in the parameters that dictate the shape of the EPR spectrum. The substitution of Sr for Ca can be accomplished in RCC's, as well as in SW-BBY's, and the changes observed in the multiline signals are the same for both PSII preparations.

The previously reported method for removing the Ca from BBY's involves incubating the protein in a 1M NaCl buffer to remove the 17 and 23 kDa proteins and

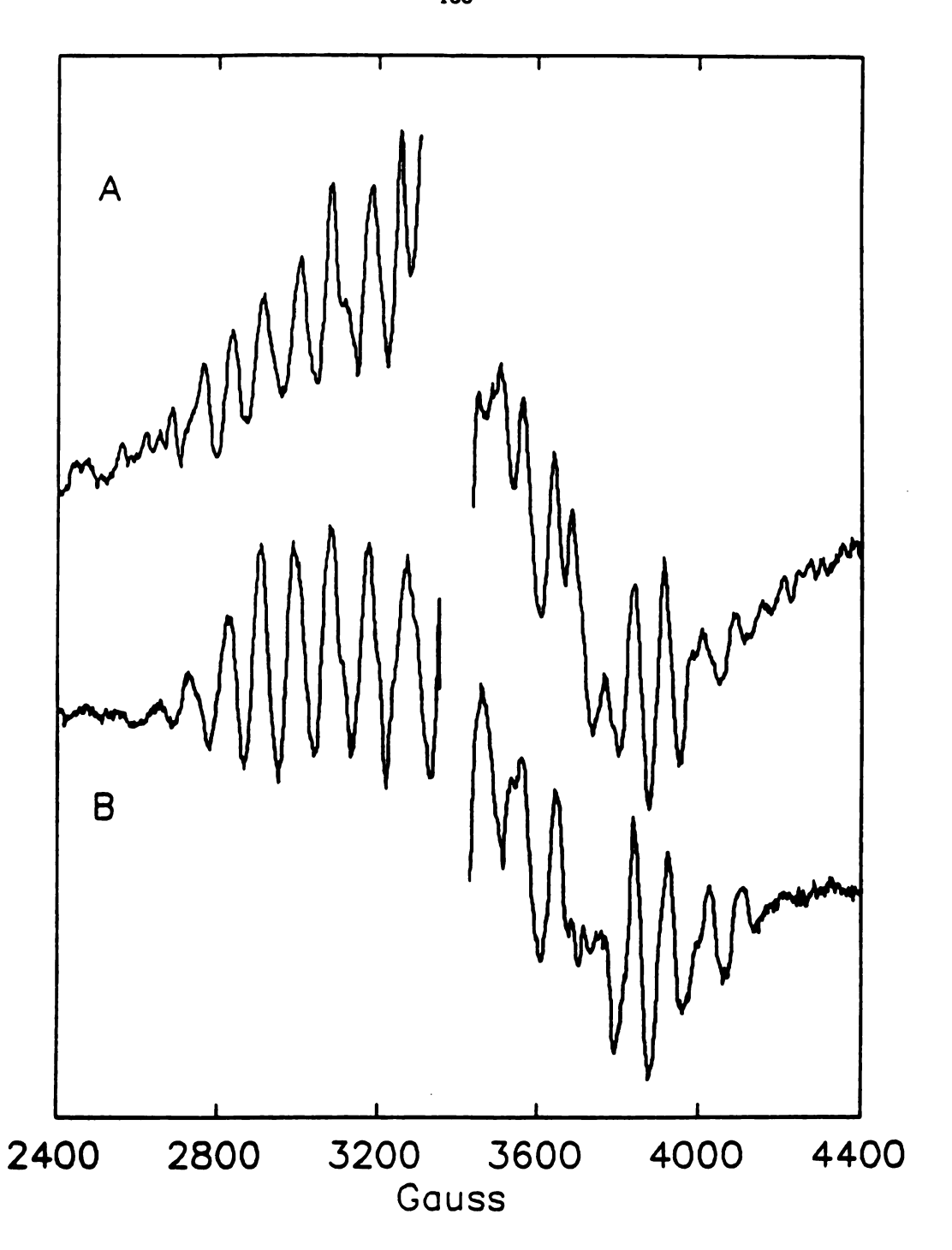


Figure 4.2 Multiline EPR spectra from reaction center complexes generated by 8 minutes of illumination at 210 K. The spectra are the light-dark difference. A) RCC's treated with 20 mM Sr²⁺ and B) RCC's treated with 20 mM Ca²⁺. Conditions: μwave power, 8 mW; μwave frequency, 9.4710 GHz; modulation, 20 Gpp; temperature, 10 K.

opening up the Ca binding site.³² The samples are incubated in the light to facilitate Ca release from the protein. It has previously been shown that, in the higher S states, the affinity for Ca, by the Ca binding sites is lower.³⁴ The chelator EGTA is added to ligate the Ca, which remains in the supernatent when the protein is recovered by centrifugation. The SW-BBY's are then resuspended with a buffer containing 20 mM Sr²⁺, which then occupies the Ca binding site.³²

In an effort to substitute Sr for Ca without the need for chelators or illumination, a different technique was developed. The RCC samples were washed with buffer A that contained neither Ca nor Sr. The samples were resuspended in the final step in buffer E that contained either 20 mM Ca²⁺ or Sr²⁺. The highfield portion of the mutiline spectra, for samples prepared in this manner, are shown in Figure 4.3A and 4.3B for Ca and Sr, respectively. RCC samples were also treated by the same procedure used to remove Ca and substitute Sr in BBY's.³² As above, the final resuspension buffer contained either 20 mM Ca²⁺ or Sr²⁺. The mutiline spectra for these samples are shown in Figure 4.3C and 4.3D for Ca and Sr, respectively. The spectra of Figure 4.3 show that the multiline signal for the two Ca containing samples are very similar, as are the two Sr containing samples. For both Sr substitution techniques, similar changes in the multiline spectrum are observed. The method of substituting Sr for Ca by simply resuspending RCC's in a high [Sr] buffer gives the same results as the more elaborate method used for BBY's.³²

The two regions of the multiline signal where the effect of Sr substitution is most evident are highlighted in Figure 4.3. First, there are shifts in the position of the peaks in the 3450-3550 G region in the Sr-substituted samples relative to the Ca samples. Second, the smaller average hyperfine coupling of the Sr-substituted sample is evident by the peak at \approx 4050 G in the Ca sample shifting downfield by \approx 25 G in the Sr sample. These modification are present regardless of which technique was used to replace the Ca with Sr.

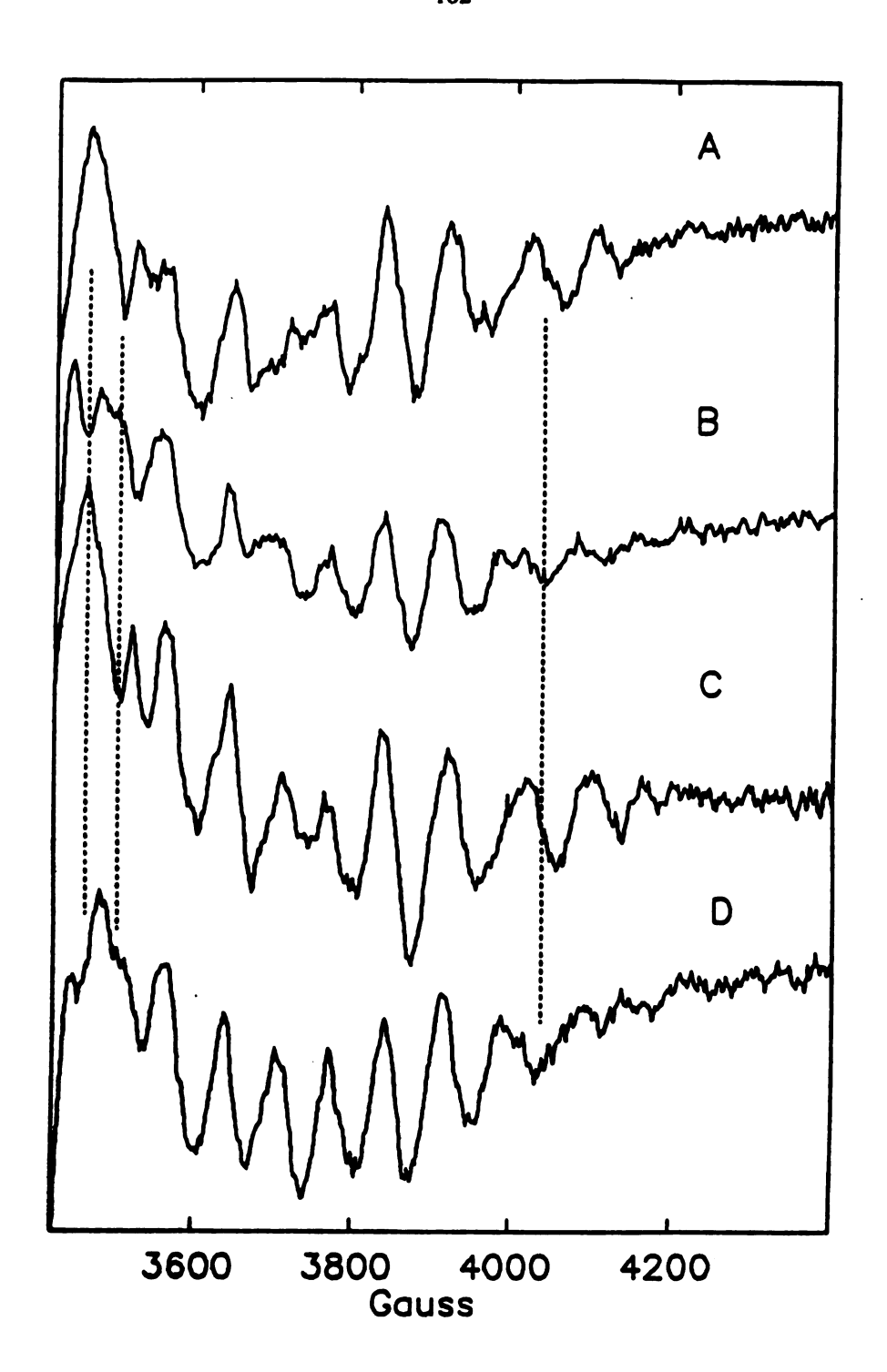


Figure 4.3 Multiline EPR spectra from reaction center complexes generated by 8 minutes of illumination at 210 K. The spectra are the light-dark difference. Spectra A and C are from RCC's that have bound Ca²⁺ and spectra B and D are from RCC's that have bound Sr²⁺. Conditions: μ wave power, 8 mW; μwave frequency,9.4710 GHz; modulation, 20 Gpp; temperature, 10 K.

There are, however, some differences in peak amplitudes between the spectra in Figures 4.4.3A and 3B and the spectra in Figures 4.3C and 4.3D. These amplitude differences are most likely the result of the different buffers used in the final resuspension of the samples. All the samples were treated with polyethyleneglycol during the preparation procedure. The samples of Figure 4.3A and 4.3B were washed one time after treatment with PEG and resuspended in a buffer (buffer E) that contained 0.4 M sucrose as a cryoprotectant. The samples of Figure 4.3C and 4.3D were washed twice after PEG treatment and were resuspended in the same buffers used by Boussac and Rutherford³² that did not contain any cryoprotectants. The multiline studies of Styring and Rutherford¹⁵, and the results in Figure 4.1, show that the shape of the multiline signal is dependent on the particular cryoprotectant present and this believed to be the explanation for the differences in the EPR spectra of the two Ca, and the two Sr containing PSII samples.

Figures 4.1, 4.2 and 4.3 show that the multiline spectra from native and Sr-substituted RCC's are the same as those observed for SW-BBY's. In addition, Sr can be substituted for Ca by incubating the RCC's in a buffer containing 20 mM Sr²⁺. The Mn complex of the OEC is thus unaffected by the further purification of BBY's to RCC's. RCC samples have been used exclusively in the following pulsed EPR studies.

Pulsed EPR studies of the multiline signal

The light minus dark two pulse electron spin echo envelope modulation (ESEEM) data from RCC's is shown in Figure 4.4. There are several paramagnets present in the dark adapted samples, including cytochrome b-559 and adventiously bound Cu²⁺, that give rise to peaks in the ESEEM spectrum. The difference spectrum is calculated to remove these peaks. The ESEEM spectrum of the multiline signal, Figure 4.4, has peaks at 4.6 and 13.8 MHz. The peak at 13.8 MHz arises from protons weakly coupled to the

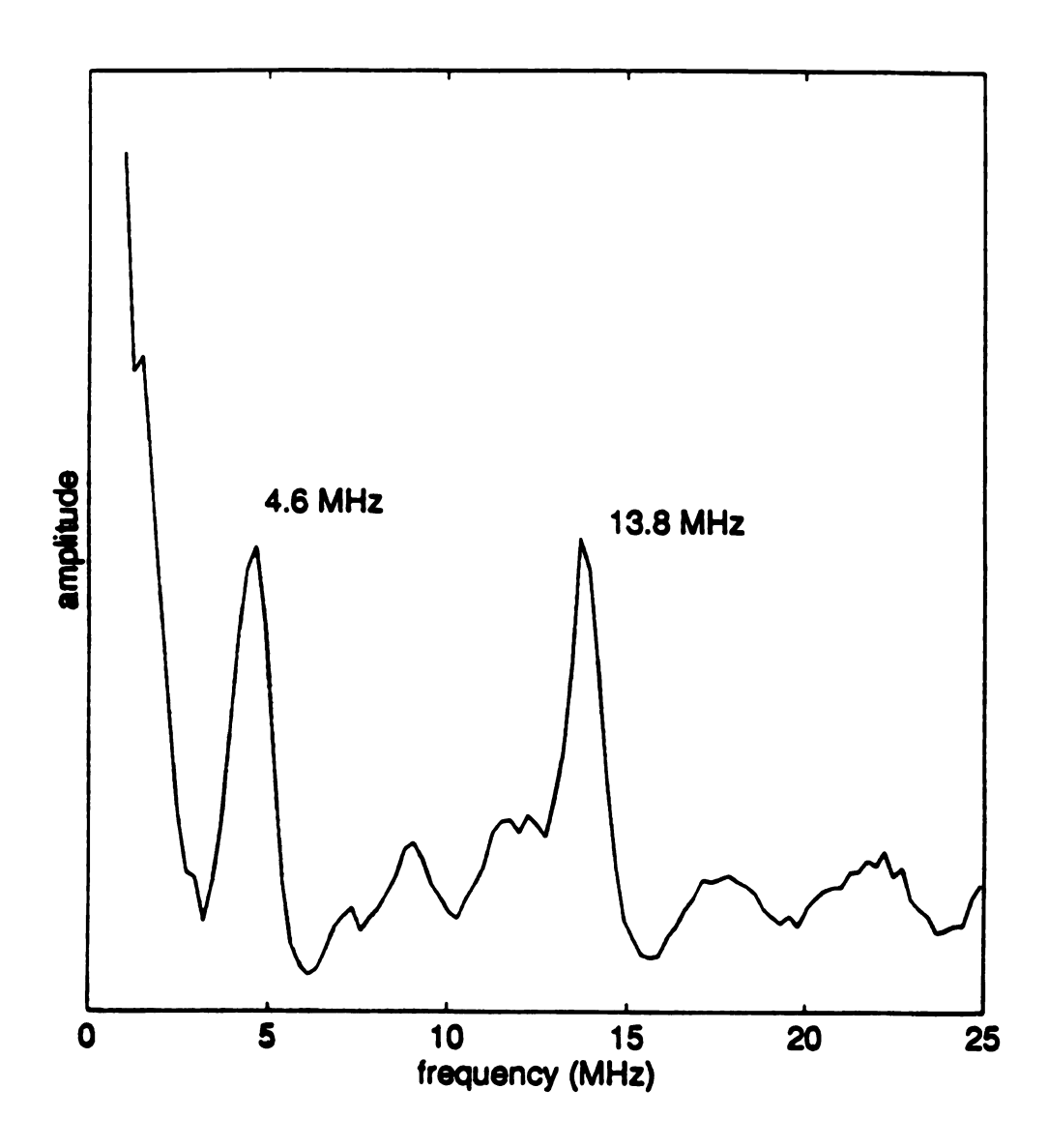


Figure 4.4 2-pulse ESEEM difference spectrum of the multiline signal from RCC's. Conditions: μ wave frequency, 8.840; magnetic field, 3250 G; τ = 200 nsec; pulse repetition rate, 90 Hz; temperature, 1.8 K.

unpaired spin of the Mn complex. Previous 2-pulse ESEEM studies of the multiline signal have detected a peak at 4.5 MHz which arises from a histidine nitrogen ligated to the Mn complex.²⁸ Due to the short lifetime of the 2-pulse echo, the peaks are generally broad and there can be an error in assigning the peak positions of ±0.5 MHz. The 2-pulse data from RCC's, as for the EPR results, are very similar to the data from BBY's and from PSII's isolated from the cyanobacteria *Synechococcus sp.*^{28,35} Similar 2-pulse experiments were conducted on the Sr-substituted RCC's that yielded the same spectrum as the Ca-containing RCC's (data not shown).

The two pulse data suffers both from lower resolution, due to the short lifetime of the 2-pulse echo, and significant errors in the observed peak positions. To combat these problems, 3-pulse techniques can be applied. Narrower linewidths and better resolution are obtained because the lifetime of the 3-pulse echo is longer than the 2-pulse echo. The error in the peak positions in 3-pulse spectra is ± 0.1 MHz. The tradeoff in these experiments is that the 3-pulse echo is less intense than the 2-pulse echo, which results in poorer signal to noise in the 3-pulse data.

The 3-pulse data for the multiline signal in RCC's is shown in Figure 4.5. The time domain data is shown for RCC's before (dark) and after illumination (light) and the difference of these two sets of data was calculated. Figure 4.6 shows the Fourier transforms of the data from Figure 4.5. The "dark" spectrum has peaks at 4.0 and 14 MHz. As for the 2-pulse data, and all subsequent data, the peak at 14 MHz arises from weakly coupled protons. The "light" spectrum has the same peak at 4.0 MHz and, in addition, peaks at 0.8, 1.60 and 4.80, which are also clearly evident in the difference spectrum. A nitrogen nucleus, hyperfine coupled to an unpaired electron, can give rise to as many as six peaks in an ESEEM spectrum. The peaks at 0.8, 1.60, and 4.80, observed in the difference spectrum acquired by using the three pulse technique, are assigned to the histidine ligand to the Mn.

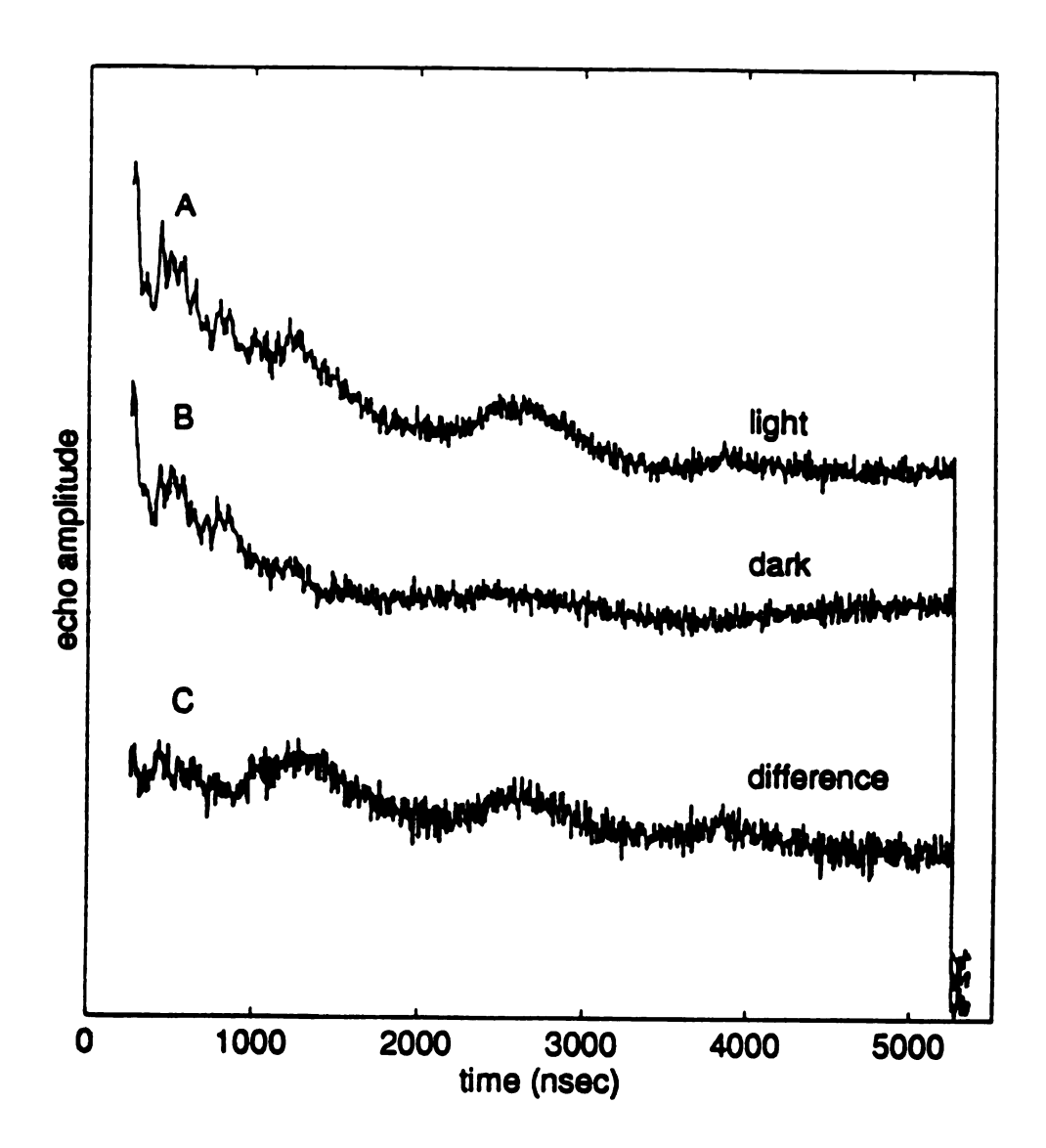


Figure 4.5 3-pulse envelope-echo decay traces for RCC's containing Ca^{2+} (A) after illumination, (B) before illumination and (C) the difference of traces A and B. Conditions: μ wave frequency, 8.955 GHz, magnetic field, 3290 G, τ = 213 nsec; pulse repetition rate, 90 Hz; temperature, 1.8 K.

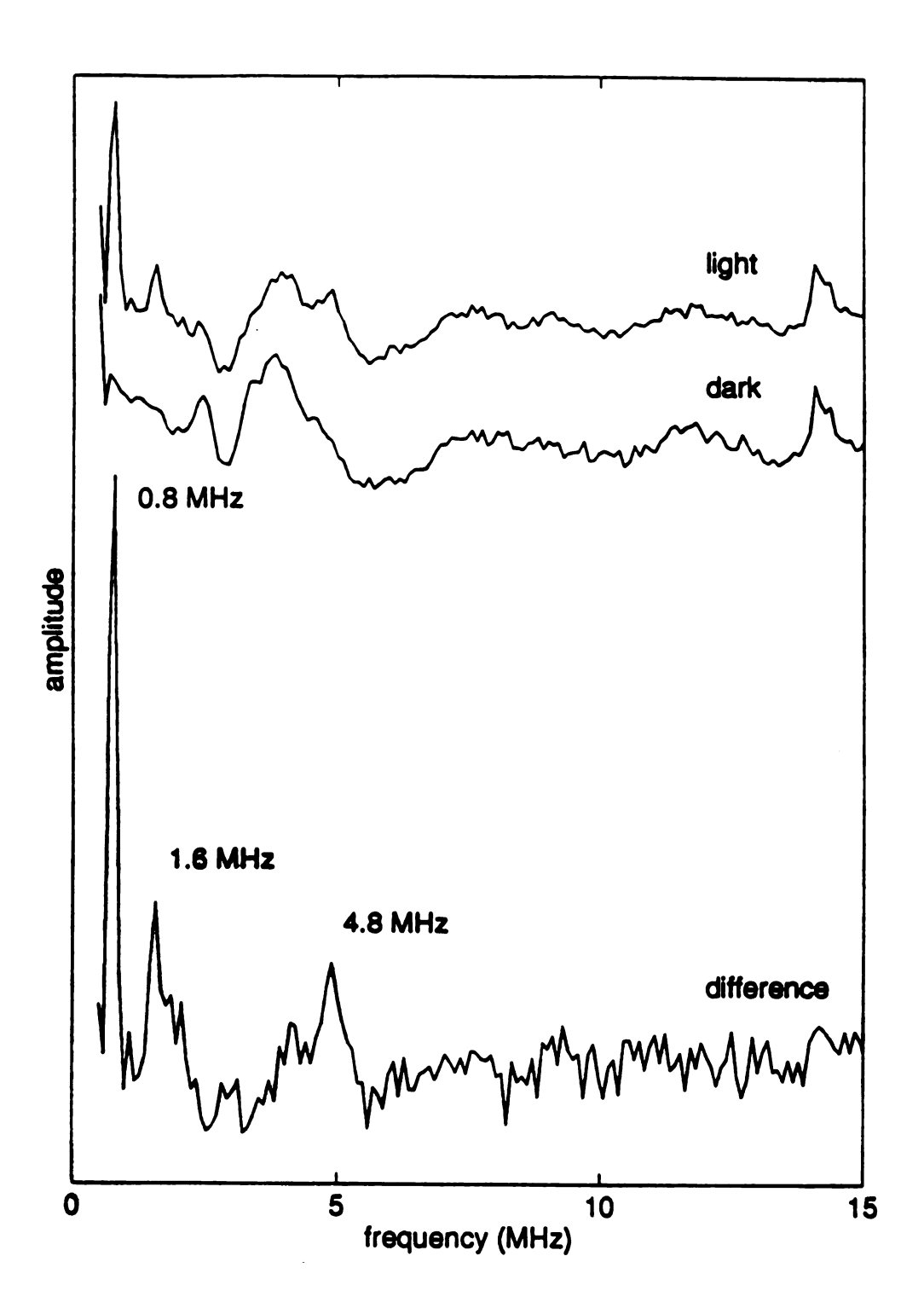


Figure 4.7 The light, dark and difference 3-pulse ESEEM spectra after Fourier transformation of the data of Figure 4.5.

When trapped at S_2 the enzyme is in the state $S_2Q_A^{-..37}$ The quinone, $Q_A^{-.}$, has an EPR signal at g=1.90 and $1.64.^{38}$ The 3-pulse data of Figure 4.6 were collected at 100 G higher field than g=2.0, which is on the edge of the $Q_A^{-.}$ EPR signal. To eliminate the possibility that the peaks in Figure 4.6 arise from $Q_A^{-.}$, ESEEM data were also collected at 100 G lower field than g=2.0 ($g\approx 2.06$). The spectra collected at the two field values were identical, showing that the difference spectrum of Figure 4.6 is solely from the multiline spectrum.

Sr-substituted RCC's were also studied by 3-pulse ESEEM and the light, dark and difference time domain data are shown in Figure 4.7. The ESEEM spectra, after Fourier transformation, are shown in Figure 4.8. The spectra were collected at the same field position as the Ca sample. The difference spectrum, Figure 4.8C, has peaks at 0.8, 1.60 and 4.80 MHz, which are identical to those observed for the Ca samples. Investigation by EPR confirms the presence of the Sr modified multiline.

At a particular magnetic field value and microwave frequency, the position of the peaks in an ESEEM spectrum that arise from a nitrogen, are a function of the hyperfine and quadrupole coupling. These in turn, are dependent on the electronic and geometric structure of the paramagnetic system. For the case of a paramagnetic metal with a non-zero spin ligand, such as the Mn-Nhistidine fragment of the Mn complex of PSII, factors that affect the value of the hyperfine and quadrupole coupling include the metal ligand bond length, covalency of the bond, and the amount of unpaired spin density on the metal. Changes in these parameters will affect the hyperfine coupling, the quadrupole coupling, or both.

For a Mn-N system, as the bond length decreases the dipolar coupling increases since the distance between the nitrogen and the unpaired spin density becomes shorter. However, a shorter metal ligand bond implies an increase in the covalency of the bond. In this case, there is more of the ligand orbitals mixed into the molecular orbital forming the bond. The increase in covalency causes more of the unpaired spin density to reside on

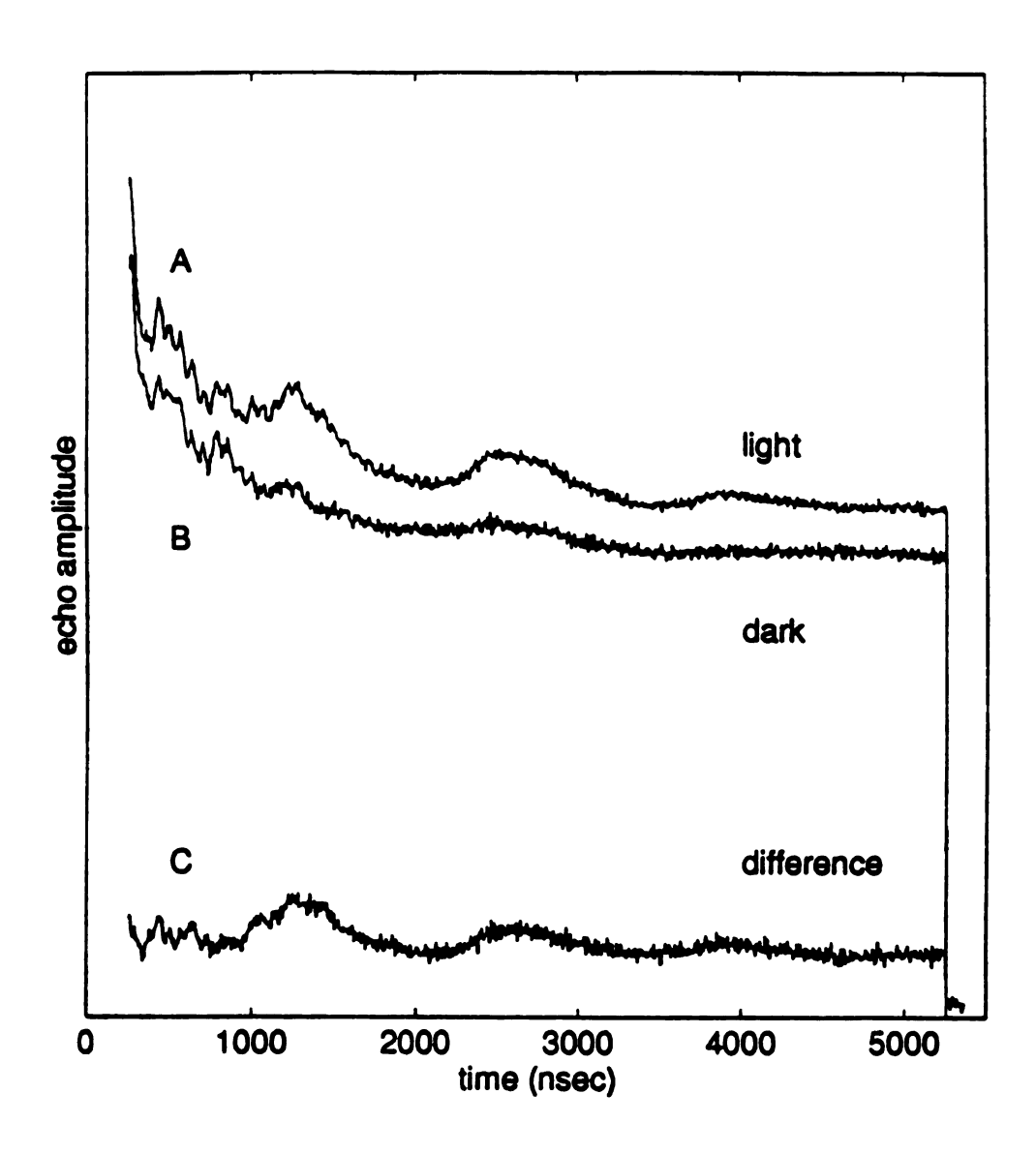


Figure 4.7

3-pulse envelope-echo decay traces for RCC's containing Sr²⁺ (A) after illumination, (B) before illumination and (C) the difference of traces A and B. Conditions: same as in Figure 4.5.

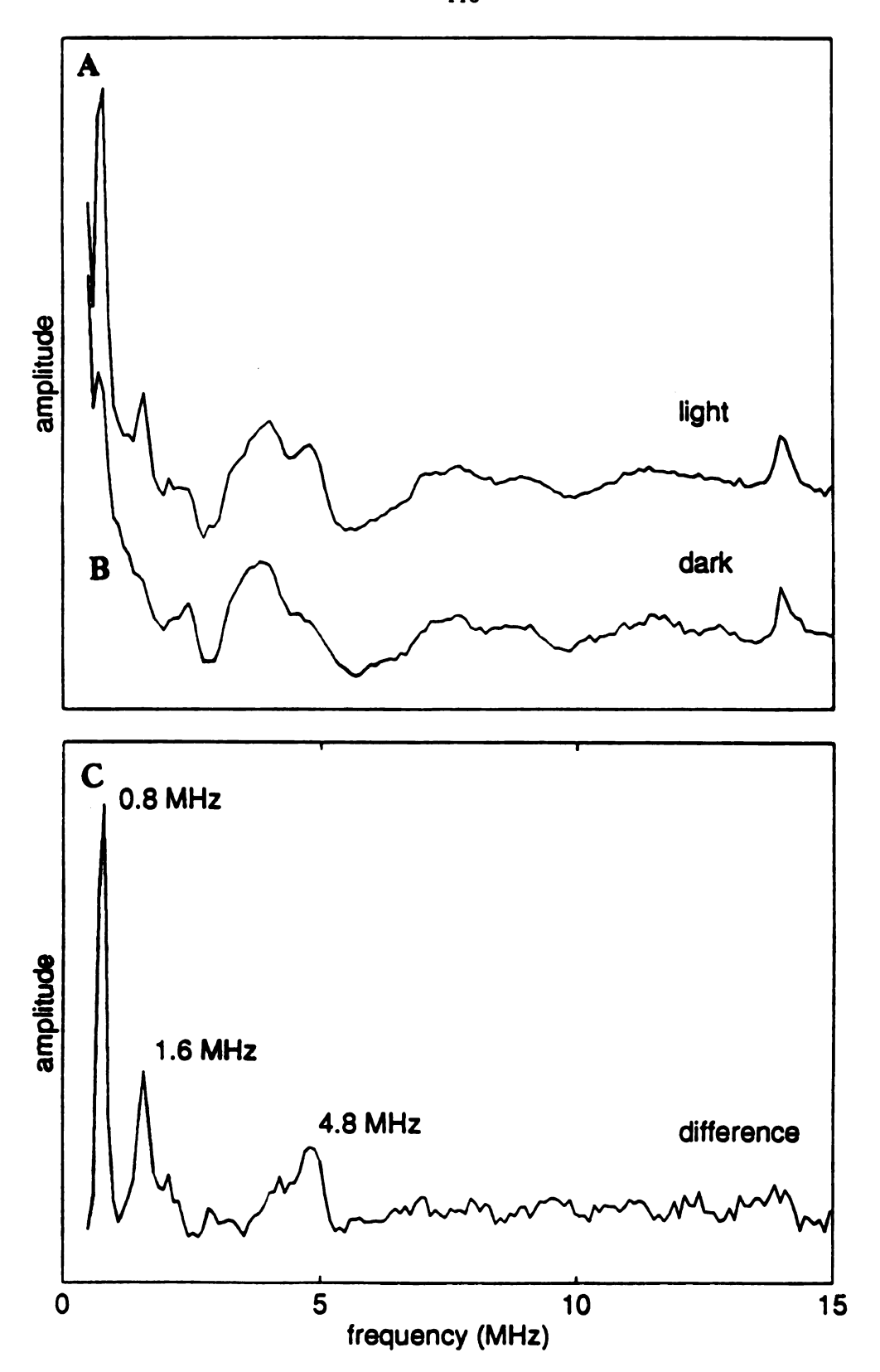


Figure 4.8 The light, dark and difference 3-pulse ESEEM spectra after Fourier transformation of the data of Figure 4.7.

the ligand, increasing the isotropic portion of the nitrogen hyperfine coupling. In addition, the more covalent metal-ligand bond means that the nitrogen lone pair is less associated with the nitrogen and would lower the electron density at the nitrogen, along the direction of the bond. This would lower the quadrupole coupling. If the bond length were to increase, the opposite effects are expected. Changes in the unpaired spin density at the metal will also influence the value of the isotropic and dipolar hyperfine coupling. Structural or electronic changes at the Mn bound to the histidine nitrogen should result in changes in the hyperfine and quadrupole coupling and result in changes in the ESEEM spectrum.

Since the ESEEM spectra for the Ca and Sr containing RCC's are identical, the histidine nitrogen-Mn interaction must not be perturbed substantially when Sr is substituted for Ca. While the above discussion on hyperfine and quadrapole coupling is qualitative, some limits as to how much the Mn-N bond can be changed before it affects the ESEEM spectra can be estimated. Studies of quadrupole coupling of imidazole ligated to Zn and Cd have shown that the metal ligand bond distance can vary by 0.2 Å before significant changes in the quadrupole coupling are observed.³⁹ If it is assumed that the entire unpaired spin is located on the Mn, then, by using the point dipole approximation, the dipolar coupling is 1.05 MHz for a 2.2 Å metal ligand bond distance. If the bond length is shortened by 0.1 Å, the dipolar hyperfine coupling increases to 1.25 MHz. Similar to the quadrupole coupling, shifts of this magnitude would be observable in the ESEEM spectrum. While these calculations are only estimates of the structural changes that may occur, they suggest that between the Ca and Sr RCC's, changes in the histidine nitrogen-Mn interaction are small.

A similar situation has been observed for several Rieske iron-sulfur centers. The iron-sulfur centers consist of an iron dimer with two μ -sulfur ligands connecting the irons. The metals are antiferromagnetically coupled and when the metals are in mixed valence state, +2 and +3, this gives rise to an S=1/2 ground spin state. ENDOR and

ESEEM studies of several Rieske centers has revealed that there are two nitrogen ligands to one of the irons. ^{40,41} The EPR spectrum from the Rieske center of cytochrome b₆f has g values of 1.90 and 2.03. ⁴² When cytochrome b₆f is treated with 2,5-dibromo-3-methyl-5-isopropyl-bezoquinone, the g value of the EPR spectrum shifts from 1.90 to 1.95. ⁴² The ESEEM spectrum, however, is unchanged, showing that the nitrogen ligation to the iron is unchanged. ⁴¹

Assuming that the g-tensor is the same or nearly the same in the Ca and Sr containing RCC samples, the modifications of the mutiline signal must arise from changes in the Mn hyperfine couplings. Previous discussions of the Sr modified multiline have attributed the differences in the mutiline signals to changes in the manganese exchange couplings, resulting from changes in the geometry of the Mn cluster. Simply changing the magnitude of the exchange couplings, however, will not alter the EPR spectrum, but the alterations of the exchange couplings must be large enough to cause a different S=1/2 spin state to be the ground spin state. The Mn tetramer model with C_{2V} symmetry, discussed above, has eight S=1/2 ground spin states, each with a different EPR spectrum. Lowering the symmetry of the Mn tetramer, such that there are four different exchange couplings, still leaves an eight-fold degeneracy in the lowest spin multiplet.

Some insight into the type of stuctural modifications that must occur to alter the exchange couplings can be obtained from previous studies of mixed valence Mn dimers. A series of di- μ_2 -oxo bridged Mn dimers, with the structure [LMn(O)₂MnL], have been synthesized in which the terminal ligands are all nitrogens.²⁴ The complex with L=1,10-phenanthroline, Mn(III,IV)phen, has Mn-nitrogen bond lengths of 2.00-2.09 Å. The μ_2 -oxo bridges are symmetrically placed between the Mn with Mn-O distances of 1.81-1.82 Å. The exchange coupling for this complex is -144 cm⁻¹, giving a S=1/2 ground state.^{24a} For the dimer with L=2,2',2"-triaminoethylamine, Mn(III,IV)tren, the Mn nitrogen bond distances cover the range 2.01-2.34 Å. The μ_2 -oxo bridges are not

symmetrically located between the Mn, with Mn-O bond lengths of 1.77 and 1.85 Å for the Mn(IV) and Mn(III) respectively. The exchange coupling for this complex is -146 cm⁻¹, nearly the same as observed for Mn(III,IV)phen.^{24b}

An estimate of the energy difference between the ground and first excited spin states of the Mn complex giving rise to the multiline signal can be calculated. The multiline signal is unchanged, except for amplitude, when recorded in the temperature range 4-20 K.¹⁴,¹⁷ This implies that the amplitude of the EPR signal from the first excited state is small, if present at all. It is estimated that the population of the first excited state, at 20 K, is no more than 10%. By using the Boltzman distribution, the first excited state is calculated to be 30 cm⁻¹ above the ground state. The approximations made in these calculations are based on the assumption that the relaxation properties are the same for the first excited state as for the ground state. A faster spin lattice relaxation rate for the excited spin state may result in weak EPR intensity, even though there is greater than 10% population of the excited state.

With a difference between spin states of $\approx 30 \text{ cm}^{-1}$, the change in the exchange couplings of the Mn complex upon a change in the ground spin state is expected to be larger than a few wavenumbers. The structural changes that are occurring within the Mn complex must then be larger than the differences in the structures of the Mn dimers discussed above. As the differences in the structures of the Mn dimers are sizeable, a change in ground spin state appears to accompany a significant change in the Mn complex of the OEC, when Sr is substituted for Ca.

A second explanation for the modification of the mutiline signal upon, substituting Sr for Ca in RCC's, is that one or more of the Mn hyperfine coupling constants is changed but without the neccessity of a change in the spin ground state. The Mn hyperfine couplings observed in the Mn tetramer of the OEC are a function of the spin projections multiplied by the hyperfine coupling observed in the monomer, equation 7.4 The isotropic component of the hyperfine coupling to M(III) and Mn (IV) vary

considerably. EPR data from Mn(III) and Mn(IV) monomers and Mn(III,IV) dimers show that the Mn hyperfine coupling is in the range 65-84 G, depending on the ligand environment.⁴³

If the ligand environment near one or more of the Mn is modified upon exchanging Sr for Ca, the hyperfine coupling of these Mn may also change. Relatively small changes in the ligand environment of a Mn can cause changes in the hyperfine coupling (see Chapter 5). This in turn would result in a modified multiline signal. The two Mn(III,IV) dimers, Mn(III,IV) tren and Mn(III,IV) phen, also demonstrate this effect. While both dimers have S=1/2 ground states, similar exchange couplings and similar ligation schemes, the EPR spectra are different. Simulations of the EPR spectra for these two Mn dimers, using only isotropic components, gave best fits with A₁=167 G and A₂=79 G for Mn(III,IV) phen and A₁=161 G and A₂=84 G for Mn(III,IV) tren. ²⁴ The hyperfine coupling of one, two or three Mn in the OEC may have different hyperfine coupling constants when Sr is present. The ESEEM results suggest that the ligand geometry near at least one of the Mn is essentially unperturbed.

EXAFS studies of BBY's and BBY's with Sr substituted for Ca show no difference in the structure of the Mn complex.⁴⁴ The Mn-Mn, Mn-O_{bridge} and Mn-terminal ligands distances are the same or only slightly different between Ca and Sr containing BBY's. The EXAFS data also shows that each Mn has 0.25 Ca, at a distance of 3.3 Å. In the Sr sample, the EXAFS data is different and there are 0.25 Sr per Mn, at a distance of 3.3 Å. The EXAFS data suggest a close proximity of the Ca(Sr) and Mn and a model based on the EXAFS data has the Ca bridged to one Mn by a carboxylato ligand.⁴⁴

The close proximity of Ca and Mn is not without precedence in biological systems, for example, the lectins contain one Ca and one Mn per subunit.⁴⁵ The crystal structure of the lectin concanavolin A has been solved to 1.8 A resolution and shows that the Mn and Ca are bridged by two carboxyl groups from two aspartates.⁴⁶ In this

protein, the Mn-Ca distance is 4.25 Å, significantly greater than the EXAFS determined distance of 3.3 Å seen in PSII. If there is a Mn-Ca distance of 3.3 Å in PSII, this may arise from a single carboxylato bridge between the metals, which may shorten the metalmetal distance.

Compilation of the ESEEM, EPR and EXAFS results shows that the effect on the structure of the Mn complex, of substituting Ca for Sr in PSII, is minimal. The slightly larger ionic radii of Sr over Ca, 1.13 Å versus 0.99 Å, appears to cause modification of the structure of the Ca binding site.³⁰ This structural change is transmitted to the Mn complex. The structural perturbation of the Mn complex may only represent effects on the terminal ligands to the Mn, which would be consistent with the EXAFS results. The small changes in the terminal ligands may cause a change in the Mn hyperfine coupling constants, which, in turn, result in the observed modified multiline signal. While a rearrangement of the spin states may occur upon substituting Sr for Ca, the results discussed above show that this need not happen and most likely the same ground spin state is present regardless of which ion is bound.

LIST OF REFERENCES

- 1) Debus, R. Biochim. Biophys. Acta, 1992, 1102, 269.
- 2) a) Kok, B., Forbush, B. and McGloin, M.P. Photochem. Photobiol., 1970, 11, 457. b) Forbush, B., Kok, B. and McGloin, M.P. Photochem. Photobiol., 1971, 14, 307.
- 3) Yocum, C.F., Yerkes, C.T., Blankenship, R.E., Sharp, R.R. and Babcock, G.T. Proc. Natl. Acad. Sci. USA, 1981, 78, 7501.
- a) Dismukes, G.C. and Siderer, Y. FEBS Lett., 1980, 121, 78. b)Dismukes, G.C. and Siderer, Y. Proc. Natl. Acad. Sci. USA, 1981, 78, 274.
- 5) Brudvig, G.W., Casey, J.L. and Sauer, K. Biochim. Biophys. Acta, 1983, 723, 366.
- 6) Hansson, O., Aasa, R. and Vanngard, T. Biophys. J., 1987, 51, 825.
- 7) Cooper, S.R., Dismukes, G.C., Klein, M.P. and Calvin, M. J. Am. Chem. Soc., 1978, 100, 7248.
- 8) Kambe, K. J. Phys. Soc. Jpn., 1950, 5, 48.
- 9) Sinn, E. Coordin. Chem. Rev., 1970, 5, 313.
- 10) Brudvig, G.W. Advanced EPR: Applications in Biology and Biochemistry, (Hoff, A.J., ed.), Elsevier, Amsterdam, 1989, pp. 839-863.
- 11) Sands, R.H. and Dunham, W.R. Quarterly Reviews of Biophysics 7, 1975, 4,443.
- 12) Abragam, A. and Bleaney, B. Electron Paramagnetic Resonance of Transition Ions, Dover Publications, New York, 1970.
- Dismukes, G.C. Mixed Valency Systems: Applications in Chemistry, Physics and Biology, (Prassides, K., ed.), Kluwer Academic Publishers, 1990.

- 14) Britt, R.D., Sauer, K. and Klein, M. Biochim. Biophys. Acta. 1992, 1250, 765.
- 15) Zimmerman, J.-L. and Rutherford, A.W. Biochemistry, 1986, 25, 4609.
- 16) Casey, J.L. and Sauer, K. Biochim. Biophys. Acta, 1984, 767, 21.
- a) DePaula, J.C., Innes, J.B. and Brudvig, G.W. Biochemistry, 1985, 24, 8114.
 b) DePaula, J.C., Beck, W.F. and Brudvig, G. W. J. Am Chem. Soc., 1986, 108, 4002 (erratum, J. Am. Chem. Soc. 109, 6565).
- 18 Kim, D.H., Britt, R.D., Klein, M.P. and Sauer, K. Biochemistry, 1992, 31, 541.
- 19) Kim, D.H., Britt, R.D., Klein, M.P. and Sauer, K. J. Am. Chem. Soc.,1990, 112, 9389.
- 20) Palmer, G. Electron Paramagnetic Resonance in: Methods for Determining Metal Ion Environments in Proteins (Darnell, D.W. and Wilkins, R.G., eds.), Elsevier, North-Holland, 1980, 153.
- 21) Haddy, A., Dunham. W.R., Sands, R.H. and Aasa, R. Biochin. Biophys. Acta, 1992, 1099, 25.
- 22) Koulougliotis, D., Hirsch, D.J. and Brudvig, G.W. J. Am. Chem. Soc., 1992, 114, 8322.
- a) Penner-Hahn, J.E., Fronko, R.M., Pecoraro, V.L., Yocum, C.F., Betts, S.D. and Bowlby, N.R. J. Am. Chem. Soc., 1990, 112, 2549. b) Guiles, R.D., Zimmerman, J.-L., McDermott, A.E., Yachandra, V.K., Cole, J.L., Desheimer, S. L., Britt, R.D., Wieghardt, K., Bossek, U., Sauer, K. and Klein, M.P. Biochemistry 1990, 29, 471. c) Guiles, R.D., Yachandra, V.K., McDermott, A.E., Cole, J.L., Desheimer, S.L., Britt, R.D., Sauer, K. and Klein, M.P. Biochemistry, 1990, 29,486.
- a) Stebler, M., Ludi, A. and Burgi, H.-B. Inorg. Chem, 1986, 25, 4743.
 b) Weighardt, K., Bossek, U., Zsolnai, L., Huttner, G., Blondin, G., Girerd, J.-J., and Babonneau, F. J. Chem. Soc, Chem. Commun., 1987 651. c) Plaskin, P.M., Stoufer, R.C., Mathew, M. and Palenik, G.J. J. Am. Chem. Soc., 1972, 94, 2122.
 d) Hagen, K.S., Armstrong, W.H and Hope, H. Inorg. Chem., 1988, 27, 967.
- 25) Christou, G. Acc. Chem. Res., 1989, 22, 328.
- Sauer, K., Yachandra, V.K., Britt, R.D. and Klein, M.P. in Manganese Redox Enzymes (Pecoraro, V., ed.), VCH Publishers, New York, 1992,141.

- a) Haddy, A., Aasa, R. and Andreasson, L.-E. Biochemistry, 1989, 28, 6954.
 b) Yachandra, V.K., Guiles, R.D., Sauer, K. and Klein, M.P. Biochim. Biophys. Acta, 1986, 850, 333.
- DeRose, V.J., Yachandra, V.K., McDermott, A.E., Britt, R.D., Sauer, K. and Klein, M.P. Biochemistry, 1991, 30, 1335.
- Tang, X.-S., Diner, B.A., Larsen, B.S., Gilchrist, M.L., Lorigan, G.A. and Britt, R.D. Proc. Natl. Acad. Sci. USA, 1993, in press.
- 30) Yocum, C.F. Biochim. Biophys. Acta, 1991, 1059, 1.
- 31) Ghanotakis, D.F., Babcock, G.T. and Yocum, C.F. FEBS Lett. 1984, 167, 127.
- 32) Boussac, A. and Rutherford, A.W. Biochemistry, 1988, 27, 3476.
- a) Ghanotakis, D.F. and Yocum, C.F. FEBS Lett., 1986, 197, 244. b) Ghanotakis, D.F., Demetriou, D.M. and Youcm, C.F. Biochim. Biophys. Acta, 1987, 891, 15.
- 34) Boussac, A. and Rutherford, A.W. FEBS Lett., 1988, 236, 432.
- 35) Britt, R.D., Zimmerman, J.-L., Sauer, K. and Klein, M.P. J. Am. Chem. Soc., 1989, 111, 3522.
- Mims, W.B. and Peisach, J. Electron Spin Echo Spectroscopy and the Study of Metalloproteins in Biological Magnetic Resonance, Vol 3 (Berliner, L.J. and Reuben, J.,eds.) Plenum Press, New York, 1981, 213.
- 37) Miller, A.F. and Brudvig, G.W. Biochim. Biophys. Acta, 1991, 1056, 1.
- 38) Nugent, J.H.A., Diner, B.A. and Evans, M.C.W. FEBS Lett., 1981, 124, 241.
- 39) Ashby, C.I.H., Cheng, C.P. and Brown, T.L. J. Am. Chem. Soc., 1978, 100, 6058.
- Gurbiel, R.J., Batie, C.J., Sivarja, M., True, A.E., Fee, J.A., Hoffman, B.M. and Ballou, D.P. Biochemistry, 1989, 28, 4861.
- 41) Britt, R.D., Sauer, K., Klein, M.P., Knaff, D.B., Kriauciunas, Yu, C.-A., Yu, L., and Malkin, R. Biochemistry, 1991, 30, 1892.
- 42) Malkin, R. Biochemistry, 1982, 21, 2945.
- a) Diril, H., Chang, H.-R., Niges, M.J., Zhang, X., Potenza, J.A., Schugar, H.J. Isied, S.S. and Hendrickson, D.N. J. Am. Chem. Soc., 1989, 111, 5102.
 b) Bonvoisin, J., Blondin, G., Girerd, J.-J. and Zimmerman, J.-L. Biophys. J., 1992, 61, 1076.

- 44) Yachandra, V.K., DeRose, V.J., Latimer, M.J., Mukerji, I., Sauer, K. and Klein, M.P. Science, 1993, 260, 675.
- Goldstein, I.J. and Poretz, R.D. in The Lectins: Properties, Functions, and Applications in Biology and Medicine (Liener, I.E., Sharon, N. and Goldstein, I. J., eds.) Academic Press, Orlando, 1986, 33.
- 46) Hardman, K.D., Agarwal, R.C. and Freiser, M.J. J. Mol. Biol., 1982, 157, 69.
- 47) Rutherford, A.W. Biochim. Biophys. Acta, 1985, 807, 189.
- 48) Beck, W.F. and Brudvig, G.W. Chem. Scripta, 1988, 28A, 93.
- 49) Berthold, D., Babcock, G.T. and Yocum, C.F. FEBS Lett., 1981, 134, 231.

CHAPTER 5

EPR AND ESEEM CHARACTERIZATION OF CYTOCHROME c OXIDASE FROM Rh. Sphaeroides

Introduction

The respiratory chain of aerobic organisms, all plants and animals (eukaryotes) and some bacteria (prokaryotes), provide much of the energy used for life sustaining processes. This chain consists of four membrane integral enzyme complexes. For eukaryotes these enzymes are located in the inner membrane of the mitochondria and for prokaryotes they are located in the cell membrane. These enzymes-nicotinamide adenine dinucleotide(NADH) dehydrogenase, succinate dehydrogenase, cytochrome bc1 complex and cytochrome c oxidase-facilitate the transfer of electrons from the reducing species NADH, E=-320 mV, to the terminal oxidant, oxygen, E=+800mV.1 The electrons are shuttled between the membranous enzymes by quinones and the soluble heme containing protein cytochrome c. The electrons are transferred between approximately 20 different redox components between NADH and O2. With a span of +1.1 V between NADH and O₂ the eventual transfer of electrons between these two species is exothermic with the free energy used to generate and sustain a proton concentration gradient across the membrane. 1 The enzymes take up protons from the intermembrane space (inside) of the membrane and deposit them in the matrix (outside) side of the membrane, this process is referred to as proton translocation or proton pumping.² The proton gradient, or electrochemical potential, that is generated is used by the enzyme ATPase to synthesize ATP which is used in other metabolic processes.

The terminal enzyme in the respiratory chain is cytochrome c oxidase, which catalyzes the reduction of oxygen to water, equation 1.

$$O_2 + 4e^- + 4H^+ \longrightarrow 2 H_2O$$
 (1)

This enzyme accounts for the use of approximately 90% of the oxygen uptake of aerobic systems. The reaction of equation 1 is exergonic and the free energy is used in proton translocation against the proton gradient.² In addition to the four protons consumed to form water in equation 1, another four protons are pumped across the membrane to give a change of 2H+/e- between the inside and the outside of the membrane.² In the eukaryote systems, the source of electrons in equation 1 is cytochrome c (cyt c), a small soluable protein that contains a single c-type heme. In some prokaryotes cyt c is the electron donor, however, in a sub-class of terminal oxidases a quinol acts as the electron donor.

While much of the work on oxidase has been carried out on mammalian systems, in particular enzyme isolated from beef hearts, more recently oxidase from bacterial systems has also been characterized. The bacterial oxidases studied to date are functionally homologous to the mammalian system, catalyzing oxygen reduction as well as pumping protons.³ Studies of these systems by spectroscopic techniques, including optical, Raman and EPR, show nearly identical results as seen for the mammalian oxidases.⁴ The bacterial oxidases thus appear to be both functionally and structurally homologous to their mammalian cousins. The bacterial oxidases, however, are much simpler being constructed of only three subunits as compared to 13 for the mammalian systems.³ The three subunits of the bacterial oxidases show a strong sequence homology to the three largest subunits of the mammalian oxidase.³

It is well established that the functional unit of the enzyme contains four redox active metal centers. Two of these are A type hemes labeled cytochrome a and a3. The enzyme also contains two coppers labelled Cu_A and Cu_B. The four metals can be

divided into two iron-copper pairs based on metal proximity and function. The pairs consist of cyt a-Cu_A, involved in electron transfer from cyt c, and cyt a₃-Cu_B the site of oxygen reduction.

In the oxidized form of the enzyme, with all four metals oxidized, Cu_A functions as the entry point of electrons into the enzyme as it is the metal reduced by cyt c.5 Cu_A and cyt a are in rapid redox equilibrium resulting in electron transfer to cyt a.6 This rapid equilibrium is consistent with EPR saturation measurements, which suggest that these two metals are close, within 8-13 Å to each other.7 Cyt a is then the site of electron transfer to the second iron-copper pair.

The cyt a₃-Cu_B pair, referred to as the binuclear center, while identical in makeup to the previous metal pair, is quite different in both metal proximity and function. In the oxidized form of the enzyme, cyt a₃ and Cu_B are paramagnetic and should be observable by EPR but neither is detected by this technique. The explanation for these results is antiferromagnetic coupling between the high spin iron (S=5/2) and the copper (S=1/2) to yield a S=2 center, which is not detected by EPR.8 This antiferromagnetic coupling is accomplished through a covalent bond and presupposes a common ligand between the two metals which has not yet been determined. This common ligand between the metals would suggest that the metals are closer together than the cyt a-CuA pair and estimates have placed this distance at <5 Å.9

Upon reduction of the binuclear center, oxygen is bound to the binuclear center and reduced to water and the electrons needed for this reduction are transferred to the binuclear center from cyt a. 10 The mechanism of oxygen reduction is not completely understood but several of the intermediates of the reaction have been detected and from these results a comprehensive mechanism has been proposed. 11 The mechanism invokes both cyt a3 and CuB as catalytic sites as would be expected from their close proximity and magnetic coupling. While the mechanism of oxygen reduction is unfolding the

mechanism and sites of proton pumping have proved elusive and are currently not well understood.

In addition to the function of the metal cofactors in oxidase, many of the ligands to the metals have also been determined. These results were obtained from the study of oxidases from several different systems and in many cases, systems where isotopic substitution could be accomplished were used. This isotopic substitution, in conjunction with a battery of spectroscopic techniques, allows a more definitive identification of the metal ligands. The predominant techniques used to determine the ligands to the four metals include optical, Raman, EPR, ENDOR and XAFS. For the two copper sites the coordination geometry is unknown and not all isotopic substitutions are possible, so these sites have not been completely characterized.

Several lines of evidence, including EPR, Raman and magnetic circular dichroism, have suggested that the two axial ligands to cyt a come from nitrogen. 12 Direct observation of the putative nitrogen ligands was detected by ENDOR. 13 Identification of the source of the ligands as histidines was accomplished by incorporation of isotopically substituted histidine into the enzyme and the observation of the appropriate shifts in the ENDOR spectra. 13 EPR studies of oxidase with NO bound to cyt a3 revealed that the proximal ligand to the heme is also a nitrogen and again isotopic substitution has shown that the ligand is a histidine. 14 The studies of cyt a3 were done on the reduced form of the enzyme where cyt a3 is six coordinate. 14

Magnetic resonance techniques have also proven to be quite valuable for studying the copper sites. The EPR spectrum of Cu_A is quite different from that observed for common inorganic copper complexes, the anisotropy in g is smaller and the Cu hyperfine coupling is smaller. In the X-band EPR spectrum of Cu_A the Cu hyperfine coupling is smaller than the linewidth and is thus not detected. The spectrum does show a strong similarity to the blue copper proteins which have two nitrogen ligands coming from histidine as well as two sulfur ligands coming from a cysteine and a methionine.¹⁵

ENDOR studies of Cu_A have revealed that there is at least one histidine and one cysteine ligand. ¹⁶ EXAFS studies suggest that the coordination sphere is completed with a second histidine and a cysteine or chloride. ¹⁷ While Cu_B is normally EPR silent, as discussed above, the enzyme can be trapped in a transient state where Cu_B is both oxidized and not magnetically coupled to cyt a₃. ¹⁸ The EPR spectrum is substantially different from that observed for Cu_A. ENDOR studies of Cu_B show that the metal contains three nitrogen ligands. ¹⁹ The EXAFS result are consistent with the ENDOR data and suggest three nitrogen ligands along with one sulfur or chloride ligand to Cu_B. ¹⁷

Along with elucidating the ligand environment of the redox active metals of oxidase their location within the protein has also been determined. Much of these results come from the bacterial oxidases due to their much simpler structure. The oxidase from *P. denitrificans* has been isolated as a two subunit enzyme which shows high activity and has EPR and optical spectra consistent with both coppers and both hemes being present.²⁰ A digestive study of this two subunit enzyme showed that subunit I contains the two hemes and a copper, which is assumed to be CuB since it is EPR silent.²¹ Subunit II must then be the site of CuA ligation. Comparison of protein sequences of subunit II from several cyt c type oxidases show that there are two histidines and two cysteines that are completely conserved. A copper binding site formed from these four conserved amino acids is consistent with the spectroscopic studies of CuA discussed above.²²

Recently, the description of Cu_A as a mononuclear site has come into question. This uncertainty stems from results that show spectroscopic similarity between the copper A site in nitrous oxide reductase (N₂OR) and the Cu_A site in oxidase⁵⁵. There is strong spectroscopic evidence that the copper A site in N₂OR is binuclear⁵⁵. A similarity in the copper binding sites of these two enzymes is also supported from comparison of the protein sequences of the copper A binding protein of N₂OR and subunit II of oxidase. A portion of the N₂OR sequence has two histidines and two cysteines which aligns with the

portion of oxidase subunit II that contains two histidines and two cysteines that are strictly conserved⁵⁶. The two proteins then have the same building blocks in which to contruct a binuclear copper binding site. These results suggest that the CuA site in oxidase may be a binuclear center.

Besides the four redox active metals discussed above the beef heart enzyme also contains one zinc and one magnesium.²³ These additional metals are an integral part of the enzyme as dialysis against a series of chelators over the pH range 6-9.5 does not remove the metals.²³ However, little is known about the location of these metal sites within the enzyme. Subunit VIa has been suggested to bind a portion of the zinc associated with oxidase as trypsin digestion studies of beef heart oxidase result in the digestion of subunit VIa and loss of one-half the bound zinc.²⁴ This subunit also has four sulfurs, enough to fill the coordination sphere of zinc which is reported to be three sulfurs and one nitrogen or oxygen.²⁴ The location of the site where the other half of the zinc and the magnesium are bound has not been determined. The function of these metals is not understood but have been suggested to play a structural role within the enzyme.

Whereas, the zinc and magnesium are present in stochiometric quantities in the mammalian enzyme, the results are quite different for the bacterial oxidases. A metal analysis of purified oxidase from *P. denitrificans* shows sub-stochiometric quantities of Zn (0.48+0.23) and Mn (0.18+0.04) and nearly stochiometric quantities of Mg (1.05+0.47) per enzyme.²² The quantity of Zn and Mg varied considerably between sample preparations resulting in the large error in the reported stochiometries.²² It is unclear from the data obtained so far as to whether there are two binding sites, as in the mammalian systems, or only one. What is clear is that the binding site(s) is not as discriminate as in the mammalian system, as evidenced by the observation of sub-stochiometric quantities of several of the metals. In addition to oxidase from *P. denitrificans*, substochiometric Mn has been observed in several other bacterial oxidases but has not been detected in the mammalian or bacterial quinol oxidases.²⁵

Unlike Mg or Zn, Mn in its +2 oxidation state is EPR detectable and thus allows a simple method of determining when Mn is present in the enzyme. Earlier work has shown that the Mn is not adventitiously bound to the *P. denitrificans* oxidase as washing the enzyme with 5mM EDTA does not remove any additional Mn as determined by using EPR.26 Previous results have shown the quantity of bound Mn, however, can be lowered by reducing the concentration of Mn in the cells growth medium. Under normal growth conditions there is 0.2 Mn per enzyme, and for cells grown in 60-fold less Mn, there is no EPR detectable Mn in the enzyme.26 The activity of the enzyme with or without Mn is nearly identical.26 Since Mn has been detected in the *P. denitrificans* oxidase this metal must be associated with one or both of the two subunits, subunit I and subunit II, forming the catalytic core of the enzyme.

The Mn is not redox active in oxidase at moderate potential, as the EPR signal arising from the +2 oxidation state is present whether the enzyme is fully oxidized or fully reduced. The EPR spectrum, however, does undergo a small change between these two forms of the enzyme. Reductive titrations of the enzyme have shown that the change in the EPR spectrum of Mn²⁺ correlates with the addition of two electrons to the enzyme.²⁷ The first electron added to the enzyme reduces cyt a while the second reduces Cu_A. The change in the EPR spectrum of Mn is the result of a structural change in the enzyme that perturbs the geometry of the Mn binding site.²⁷

In order to understand better the mechanism of oxygen reduction and proton translocation of oxidase, a complete description of its structure would be invaluable. To date, crystals of the enzyme with high enough resolution to determine tertiary structure have not been obtained. However, significant insight into the enzyme's structure has been obtained with biochemical and spectroscopic techniques as discussed above. A clearer picture of the structure of this protein, in particular the structure near the metal sites, can be obtained from knowing the actual amino acids that are ligands to the metals. This can be accomplished by using the technique of site-directed mutagenesis,

that is, the substitution of one amino acid for another at a particular site in the enzyme. This technique is carried out in bacteria because of the simpler genetic make-up of these systems and the ability for rapid large scale replication of the modified system. The bacterial system *Rb. sphaeroides*, discussed in this text, was chosen for the study of cytochrome oxidase because it contains a cytochrome c oxidase and previous genetic manipulations have been carried out on this bacteria in the study of the *bc*1 complex and the photosynthetic reaction center.²⁸

The application of directed mutagenesis to subunit I has already proven very valuable in identifying the ligands to the three metal centers cyt a, cyt a3 and CuB that are ligated to this subunit. These three metals would have an aggregate of six histidines. Comparison of the protein sequence of subunit I from various species reveal six strictly conserved histidines.²⁹ Raman and IR studies of oxidase enzyme that has been mutated at these six conserved histidines leads to the assignments of his102 and his421 as the ligands to cyt a, his419 as the ligand to cyt a3 and his333, his334 and his284 as the ligands to CuB.³⁰ Additional mutagenesis studies are underway to obtain a better understanding of the structure and function of oxidase.

The work on cytochrome c oxidase presented here has two main focuses. First, a comprehensive EPR characterization of oxidase from *Rb. sphaeroides* was undertaken to determine if the enzyme is spectroscopically, and therefore most likely structurally, homologous to other well studied oxidases. The mutagenesis results discussed above have given valuable insight into the protein environment near the metal centers in subunit I and spectroscopic identity with similar oxidases isolated from other systems would allow these results to be applicable across this family of enzymes.

Second, is to gain insight into the one or more binding sites in oxidase that bind Mn. Continues-wave and pulsed-EPR was used to elucidate information such as the symmetry of the metal ligation, the magnitude of the structural changes at the metal

binding site upon oxidation change of the enzyme and the determination of ligands to the Mn.

Complementing the spectroscopic studies is the application of directed mutagenesis in an effort to identify the specific ligands to Mn. Knowing the ligands to the metal and their position in the protein will aid in the further characterization of the structure of the enzyme as well as provide insight into the role of the tightly bound Mn.

Lastly, efforts were made to determine if th metal binding sites are specific for the divalent metals bound to oxidase or if the metals are competitive with each other for the one or more metal binding sites. To this end *Rb. sphaeroides* cells were grown in a series of media containing different concentrations of Mn, Zn and Mg. The quantity of Mn bound to the enzyme was monitored by EPR.

The remainder of this chapter is divided into two sections. The first part discusses the spectroscopic characterization of oxidase purified from *Rb. sphaeroides* while the second focuses on the studies of the tightly bound Mn. Each section will contain a discussion of the theory and application of EPR, beyond that discussed in chapter 2, that is applicable to the system under study.

Materials and Methods

Cytochrome c oxidase was purfied from *Rb. sphaeroides* by a procedure decribed previously.⁴³ The enzyme is in a buffer containing 0.2% lauryl maltoside, 10 mM KH₂PO₄ and 250 mM KCl at pH=7.2. In addition, to remove any adventitious Mn, EDTA was added to the sample to a final concentration of 50 mM. To remove the EDTA the enzyme was washed with a 50 mM KH₂PO₄ solution at pH=7.2 using a Centricon 30 device from Amicon. After this wash, the enzyme was collected and stored at -80 °C until studied by EPR in a buffer containing 1% lauryl maltoside, 50 mM KH₂PO₄ and 2.5 mM KCl at pH=7.2. The oxidase mutants were contructed as described elsewhere and

were purified by the same procedure as the wild type enzyme.³⁰ The reduced enzyme was generated by adding an aqueous solution of NaS₂O₄ to a final concentration of 10 mM and incubating the sample for 10 minutes at 4 °C. The sample was then frozen and stored at 77K. The concentration of oxidase was in the range 30-100 μ M. Enzyme concentrations were determined from the aborbane at 605 nM by using an extinction coefficient of 40 mM⁻¹ cm⁻¹. Samples at the higher concentrations were used for the pulsed EPR experiments. For EPR experiments approximately 200 μ L of sample was loaded into a standard 4mm O.D. quartz EPR tube and frozen and stored at 77K. Sample size of approximately 75 μ L were used for the pulsed EPR experiments.

X-band EPR spectra were recorded on a Bruker ER200 series spectrometer using a TE₁₀₂ cavity. Sample temperature of 110 K was achieved using flowing N₂ gas that was colled with LN₂. The LN₂ dewar was home built based on the Bruker design. Rapid N₂ flow rates were used to minimize thermal gradients in the sample. For data collected at 10K an Oxford ESR-9 continues LHe flow cryostat was used. The g-values were determined by direct measurement of the magnetic field and microwave frequency. For these measurements a Bruker ER035M NMR gaussmeter and an EIP frequency counter were used.

The pulsed EPR experiments were performed on a home built spectrometer located in the laboratory of Prof. J. McCracken, Michigan State University and described elsewhere. The ESEEM data were collected by using the three pulse, stimulated echo technique. The time, T, between the second and third pulses was 40 nsec for all experiments. The three pulses all had the same width (15 nsec) and power. The data were collected at 2K by continues pumping on the LHe. The aquisition rate was 30 Hz with each time point being the average of 30 events. The interval between data points was 5 ns. The remainder of the experimental conditions used are listed in the figure captions. The ESEEM spectra were obtained by Fourier transfer using the dead-time recontruction technique of Mims. 83

Mn spin count:

The bound Mn was released from the enzyme by treatment with 1N HCl. The sample was allowed to incubate for 4 hours and then centrifuged to remove the protein material. The supernatent, containing the Mn, was removed. The residual protein material was incubated overnight in 1N HCl, centrifuged, and the supernatent recovered. The two supernatents were not combined and the EPR spectrum of each was recorded. A series of Mn standards, in the concentration range 15-125 M, of MnSO4 in 1N HCl were made and the EPR spectrum was recorded. The EPR spectrum of the two oxidases sample supernatents were also aquired. These spectra were recorded at ambient temperature using a flat cell sample holder with a volume of 250 L and a Varian TM₀₀₁ cavity. The amplitude of the third peak from the low field side was plotted versus [Mn] to establish a calibration curve. The amplitudes for the two oxidase samples were summed and compared to the calibration curve to determine its [Mn]. From the initial volume and concentration of the untreated the stociometry of bound Mn was determined.

Mn treated oxidase sample

The following treatment was carried out with the oxidase sample that had been purified from cells grown in the presence of 0.5 M Mn. Mn was added to the sample to a final [Mn] of 1mM. The sample was allowed to incubate for 15 minutes and then EDTA was added to 50 mM. The EDTA was washed out by the procedure discussed above. In addition the sample was passed over a 1 ml Sephedex G-50 column. The sample was washed off the column with a buffer containing 0.2% lauryl maltoside and 50 mM KH₂PO₄ at pH=7.2 which is also the final buffer for this sample.

Model building

Protein model building was done using the program Hyperchem from Autodesk on a Silicon Graphics Iris Indigo workstation. The models used all L-conformers of the amino acids.

Results and Discussion

EPR Characterization of Rb. sphaeroides oxidase

EPR of Low Spin Ferric Hemes

For low spin ferric hemes the iron is d^5 giving a S=1/2 system which is detectable by EPR. In this discussion of low spin hemes reference will always be made to the +3 oxidation state of the iron as the +2 oxidation state is S=0 or S=2 neither of which is detectable by EPR. The low spin hemes have a rhombic g-tensor with principal values of approximately g_z =3.0, g_y =2.2 and g_x =1.5, giving rise to peaks in the EPR spectrum at approximately 2200, 2800 and 4500 gauss respectively at X-band. EPR studies of single crystals of hemes have shown that the direction of g_x and g_y are in the heme plane while gz is nearly normal to the plane.31

In the low spin hemes the iron is six coordinate with four equatorial ligands provided by the nitrogens of the macrocycle and the two axial ligands provided by the protein. Since the g-tensor is rhombic, the symmetry at the iron is lower than tetrahedral. The energy level diagram for a low spin heme is shown in Figure 1 along with the orbital occupancy. The d_{XZ} and d_{YZ} are split apart due to the unequal interaction between these orbitals and the axial ligands. Application of an external magnetic field will split the d_{YZ}

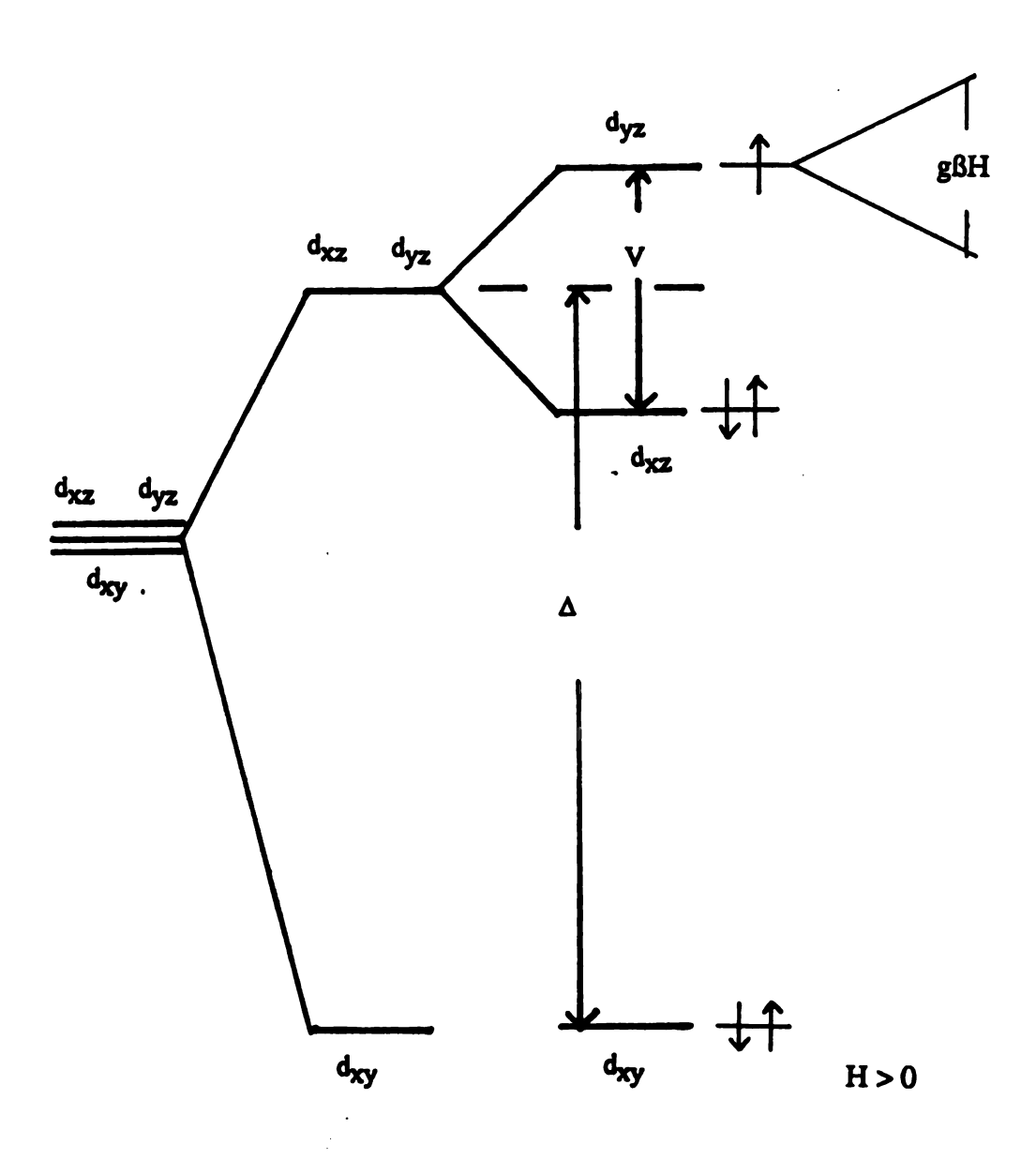


Figure 5.1 Energy level diagram for the t_{2g} d orbitals in a site with rhombic distortions and in the presence of an applied magnetic field.

orbital, which contains the unpaired electron, with the magnitude of the splitting described by equation 2, Figure 1.

$$hv = g\beta H$$
 (2)

As discussed above the value of g is different for the three principal directions of the g-tensor axis system. The g values deviate from the spin only g-value of 2.0023 due to the coupling of spin and orbital angular momentum.³² This is a result of the fact that the d_{yz} orbital is a linear combination of the d_{yz} , d_{xz} and d_{xy} orbitals allowing a mixing of the spin and orbital angular momentum. The mixing is small, however, with only small amounts amount of the d_{xz} and d_{xy} orbitals mixing with the d_{yz} orbital.³²

With methods determined by Griffith³³ and Kotani³⁴ and lucidly described by Weissbluth³² the relative energies of the t_{2g} set of d orbitals can be calculated from the g values observed by EPR. This is accomplished by using equations 3 and 4,

$$V = g_X / (g_z + g_y) + g_y / (g_z - g_x)$$
 (3)

$$\Delta = g_X / (g_Z + g_y) + g_Z / (g_y - g_X) - V/2$$
 (4)

where Δ and V are labeled the tetragonal and rhombic splittings shown in Figure 1.

From crystal field theory it is expected that as the strength of the ligands to the iron change the relative energies of the d-orbitals will change. This in turn affects the mixing of the orbitals, which affects the mixing of spin and orbital angular momentum and changes the g values. This can also be seen from equations 3 and 4 where changes in ligand strength will change Δ and V. Changes in the strength of a ligand is then detected as a change in the g values

Peisach and Blumberg used these equations to determine the tetragonality (Δ), a measure of ligand strength, and rhombicity (V/Δ), a geometric factor for a large number of low spin hemes.³⁵ Plotting V/Δ vs Δ revealed that systems with similar axial ligands

to the iron fall into similar regions of the plot. Calculation of V/Δ and Δ thus allows determination of the axial ligands for the system under study.

 $Cu_{\mathbf{A}}$

The EPR spectrum of oxidized oxidase recorded at 10 K is shown in Figure 2. Observable are the signals from cyt a, Cu_A and Mn. In addition, there is a signal at g=2.19 of unknown origin. Figure 2 B and C were recorded at 108 K and show an expanded g=2 region of the spectrum for Rb. sphaeroides and beef heart, respectively. At this higher temperature the spectrum for cyt a is not observable due to its fast spin relaxation. The spectrum from beef heart shows the EPR signal for Cu_A, while the spectrum for the bacterial samples shows Cu_A and manganese concurrently. The peaks identified at g=2.15, 1.93 and 1.88 are from the Mn signal. Samples of Rb. sphaeroides oxidase that contain no bound Mn show clearly that the Cu_A signal is the same as that detected in the beef heart sample. The Cu_A site is thus conserved between Rb. sphaeroides and the mammalian system.

Cyt a

The EPR spectrum of cyt a, a low spin heme, has a rhombic lineshape with peaks at g=2.83, 2.31 and 1.62. Application of equations 3 and 4 gives tetragonality and rhombicity factors of 3.31 and 0.67 respectively. These values were calculated by using the axis system of Palmer.³⁶ These values fall within the H region of the crystal field diagrams, a region that contains hemes that are known to be ligated by two imidazoles or histidines.³⁵ The H region is specific to hemes that have one or both of the ligands deprotonated.³⁵ The bishistidine ligation of cyt a observed in the mammalian cyt c type oxidase is conserved in the system studied here.

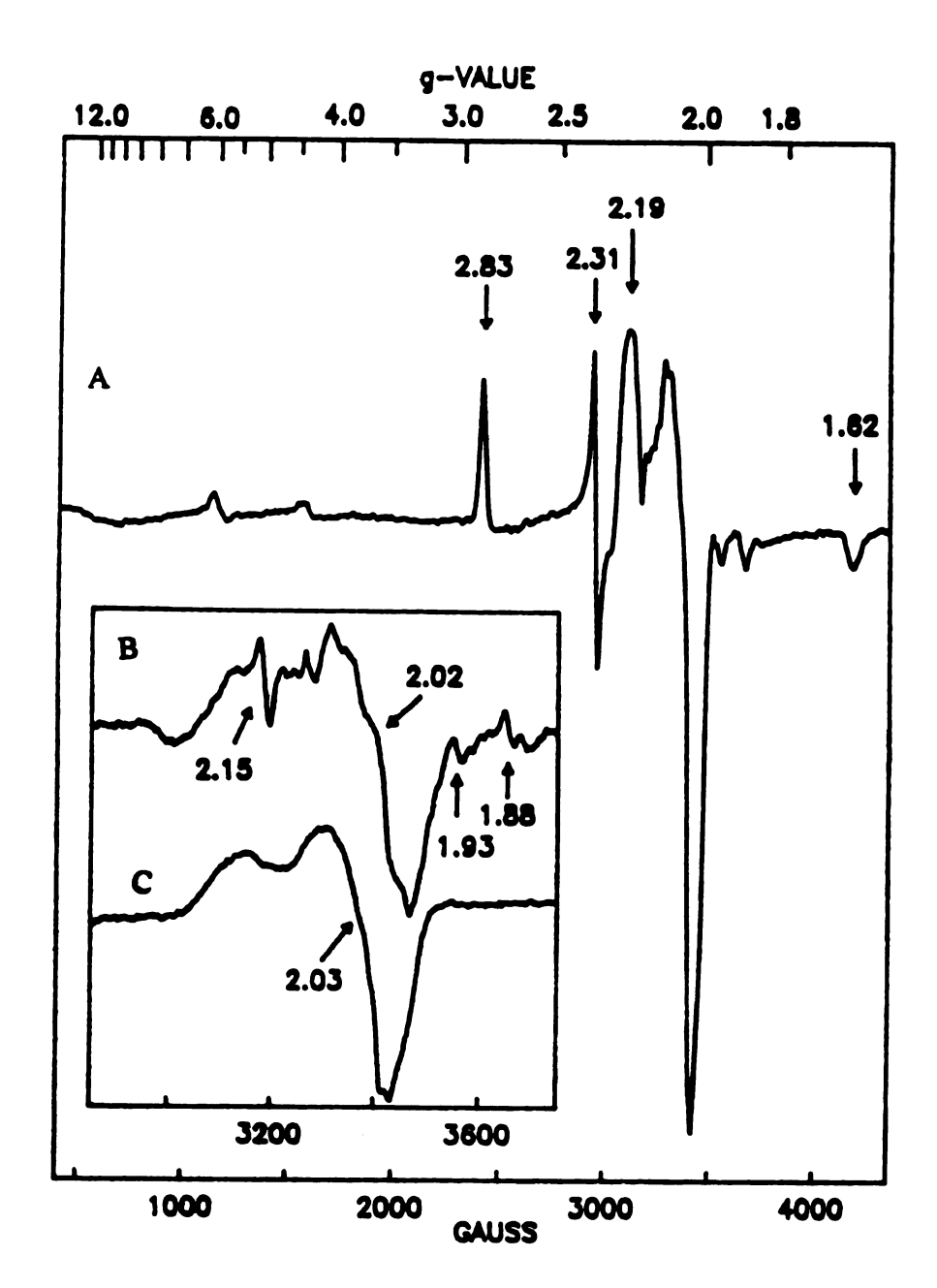


Figure 5.2 EPR spectrum of *Rb. sphaeroides* oxidase at (A) 10 K and (B) 110 K. Figure C is the EPR spectrum from beef heart oxidase at 110 K. Conditions: (A) μwave power; 2 mW, modulation; 12.5 Gpp, (B and C) μ wave power; 20 mW.

The value of g_Z of low spin hemes is sensitive to the protonation state of the imidazole ligands. Heme a, in solution at neutral pH with bisimidazole ligation, has g_Z =2.96. When the pH is raised to 11.3 and both imidazoles are deprotonated g_Z shifts to 2.71. In addition the value of Δ shifts from 3.02 to 4.11.37 Similar effects have been observed for bisimidazole ligated tetraphenyl porphyrin. With both imidazoles protonated g_Z =2.87 and Δ =3.17. Hydrogen bonding to one of the ligands shifts g_Z to 2.85 and Δ to 3.34 and hydrogen bonding to both ligands causes a further shift of g_Z and Δ to 2.80 and 3.82 respectively.38

Comparison of the model studies with the results from cyt a indicate that one or both of the ligands is deprotonated or is involved in a strong hydrogen bond. Similarly the hemes of soybean leghemoglobin (2.82, 2.24, 1.69)³⁹ and metmyoglobin (2.80, 2.25, 1.67)⁴⁰ with one histidine and one imidizolate ligand, have g values nearly identical to those of *Rb. sphaeroides* cyt a. In an attempt to discriminate between hydrogen bonding or deprotonation, the effect of low pH treatment was examined. At pH 5.5, the lowest pH where the enzyme retains activity, an imidizolate might be protonated causing a shift in gz, while a hydrogen bond would be unaffected. Turnover of the enzyme at pH 5.5 and extensive incubation at low pH caused no change in the EPR spectrum. This result is consistent with a strong hydrogen bond to a ligand of cyt a.

The oxidase from *P. denitrificans*⁴¹ has g values for cyt a that are similar to those from *Rb. sphaeroides* and both are shifted from the g values of 3.03, 2.21 and 1.45 observed for beef heart oxidase.⁴² The data from beef heart oxidase correspond to bishistidine ligation with both ligands protonated. In the bacterial systems there must be a hydrogen bond acceptor that is stronger and/or closer to one or both of the histidine ligands that is not present in beef heart. The hydrogen bond acceptor(s) has not been determined.

The present EPR analysis of oxidase from Rb. sphaeroides reveals that to the extent of this characterization the Cu_A and cyt a sites are equivalent to those studied in

other cytochrome c oxidases. Due to the coupling of the cyt a₃ and Cu_B metals these sites could not be studied by EPR. Additional characterization of this enzyme by optical and raman also show that the enzyme is structurally homologous at the metal sites to the other members of this family of oxidases.⁴³ The protein sequence from *Rb. sphaeroides* also shows a high degree of homology with the three largest subunits from beef heart oxidase, which are believed to make up the catalytic core of the enzyme. Comparison of the DNA-derived amino acid shows an identity between the *Rb. sphaeroides* and beef heart sequences of 52%, 39% and 49% for subunits I, II and III, respectively⁵⁷. The combination of these results show that the oxidase from *Rb. sphaeroides* has a high degree of structural similarity to the mammalian oxidase. These results clearly establish the oxidase of *Rb. sphaeroides* as an excellent bacterial model for examining the structural basis of the catalytic function of the more complex eukaryotic enzyme.

Mn in cytochrome oxidase

EPR

In almost all cases Mn²⁺ is observed to be high spin, that is with 5 unpaired electrons and a total spin S=5/2.⁴⁴ The Mn²⁺ ion is thus paramagnetic and since it has a half-integer spin it can be easily detected by EPR. The spin relaxation of Mn²⁺ is slow enough that EPR spectra can be obtained at room temperature, where many of the studies are done. EPR studies of Mn²⁺ are abundant both in inorganic complexes and in biological systems and the magnetic parameters for this system are well understood.

For Mn2+ in the gas phase the five unpaired electrons have a spherical distribution about the nucleus. However when the ion is placed in a condensed phase, where there is a non-spherical potential, the electron distribution will be distorted. The extent of this distortion is characterized by the zero field splitting(ZFS) tensor. This tensor is described by the parameters D and E. For an axial system, a system with a 3-

fold or higher axis of symmetry, D≠0 and E=0. In systems of lower symmetry the ZFS tensor is rhombic and D≠0 and E≠0. The ZFS tensor is traceless and in the case of rapidly rotating system, such as a small molecule in solution the ZFS tensor will average to zero and there will be no ZFS detected in the EPR spectrum. In the case where a sample is not allowed to tumble, a frozen protein solution, the effect of the ZFS will be observed. The electronic environment around the Mn²+ nucleus can be distorted by unequal bond distances to similar ligands, deviations from octahedral or tetrahedral bond angles, several different types of ligands and electrostatic forces. The value of D has been observed to range from 0 to several thousand gauss whereas E can be no larger than D/3.44

A system with S=5/2 will have six possible electronic spin states $m_S=\pm 5/2$, $\pm 3/2$ and $\pm 1/2$. In the case of Mn²⁺ where the nuclear spin (I) is 5/2 there are also six possible nuclear spin states $m=\pm 5/2$, $\pm 3/2$ and $\pm 1/2$. The selection rules for EPR are $\Delta m_S=\pm 1$ and $\Delta m=0$. The EPR spectrum then consists of five fine structure transitions, where $\Delta m_S=\pm 1$, and the fine structure transitions are further split into six peaks by the nuclear spin. In total there are 30 allowed EPR transitions. In the case where the ZFS has been averaged to zero, the six fine structure transitions will be degenerate and the EPR spectrum for this case will consist of six lines which arise from the hyperfine coupling to the Mn nucleus. In other words there are five allowed EPR transitions, $\Delta m_S=\pm 1$, which are split into 6 lines because of hyperfine coupling and overlay each other because of the degeneracy of the electronic spin states. This is the case for hexaqua manganese in water. When the ZFS is not averaged to zero, the five sets of peaks are spread out from each other and the EPR spectrum can cover as much as 5000 G versus about 600 G for Mn²+(H₂O)₆.⁴⁴

The ZFS tensor is anisotropic which means that the ZFS value will depend on orientation of the Mn complex relative to the applied magnetic field. As a frozen solution contains Mn complexes in all orientations, the EPR spectrum will be a composite of the EPR spectra for each orientation; this is termed a powder pattern spectrum. As the value

of the ZFS increases the spectrum will be spread out over a wider range and since the total area of the EPR signal does not change, the intensity must become smaller. The energy of the electronic spin states $m_S=\pm 5/2$ and $\pm 3/2$ are strongly dependent on the ZFS parameters D and E and thus the EPR transitions between these states are, in many cases, severely broadened and, in frozen solutions, are too weak to detect.⁴⁵ However, the $m_S=\pm 1/2$ states are only weakly dependent on these terms and are narrower and more intense and are generally the only peaks seen for frozen solutions.⁴⁵ Even though the $m_S=\pm 1/2$ transitions are only weakly dependent on D and E, the magnitude of these terms still significantly affects the shape of the EPR spectrum.⁴⁵

In addition to the allowed EPR transitions discussed above, peaks from forbidden transitions are also present in the spectrum. These come from transitions: $\Delta m_S = \pm 1$ and $\Delta m_I = \pm 1$. Since these peaks are formally forbidden, their intensity is much weaker than the allowed transitions. The intensity ratio of the forbidden to allowed transitions is dependent on the magnitude of D. Approximation of the value of D can be obtained from this ratio.⁴⁶

In frozen solutions of metallo-proteins broad linewidths are observed in the EPR spectra, which is the result of microheterogeneity of the ligand environment around the metal. The bond lengths and angles of the ligands can have a range of values across the protein sample. This structural microheterogeneity causes the magnetic parameters g, A, D and E to have a corresponding spread about their observed values. As the EPR spectra for Mn2+ is stongly affected by the value of D and E, a spread in these values will significantly affect the linewidth of the EPR spectrum. This is in contrast to the behavior observed for powders of small inorganic complexes where the distribution of D and E are quite small and very narrow linewidths are observed. 47,48

From the study of a large number of Mn complexes, some generalities can be made about the EPR parameters for this ion. In most cases the electron g-value is observed to be near the free spin g value of 2.0023 and the g-tensor is isotropic or very

nearly so.⁴⁴ Mn²⁺ also has a nuclear spin I=5/2 and hyperfine coupling between the the unpaired electrons and the nuclear spin results in 6 lines in the EPR spectra. The hyperfine coupling (A), for Mn²⁺ in an octahedral environment, is normally in the range 80-100 G, whereas for tetrahedral environments, it is normally in the range 60-70 G.⁴⁴ As for the case with the electronic g values, the hyperfine coupling tensor is very nearly isotropic.⁴⁴

Many Mn systems have also been studied with Q-band (35 GHz) EPR. At Q-band D and E have a much smaller effect on the spectra whereas g and A become much more important. Also the intensity of the forbidden transitions is inversely related to the microwave frequency and thus is much smaller at Q-band. The smaller effect of D and E and the decrease in the forbidden transition intensities results in narrower linewidths and a better resolved spectrum at Q-band.

Mn quantitation

Metal analysis of oxidase from *P. denitrificans* has shown that the quantity of bound Mn is substochiometric.²² In order to determine if the quantity of bound Mn is related to the quantity of Mn in the growth media cultures were grown in a series of [Mn], with the growth conditions listed in Table 1. The EPR spectra for the different samples is shown in Figure 3. In Figure 3A, with no bound Mn, it is clearer that the Cu_A signal is identical to that from beef heart oxidase, Figure 3D. In Figure 3E, where the Cu_A signal is barely detectable, the complete Mn signal can be observed. The spectrum of Figure 3B is from a sample grown in the normal [Mn].

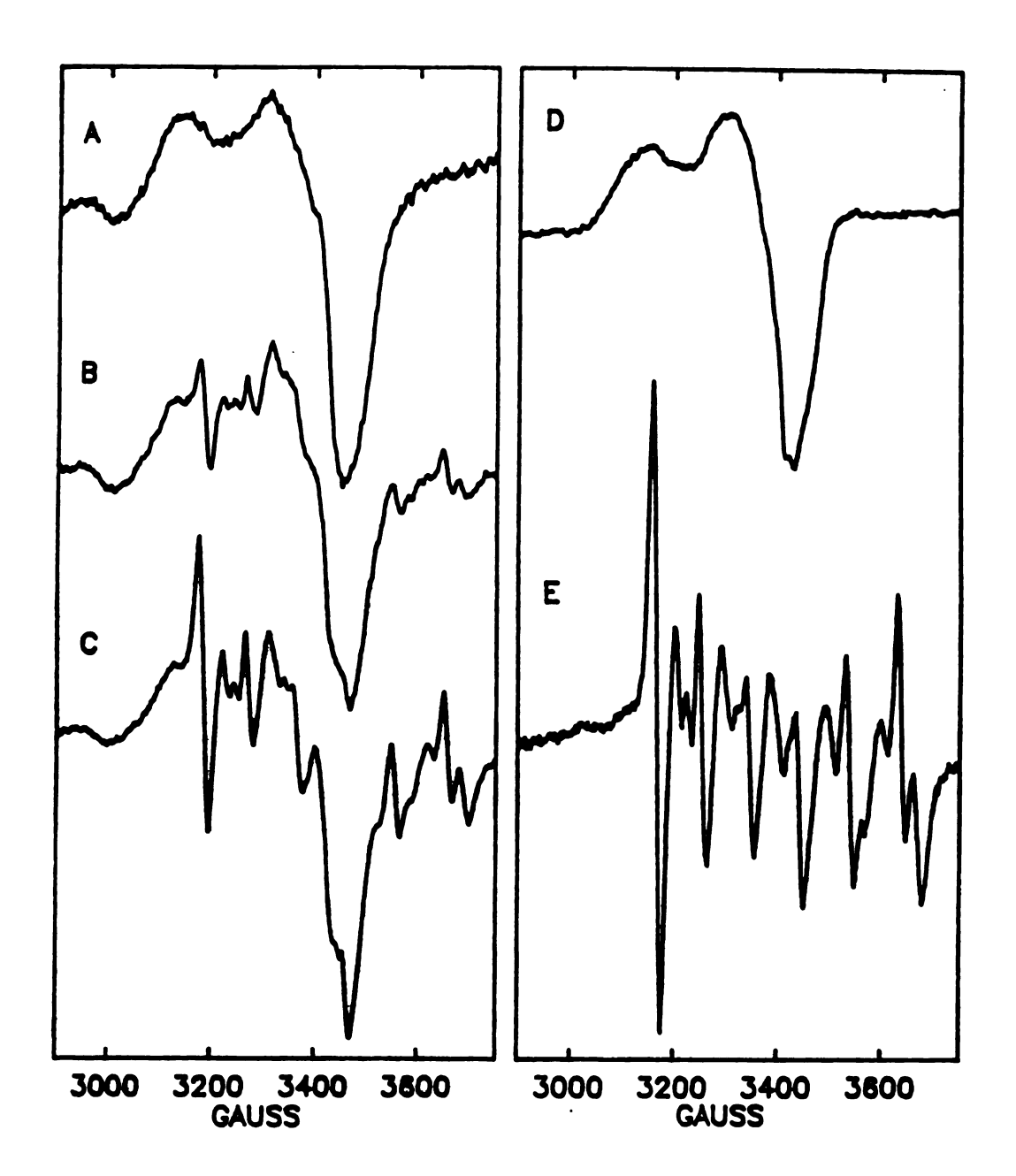


Figure 5.3 The g=2.0 region of the EPR spectrum from *Rb. sphaeroides* grown in the presence of different [Mn]: A) 0, B) 9μM, C) 27 μM, D) 1mM. E) beef heart oxidase. Conditions: μwave power; 20 mW, modulation; 12.5 Gpp, Temperature; 110 K.

Table 1: Stochiometry of bound Mn in Rb. sphaeroides oxidase

sample #	Mn (μm)	Mg (μM)	Mg/Mn	% Mn binding	Enzyme activity (turnover/sec)
1	0.5	1200	2400	0	1487
2	9.0	1200	133	1.3	1468
3	27	1200	44	4.1	1475
4	1000	1200	1.2	48	1449
5	700	50	0.07	70	1520
6	9.0	10,000	1111	0.4	1553

Quntitation of the quantity of bound Mn from the sample of Figure 3E, by EPR spin counting, yields a stochiometry of 0.7 Mn/enzyme. For the remainder of the samples listed in Table 1, the stochiometry of Mn incorporation was determined by comparing the amplitude of the Mn EPR signal to the amplitude of the g_z component of the cyt a signal. All spectra were recorded under identical conditions. Quantitation by spin counting was below detection at room temperature where these experiments were performed. The percent occupancy of Mn are listed in Table 1.

This manganese does not represent adventitiously bound manganese but rather manganese bound to a specific metal binding site. These samples have been washed with 50 mM EDTA which will remove non-specifically bound Mn. Two results provide strong evidence that the manganese is specifically bound and incorporated into the protein. First, the expected EPR signal from adventitious Mn is not observed in Figure 3. Second, in order to show that the adventitious manganese can be removed, the oxidase sample containing no bound manganese was incubated with 1mM manganese for 2 hours giving

giving rise to a large manganese EPR signal, Figure 4B. The sample was then washed with 50 mM EDTA, identical to the normal purification procedure, after which the manganese EPR signal was completely absent, Figure 4C. In those samples with bound Mn the Mn is buried in the protein and not EDTA accessible. The metal may be bound during folding of a subunit or during the assembly of the enzyme. When the enzyme is fully assembled the metal is to a large extent isolated from the solvent and not extractable. A similar experiment was done with oxidase from *P. denitrificans* yielding the same results.²⁶

Even though only 0-70% of the oxidase contains manganese, the metal binding site is most likely not empty in the rest of enzyme molecules. It seems unlikely that a metal binding site would be constructed in the protein and then left vacant. The site though may not be specific to only one particular metal. The variation in the manganese quantity observed with change in [Mn] in the growth medium suggests a competition between manganese and other metals for the binding site. Substitution of metals in proteins generally involves metals with the same charge and similar ionic radii. This metal binding site would thus prefer divalent metals with radii similar to manganese of 0.97 Å. Since no additional EPR signals are detected the other metals competing with manganese must be diamagnetic. The growth medium contains the metals Mg, Ca, Fe, Mo, Zn, Mn, Cu, and Co.⁴⁹ From this group the only diamagnetic divalent ions are Mg, Ca, and Zn, all three of which have ionic radii similar to manganese. Metal analysis studies of oxidase from *P. denitrificans* show the presence of Mg and Zn (the growth media for *P. denitrificans* contains the same metals as for *Rb. sphaeroide*⁵⁰), however, the presence of Ca was not monitored in these experiments.²²

The substitution of manganese for magnesium is ubiquitious in biological systems.⁴⁵ This substitution of metals can be rationalized in terms of the preference for ligand types and geometry. Both Mg and Mn are usually observed as six coordinate with oxygen and nitrogen as ligands.⁵¹ This is quite different from that observed for zinc

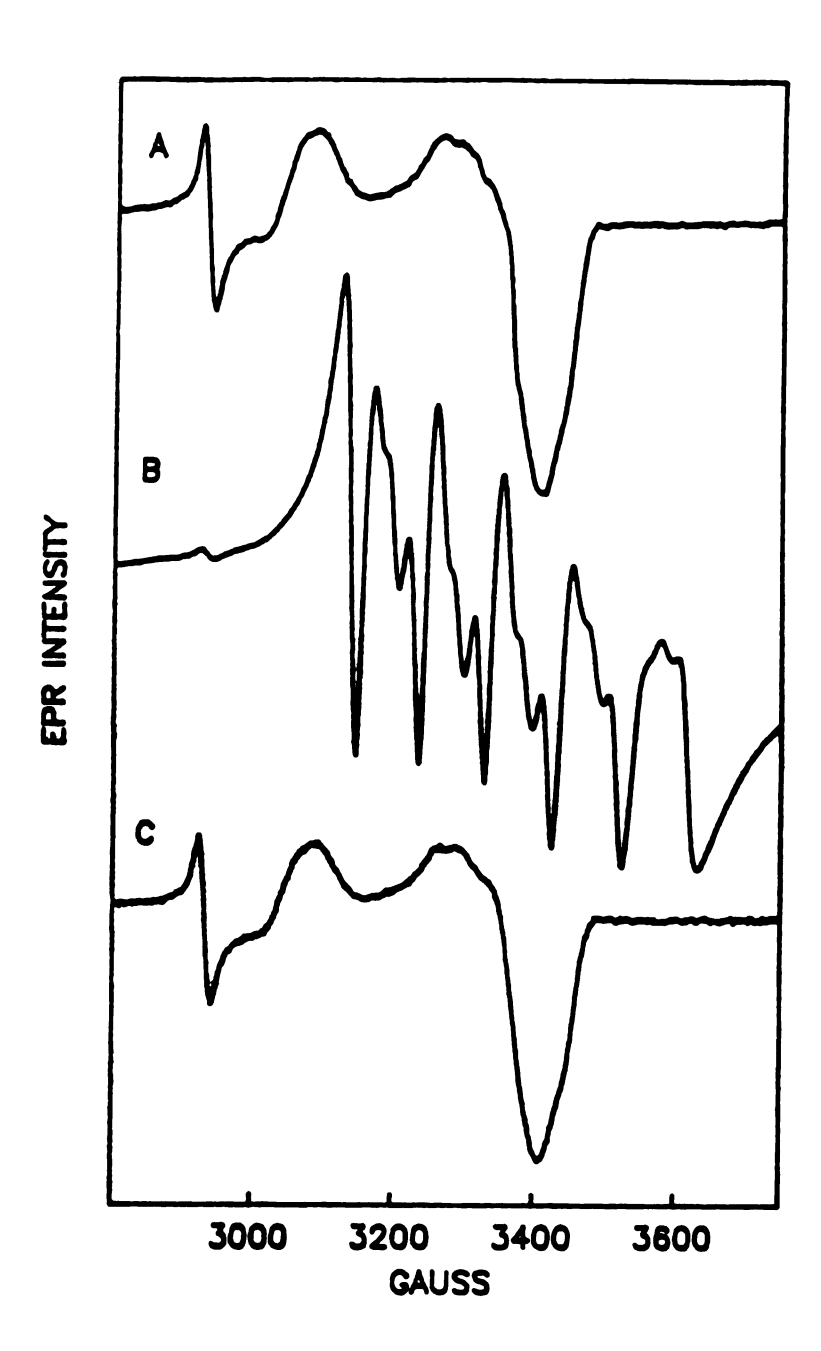


Figure 5.4 A) EPR spectrum *Rb. sphaeroides* oxidase grown in the presence of [Mn]=0.5μM, B) after incubation with 1mM [Mn], and C) after washing the sample with 50 mM EDTA. Conditions: μwave power; 2 mW, modulation; 12.5 Gpp, temperature; 10 K

containing proteins where the coordination site is usually four coordinate.⁵² While zinc is found to have ligands that are similar to Mn and Mg, namely glutamates, aspartates, histidines and water in many cases it also has one or more sulfur ligands from cysteine. With these differences in preferences in coordination sites it appears that zinc would not enter the site that binds Mg and Mn. However, in inorganic complexes zinc is commonly observed to be six coordinate.⁵³ The ligands in these complexes range from six oxygen to six nitrogen. Substitution of Mn into the zinc sites of these complexes is accomplished with little or no change in the crystal stucture.⁵⁴ It is expected then that zinc can compete with Mn for the metal binding site in oxidase.

In order to determine if Mn is competing with Mg for the same binding site, cultures were grown in different Mg concentrations, analogous to the experiments done with Mn. Figure 5 shows the results when the [Mn] was kept constant but the [Mg] was raised from 1.2 mM, Figure 5A, to 10 mM, Figure 5B. With the increase in the [Mg] present the stochiometry of the bound Mn decreases from 1.3% to 0.4 %, Table 1. The decrease in the bound Mn can most easily be seen at the high field side of the spectra in Figure 5. Mn and Mg thus appear to compete for the metal binding site(s) within oxidase. This is evident from a plot of percent occupancy of Mn versus the [Mn]/[Mg], Figure 6. For the lower metal concentration ratios the plot is linear, showing the direct competition between the two metals. Mn incorporation appears to saturate at high [Mn]/[Mg] levels indicating that other factors limit the extent of Mn binding. This limitation may be the maximum steady state concentration of free Mn within the cell. The metal concentrations inside the cell are not known. While the [Mg] is increased in the growth medium this increase may not be reflected inside the cell. The two samples, represented by the last two points of Figure 6, while having different [Mn]/[Mg] levels in the growth medium may have similar [Mn]/[Mg] levels inside the cell. In all these experiments the [Zn] was kept constant. Whether Zn is also binding at this site has not yet been determined.

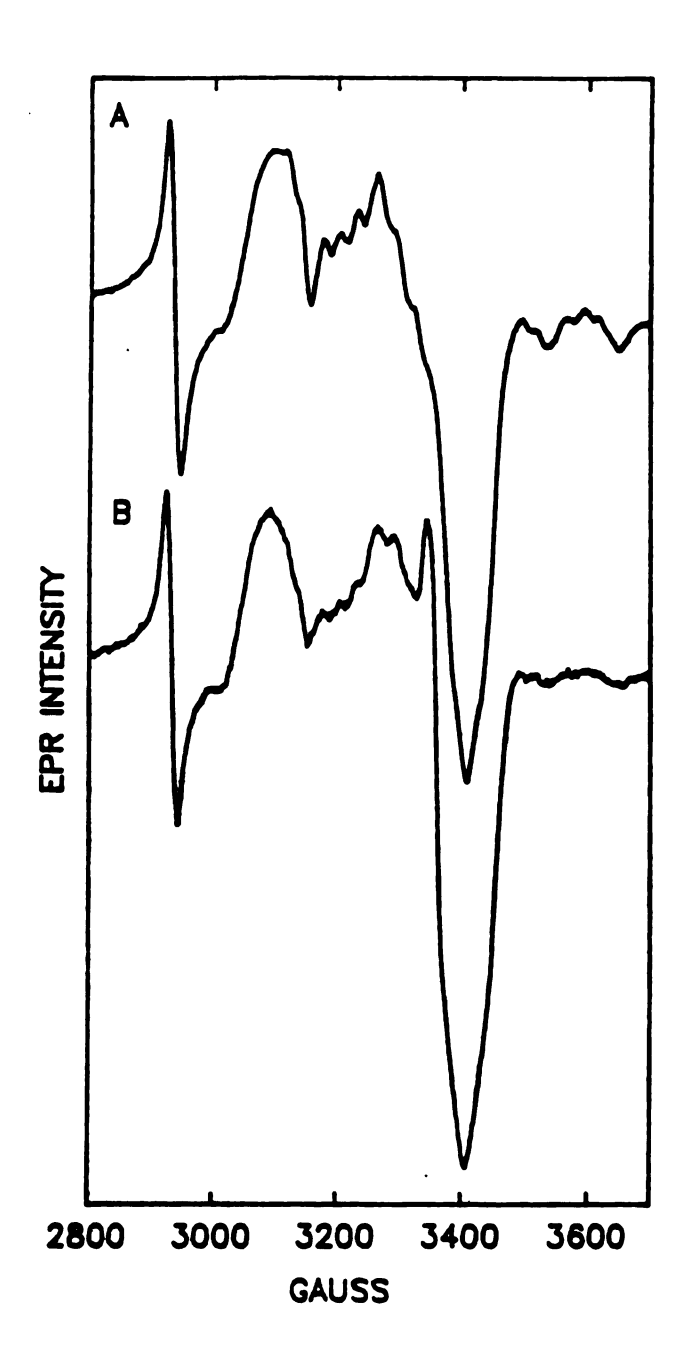


Figure 5.5 EPR spectrum of *Rb. sphaeroides* oxidase grown in the presence of [Mn]=9µM with [Mg] equal to A) 1.2 mM and B) 10 mM. Conditions: same as Figure 5.4.

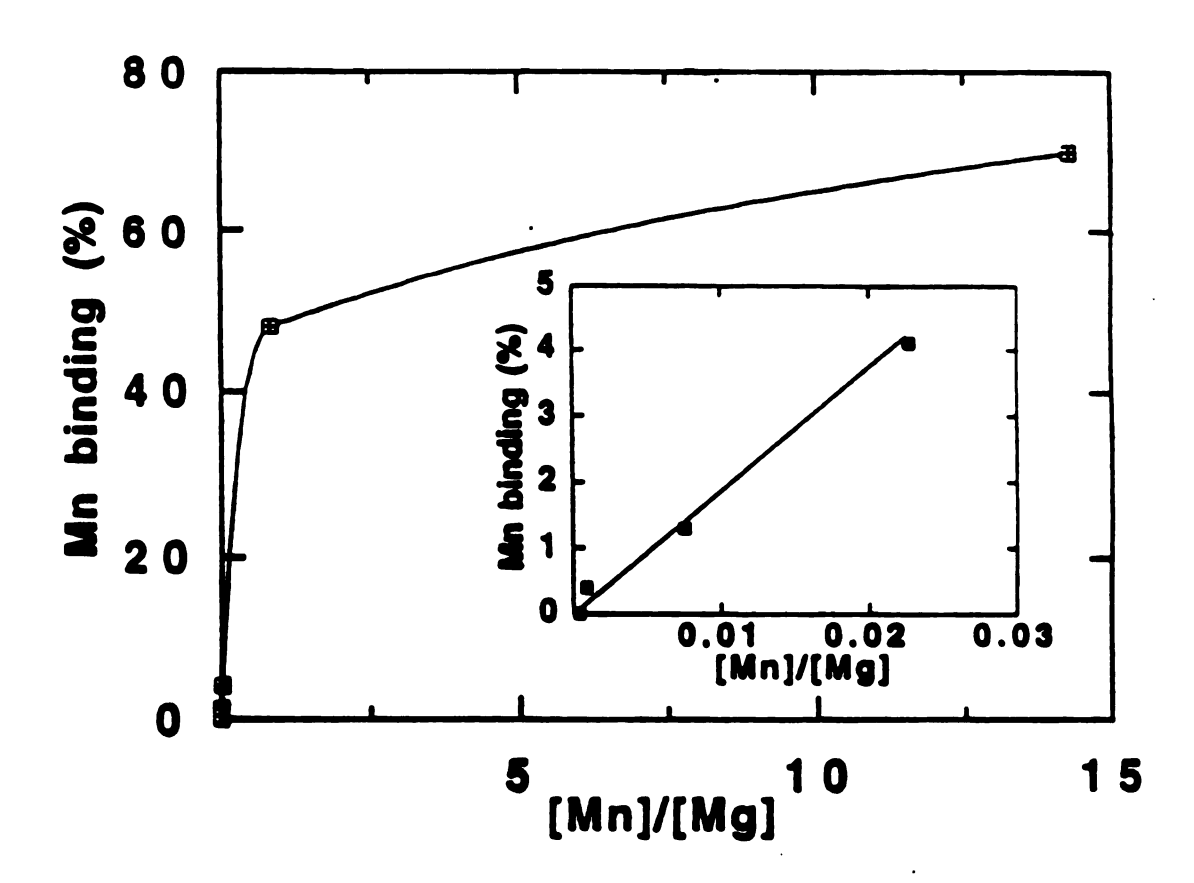


Figure 5.6 Plot of the % Mn binding to Rb. sphaeroides oxidase versus the [Mn]/[Mg] ratio in growth medium. Insert: expansion of first four points.

Experiment #4 in Table 1 shows that at nearly equal concentrations of Mn and Mg there is Mn to bound to approximately half of the enzyme present. If no other metals besides Mn and Mg are bound to this site the affinity of this site for these two metals is about the same. Since other metals, including Zn and Ca, may bind to this site the quantity of bound Mg may be lower than predicted above. This would mean that the binding affinity of the metal site for Mg is, at a maximum, approximately the same as for Mn. These results are bases on the assumption that the ratio of metal concentrations is the same in the cell as in the growth medium.

The enzyme activity results of Table 1 also show that the enzyme is insensitive to the metal bound at the metal binding site. The enzyme activity, measured as turnover number, is nearly the same for samples containing 0-70% Mn. While the binding of a divalent cation radical may be important for proper operation of the enzyme the exact metal that is bound appears not to be critical.

Mn binding site location

A series of mutants in subunit I were examined to determine if specific amino acids can be associated with the divalent metal binding site. As above, EPR was used to determine if there is bound manganese and, if so, in what quantity. The mutations can be divided into two classes: 1) mutations in the helix 9-helix 10 interhelix loop (9-10 loop)and 2) mutations of the completely conserved histidines. The data from these mutations are listed in Table 2.

Table 2: Mn binding stochiometry and enzyme activity for subunit mutants

Mutant	[Mn] in culture medium	% of oxidase enzyme with bound Mn	electron transfer activity(% of wildtype)
H411N	9	0	0
H411A	9	0	50
H411A	27	0	50
D412N	9	0	44
D412N	27	0	44
T413N	9	1.3	94
Y414F	9	2.0	69
H284A	9	0.2	0
H284Q	9	0.5	0
H333N	9	0.7	0
H333Y	9	0	0

9-10 loop mutants

Subunit 1 from *Rb. sphaeroides* oxidase is predicted to have 12 transmembrane helices from hydropothy profile analysis.³⁰ Between helices 9 and 10 is a 16 amino acid extramembrane loop. This interhelix loop contains four highly conserved residueshis411, asp412, thr413 and tyr414.⁵⁸ Since his411 is conserved in all oxidases except one, this amino acid is predicted to serve some important role within the protein.⁴³ The other six completely conserved histidines act as ligands to cyt a, cyt a₃ and Cu_B.³⁰ Mutations of his411 to alanine (H411A) and asparagine (H411N) result in the enzyme that does not bind Mn, Figure 7A and E. The effect on the activity of the enzyme is different between the two mutants with H411A showing near wild type rates while H411N is completely inactive, Table 2. Similar results are seen for the mutation of

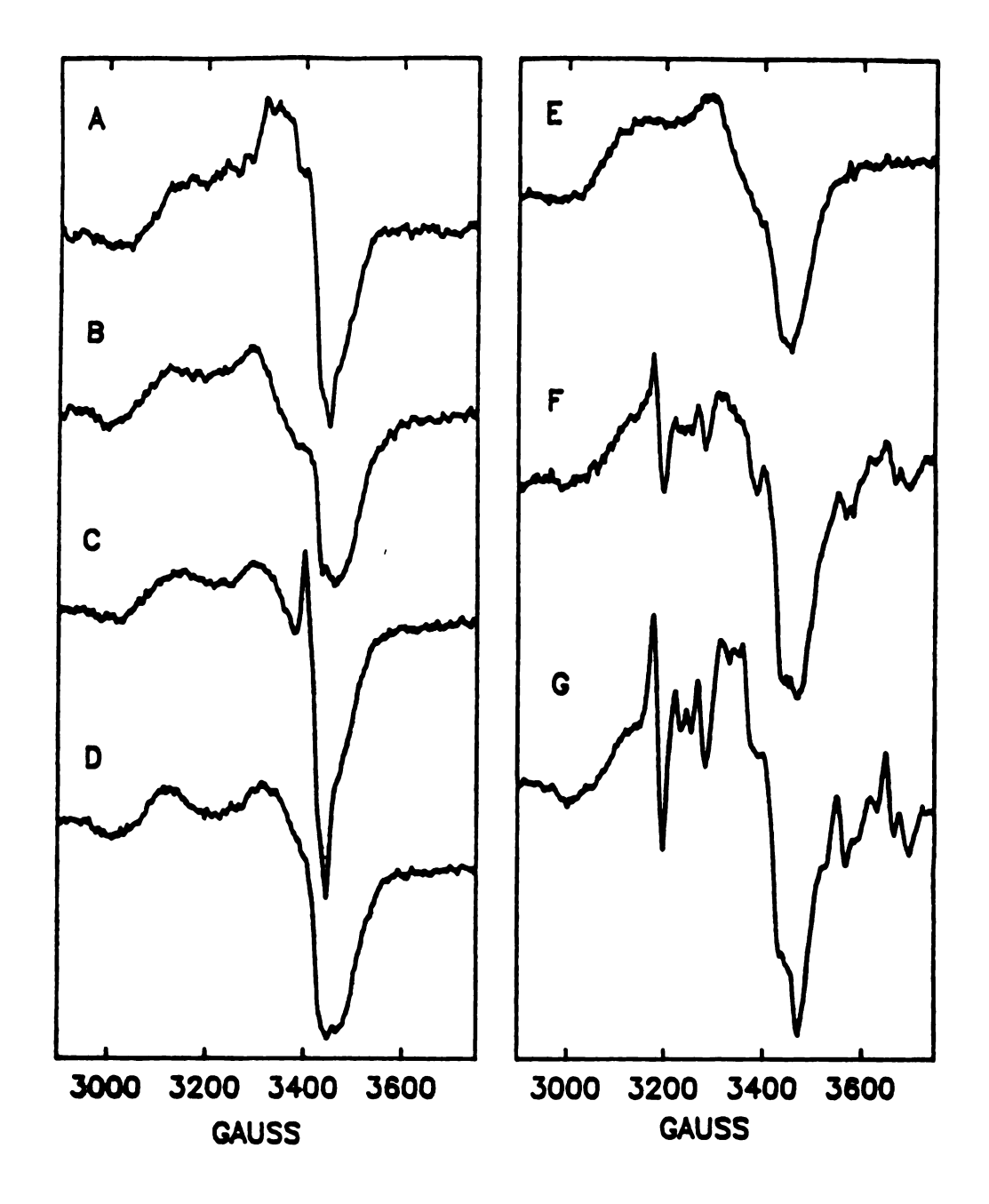


Figure 5.7 EPR spectra of subunit 1 mutants: A) H411A, B) D412N, C) H411A, D) D412N, E) H411N, F) T413N, G) Y414F. Samples were grown in the presence of [Mn] = 9 μ M except spectra C and D where [Mn] = 27 μ M. Conditions: same as Figure 5.3.

asp412 to asparagine (D412N), Figure 7B . This mutation also produced an enzyme that does not bind Mn and retained only approx 30% activity of wild type samples. Growth of the cells containing the H411A and D412N mutations in media containing 27 μ M manganese still did not produce any significant Mn binding in oxidase, Figure 7C and D. Quite different results are seen for mutations at thr413 and tyr414. Exchanging thr413 for asparagine (T413N) had no effect on either manganese binding or enzyme activity, Figure 7F Substitution of phenylalanine for tyrosine 414 (Y414F) does not affect the enzyme activity but does appear to enhance the binding affinity of the enzyme for manganese as the occupancy of bound manganese is approximately 2% versus 1.3 % for wild type enzyme, Figure 7G.

Compilation of the results for this series of mutants leads to a partial definition of the Mn binding site. The complete loss of manganese binding in the his411 and asp412 mutants implicate these residues as part of or closely associated with the metal binding site. Both histidines and asparagines are common ligands to manganese binding proteins (see below). The fact that a mutation at a single site results in no bound Mn indicates that there is only one Mn binding site in the enzyme. Further evidence for this region of the protein being part of the binding site comes from the Y414F mutant. This mutation may cause a change in the structure of the binding site thus affecting the binding affinity of the site for the different metals. The change however must be small as the manganese EPR spectra is the same as that detected in the wild type sample. This structural change may be caused by a breaking of a hydrogen bond when the phenol oxygen is lost in the mutant.

A more detailed description of the location of the Mn binding site can be inferred from optical and raman studies of the 9-10 loop mutants. The H411N mutation shows shift in the λ_{max} in the absorption spectrum of cyt a3 and the peaks in the raman spectrum associated with cyt a3 are absent. The loss of these raman peaks is likely the result of peak broadening from a distorted binuclear site, allowing multiple orientations of the heme and its substituent groups. However, the raman peaks from cyt a

are unchanged. FT-IR data also show a highly distorted binuclear center. Mutation of his411 causes a significant structural rearrangement to occur at the binuclear center.

The D412N mutation shows optical and raman spectra that are nearly wild type. The only difference being a small shift in the Fe-N_{his} stretch of cyt a₃ from 214cm⁻¹ to 218 cm⁻¹. Mutation at this site causes only a weak disturbance of the cyt a₃ but, in contrast to his411 mutations, the effect is on the distal side of the heme. The T413N mutant shows wild type optical, raman and FT-IR spectra indicative of no structural or electronic changes occuring at the two hemes when this site is mutated. This amino acid is most likely further away from the hemes than his411 or asp412. Mutation of tyr414 results in a shift in the λ max of the absorption spectrum of cyt a but not in the spectrum of cyt a₃. The localization of the effect of tyr414 mutations on the two hemes places this residue near cyt a.

From the spectroscopic studies of the mutants of the 9-10 loop a model for the postion of this loop in the protein can be constucted. Figure 8 is a model of the portion of subunit 1 that is involved in metal binding. The view of this figure is normal to the membrane plane and down the axis of the helices. The four residues that have been mutated are highlighted and the arrows show the site within the protein that is affected by mutagenesis. His411 and asp412, the putative ligands, to Mn then are proposed to be located near the binuclear center.

Further evidence for the placement of the Mn near the binuclear center comes from mutations of the proposed Cu_B ligands his333 and his284. Mutations at these two sites cause no change in the raman spectrum of cyt a but a loss of the raman peaks from cyt a₃. Cyt a₃ and the binuclear center are severly disrupted by these mutations.³⁰ These mutations also result in decreased levels of Mn binding. H284A and H284Q bind 10-30% the quantity of Mn observed in the wild type oxidase while H333N binds 50% and H333Y binds no Mn, Table 2. Since the cyt a raman spectra for these mutants is unchanged, the structural changes that occur in the enzyme upon making these mutations

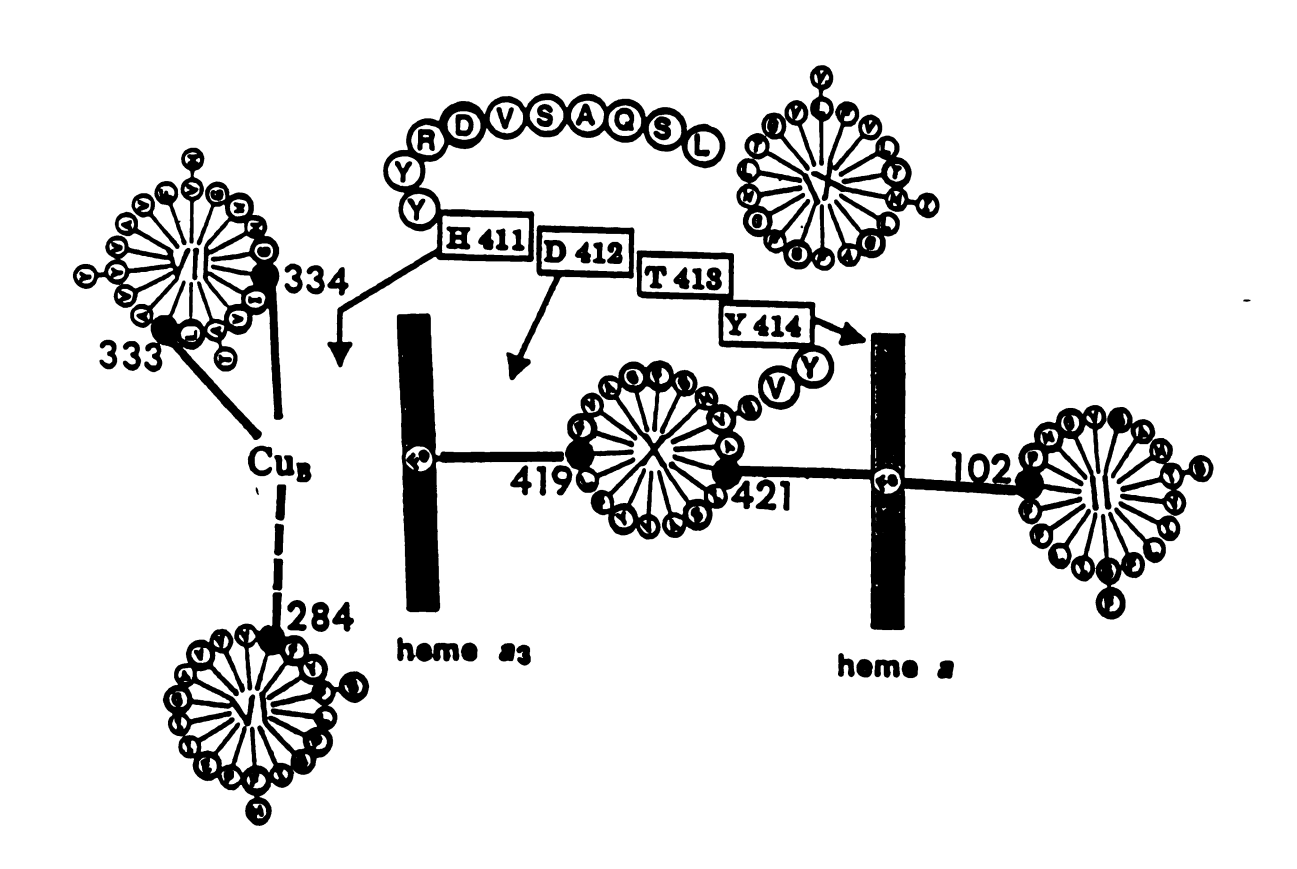


Figure 5.8 Model of the metal binding sites in subunit 1 of *Rb. sphaeroides* oxidase. The view is along the axis of the transmembrane helices.

appear to be localized to the binuclear center.³⁰ These results support the model of Figure 8 with the Mn binding site near the binuclear site.

The Mn EPR spectra for the his284 and his333 mutants is the same as that observed in the wild type samples. While a distribution of structural conformers is the explanation for the loss of the raman peaks of cyt a3 this does not occur at the Mn binding site. The Mn is either binding to that fraction of enzymes that have a native Mn binding site conformation or binding of the metal causes the site to regain its native conformation.

EPR characterization of Mn in Rb. sphaeroides oxidase

In an effort to gain more insight into the structure of the Mn binding site in oxidase multifrequency cw- and pulsed-EPR experiments have been performed. The X-band EPR spectra of Mn in *Rb. sphaeroides* oxidase have been recorded at 10 K and 110 K for both the fully oxidized and fully reduced forms of the enzyme, Figure 9. The Q-band EPR data of the oxidized and reduced enzyme was recorded at 120 K, Figure 10. In the X-band spectra for the oxidized form of the enzyme the signals from Cu_A and cyt a have been removed by subtracting the spectrum from the enzyme grown in 0.5 μ M Mn media, which showed no Mn EPR signal. The differences in the X-band data between 10 K and 110 K are most likely the result of changes in the ZFS parameters D and E. Temperature dependence of D and E has been observed in Mn inorganic complexes.⁵⁹

The Q-band EPR data was simulated with the program NEWMNSIM developed in the laboratory of Dr. Geoge Reed. The energy levels for $Mn^{2+}(S=5/2, I=5/2)$ were determined using perturbation theory and calculated to third order. The expressions used to calculate the energy levels were derived assuming that the g and A tensors are isotropic while the zero field spitting tensor can be axial or rhombic. The simulation program only calculates the $m_S=1/2 \rightarrow 1/2$ transition including the forbidden transitions.

The input variables for the simulation program are: g value, Mn hyperfine coupling, D, E and linewidth.

From the simulation of the Q-band data the g values have been determined to be 2.0026+0.0001 and 2.0027+0.0001 for the oxidized and reduced enzyme, Table 3. These results are consistent with previously reported g values of protein bound Mn.⁴⁵ The Mn hyperfine couplings are 95.2 G for the oxidized and 94.7 G for the reduced forms of the enzyme, Table 3. These values of A are indicative of Mn in a six coordinate environment with principally oxygen and nitrogen ligands. The decrease in A upon enzyme reduction is indicative of a decrease in the unpaired spin density located on the Mn. If in the reduced enzyme one or more of the Mn ligand bonds becomes more covalent more of the unpaired spin density resides on the ligands, decreasing the magnitude of A.

Table 3: EPR parameters determined from simulations of the Q-band EPR data.^a

Oxidation state of oxidase	g-value	Mn hyperfine coupling	D	E	Linewidth
oxidized	2.0026	95.2±0.2	115 <u>+</u> 25	25 <u>+</u> 10	6.0
reduced	2.0027	94.7 <u>+</u> 0.2	125±15	45 <u>±</u> 5	5.0

a all values except the g values are in gauss

In the Mn EPR spectrum only the transitions between the $m_S=\pm 1/2$ spin states were observed, Figure 9 and 10. The other four fine structure transitions are severely broadened and undetectable. By using the splitting observed in the highest field peak and the intensity ratio of forbidden and allowed transitions of the X-band EPR spectrum, at 110 K, D is calculated to be approximately 150 G in the oxidized form. 46,60 These approaches are not exact and only give an estimate of the value of D. In contrast to the value of D, there are no simple approaches to determining E. However, some insight into

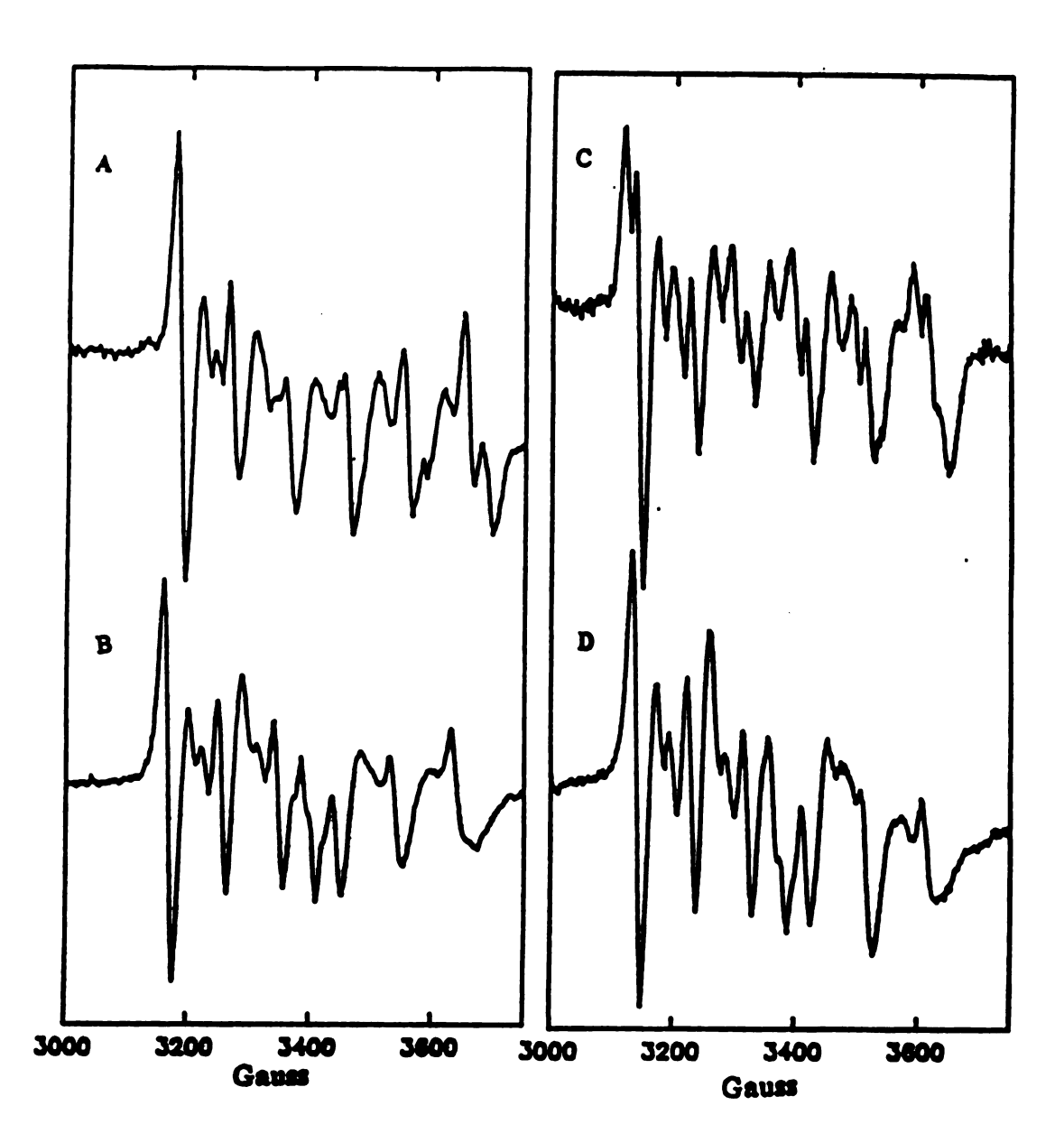


Figure 5.9 EPR spectra of A) oxidized and B) reduced oxidase recorded at 110 K. EPR spectra of the oxidized (c) and reduced (D) enzyme recorded at 10 K. Conditions: (A and B) same as Figure 5.3; (Cand D) same as Figure 5.4.

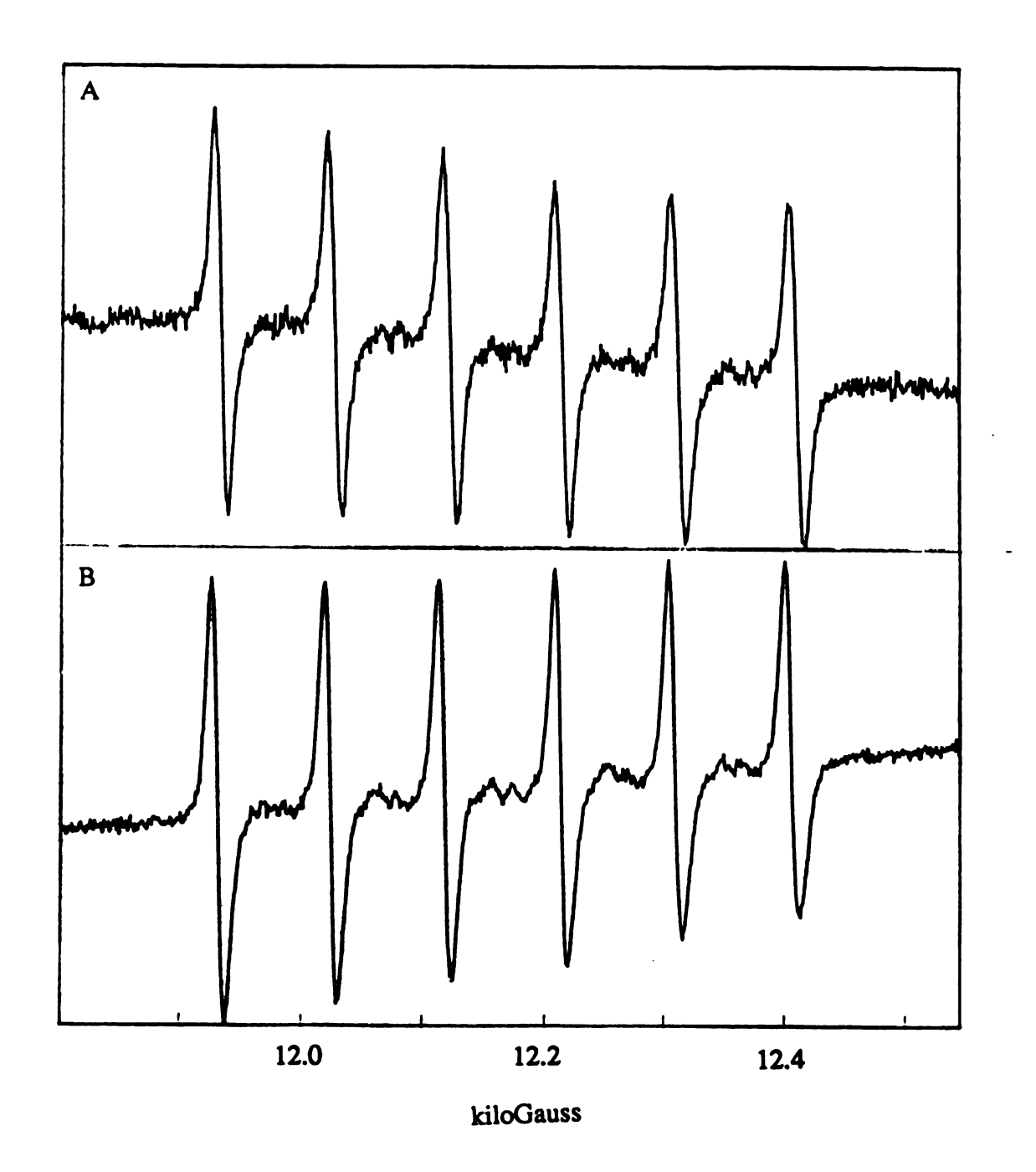


Figure 5.10 Q-band EPR spectra of the oxidized (A) and reduced (B) Rb. sphaeroides oxidase. Conditions: µwave power; 1 mW, modulation; 5 Gpp, temperature; 150 K.

the ratio of E to D can be obtained from the lineshape of the spectrum.⁴⁵ Comparison of our data with the EPR spectrum of a ternary complex of creatine kinase shows a strong similarity in the lineshapes.⁶¹ While the values of D and E are larger for creatine kinase, the value of E/D of 0.2, which controls the lineshape, is very similar to that seen in oxidase.⁴⁵ The values of D and E determined by simulation of the Q-band EPR results from oxidase are consistent with the X-band data, yielding D=115±25 G and E=25±15 G with E/D=0.22. The errors reported for D and E are determined from visual comparison of the simulated and experimental data. When only the six-line pattern from the M=±1/2 spin states is observed, errors in the simulation results can be on the order of 20%.

The spectrum from the reduced enzyme shows slighty larger forbidden transition intensities in the X-band spectrum as compared the the oxidized enzyme, indicative of a small increase in the value of D upon reduction of the enzyme.⁴⁶ The highest field peak in the spectrum, from the reduced enzyme, collapses compared to that seen in the oxidized enzyme spectrum, which indicates that the value of E has decreased.⁴⁵ Since the lineshape change is small the change in E must also be small. X and Q-band spectra obtained for the lectin soy bean aggulutin are very similar to that seen for the reduced enzyme where simulations at both X and O-band give D=120 G and E=25 G with E/D=0.2.62 The small increase in D detected in oxidase at X-band is consistent with the Q-band simulation results where D=125±20 G. The value of E however shows a discepency between the X- and O-band data. Our simulations show an increase in E (45±5 G) at Q-band where for X-band the spectra suggest E decreases. As discussed above the O-band data are more sensitive to changes in g and A than is the X-band data.⁴⁵ The increase in the asymmetry of the high field peaks of the Q-band data, upon reduction of the enzyme, may be a result of an increase in the anisotropy of g and/or A, in the reduced enzyme, rather than an increase in E. Since the X-band data is more sensitive to changes in D and E it appears that E decreases upon reduction, while the increase in D may result in an increase in the anisotropy of g, A or both.

Although the structure of the metal binding site does change upon reduction of CuA and heme a^{27} the small changes in the D and E values observed here indicate that the changes are minimal. Studies of the crystal structures of manganese binding protein show that the manganese is usually six coordinate and nearly octahedral.⁶³ The deviation from octahedral symmetry in these proteins is moderate, a spread of approximately 30° in bond angles and 0.5 Å in bond lengths. The value of D for these proteins are in the range 150-400 G.⁶²,63,70 The small changes for D and E seen above, ΔD =10 G and ΔE =20 G, thus represent only minor changes in the structure of the metal binding site. Currently there is not a quantitative correlation between deviations from octahedral symmetry and the ZFS parameters. An estimate of the change at the Mn binding site in oxidase based on the small changes observed for D and E are 0.1 Å in bond length and 10° in bond angle. These changes may be cumulative over the six ligands.

As mentioned above the metal binding site in proteins show heterogeneity in their structure which can be seen for cytochrome oxidase by the broad lines in the EPR spectra. The simulation routine used allows a gaussian spread in D to be used when calculating the spectra. From the simulations of the spectra for both oxidized and reduced enzymes best fits were obtained with a spread in D of 0-120 G. Within this range the spectra were not very sensitive to the magnitude of the distibution of D. The linewidths seen for the reduced enzyme are also slightly narrower than those for the oxidized enzyme at both X and Q-band microwave frequencies, indicating that the heterogeneity is less in the reduced form. The change in the EPR linewidth is not a function of saturation properties of the EPR signal as spectra recorded at a 30 fold decrease in power showed the same trend in linewidths for both redox states of the enzyme.

The larger heterogeneity in the structure of oxidase in the oxidized form observed here by EPR has been detected by other methods. 12 The isolated enzyme, in the fully oxidized form, exhibits a Soret maximum in the absorption spectra, which has strong

contributions from both cyt a and cyt a₃, that varies over the range 417-425 nm.⁶⁴ This value varies between preparations even when using the same purification procedure. This is a clear indication that more than one distinct conformation is present and the proportion of each differs between preparations. EPR studies of oxidase revealed three forms of the enzyme that are interconvertible.⁶⁵ The heterogeneity has been associated with the binuclear center conformation⁶⁵, however, this heterogeniety is not detected in the reduced form when studied optically.¹² In this form of the enzyme the metals are diamagnetic and not detectable by EPR, so an EPR analysis cannot be conducted. The narrowing of the linewidth of the EPR signal from Mn in the reduced form correlates well with previous optical and EPR data.

The X and Q-band EPR results show that the Mn is located in an octahedral site that is highly symmetric with predominantly oxygen and nitrogen ligands. This site undergoes a small perturbation in structure when the enzyme is reduced. The changes are estimated to be on the order of 0.1 Å in bond length and 10° in bond angles. The large linewidths observed in the EPR spectra, however, preclude the observation of weak hyperfine couplings to the metal, which may include ligands to the metal.

Pulsed EPR

In addition to the hyperfine coupling between the unpaired electrons of Mn²⁺ and the manganese nuclei, which gives rise to the six-line spectrum, there may also be hyperfine coupling to other nuclei, which have a nuclear spin and are spatially close to the metal. In these samples the only non-zero spin nuclei are nitrogens and protons. In the EPR spectrum of Mn²⁺ in oxidase only the hyperfine coupling between the unpaired electrons and the manganese nucleus are detected. If the hyperfine coupling to other nuclei were large this would cause additional splitting of the EPR spectrum. Hyperfine couplings to nitrogens or protons must then be smaller that the linewidth of the EPR

spectrum which is 5 gauss (15 MHz). As discussed in Chapter 2, an excellent technique for detecting small hyperfine couplings is ESEEM and this technique was used to study the protein environment near the tightly bound Mn in oxidase. Previous applications of ESEEM to study Mn binding proteins have been productive in detecting protons, nitrogens and phosphorus that are part of, or close to, the binding site of the metal.⁶⁶

The ESEEM spectrum recorded is a composite from all paramagnetic species that have intensity in the EPR spectrum at the field position that the ESEEM experiment was performed. The 3-pulse ESEEM data from oxidase collected at g=2.0 may show peaks from hyperfine coupling to nitrogen and proton from cyt a, CuA and Mn, all of which have EPR intensity at this field value. In order to separate the peaks originating from Mn, oxidase samples that contain no Mn and 0.7 Mn per enzyme were studied. Both the fully oxidized and fully reduced forms of the enzyme were studied. The 3-pulse ESEEM spectra for these samples, in addition to the spectrum from beef heart oxidase, are shown in Figure 11. The spectra were aquired at 2 K since this gave better signal-to-noise than data collected at 4.2 K. Other than changes in signal-to-noise the spectra at 4.2 and 2 K were the same. Spectra collected at higher sample repitition rates show a loss of resolution so a repitition rate of 30 kHz was used. The spectrum of the reduced oxidase sample containing no bound Mn showed no peaks in the spectrum (data not shown). This result implicates the peaks observed in the spectra of Figure 11 as originating from heme a, CuA or Mn²⁺. The spectrum from the beef heart sample, Figure 11D, and the bacterial sample that contains no Mn, Figure 11C, show the peaks that arise from the heme a and Cu_A. The reduced form of the 0.7 Mn/enzyme sample, with cyt a and Cu_A. now in their diamagnetic form, shows the peaks that come from Mn, Figure 11B.

The oxidized 0.7 Mn/enzyme sample is then a composite of the spectrum of all three metals, Figure 11A. In order to assign the peaks, ESEEM spectra were recorded at several field values. From Figure 2 it is clear that at g=1.90 there is little contribution from Cu_A, while cyt a still has EPR intensity (the EPR spectrum for cyt a ranges from

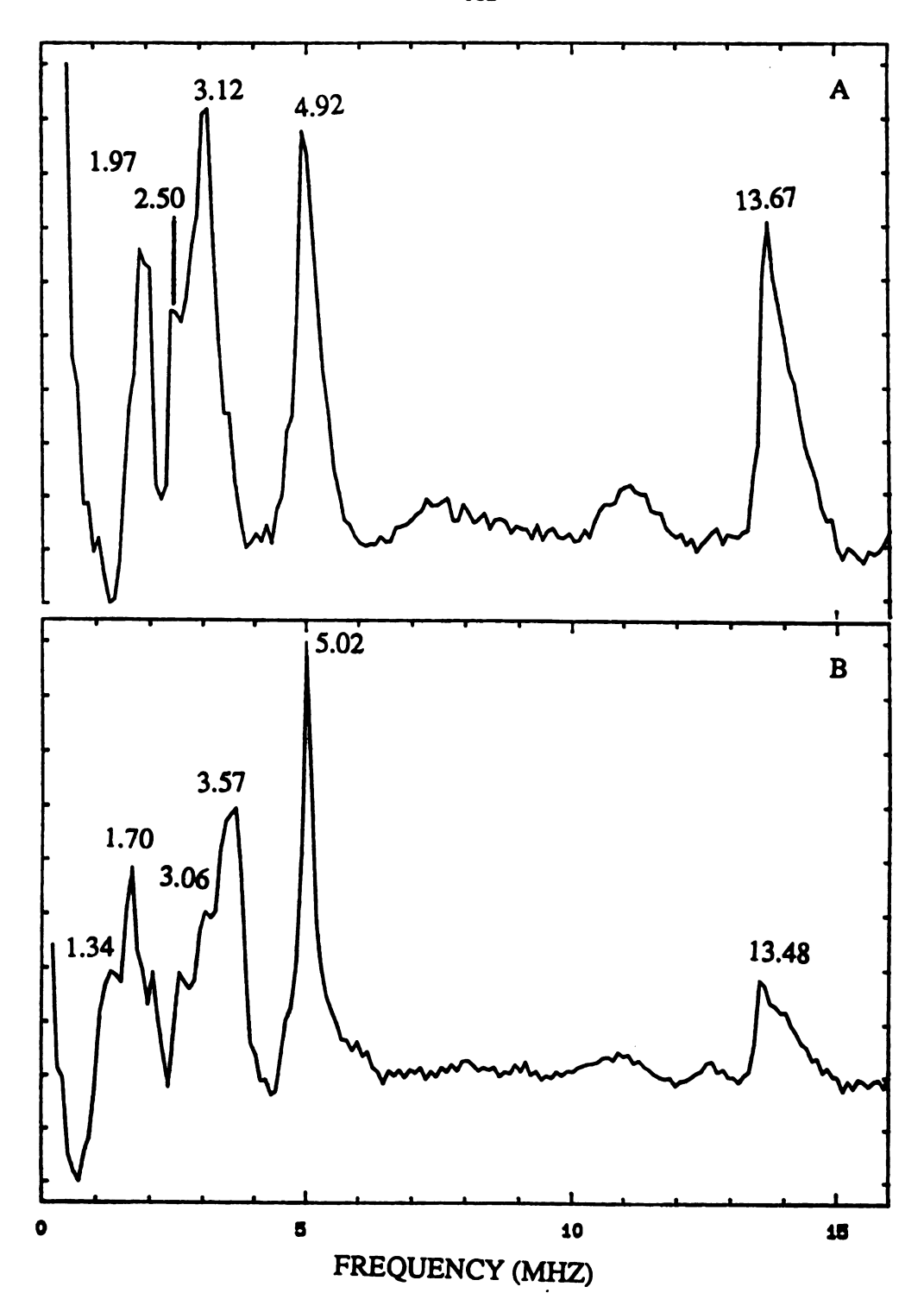
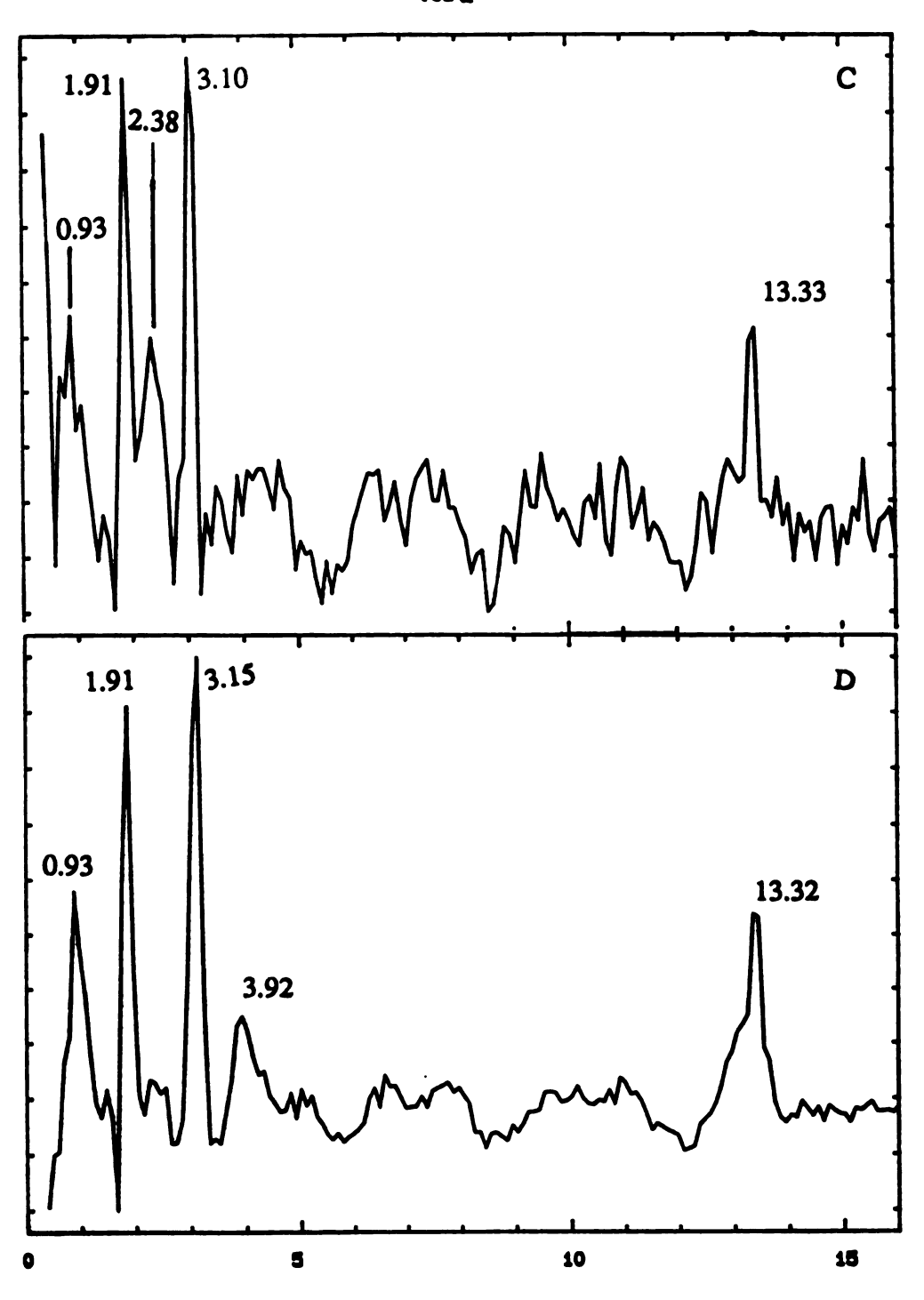


Figure 5.11 3-pulse ESEEM spectra of *Rb. sphaeroides* oxidase grown in the presence of [Mn] = 1 mM, in the (A) oxidized and (B) reduced forms. Spectrum C is from oxidase with no bound Mn and spectrum D is from beef heart oxidase. Conditions: tau; 225 nsec, g=2.01.



FREQUENCY (MHz)

2000-4600 G). The ESEEM spectrum recorded at g=1.90 for the oxidase sample containing no Mn was devoid of any peaks(data not shown). The peaks seen in the spectrum collected at g=2.0 for this sample, Figure 11C, must then arise from Cu_A. If peaks from cyt a were detected at g=2.0 they would still be present when data was recorded at g=1.90. The spectrum recorded at g=1.90 for the oxidized form of the 0.7Mn/enzyme sample is then solely from Mn and is shown in Figure 12 along with the results from the reduced enzyme.

In order to determine if the peaks in the spectra of Figure 12 arise from hyperfine coupling to nitrogen or hydrogen multifrequency experiments were carried out. Figure 13 shows the ESEEM spectra for the reduced enzyme sample of Figure 12 that were acquired using microwave frequencies of 8.90 and 11.20 GHz. At g=1.90 this corresponds to magnetic field values of 3500 and 4200 gauss respectively. Peaks arising from protons would then shift by 4 MHz between the two spectra of Figure 13, while for nitrogen the shift should be 0.6 MHz or less. Comparison of the spectra of Figure 13 shows that the shifts are those expected for hyperfine coupling to nitrogen. This is most clearly seen from the peak at 5.2 MHz in Figure 13A that shifts to 5.55 MHz, Figure 13B.

Quantitative interpretation of the spectra of Figure 12 and 13 is currently not possible due to the complexity of the spectra. In the EPR spectrum of the Mn, in oxidase, only the $m_S = +1/2 \rightarrow -1/2$ fine structure transition is detected, while the other four fine structure transitions are not observed due to their weak intensity. However, the ESEEM spectrum arising from these four weak fine structure transitions can be detected. Simulations of the Q-band EPR spectrum from the N-ras p21 protein, a single Mn binding protein, which has similar A and D values as the Mn in oxidase, has revealed that the five fine structure transitions severlely overlap each other. Simulations of the 2-pulse ESEEM data from this protein, has shown that the five separate ESEEM spectra, from each of the five fine structure transitions, all have significant intensity and that they are all different. The 2-pulse ESEEM spectrum is the composite of the separate

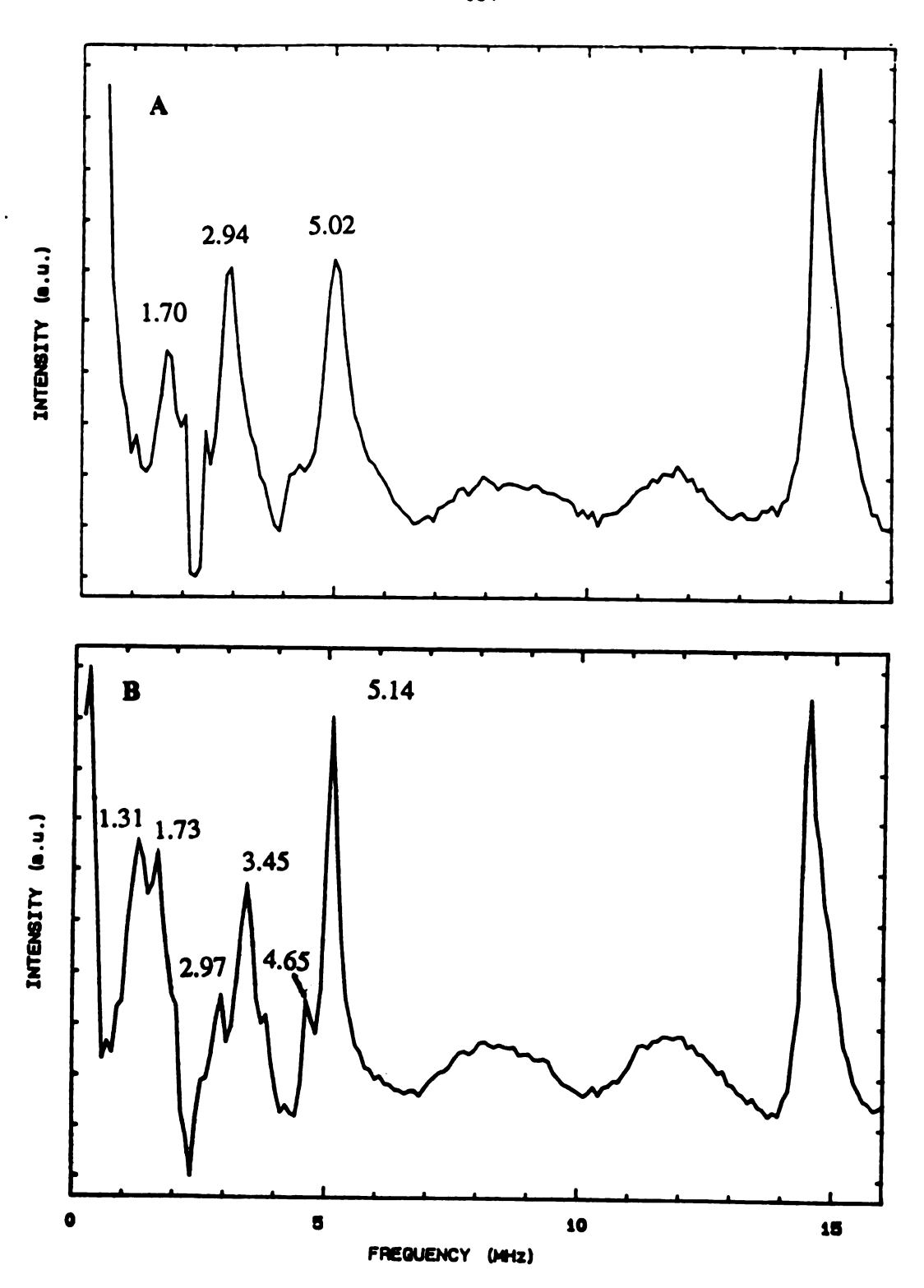


Figure 5.12 3-pulse ESEEM spectra of *Rb. sphaeroides* oxidase grown in the presence of [Mn] = 1 mM, in the (A) oxidized and (B) reduced forms collected at g=1.90. Conditions: same as Figure 5.11.

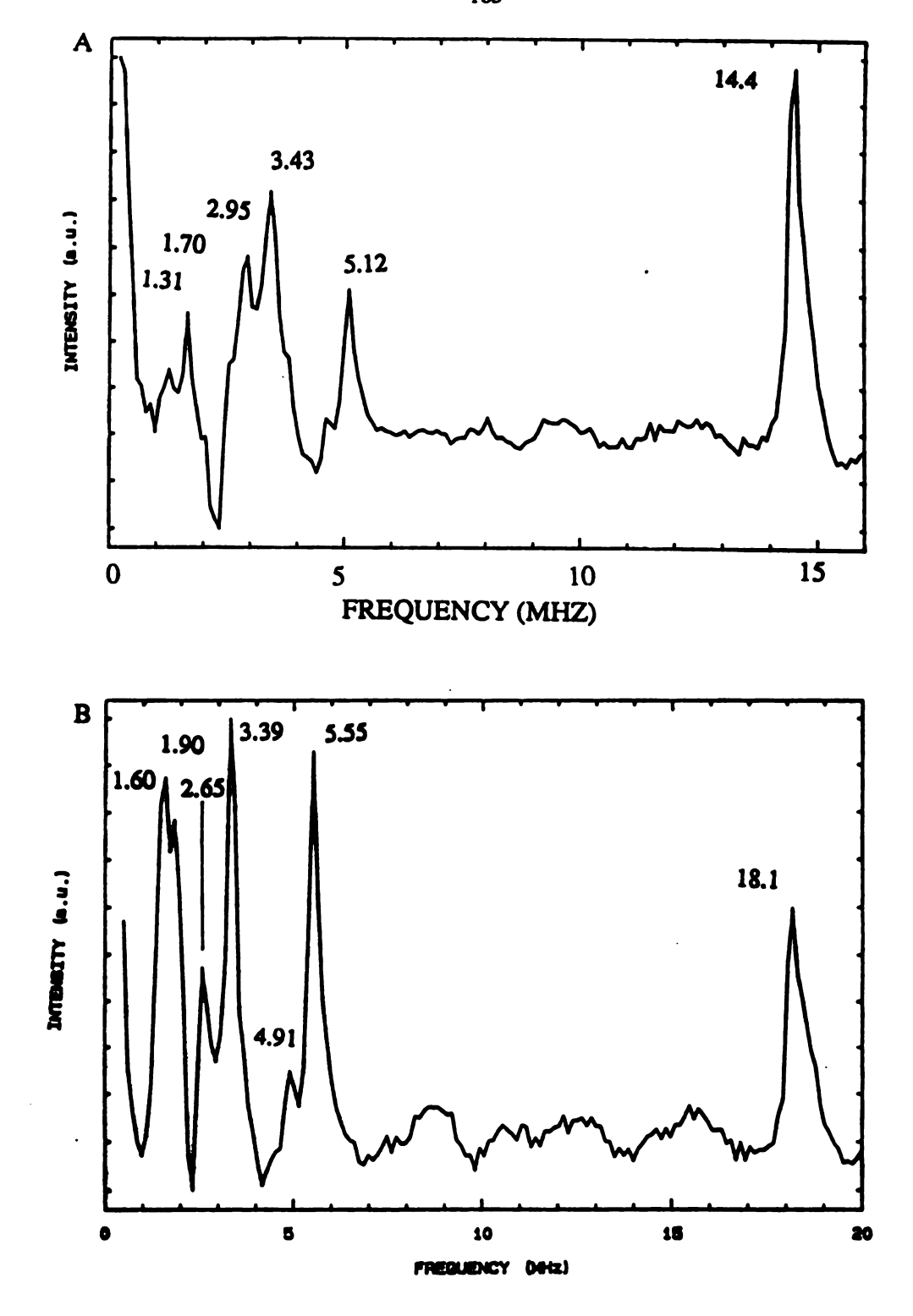


Figure 5.13 3-pulse ESEEM spectra of *Rb. sphaeroides* oxidase grown in the presence of [Mn] = 1 mM, in the reduced form, collected at g=1.90. Microwave frequencies are 8.9 GHz (A) and 11.2 GHz (B). Conditions: same as Figure 5.11 except (A) tau = 300 nsec and (B) tau = 252 nsec.

ESEEM spectrum which come from the five fine structure transitions.^{67,68} As spectra are recorded at different field values the relative intensity of the fine structure transitions will change. This will cause a change in the relative intensity of the five different ESEEM spectra and changing the shape of the composite spectrum.⁶⁸ Current work is beginning to resolve the complexities of spectra from S=5/2 systems and accurate simulations should soon be possible.^{67,68}

A more qualitative understanding of the ESEEM spectra from the Mn of oxidase can be obtained from comparison with data from other Mn binding proteins. The ESEEM spectra from a series of lectins including concanavolin A and pea lectin show a consistent set of nearly identical spectra.⁶⁹ From mutifrequency studies it was shown that the peaks originate from hyperfine coupling to one or more nitrogens. These spectra are also similar to the spectrum obtained for Mn in the presence of a large excess of imidazole.⁶⁹ As the crystal structures of concanavolin A and pea lectin show a single nitrogen ligand to the Mn, the ESEEM spectra for these proteins is interpreted as arising from hyperfine coupling to the ligating histidyl nitrogen.⁶⁹ The ESEEM spectra from the reduced form of oxidase shows a strong similarity with the spectrum observed for pea lectin, which has peaks at 1.4, 2.0, 2.7, 3.3 and 4.9 MHz and a very similar line shape.⁶⁹ As noted above, the oxidase EPR data are also similar to that reported for pea lectin. The ESEEM results for oxidase are thus indicative of a histidine ligand to the Mn. Since the interpretation of the ESEEM is not quantitative it is not possible to determine the number of nitrogens coordinated to the Mn. However, the strong similarity between the oxidase and lectin data, where it is known that there is only one nitrogen ligand, suggests that there is only one nitrogen ligand to the Mn in oxidase, which is a histidine. The mutagenesis results show that the source of the nitrogen is most likely his 411.

As obseved for the EPR data, the ESEEM spectrum of Mn in oxidase also changes upon reduction of the enzyme, Figure 12. Since the position of the peaks in the ESEEM spectrum is determined by hyperfine and quadrapole coupling, it is the change

in the magnitude of these values that will cause changes in the ESEEM spectrum. For the nitrogen ligand observed in the ESEEM spectrum of Mn in oxidase, factors that influence the value of the parameters listed above include bond length, bond angle and possibly rotation of the imidazole portion of the histidine side chain. Secondary effects from changes at other ligands to the metal may also affect the ESEEM spectrum. If one or more of the other ligands were to form a stronger bond with the Mn, with a change in the oxidation state of the enzyme, this could cause a larger portion of the unpaired spin density to reside on the ligand. This would cause a decrease in both the isotropic and dipolar parts of the hyperfine coupling. The decrease in the hyperfine coupling to the Mn, observed in the Mn EPR data upon reduction of the enzyme, shows that a portion of the unpaired spin density has moved from the Mn to the ligands. The changes in the ESEEM spectra are minor, however, and structural changes that occure at the Mn site, as suggested by the EPR data, are slight.

Model for the Mn binding site:

While the complete stucture of the Mn binding site is not understood, much is known about this metal binding site from the subunit I mutagenesis experiments and the EPR and ESEEM characterization of the bound Mn. Additional information about Mn binding sites in proteins can be gleaned from the several solved crystal structres of Mn binding proteins.⁶³ By using these two sets of information several models for the Mn binding site in oxidase have been contructed.

A study of the crystal structures of Mn-binding proteins reveal some common characteristics within this class of proteins. The only residues that have been detected as ligands to the Mn are glutamate, aspartate and histidine in manganese specific binding sites. One or two water molecules are also common ligands to the metal and in some cases the ligand sphere is completed with a backbone carbonyl.⁶³ The ligand geometry

around the the metal is six coordinate with a near octahedral geometry in the proteins characterized to date. There are, in all cases, moderate distortions away from this octahedral symmetry. Bond angles between ligands cis to each other range from 63-121° and the angle between trans ligands range from 151-177°. The bond lengths can also vary considerably; the Mn-O bond lengths for glutamates and aspartates are observed to lie in the range 1.92-2.37 Å. The Mn-N distance for histidine covers a smaller range, 2.2-2.3 Å and, for bound water, the observed bond lengths are 2.0-2.3 Å. It is this variation in bond distances and angles, along with the variation of ligand types, that lead to the appearence of non-zero D and E values.⁴⁵

The crystal structures of concanavolin A and parvalbumin show significant distortions from octahedral symmetry at the Mn binding site. For concanavolin A the metal ligand bond lengths are very nearly equal while the bond angles cover the ranges discussed above. The opposite is seen for parvalbumin, where the bond angles cover a small range and are near the values expected for octahedral symmetry, while the bond lengths differ by 0.5 Å. EPR studies of these proteins reflect these distortions with some of the larger D and E values reported for this class of proteins. Detailed simulations of the Q and X-band EPR spectra for concanovolin A show that D=230 G and E=46 G.62 For parvalbumin the value of D was estimated to be 400 G and E was not determined. 70 The EPR data for a series of plant lectins showed smaller ZFS parameters, D=140-170 G.⁷¹ As discussed above these values are close to those observed for Mn in oxidase. The lectin from pea has also been studied by EPR, however, the value of D was not determined.⁷² Comparison with the EPR data from the other plant lectins shows that the value of D for the pea Lectin is also in the range of 120-170 G. In the crystal structure of pea lectin the bond angles cover a smaller region and are much closer to the ideal 900 and 180°. The bond distances are also grouped closer together and close to the average for the Mn binding proteins. 63 This more symmetric environment of pea lectin correlates well with the estimated value of D.

With the similarity in EPR and ESEEM data between pea lectin and oxidase, the structure of the Mn binding site in this lectin was used as a template to contruct a model for the Mn binding site in oxidase. Ligands to the metal include a nitrogen from the imidazole group of his411 and possibly an oxygen from asp412. Since aspartates have a carboxy group this side chain may act as a bidentate ligand. In addition, previous studies by EPR of water exchange in the oxidase from *P. denitrificans* has shown that there is at least one water bound to the metal.²⁷ The two residues plus the water may account for as many as four of the six ligands. Within this context modeling was done to to investigate ligation environments that are compatable.

In the initial model, the only restiction used was that the dihedral angles of the protein backbone fall within the normally occupied regions of the Ramachandran plots. Efforts to develop a model where asp412 acted as a bidentate ligand with his411 also as a ligand were not possible. No side chain orientation allow us to obtain reasonable bond lengths or angles. Relaxing the ligand environment such that asp412 is a monodentate ligand allowed us to contruct a more reasonable binding site geometry. In this model the Mn-O bond length was 2.12 Å and the Mn-N bond length was 2.26 Å. The ligands could only be trans to each other with an angle of 170°. These values are very similar to those seen in pea lectin. In this model there is a limited range of orientations that the protein backbone can take to direct the two side chains in the direction needed to ligate the metal. Assuming octahedral symmetry the allowed range of orientations of the backbone leave only a small pocket at one of the ligand positions. This may be the position of the water ligand but there may even be steric hinderance to a water molecule entering this pocket. This suggests that both his411 and asp412 may not be ligands. This would be consistent with the crystal stuctures of Mn binding proteins where the nearest residues sequentially, in the protein, that are ligands are two residues apart. 63

While his411 and asp412 are both important in constructing the Mn binding site they may serve different roles. From the ESEEM data, the histidine is assigned as a

ligand whereas D412 may serve as a hydrogen bond acceptor and form a hydrogen bond with the water molecule ligated to the metal, Figure 14. This model has the Ne nitrogen of histidine as the ligand to Mn with a bond length of 2.20 Å. The Mn-O(H₂O) bond length is 2.15 Å and the N_{his}-Mn-O_{H₂O} is 90°. This configuration shows a metal binding site with characteristics similar to the pea lectin which has two water ligands. The crystal structures of Mn binding proteins show hydrogen bonds between water molecules, that are ligands to the metal, and aspartates and glutamates. In contrast to the model where both his411 and asp412 are both ligands, this model leaves four open ligand binding sites that are not sterically hindered. This model is also consistent with the mutagenesis results, in that mutation of his411 or asp412 causes either a loss of a ligand or the loss of an important hydrogen bond, both of which disrupt the metal binding site and cause loss of the metal.

The model descibed above accounts for only two of the six ligands to the metal. Assigning his411 as a ligand places the metal outside the membrane on the periplasmic side. This is also the side of the enzyme that contains the soluble portion of subunit II. The remaining ligands to the metal then most likely have two sources: the other interhelix loops of subunit I or residues from subunit II. Within the proposed helical portion of subunit I there are no glutamates, aspartates or histidines near the periplasmic end of the helices that could serve as ligands. In the interhelix region of subunit I, there are 11 possible ligands. In particular there is an aspartate, asp400, in the same loop as his411 and asp412. No mutagenesis work has been carried out on this residue, so its involvement in the metal binding site is unknown. The length of several of the interhelix loops on the same side of the membrane as the 9-10 loop are large compared to the surface area of the membrane embedded portion of the protein. It is possible for several of these loops to overlap each other and form the manganese binding site.

The second possibility is that the manganese may have some of its ligands supplied by subunit II. The sequences from subunit II contain several conserved

glutamates and aspartates that could be ligands to the Mn. A metal binding site at the interface of two proteins has been observed in the bacterial reaction center, a membrane bound enzyme whose crystal structure has been solved.⁷⁵ This enzyme contains three membrane integral proteins labelled L, M and H. The two subunits L and M are linked together at their interface by a iron ion. The iron is ligated by four histidines, two each from each subunit.⁷⁵ The role of the iron ion appears to be structural, as it is not involved in the redox reactions of the enzyme. The site, while highly metal specific, will substitute a series of divalent metals including manganese and zinc for iron without a reduction in activity.⁷⁶

Role of bound Mn

Since the Mn is not redox active, it is not involved in the electron transfer reactions within the enzyme. The metal most likely performs a structural role within the enzyme. Due to its proximity to the binuclear center the Mn may be involved in controlling the protein environment in the vicinity of CuB and cyt a3. The structure of the binuclear center is expected to be well controlled due to the enzymatic activity occurring at this site. In addition to oxygen reduction to water, this site must also correlate electron transfer steps with protonation steps and to gate electron transfer from cyt a to the binuclear center. Considering this role for Mn, the ligands to this metal would be expected to originate from subunit I. The ligands may be from one or more of the extramembrane loops on the same side of the membrane as his411.

If the Mn is necessary for retaining the proper structure of the binuclear center, it would be expected that loss of the Mn, or the other metals binding at this site, would cause a disruption of the stucture of the binuclear center. This correlation holds for the mutants H284A and H333Y which show lower quantities of bound Mn, when compared to wild type, and loss of the raman peaks from cyt a₃. In addition, the enzyme is

completely inactive. However, the mutant H411A, in the 9-10 loop, shows a normal cyt a3 raman spectrum, indicative of a native site, a complete loss of Mn and a 50% loss in activity. Since this residue is a ligand to the Mn it is doubtfull that any metal is binding at this site in the mutant. These results imply that the loss of Mn, or any other metal at this site, effects the activity of the enzyme but not the structure of the binuclear center. The Mn then is not essential for proper binuclear center structure and must be serving some other role within the enzyme.

Since some of the ligands to Mn may come from subunit II, the Mn may be present to facilitate the correct interaction of subunits I and II. For example, a proper alignment of subunits I and II may be necessry for rapid electron trasnfer between Cu_A and cyt a; this alignment may be provided by the metal bridge. This is consistent with the bacterial quinol oxidases that do not bind Mn but also do not contain Cu_A.⁷⁷ In these systems a well defined interaction between the two subunits may not be as important. There is evidence for the metal serving as a bridge between subunits I and II from studies of the oxidase from *P. denitrificans*. Purified subunit I of *P. denitrificans* oxidase retains the EPR signal for cyt a but the manganese signal is absent.²⁷ Removal of subunit II and with it one or more potential ligands to the manganese may destroy the metal binding site. As mentioned above, the manganese ligand environment is affected by the oxidation state of Cu_A, suggesting a spatial proximity between the manganese and subunit II.

Function of the conformational change at the Mn binding site:

Cytochrome oxidase tightly binds cyanide at cyt a₃ which inhibits oxygen reduction.⁷⁸ The rate at which cyanide binds depends on whether the enzyme is in the open or closed forms. The fully oxidized enzyme is in the closed form and binds cyanide with a rate constant of approximately 10 M⁻¹s⁻¹. In the partially reduced form of the enzyme, with Cu_A and cyt a reduced, the enzyme is in the open conformation and the rate

constant for cyanide binding increases by $10^5.79$ In the open form of the enzyme cyanide apparently has greater accessibility to the binuclear center. The protein thus undergoes a conformational change upon partial reduction, which presumably has a functional significance. Under normal conditions the oxygen does not bind to the binuclear center until both metals are reduced. The conformation change from the closed to the open form in the two electron reduced enzyme may allow oxygen to approach the binuclear center and then, upon reduction, oxygen binding to the binuclear center can occur rapidly. The rate of oxygen binding, $k=3.5\times10^4$ s⁻¹, is rapid compared to the rate of intramolecular electron transfer to the binuclear center, with rate constants of 90 s⁻¹ and $20 \text{ s}^{-1}.80,10$

It has also been reported that electron transfer from cyt a to the binuclear center cannot occur until the addition of two electrons, reducing Cu_A and cyt a. 81 Again, some conformational change must occur to control the flow of electrons within the enzyme. This conformation change of the protein has been postulated to be part of the enzymes proton pumping mechanism of the enzyme, however, to date there is no data to support this proposal.

The manganese itself has not been implicated either as the site that is causing the conformational change in the protein or in the proton pumping mechanism. The Mn appears to only be acting as a reporter of changes in the enzymes structure. The change in the EPR spectrum of Mn upon reduction of the enzyme does, however, give an additional sensitive technique to monitor the shift from the open to closed forms.

Conclusion

The cyt c type oxidase from *Rb. sphaeroides* is spectroscopically nearly identical to that seen for the exstensively studied beef heart oxidase. In addition it is also nearly the same as that observed for the well studied bacterial oxidase from *P. denitrificans*.

The only difference in the EPR data between Rb. sphaeroides and beef heart is a shift in the g_Z values of cyt a which is explained by one or two strong hydrogen bonds to the histidine ligands of cyt a.

Similar to other bacterial cyt c oxidases, the enzyme also binds substochiometric quantities of Mn. The Mn is tightly bound and an integral part of the enzyme. The amount of bound Mn can be affected by the relative amount of Mn and Mg in the growth medium with an upper limit of the bound Mn stochiometry of 0.7 Mn/oxidase. This limitation is most likely imposed by the regulatory mechanism of the cell, as to the final metal concentrations inside the cell. The Mn binding site also binds Mg and may also bind other metals that are in the +2 oxidation state. Mutagenesis experiments implicate residues his411 and asp412 of the 9-10 interhelix loop as constructing the Mn binding site. From the studies of other mutants in this loop and mutants near the binuclear center the Mn binding site appears to be located near the binuclear center

EPR characterization of the Mn shows that its binding site is six coordinate with predominantly oxygen and nitrogen ligands. Pulsed-EPR studies of the Mn shows ligation to a single nitrogen that appears to originate from a histidine. This nitrogen is believed to originate from his411. The EPR spectra of Mn in the fully oxidized and fully reduced forms of the enzyme show small differences. From the X-and Q-band EPR data, the changes in the zero field splitting parameters D and E between the reduced and oxidized enzyme are ≤ 30 G. From comparison with the EPR data and crystal structures of Mn binding proteins these changes in D and E are estimated to represent changes in metal ligand bond lengths of 0.1 Å and/or bond angles of 10° . The cw and pulsed EPR data also show a similarity to the spectra from lectins, which are single Mn binding proteins.

By using the crystal structure of pea lectin as a template, a model for the Mn binding site in oxidase was constructed. A plausable model has his411 as a ligand to the metal and asp412 acting as a hydrogen bond acceptor to a water ligand. This leaves four

empty binding site on the metal that are filled by other residues of the enzyme. While some of these may come from subunit I evidence suggests that one or more also come from subunit II.

While the role of tightly bound metals in the +2 oxidation state to oxidase have in the past been simply described as structural, the data presented here, at least for Mn, sheds some light onto the function of this ion in the enzyme. The Mn appears to act as a bridge between subunits I and II, providing a mechanism for aligning them in an optimal confiugation, for electron transfer between Cu_A and cyt a. Whether this Mn/Mg binding site is the same site that binds only Mg in the beef heart oxidase is unknown. However, the HDTY sequence in the 9-10 interhelix loop is also conserved in the beef heart oxidase. If this is the same site, through the course of evolution, this metal binding site may have acquired a higher degree of specificity for Mg than observed for the bacterial oxidases.

LIST OF REFERNCES

- 1) Nicholls, D.G. and Ferguson, S.J. Bioenergetics 2, Acedemic Press, London, 1992
- 2) Wikstrom, M.K.F. Nature, 1977, 266, 271
- 3) Saraste, M., Holm, L., Lemieux, L., Lubben, M. and van der Oost, J. Biochem. Soc. Trans., 1991, 19, 613.
- 4) Brown, S., Moody, A.J., Mitchell, R. and Rich, P.R. FEBS Lett. 1993, 316, 216.
- 5) Hill, B.C. J. Biol. Chem., 1991, 266, 2219
- 6) Antalis, T.M. and Palmer, G. J. Biol. Chem., 1982, 257, 6194
- 7) Goodman, G. and Leigh, J.S. Biochemistry, 1985, 24, 2310
- 8) Van Gelder, B.F. and Beinert, H. Biochim Biophys Acta, 1969, 189,1
- 9) Scott, R.A. and Schwartz, J.R. Biochemistry, 1986, 25, 5546.
- a) Lindsay, J.G., Owen, C.S. and Wilson, D.F. Archs. Biochem. Biophys. 1975, 169, 492;
 b) Malatesta, F., Sarti, P., Antonini, G., Vallone, B. and Brunori, M. Proc. Natn. Acad. Sci., 1990, 87, 7410
- 11) Babcock, G.T. and Wikstrom, M. Nature, 1992, 356
- 12) Babcock, G.T., in Biological Applications of Raman Spactroscopy, (Spiro, G.T. Ed.), John Wiley and Sons, New York, 1988, p 293
- 13) Martin, C.T., Scholes, C.P. and Chan, S.I. J.Biol. Chem. 1985, 260, 2857
- 14) Stevens, T.H. and Chen, S.I. J.Biol. Chem., 1981, 256, 1069
- 15) Guss, J.M. and Freeman, H.C. J. Mol Biol., 1983, 169, 521
- 16) Stevens, T.H., Martin, C.T., Wang, H., Brudvig, G.W., Scholes, C.P. and Chan, S.I. J.Biol. Chem., 1982, 257, 12106
- 17) Li, P.M., Gelles, J., Chan, S.I., Sullivan, R.J. and Scott, R.A. Biochemistry, 1987, 26, 2091
- 18) Reinhammar, B., Malkin, R., Jensen, P., Karlsson, B., Andreasson, L-E., Aasa, R., Vanngard, T. and Malmstrom, B.G. J. Biol. Chem., 1980, 255, 5000

- 19) Cline, J., Reinhammar, B., Jensen, P., Venters, R. and Hoffman, B.M. J. Biol. Chem., 1983, 258, 5124
- 20) a) Ludwig, B. and Schatz, G. Proc. Natl. Acad. Sci. USA, 1980, 77, 196; b) Haltia, T., Finel, M., Nakari, T., Raitio, M., Wikstrom, M. and Saraste, M. EMBO J., 1989, 8, 3571.
- 21) Muller, M., Schlapper, B. and Azzi, A. Proc. Natl. Acad. Sci USA, 1988, 85, 6647
- 22) Buse, G. and Steffens, G.C.M. J. Bioener. Biomem., 1991, 23, 269
- 23) Einarsdottir, O. and Caughey, W.S., Biochem. Biophys. Res. Comm., 1985, 129, 840
- 24) Naqui, A. Powers, L., Lundeen, M., Constantinescu, A. and Chance, B. J. Biol. Chem. 1988, 263, 12342
- 25) a) Numata, M., Yamazaki, T., Fukumori, Y. and Yamanaka, T., J. Biochem., 1989, 105, 245; b) Lauraeus, M., Haltia, T., Saraste, M. and Wikstrom, M., Eur. J. Biochem., 1991, 197, 699
- 26) Seelig, A., Ludwig, B., Seelig, J. and Schatz, G., Biochim. Biophys. Acta, 1981, 636, 162
- 27) Haltia, T., Biochim. Biophys. Acta, 1992, 1098, 343
- 28) Donahue, T. and Kaplan, S. Methods Enzymol. 1991, 204, 459
- 29) a) Gabel, c. and Maier R.J. Nucleic Acuds Res. 1990, 18, 6143; b) Bott, M., Bollinger, M. and Hennecke, H. Mol. Microbiol., 1990, 4, 2147
- 30) Shapleigh, J.P., Hosler, J.P., Tecklenburg, M.M.J., Kim, Y., Babcock, G.T., Gennis, R.B. and Fersuson-Miller, S., Proc. Natl. Acad. Sci. USA, 1992, 89, 4786
- 31) Quinn, R., Valentine. J.S., Byrn, M.P. and Strouse, C.E. J. Am. Chem. soc., 1987, 109, 3301
- 32) Weissbluth, M. Struct. Bonding, 1967, 2, 1
- 33) Griffith, J.S. Biopolymers, Symp. 1 1964, 35
- 34) Kotani, M. Biopolymers, Symp 1 1964, 67
- a) Blumberg, W.E. and Peisach, in Bioinorganic chemistry Advan. Chem. Series., 100 (Gould, R.F., ed.), American Chemical Society, Washinhton, D.C., 1971, p271; b) Peisach, J., Blumberg, W.E. and Adler, A. Annal. N.Y. Acad. Sci., 1973, 310
- 36) Palmer, G. Biochem. Soc. Trans., 1985, 13, 548
- 37) Babcock, G.T., Steelandt, J.V., Palmer, G., Vickery, L.E. and Salmeen, I. in Cytochrome Oxidase (King, T.E., ed.) Elsevier, Holland, 1979, p105

- 38) Walker, F.A. Reis, D. and Balke, V.L. J. Am. Chem. Soc., 1984, 106, 6888
- 39) Sievers, G., Gadsby, P.M.A., Peterson, J. and Thomson, A.J. Biochim. Biophys. Acta., 1983, 742, 637
- 40) Gadsby, P.M.A., Thomson, A.J. FEBS LETTERS, 1982, 150, 59
- 41) a) Erecinska, M., Wilson, D.F. ang Blaise, J.K. Biochim. Biophys. Acta., 1979, 545, 352; b) Albracht, S.P.J., Van Verseveld, H.W., Hagen, W.R., and Kalkman, M.L. Biochim. Biophys. Acta., 1980, 593, 173
- 42) Aasa, R., Albracht, S.P.J., Falk, K., Lanne, B. and Vanngard, T. Biochim. Biophys. Acta., 1976, 422, 260
- 43) Hosler, J.P., Fetter, J., Tecklenburg, M.M.J., Espe, M., Lerma, C. and Ferguson-Miller, S., J. Biol. Chem., 1992, 267, 24264
- 44) Misra, S.K. and Sun, J-S. Magnetic Resonance Review, 1991, 16, 57
- 45) Reed, G.H. and Markham, G.D. Biol. Mag. Res. 1984, 6, 73
- 46) Shaffer, J.S., Farach, H.A. and Poole, C.P., Jr., Phys. Rev., 1976, B13, 1869
- 47) Beltran-Lopez, V. and Castro-Tello, J., J. Mag. Res., 1980, 39, 437
- 48) Kudynska, J., Zhang, Y.P. and Buckmaster, H.A., J. Mag. Res., 1992, 96, 445
- 49) Sistrom, W.R., J. Gen. Microbiol., 1962, 28, 607
- 50) Ludwig, B., Methods in Enzymology, 1986, 126, 153
- 51) a) Metal Ions in Biological Systems 26(H.Sigel and A. Sigel, eds.) Marcel Dekker, New York, 1990, p1; b) Larson, E.J. and Pecoraro, V.L., in Manganese Redox Enzymes, (Pecoraro, V.L., Ed.) VCH Publishers, 1992, 1.
- 52) a)Eriksson, A.E., Jones, T.A. and Liljas, A. Proteins, 1988, 4, 274; b) Tainer, J.A., Getzoff, E.D., Beem, K.M., Richardson, J.S., Richardson, D.C. J. Mol. Biol., 1982, 160, 181; c) Holmes, M.A. and Matthews, B.W. J. Mol.Biol., 1982, 160, 623
- 53) a) Drumheller, J.E. and Rubins, R.S., J. Chem. Phys., 1986, 85, 1699, b) Wolterman, G.M. and Wasson, J.R., Inor. Chem., 1973, 12, 2366; c) Jain, V.M. and Venkateswarlu, P., J. Phys. C: Solid State Phys., 1979, 12, 865; d) Wolterman, G.M. and Wasson, J.R., Chem. Phys. Lett., 1972, 16, 92
- 54) a) Marcos, D.M., Folgado, J-V. and Beltran-Porter, D., Poyhedron, 1990, 9, 2699; b) Joeston, M.D., Hussain, M.S. and Lenhert, P.G., Inor. Chem., 1970, 9, 151
- a) Kroneck, P.M.H., Antholine, W.E., Kastrau, D.H.W., Buse, G., Steffens, G.C.M. and Zumft, W.G. FEBS, 1990, 268, 274; b)Scott, R.A., Zumft, W.G., Coyle, C.L. and Dooley, D.M. Proc. Natl. Acad. Sci. USA, 1989, 86, 4082; c) Kroneck, P.M.H., Antholine, W.A., Reister, J. and Zumft, W.G. FEBS LETTERS, 1988, 242, 70; d) Farrer, J.A., Thomson, A.J., Cheesman, M.R., Dooley, D.M. and Zumft, W.G. FEBS LETTERS, 1991, 294, 11

- 56) Kelly, M., Lappalainen, P., Talbo, G., Haltia, T., van der Oost, J. and Saraste, M. J. Biol. Chem. in press
- 57) a) Shapleigh, J.P., and Gennis, R.B. Mol. Microbiol. 1992, 6, 635; b) Cao, J., Shapleigh, J.P., Gennis, R.B., Revzin, A. and Ferguson-Miller, S. Gene, 1991, 101, 133; c) Cao, J., Hosler, J., Shapleigh, J.P., Revzin, A. and Ferguson-Miller, S. J. Biol. Chem., 1992, 267, 24273
- 58) Hosler, J.P., Shapleigh, J.P., Tecklenburg, M.M.J., Thomas, J.W., Kim, Y., Espe, M., Fetter, J., Babcock, G.T., Alben, J.O., Gennis, R.B. and Ferguson-Miller, S. Biochemistry (in press), 1993.
- 59) Drumheller, J.E. and Rubins, R.S. J. Phys. Chem. 1986, 85, 1699; b) Marcos, D., Folgado, J-V., Beltran-Porter, D., Prado, M., Pulcinelli, S.H. and Almeida_Santos, R.H. Polyhedron, 1990, 9, 2699
- 60) Weltner, W., Jr., Magnetic Atoms and Molecules, Van Nostrand Reinhold, New York, 1983
- 61) Reed, G.H. and Leyh, T.S., Biochemistry, 1980, 19, 5472
- 62) Meirovich, E. and Poupko, R., J. Phys. Chem., 1978, 82, 1920
- a) Declercq, J-P., Tinant, B., Parello, J. and Rambaud, J., J. Mol. Biol., 1991, 220, 1017;
 b) Becker, J.W., Reeke, G.N., Wang, J.L., Cunningham, B.A. and Edelman, G.M., J. Biol. Chem., 1975, 250, 1513;
 c) Yamashita, M.M., Almassy, R.J., Janson, C.A., Cascio, D. and Eisenberg, D., J. Biol. Chem., 1989, 264, 17681;
 d) Einspahr, H., Parks, E.H., Suguna, K., Subramanian, E. and Suddath, F.L., J. Biol. Chem., 1986, 261, 16518;
 e) Whitlow, M., Howard, A.J., Finzel, B.C., Poulos, T.L., Winborne, E. and Gilliland, G.L., Proteins, 1991, 9, 153
- 64) Baker, G.M., Noguchi, M. and Palmer, G., J. Biol. Chem., 1987, 262, 595
- 65) Brudvig, G.W., Stevens, T.H., Morse, R.H. and Chan, S.I., Biochemistry, 1981, 20, 3912
- a) Tipton, P.A., McCracken, J., Cornelius, J.B., Peisach, J. Biochemistry, 1989, 28, 5720;
 b) Eads, C.D., LoBrutto, Kumar, A. and Villafranca, J.J. Biochemistry, 1988, 27, 165;
 c) Tipton, P.A. and Peisach, J. Biochemistry, 1991, 30, 739;
 d) LoBrutto, R., Smithers, G.W., Reed, G.H., Orme-Johnson, B.H., Tan, S.L. and Leigh, J.S. Biochemistry, 25, 5654
- 67) Coffino, A.R. and Peisach, J. J. Chem. Phys., 1992, 97, 3072
- 68) Larsen, R.G., Halkides, C.J. and Singel, D.J. J. Chem. Phys., 1993, 98, 6704
- 69) McCracken, J., Peisach, J., Bhattacharyya, L. and Brewer, F. Biochemistry, 1991, 30, 4486
- 70) Hartshore, D.J. and Boucher, L.J., in Calcium Binding Proteins, (Drabikowski, W. Ed) Elsevier, Amsterdam, 1974, p30
- 71) Meirovitch, E., Brumberger, H. and Lis, H., Biophysical Chemistry, 1978, 8, 215

- 72) Bhattacharyya, L. Freedman, J., Brewer, C.F., Brown, R.D. and Koenig, S.H. Arch. Biochem. Biophys. 1985, 240, 820
- 73) Holm, L., Saraste, M. and Wikstom, M., EMBO J., 1987, 6,2819
- 74) Saraste, M., Q. Rev. Biophys., 1990, 23, 331
- 75) a) Deisenhofer, J., Epp, O., Miki, K., Huber, R. and Michel, H., Nature (london), 1985, 318, 618; b) Allen, J.P., Feher, G., Yeates, T.O., Komiya, H. and Rees, D.C., Proc. Natn. Acad. Sci. USA, 1987, 84, 5730
- 76) Debus, R.J., Feher, G. and Okamura, M.Y., Biochemistry, 1986, 25, 2276
- 77) Musser, S.M., Stowell, M.H.B. and Chan, S.I. FEBS Lett., 1993, 327, 131.
- 78) a) van Buren, K.J.H., Zuurendonk, P.F., van Gelders, B.F. and Muysers, A.O. Biochim. Biophys. Acta. 1972, 256, 243; b) van Burren, K.J.H., Niocholls, P. and van Gelder, B.F. Biochim. Biophys. Acta. 1972, 256, 258.
- 79) a) Jones, M.G., Bicker, D., Wilson, M.T., Brunori, M. Colosimo, A. and Sarti, P. Biochem J. 1984, 220, 57; b) Jensen, P., Wilson, M.T., Aasa, R., and Malmstom, B.G. Biochem J. 1984, 224, 829
- 80) Blackmore, R.S., Greenwood, C. and Gibson, Q.H. J. Biol. Chem. 1991, 266, 19245
- 81) Brzezinski, P., Thornstrom, P-E. and Malmstrom, B.G. FEBS LETTERS, 1986, 194, 1
- 82) McCracken, J., Shin, D.H. and Dye, J.L. Appl. Magn. Reson., 1992, 3, 305.
- 83) Mims, W.B. J. Magn. Res., 1984, 59, 291.